

AD-A193 363

RESEARCH ON OCEAN FORECASTING AND NONLINEAR WAVE
PROPAGATION AND NUMERICAL HYDRODYNAMICS IN THE OCEAN
(U) BERKELEY RESEARCH ASSOCIATES INC CA JAN 88

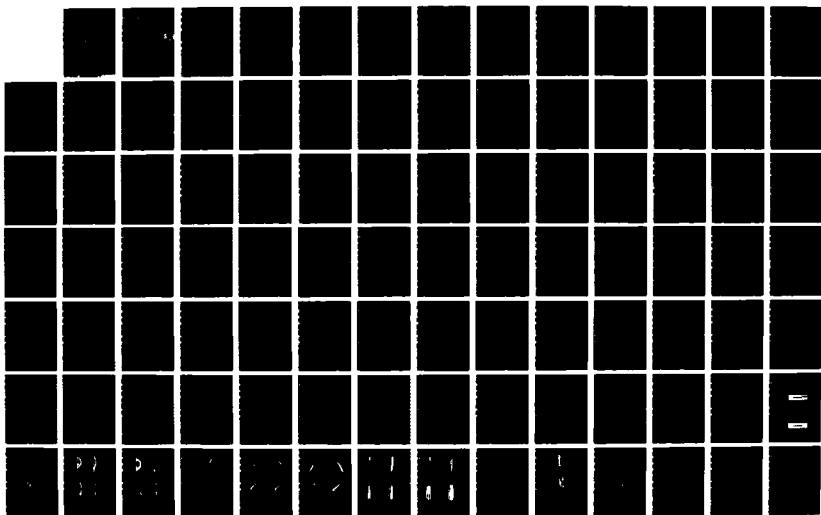
172

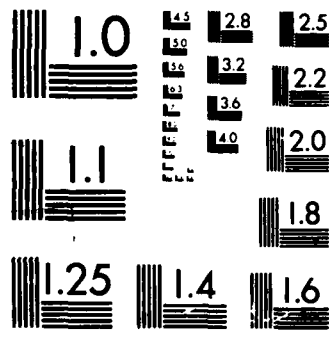
UNCLASSIFIED

BRA-88-W016R N00014-85-C-0680

F/G 8/3

NL





AD-A193 363



BERKELEY RESEARCH
ASSOCIATES, INC.

DTIC FILE COPY

4

BRA-88-W016R
January 1988

RESEARCH ON
OCEAN FORECASTING
AND
NONLINEAR WAVE PROPAGATION
AND NUMERICAL HYDRODYNAMICS
IN THE OCEAN

Final Report

Contract N00014-85-C-0680

for

Naval Ocean Research and Development Activity
NSTL Station, Mississippi 39529

by

Berkeley Research Associates, Inc.
P.O. Box 241
Berkeley, California 94701

DISTRIBUTION STATEMENT A

Approved for public release
Distribution Unlimited

DTIC
ELECTE
APR 07 1988
S
Q
D

88 2 23 103

BRA-88-W016R
January 1988

RESEARCH ON
OCEAN FORECASTING
AND
NONLINEAR WAVE PROPAGATION
AND NUMERICAL HYDRODYNAMICS
IN THE OCEAN

Final Report
Contract N00014-85-C-0680

for

Naval Ocean Research and Development Activity
NSTL Station, Mississippi 39529

by

Berkeley Research Associates, Inc.
P.O. Box 241
Berkeley, California 94701

EXECUTIVE SUMMARY

DISCUSSION

NPE (Nonlinear Progressive-wave Equation Model)

I. INTRODUCTION

II. MODIFICATIONS TO CODE

- A. Damping Region
- B. Range Dependent Sound Speed Profile
- C. Diffusion Timestep Constraint
- D. Tensile Cutoff
- E. Link to CSQ Code at Sandia

III. SIMULATIONS OF DIFFERENT ENVIRONMENTS

- A. Shallow Ocean: Phase Shifting at Fluid-Fluid Interface
 - 1. Reflection and Transmission: Linear Theory
 - 2. Results
- B. Deep Ocean
- C. Ice Surface

IV. CHECKS AND DIAGNOSTICS

- A. Dispersion of a Wave Packet
 - 1. Normal Modes
 - 2. Frequency Spectra
- B. Error Plots

V. CONCLUSIONS

TOPS (Thermodynamic Ocean Prediction System)

I. INTRODUCTION

Accession For	
NTIS CRA&I	<input checked="" type="checkbox"/>
DTIC TAB	<input type="checkbox"/>
Unannounced	<input type="checkbox"/>
Justification	
By <i>per ltr</i>	
Distribution /	
Availability Codes	
Dist	Avail and/or Special
<i>A-1</i>	



II. STATISTICAL PREDICTIONS OF TEMPERATURES IN THE UPPER OCEAN ON SYNOPTIC TIME SCALES

- A. Data
- B. Results
- C. Overview

III. COMPARISON OF MODEL-PREDICTED SHEAR WITH OBSERVATIONS DURING MILE

- A. Model Description
- B. MILE Data
- C. MILE Simulation
- D. Comparison of Observed and Predicted Shear
- E. Inertial Wave Dispersion
- F. Internal Waves
- G. Forecasting Shear Below the Mixed Layer

IV. REAL-TIME SHEAR PREDICTIONS

- A. Comments
- B. Mean Temperature Profile with Depth
- C. Mean Temperature Variance Profiles
- D. Mixed Layer Depth Variability
- E. Frequency Distribution of Various Parameters

V. CONCLUSIONS

Hibler Ice Model

I. INTRODUCTION

II. FORCASTING ICE THICKNESS AND CONCENTRATION IN THE ARC

- A. Model Description
- B. Model Design

C. Model Results

D. Operational Model

III. CONCLUSIONS

BIBLIOGRAPHY

APPENDICES

Appendix A

Section I. Introduction

Section II. The Kalman Filter

Section III. Experimental Design, An Overview

Section IV. Specifying the Filter

Appendix B

1. Statistical Methods

2. Estimating B, G(0)

3. Avoiding Overfitting

FIGURES

TABLES

EXECUTIVE SUMMARY

This final report presents research carried out by Berkeley Research Associates, Inc. under Contract N00014-85-C-0680 with the Naval Ocean Research and Development Activity (NORDA). The report covers the performance period 3 July 1985 through 30 September 1987. During this period, in conjunction with our ongoing effort with NORDA, we carried out research which would improve the accuracy of the NPE (Nonlinear Progressive-Wave Equation), TOPS (Thermodynamic Ocean Prediction System) and Hibler Sea Ice models and would reduce the discrepancies between the models and actual experimental observations. In the following paragraphs we will summarize the work carried out on these models during this performance period.

In order to simulate a greater variety of ocean environments, the NPE computer code has been modified to include a damping region. The inclusion of these enhancements has provided a means to better understanding real oceans. Simulating only the region surrounding and encompassing a moving pulse by moving in the frame of reference of that pulse, the NPE contains a boundary at the bottom of its simulation grid capable only of reflecting the propagating sound waves. In a real ocean environment, one finds that sound waves propagate downward in depth and reflect from such boundaries as the ocean sediment, yet they do not completely reflect from these boundaries as they would from a hard boundary. Rather, some of the sound waves will penetrate the bottom, reflecting, refracting, diffracting and steepening within the sediment, some upward toward the surface, some downward into the sediment (and out of the simulation region). Therefore, a damping region is required to prevent sound waves from reflecting from the bottom of the grid and reentering the simulation. We have therefore included a damping region into the NPE code and have been successful in eliminating these undesirable reflections.

Also important in allowing for the simulation of a greater variety of ocean environments is the implementation of a range dependent sound speed profile. As the NPE demarcates the boundary between an ocean and its sediment by a jump in sound speed, the ocean with one sound speed and the sediment with a somewhat higher one, it is easy

to see that a sound speed profile that is constant in range will allow for only flat boundaries between the ocean and the sediment. By incorporating a sound speed profile which varies with range, more complicated ocean-sediment boundaries may be simulated. We have therefore included a function into the NPE code which is called each timestep to change the ocean-sediment boundary based on the range of the simulation grid and have been successful in simulating various ocean systems with sloping bottoms.

While it is important to increase the variety of problems being simulated by the NPE, it is also important that we continue to improve upon its accuracy. For some time now, the NPE code has maintained a timestep constraint which adjusts the size of the timestep, based on the nonlinearity in the simulation, to an accuracy dictated by the user. Recently, the NPE code has been modified to also include a diffusion timestep constraint. By writing the diffraction portion of the NPE in the form of a continuity equation, the root mean square velocity is calculated and used to obey the Courant-Friedrichs-Lewy condition within a specified level of accuracy. The use of this constraint is an improvement over the previous method used, namely that of manually calculating the initial timestep and keeping it constant throughout the (linear portion of the) simulation.

Also used to provide for greater accuracy is the implementation of a tensile cutoff. In the "real" world, one finds that pressures that are less than zero do not exist. In a "simulated" world, one must "tell" the simulation that such pressures do not exist. We have therefore included a tensile cutoff into the NPE code which prevents the pressure from falling below zero. By using an assumed adiabatic equation of state, we calculate what the overdensity, ρ_{min} must be to correspond to a zero total pressure. We then solve the NPE as usual and, for each timestep, set any overdensity falling below ρ_{min} to the value of ρ_{min} . Therefore, the total pressure at any point or time of the simulation will be at least zero.

Of course the NPE requires that an initial pulse with certain initial conditions be input into the code. While in the past we have primarily used simple initial pulses for diagnostic purposes (being that it is easier to predict what a simple pulse will do as it propagates than to do so for a complicated pulse), it is important for the NPE to have

some way of including a real ocean initial condition. We have therefore written the code required to take the output of the nonlinear CSQ code from Sandia and input it into the NPE as an initial condition. The NPE will therefore be capable of simulating oceans in which the initial conditions are indicative of a real ocean.

The remainder of the NPE section of this report is used to show some results which have been accumulated throughout this performance period. Shallow, deep and ice containing oceans are simulated, and the results of error and diagnostic tests are shown.

In predicting temperature profiles in the upper ocean, different statistical models may be used. Of those presently used, the simplest is that of climatology. This method is primarily used when recent observations in an area are unavailable. Next up the ladder of complexity is persistence. This method is used when recent temperature profiles are available. Uppermost in complexity are the thermo-dynamic models. An example of such a model is the Mellor-Yamada Type II Model which is used in FLENUMOCEANCEN's (Fleet Numerical Ocean Prediction System) operational northern hemisphere ocean forecast model TOPS (Thermal Ocean Prediction System).

During this past performance period, we examined the ability of statistical techniques to forecast upper ocean deviations from climatology on 1 to 7 day time scales. Deviations in the 2.5 to 62.5 meter region in depth were predicted using available information on surface conditions and "recent" deviations at the same location. The results represented the best predictions that regression procedures could give when blending surface data with recent profiles. Methods were developed and tested on data collected during 1983 and 1984 from OWS Romeo in the North Atlantic.

Information on changes in sea surface temperature (SST) could be combined with recent deviations from climatology to improve on persistence in the upper 2.5 to 17.5 meter depths. Below 17.5 m, changes in SST and temperature were too slightly correlated for linear prediction of the latter to be effective. Surface forcing information, including wind stress and heat fluxes, were examined for their usefulness in prediction. While wind stress was correlated with temperature changes near the surface, the ability of statistical

predictions which incorporated knowledge of wind stress was little better than persistence. To improve on persistence, we believe that statistical methods require information as strongly correlated with temperatures below the surface as SST.

We also used a one-dimensional mixed-layer model which employed the Mellor-Yamada Level II turbulence closure scheme as used in TOPS to simulate shear observed in the upper ocean during MILE (Mixed Layer Experiment). In the upper 20 m the magnitude of the predicted shear agreed fairly well with that observed. There was also some agreement in the variability of the shear due to surface forcing. Between 20 and 30 m, the model-predicted shear increased only during the strong wind events which deepened the mixed layer to those depths while the observed shear had a more constant average magnitude and much more variability on short (sub-inertial) timescales. Below 30 m, which was below the deepest penetration of the mixed layer, the model predicted very little shear. The observations, however, showed considerable shear between 30 and 50 m which was the depth of the seasonal thermocline. The average magnitude of the shear in this region was comparable to or larger than that in the mixed layer and most of the variability was on inertial and shorter timescales. A spectral analysis of shear in the seasonal thermocline showed the largest peak at the local inertial frequency and significant contributions from the semi-diurnal internal tide and higher frequency motions.

It was speculated that most of the discrepancy between the observed and predicted shear below 20 m was due to the dispersion of inertial motions and to internal waves. Between 20 and 30 m the inertial motions were likely generated by a mixture of direct local wind-driving and dispersion with dispersion helping to maintain the level of the shear when the mixed-layer was shallow. Below 30 m the inertial motions must be caused primarily by dispersion since vertical mixing did not extend to these depths during MILE.

Using 24-hourly output of temperature, salinity and velocity from TOPS, we displayed the performance of a statistical study of the mean and variance distributions of several upper oceanic environmental parameters: temperature, temperature variance, mixed layer depth, Brunt-Väisälä frequency (N), scalar shear (S), Richardson number (N^2/S^2) and eddy diffusion coefficient. The computations covered a 90-day period from February 1 to

May 1, 1985, at eight ocean stations. Seven of these locations corresponded to weathership locations: Papa, November and Victor in the Pacific, and Romeo, Lima, Charlie and Mike in the Atlantic.

The analysis of the results included frequency of occurrence distributions over various time intervals and at various depth levels as well as the overall distributions. We also examined the vertical profiles of temperature and its variance, Brunt-Väisälä frequency and eddy diffusion as a function of month, ocean station and time of day.

Finally, we used a hydrodynamic/thermodynamic sea ice model to predict sea ice concentration, thickness and drift. The operational model, the Polar Ice Prediction System (PIPS), is based on the Hibler (1979) model only with the addition of thermodynamics similar to that used by Semtner(1976). It is driven by atmospheric forcing from the Navy Operational Global Atmospheric Prediction System (NOGAPS) model, as well as monthly mean climatological ocean currents and oceanic heat fluxes.

Prior to its development, empirical models using the interaction between ocean currents, sea ice and winds were used at FLENUMOCEANCEN. The first operational model was that of Skiles (1968). It related ice drift to geostrophic wind and mean upper ocean currents. It was eventually replaced by a model by Thorndike and Colony (1982). This linear free drift model used an updated representation of ice drift based on numerous observations of drift, geostrophic winds and mean ocean currents. However, while both of these models predicted ice drift, they could not predict ice thickness and concentration. On the other hand, the PIPS model couples the ice movement and growth to thickness and concentration and therefore predicts the characteristics of the ice thickness and concentration as well as temporal changes in these fields. Results using the model are given and compared to observed data.

NPE (Nonlinear Progressive-Wave Equation Model)

I. INTRODUCTION

Traditional approaches (Jensen and Kuperman, 1982) for investigating acoustic wave propagation in an ocean-like waveguide have included the following linear theoretical tools: rays, normal modes (NM), and the parabolic equation (PE) approximation to the linear wave equation. Ray theory contains artificial singularities at focii and caustics and does not include diffraction. Normal modes become cumbersome when extended to include range dependence. The extensively used PE method, a far field approximation to the wave equation, is more amenable to a range dependent environment (Tappert, 1977). When the propagating signal is nonlinear and/or nonsinusoidal in time, however, the NM and PE become less attractive as solution techniques.

An alternative to these methods is the nonlinear progressive wave equation (NPE), which has been shown (McDonald and Kuperman, 1985; McDonald and Kuperman, 1987) to be nonlinear time domain equivalent of the PE. Specifically formulated to study weak shocks and finite amplitude pulses, the NPE is cast in a frame which moves at a constant speed approximately that of the wave.

The NPE is derived by combining fluid momentum and mass continuity equations and substituting an assumed adiabatic equation of state. Retaining lowest order nonlinearity and assuming propagation within a narrow cone of angular half width θ , one can derive a second order nonlinear wave equation for a dimensionless density perturbation R :

$$\frac{\partial^2 R}{\partial t^2} = \nabla^2 c^2 (R + \beta R^2) + O(R^3, R^2 \theta^2), \quad (1)$$

where $\beta = 1 + \partial \log c / \partial \log \rho$, $c^2 = \partial p / \partial \rho$, and $R = \rho' / \rho_0$; c is the local sound speed, p the pressure and β is a thermodynamic variable whose value in the ocean is approximately 3.5. The total density at a given point is $\rho = \rho_0 + \rho'$ where ρ_0 is constant and ρ' is a small but finite perturbation.

Equation (1) is cast in the rest frame of the fluid. By transforming to a frame moving in the x direction at a speed c_o , an approximate first order equation (the NPE) for forward going waves can be derived (McDonald and Kuperman, 1987). Taking $c = c_o + c_1$, where c_1 is a small environmental fluctuation, the NPE is stated as

$$\frac{\partial R}{\partial t} = -\frac{\partial}{\partial x}(c_1 R + \frac{\beta c_o}{2} R^2) - \frac{c_o}{2} \nabla_{\perp}^2 \int_{x_f}^x R dx \quad (2)$$

The operator D/Dt denotes time differentiation in the moving frame. The lower limit x_f of integration is taken to be in the quiescent medium ahead of the wave. On the right hand side of Eq. (2), the c_1 term is refraction, the quadratic term is nonlinear steepening and the integral term is diffraction (implicitly including geometric spreading).

Equation (2) is integrated numerically using Crank-Nicholson for the diffraction term, and flux corrected transport (FCT) methods (Boris and Book, 1973; Zalesak, 1979; McDonald, Ambrosiano and Zalesak, 1985; McDonald and Ambrosiano, 1984) for the x derivative. The environmental sound speed fluctuation c_1 is user defined and can be range and depth dependent. R in Eq. (2) is related to pressure using the approximate equation of state for water,

$$p = \frac{\rho_o c_o^2}{n} [(R + 1)^n - 1], \quad \text{where } n = 7.15 \quad (3)$$

As a linear model ($\beta = 0$ in Equation (2)), the NPE has many advantages over the frequency domain models. Essentially derived as a wave equation, the NPE may be used to find the solution of a problem with a wide band of frequencies. For a model like the parabolic equation (PE), on the other hand, only a single frequency may be solved for at a time with the solutions for the frequencies superimposed. The PE also assumes a continuous sinusoidal wave as the source, while the NPE is more amenable to a pulse. The Normal Modes method has difficulty with a range dependent environment, and Ray Theory does not include diffraction. These problems do not exist with the NPE. Of course, the primary objective behind the NPE is to solve nonlinear problems for a long and narrow wave guide.

II. MODIFICATIONS TO CODE

A. Damping Region

To prevent the reflection of sound waves from the bottom of the simulation grid, a damping region is needed. Figures 1 and 2 show two possible orientations for a simulated ocean environment, the former for a shallow ocean, the later for a deep ocean. In a shallow ocean, the sediment is for the most part considered infinite and therefore does not reflect as a hard surface. In a deep ocean, the ocean is deeper than the simulation grid extends, eventually reach the same infinite sediment found in the shallow ocean case. In simulating either environment, there is an "artificial" boundary formed by the bottom of the simulation grid. As it is usually undesirable to allow reflections from this boundary, a damping region is essential.

To implement a damping region, a damping term must be added to the right hand side of Eq. (2) of the form

$$\frac{\partial R}{\partial t} = -\nu(z)R \quad (4)$$

where $\nu(z)$ is a depth dependent decay factor

$$\nu(z) = \nu_o \tanh(z/\lambda dz). \quad (5)$$

Here, ν_o is the decay constant and λdz is the characteristic decay length. To prevent damping, the decay constant is set to zero.

B. Range Dependent Sound Speed Profile

In shallow ocean simulations, a boundary between the ocean and its sediment must be defined. One way of including a sediment into a simulation is to use a range dependent sound speed profile to define that boundary with the ocean having one sound speed, the sediment having another. We have therefore altered our NPE code to incorporate a function defining the depth of the sediment as a function of range. This function is called

each timestep, and the sound speed profile of the simulation region is adjusted accordingly. With the simulation frame moving at a sound speed c_o , the array c_1 is the variation of the sound speed from c_o at each point on the grid. As the frame moves forward in range, it falls upon a different portion of the ocean and sediment being simulated, and therefore the sound speed profile c_1 is changed.

Once the array c_1 is determined, it is used to solve for refraction in the NPE. As the sound speed variations do not affect diffraction, we may exclude the integral on the right hand side of Eq. (2). The equation may then be rewritten as

$$\frac{\partial R}{\partial t} = -\frac{\partial}{\partial x}(Rv), \quad \text{where } v = (c_1 + \frac{\beta c_o}{2}R). \quad (6)$$

This equation is solved using a one-dimensional Flux Corrected Transport scheme (Boris and Book, 1973; McDonald and Ambrosiano, 1984; Zalesak, 1979) which solves for $R_{i,j}$ in range, i , for each j in depth.

C. Diffusion Timestep Constraint

The NPE uses a variable timestep with restrictions placed on it by both the Crank-Nicholson integration and the Flux Corrected Transport. While we have always used a timestep constraint for the nonlinear FCT, we have only recently added one for diffraction. It is determined by excluding the two left-most terms on the right hand side of Eq. (2), leaving

$$\frac{\partial R}{\partial t} = -\frac{c_o}{2} \int_{x_j}^x dx \frac{\partial^2}{\partial z^2} R. \quad (7)$$

for an (x,z) Cartesian coordinate system. Writing the above in the form of a continuity equation gives

$$\frac{\partial R}{\partial t} = -\frac{\partial}{\partial z} \left[\frac{c_o}{2} \int_{x_j}^x dx \frac{\partial}{\partial z} \right] R \quad (8)$$

which has the general form

$$\frac{\partial \rho}{\partial t} = -\frac{\partial}{\partial z}(\rho v), \quad \text{where } v = \frac{\text{flux}}{\rho}. \quad (9)$$

From Eqs. (8) and (9), one has

$$v_{rms} = \frac{\|\frac{c_0}{2} \int_{x_j}^x dx \frac{\partial}{\partial z} R\|}{\|R\|} \quad (10)$$

and the timestep is limited by

$$\delta t = \min(\delta t_o, \delta t, \frac{\delta z}{v_{rms}} \cdot CFL) \quad (11)$$

where δt_o is the initial timestep, and CFL is the maximum Courant-Friedrichs-Lewy condition set by the user. Though the Crank-Nicholson integration is stable, the inclusion of a timestep constraint insures greater accuracy as δt is adjusted each timestep to be less than a predetermined limit.

For completeness, we see that the size of δt is set by Flux Correction in a similar manner. Excluding the diffraction term in Eq. (2) gives

$$\frac{\partial R}{\partial t} = -\frac{\partial}{\partial x}(c_1 + \frac{\beta c_0}{2} R)R. \quad (12)$$

Again in the form of Eq. (7), one may write

$$v_{max} = \max_{ij}(c_{1ij} + \frac{\beta c_0}{2} R_{ij}) \quad (13)$$

for all points i and j on the grid at time t .

$$\delta t = \min(\delta t_o, \delta t, \frac{\delta x}{v_{max}} \cdot CFL). \quad (14)$$

D. Tensile Cutoff

In the real ocean, the pressure at any given point is never less than zero. In a simulation, however, this is not the case. Unless restricted not to do so, the pressure may become negative. To prevent this from happening, a relation between the overdensity and

the pressure is used to determine when the overdensity drops to a level below which the pressure is zero. The overdensity is then set to the overdensity corresponding to a zero pressure.

Assuming a zero pressure for an undisturbed fluid, an approximate adiabatic equation of state for water (the equation of Tait) is

$$p' = \frac{\rho_o c_o^2}{n} \left[\left(\frac{\rho}{\rho_o} \right)^n - 1 \right] \quad (15)$$

where $n = 7.15$, p' is the pressure of the disturbance, ρ_o is the density of water, ρ is the overdensity of the disturbance and c_o is the speed of sound in the water (Cole, 1948). Therefore, the total pressure is $p = p' + p_o$ where $p_o = \rho_o g(z_s - z)$ is the undisturbed pressure, g is the acceleration due to gravity, z_s is the depth assigned to the ocean surface and z is the depth of the given point at which the pressure is being determined. Therefore a zero pressure corresponds to an overdensity of

$$\rho_{min} = \left[1 - \frac{ng}{c_o^2}(z_s - z) \right]^{\frac{1}{n}} - 1 \quad (16)$$

We simply set the overdensity equal to ρ_{min} when the overdensity falls below ρ_{min} .

E. Link to CSQ Code at Sandia

Sandia's CSQ computer code is used to solve nonlinear ocean acoustics problems, yet unlike the NPE, it is only useful for short range simulations. As the NPE is best suited for long range problems, using the short range results of the CSQ is a useful way of obtaining accurate initial density perturbations as input for the NPE. The grids for the two models may not coincide, however. We therefore use a bilinear interpolation in both range and depth to interpolate the CSQ grid onto the NPE grid. Any NPE grid points falling beyond an edge of the CSQ grid are assigned the value of the closest edge at the corresponding depth (or range).

Output from the CSQ code consists of the arrays $RADCSQ(ICSQ)$, $ZCSQ(JCSQ)$ and $RCSQ(ICSQ, JCSQ)$ where the former two of these are the radial distances and

depths of the grid points respectively, the grid being $ICSQ$ points in range by $JCSQ$ points in depth. The normalized overdensities at the grid points are $RCSQ(ICSQ, JCSQ)$. The required input for the NPE code (along with other parameters such as number of timesteps, size of initial timestep, etc.) consists of $RANGE$, NX , NZ , DX and DZ . These are, respectively, the initial range of the simulation grid, the number of x-grid points, the number of z-grid points, the size of the increment in range and the size of the increment in depth. Using all of the above as input, we interpolate the values of $RCSQ(ICSQ, JCSQ)$ onto the NPE grid, $RNPE(NX, NZ)$, which is then used as input for the NPE.

III. SIMULATIONS OF DIFFERENT ENVIRONMENTS

A. Shallow Ocean: Phase Shifting at Fluid-Fluid Interface

1. Reflection and Transmission: Linear Theory

Consider a fluid-fluid interface as pictured in Figure 3 where fluid 1 has a sound speed of c_0 , fluid 2 of $c' = c_0 + c_1$ and $c_0 < c'$. Snell's law gives for linear plane wave propagation,

$$\frac{c_0}{c'} = \frac{\cos \alpha}{\cos \varphi}. \quad (17)$$

Let the incident, reflected, and transmitted waves be

$$\begin{aligned} & e^{i(k_0(x \cos \alpha - z \sin \alpha) - \omega t)}, \\ R(\alpha) & e^{i(k_0(x \cos \alpha + z \sin \alpha) - \omega t)}, \text{ and} \\ T(\alpha) & e^{i(k'(x \cos \varphi - z \sin \varphi) - \omega t)}, \end{aligned} \quad (18)$$

where $R(\alpha)$ and $T(\alpha)$ are reflection and transmission coefficients. The notation conflict between the density perturbation R and the reflection coefficient $R(\alpha)$ is resolved by the argument α for the reflection coefficient. Interface conditions are continuity of pressure and its normal derivative.

Solving for the reflection coefficient as a function of α , we find that

$$R(\alpha) = \frac{1 - \epsilon}{1 + \epsilon} \quad (19)$$

where

$$\epsilon = \frac{1}{\sin \alpha} \sqrt{\frac{c_0^2}{c'^2} - \cos^2 \alpha}. \quad (20)$$

Likewise for the transmission coefficient,

$$T(\alpha) = \frac{2}{1 + \epsilon}. \quad (21)$$

For the critical angle, (18) and (20) yield

$$\cos \alpha_c = \frac{c_0}{c'}, \quad \varphi = 0 \quad (22)$$

Equations (19) and (20) predict positive reflection for $\alpha > \alpha_c$, and negative reflection for $\alpha \rightarrow 0$. $R(\alpha)$ is complex with unit modulus for $\alpha_c > \alpha > 0$, with $R(\alpha_c) = 1$ and $R(0) = -1$. The reflected wave then suffers a phase change ranging from 0 at $\alpha = \alpha_c$ to 180 degrees for $\alpha \rightarrow 0$. The transmitted wave becomes evanescent in z for $\alpha < \alpha_c$, so that no energy radiates deep into the lower medium. (For a more detailed discussion of reflection and transmission at a fluid-fluid interface, see Ingenito, Ferris, Kuperman and Wolf, 1978.)

2. Results

The results presented here use the NPE to simulate an idealized ocean configuration from a frame moving at the water sound speed c_0 (Figure 4, Region 1). The ocean bottom (Figure 4, Region 2) is idealized to be a level, homogeneous fluid with sound speed $c_0 + c_1$. Beneath the bottom a damping zone (Region 3) has been used to absorb downward propagating waves which would reflect from the bottom of the grid and reenter the simulation.

Figure 4 shows density perturbation contours used for the initial condition $R(x, z, 0)$ of the simulation. Azimuthal symmetry is assumed. Shown is a spherical wave whose radial profile is a half sine wave with density perturbation R (Eq. (2)) ranging from 0.0 to 0.1. A density perturbation of this magnitude, but not necessarily of this shape, could result from an underwater explosion. Range is taken in the x -direction and depth is taken in the z -direction. The grid spacings are $\delta x = 2\text{m}$ and $\delta z = 4\text{m}$. Region 1 describes the ocean, Region 2 the sedimentary ocean bottom and Region 3 the damping region with depths of 400 meters, 80 meters and 120 meters respectively. The width of the simulation box is 200 meters. The sound speed in the ocean is 1500 m/s and that in both the sediment and damping region is 1600 m/s. The initial time step is .01 seconds and is thereafter adjusted to be no greater than half of that allowed by the Courant-Friedrichs-Lewy condition.

From these initial conditions, both linear and nonlinear runs were made ($\beta = 0$ and 3.5 respectively). For the linear case, Figure 5 shows snapshots at times when the grid had traveled 225, 750, 1200 and 2400 meters. For the nonlinear case, Figure 6 shows them at 205, 730, 1200 and 2650 meters. Although the contour scalings change from frame to frame, it is quite clear in both cases that as the range increases, the reflection from the fluid - fluid interface goes from being positive to negative (solid contours are positive values, dotted ones are negative). While in the linear case there is already quite a significant negative reflection at a range of 1200 meters, this is not so in the nonlinear case; the reflected waves have amplitudes more than half those of the incident waves in the linear case while they have amplitudes only about a sixth those of the incident waves in the nonlinear case.

A close look at Figures 5 and 6 reveals another subtle but significant difference: the nonlinear wave travels slightly faster than the linear wave. (Equation (2) reveals a nonlinear contribution to the effective local sound speed). Therefore, the effective sound speed jump from Region 1 to Region 2 is not quite as great in the nonlinear case as it is in the linear one. This increases the effective transmission coefficient across the interface for small angle incidence. For $\alpha < \alpha_c$, ϵ in Eq. (20) is imaginary, and $\|T\|$ increases with c_0 , if c' is held fixed. Figures 5 and 6 reveal that more energy is in fact dumped from Region 1 to Regions 2 and 3 in the nonlinear case than in the linear case. (Since the grazing angle is subcritical, the energy does not radiate deep into the bottom, but resides in a skin layer where incident and reflected energy fluxes are in equilibrium). It seems quite possible that the difference in effective sound speed profiles is the explanation. This difference also means that the critical angle is smaller in the nonlinear case, and therefore the waves will have to travel a greater distance before negative reflections emerge (Plante, Ambrosiano and McDonald, 1987).

B. Deep Ocean

In deep ocean simulations, there is no sediment separating the ocean and the damping region (see Figure 2). Figure 7 shows the initial waveform used in our simulation. The initial range of the simulation is 4194 m, the width of the grid 1050 m and the depth of

the grid 6000 m. The lower 400 m of the grid is a damping region. (Referring to Figure 2, $n_x = 700$, $n_z = 750$ and $noabsorb = 700$.) The grid spacings are $\delta x = 1.5$ m and $\delta z = 8.0$ m, and the initial timestep is .005 seconds. The speed of sound in the ocean is 1540 m/s at the surface, 1495 m/s at a depth of 1000 m and 1560 m/s at depths of 5500 m to 6000 m. At intermediate depths, the sound speeds are linearly interpolated from these values. The source is a single-cycle sine wave of wavelength 15 m placed at a depth of 100 m. With the required boundary condition being that of a pressure release surface ($p = 0$), a negative image source is also placed 100 m above the surface. The speed of the moving grid is 1510 m/s with respect to the fixed ocean frame. The maximum overdensity (ρ'/ρ_0) of the initial sine wave is 0.01. For the linear case, $\beta = 0.0$, and for the nonlinear case, $\beta = 3.5$.

Figure 8 shows contour plots of the overdensities on the grid after it has traveled 19294, 41944, 64594 and 72144 m for the linear case, and Figure 9 shows the overdensities at the same ranges for the nonlinear case. It is immediately apparent that the pulse in the nonlinear case remains less confined than in the linear case. In particular, the caustic which has formed at a range of 64594 m is quite noticeable in the nonlinear case yet is barely seen in the linear case. It is interesting to notice, however, that in the linear case, at the depth of the source and in the center of the grid (about five tick marks from either side of the grid), the contours are fairly concentrated while in the nonlinear case, the contour lines are concentrated both before and after rather than at the center of the grid. The pulse as a whole has followed the same basic path in both the linear and nonlinear cases, yet the local density perturbations have been altered considerably.

C. Ice Surface

Figures 10 and 11 show contour plots for a simulation in which an ice layer was included near the ocean surface. Similar to the sedimentary bottom in the shallow ocean simulation, the ice layer is simply a portion of the grid in which the sound speed is greater than that in the ocean. In our ice simulation, $n_x = 100$, $n_z = 150$, $dx = dz = 5$ m and the initial timestep is .005 seconds. The interface between the ocean and the ice (delineated

by the horizontal lines on the grids in Figures 10 and 11) is 100 m below the surface, and the damping region extends from a depth of 500 m to the bottom of the grid. The source is a single cycle sine wave with a half angle of 20 degrees and maximum overdensity of 0.9. Again, $\beta = 0$ for the linear case, $\beta = 3.5$ for the nonlinear case.

As in the shallow ocean simulations, the difference in sound speed between the two fluids (in this case ice and ocean) is greater in the linear case than in the nonlinear case. Again, this is due to the additional nonlinear velocity of the pulse in the ocean which is eliminated in the linear case. Therefore, the critical angle should also be greater in the linear simulation than in the nonlinear simulation, and more of the pulse should penetrate the boundary in the nonlinear case. Figures 10 and 11 readily confirm this effect as more contours can be found in the ice in Figure 11 than in Figure 10. Decreasing the sound speed jump between the ice and ocean would only increase the penetration of sound waves into the ice.

CHECKS AND DIAGNOSTICS

A. Dispersion of a wave packet

1. Normal Modes

Large amplitude waves, such as those resulting from an underwater explosion, interact differently with the ocean bottom than small amplitude waves because of the nonlinear contribution to the local sound speed. Because of this effect we also expect the dispersion of a nonlinear pulse to be different than in the linear case. In this section we present numerical results using the NPE model designed to highlight some of these differences.

A simple study of dispersion can be performed using the NPE in a manner reminiscent of actual ocean experiments. Again we consider a shallow ocean configuration as pictured in Figure 1. We assume in this case an ocean depth of 200 m together with 200 meters of sediment, the lower two-thirds of which is damped. At a depth of 50 m, we initialize a three-cycle sine-wave packet with a wavelength consistent with a frequency of 50Hz for the assumed sound speed in the water column and limit the angular spread to 38 degrees. The sound speed is taken to be 1500 m/s in the ocean, 1550 m/s in the sediment and damping region. The initial perturbation is then allowed to propagate downrange. Data from a hypothetical array of fifteen hydrophones placed at various downrange locations is collected during the run as a collection of time series. We ran this configuration out to 20 km for the linear case ($\beta = 0$) and repeated the simulation for the nonlinear case ($\beta = 3.5$). An initial amplitude $R = \rho/\rho_0 = 0.2$ was chosen. The linear calculation is completely insensitive to the chosen amplitude. In the nonlinear case this choice represents a very powerful perturbation such as an explosion.

Linear wave theory analysis (Jensen and Kuperman, 1982) predicts that at all except very short ranges propagation occurs in discrete normal modes of the shallow water waveguide. In normal mode analysis, solutions ϕ to the wave equation for a harmonic point source of a single frequency (for the case of azimuthal symmetry) are expanded in a set of complete normal modes

$$\phi(r, z) = \frac{i}{4} \rho(z_0) \sum_n u_n(z_0) u_n(z) H_0^{(1)}(kr) \quad (23)$$

where $\rho(z_0)$ is the density at the source depth z_0 and $H_0^{(1)}(kr)$ is the Hankel function of the first kind. The normal modes $u_n(z)$ are eigenfunctions of the equation

$$\frac{d^2 u_n(z)}{dz^2} + [k^2(z) - k_n^2] u_n(z) = 0 \quad (24)$$

In Eq. (24), $k(z)$ is the wavenumber and k^2 is the eigenvalue. The waveguide being dispersive, these normal modes propagate at different speeds. Thus the modes will separate as the pulse propagates downrange. The normal modes of the waveguide may be calculated numerically using the SACLANTCEN normal mode propagation model SNAP (Jensen and Ferla, 1979). Using the same parameters as in our simulation, normal mode analysis predicts the three modes depicted in Figure 12.

Figure 13 shows the hydrophone time-series plotted as a function of reduced time for simulation data taken from the linear case. Reduced time is defined for each vertical array at a given range as the actual time minus the time at which the pulse first arrives at the hydrophone array. Figure 13(a) shows the readings for the hydrophone array at 600 m downrange. Further downrange at 20 km, the modes have separated completely as can be clearly seen in Figure 13(b). The dashed lines in Figure 13(b) indicate approximate arrival times of the normal modes. Figure 13(c) shows the normalized amplitudes at each of these arrival times as a function of hydrophone depth. We can see that the general appearance of the modes is consistent with the predictions of normal mode analysis. The position of the maximum amplitude of the first mode as well as positions of the nodes in the second and third modes are in good agreement with theory.

The hydrophone data in the nonlinear case reveal distinct differences from the linear results. Figure 14(a) shows these results for a range of 600 m. One difference that is immediately apparent is the obvious steepening evident in the nonlinear case. The individual waveforms are also more complex. A comparison of normal modes between linear and nonlinear cases is not completely justifiable since decomposition of the acoustic signal

into normal modes is strictly valid only for linear waves. However, some comparison can be made between the two cases for the following reasons. First, since the compressibility of water is slight, nonlinearities are necessarily somewhat weaker than they would be in other highly-nonlinear problems. Second, as we saw in previous section, one effect of nonlinearity on the fluid-fluid interface is to make the bottom more transparent. Therefore the initial amplitude of the perturbation is substantially reduced after a few encounters with the water-sediment boundary. This rapid loss of wave amplitude to the sediment is an important aspect of the nonlinear case which we will quantify below. As the wave amplitude in the nonlinear pulse decays its interaction with the waveguide becomes essentially linear.

With these points in mind we examine the hydrophone data from the simulation of the nonlinear wave shown in Figure 14(b) at 20 km downrange. Although the results evidently differ from Figure 13(b), we can make out the arrival of the first two modes as indicated by the dashed lines. The third mode, because of the low amplitude, is less discernable in the complicated wake of the pulse. Plotting the hydrophone signal amplitudes of first two modes along the dashed lines yields Figure 14(c). Again there is relatively good agreement between these modes and the eigenmodes pictured in Figure 12. An exception is mode one identified in the first three dashed lines of Figure 14(b) and plotted in 14(c). While the mode profile at the third location agrees very well with the linear result, the first two profiles are distinctly different exhibiting an amplitude maximum at a shallow depth of about 70 m rather than the deeper 110 m predicted by normal mode analysis. Since these slices in depth are taken near the front of the propagating signal, this departure from the linear result may be an indication of the change in the eigenmode caused by the nonlinearly enhanced local sound speed near the interface and associated losses to the sediment.

The results of the normal mode comparison can be summarized as follows. Agreement is very good between the eigenmodes predicted by linear analysis and the modes that emerge during propagation of a wave packet in the linear NPE calculation. The results show that the NPE model faithfully reproduces linear theoretic results in the linear regime. In the nonlinear regime, the concept of normal modes is inappropriate when the wave

amplitude is large and so nothing can be said. Time series of the amplitude sampled near the source depth at a relatively short distance downrange exhibit the steepening expected of a weak shock wave. As the nonlinear pulse propagates, the combined effects of bottom transparency and the usual attenuation with range reduces the amplitude. The wave thus transitions to the linear regime, becoming less steep. Far downrange, dispersion separates the waveform into normal modes recognizable from linear theory. However, the signature of the linear wave is distinct from that of the nonlinear case which contains the effects of steepening and subsequent unsteepening as well as loss to the sediment. The first eigenmode also appears to be distorted near the front of the pulse probably owing to bottom losses.

2. Frequency Spectra

In the previous section we examined normal modes of the waveguide by sampling time series from vertical arrays of points at several locations downrange. We may also sample time series along a long horizontal array of collection points at the source depth. Fourier analysis of these time series yields interesting information about the frequency components of the wave.

We repeated the simulations of Section 1 and Fourier analyzed the time series into frequency spectra. Figure 15 shows the spectra at specific locations downrange for the linear case. The salient feature of these snapshots, ranging from 600 m to 20 km, is that the spectrum remains peaked near the initial central frequency of 50Hz for the duration of the simulation with less being found at higher and lower frequencies at greater ranges.

Figure 16, depicting the nonlinear results, presents a striking contrast. While the predominant frequency remains near 50 Hz, sidelobes containing other frequencies are plainly evident. At relatively close range, as shown in Figure 16(a), there are a number of higher frequencies seen as high as 500 Hz or more. This is the stage at which the wave steepens into a shock giving rise to high-frequency components. As the wave continues to propagate, the composition of frequencies changes. At 5 km downrange and beyond, low frequencies emerge and contribute substantially to the spectrum.

In summary, comparison of frequency spectra in linear and nonlinear cases reveals plain and obvious differences. The linear wave tends to lose its higher and lower frequency components as it propagates downrange with the vast majority of the spectrum being focused in a narrow band centered at 50 Hz. The nonlinear wave, while losing its higher frequency components initially originating from the steepness of the initial pulse, continues to shift toward lower frequencies as it moves downrange, though it also remains peaked at 50 Hz. The loss of the higher frequencies indicates the unsteepening of the wave.

B. Error Plots

To determine the accuracy of the NPE, we test it against an analytic solution calculated by placing multiple images both above the ocean surface and below the bottom. The images are placed such that the surface is a pressure release ($p = 0$) and the bottom has a zero derivative ($\frac{\partial p}{\partial z} = 0$) at all times. There is no damping region, and the speed of sound is 1520 m/s everywhere so that there is no sediment or ice. The grid spacing is $dx = 0.7$ m and $dz = 1.75$ m, and the number of grid points are $nx = 100$ and $nz = 400$. The initial timestep is 0.1 seconds. We ran two simulations, the first with a gaussian of half angle 72 degrees and initial range of 140 m, the second with a gaussian of half angle 3 degrees and initial range of 6893 m. Both sources are placed 280 m below the surface.

Figure 17 shows horizontal cross-sections of the simulation grid at ranges from 0.1 m to 4.2 m. The dashed lines are for the pressures of the analytic solution, the solid lines are for the pressures calculated with the NPE. Notice that the two completely overlap in Figure 17(a) because the analytic solution is used as input for the NPE. Notice in Figure 17(b), however, that the two diverge somewhat only to re-converge in Figures 17(c) and (d). The rms error for this run is shown in Figure 18, the error calculated for the entire grid each timestep throughout the simulation and assigned to the range of the left edge of the grid. Notice that at a range of 0.9 m, the error is approximately 7 %. The error peaks at a range of about 500 m and decreases to a level of less than 3 % at a range of 4100 m.

Figure 19 shows the cross-sections for a simulation starting at a range of 6893 m,

corresponding to an initial half angle of only 3 degrees, and extending to a range of 16718 m. Notice that in Figures 19(a), (b), (c) and (d), the NPE and analytic solutions are nearly equal. Figure 20 shows that throughout the simulation, the error is always less than 1 %. It is obvious that the NPE is much more accurate for small angles of propagation than large angles, as expected since in its derivation, approximations are made which decrease its accuracy for high angles.

V. CONCLUSIONS

In summary, we have continued to modify the NPE both to make it more efficient and to make it more general. We have introduced a damping region to prevent reflections from the bottom of the grid, added an option allowing for the inclusion of a range dependent sound speed profile for shallow ocean problems, modified the timestep constraint to adjust not only for refraction and nonlinearity but also for diffusion and provided an ability to link the NPE to the shorter range nonlinear CSQ computer code from Sandia. We have examined both linear and nonlinear cases of shallow and deep oceans as well as those of an ocean with a layer of ice at its surface and have seen that there are appreciable differences between linear and nonlinear simulations. By placing arrays of hydrophones in range and depth, we have also examined the structure and splitting of modes as the pulse travels downrange; in the nonlinear case, we have seen that there is a shift in the spectrum from high to low frequencies as the shock unsteepens while in the linear case, the spectrum remains primarily peaked at the initial dominant frequency. Our error plots have shown that there are significant reductions in error as the angle of incidence of propagating waves is decreased.

TOPS (Thermodynamic Ocean Prediction System)

I. INTRODUCTION

It is an important goal of oceanographic research to better produce accurate temperature profiles at given locations in the ocean system. While these predictions may be made at various levels of sophistication, climatology is the simplest forecast when recent observations in the area are unavailable. When these observations are available, persistence is used. The most sophisticated and data intensive methods are thermo-dynamic models such as the Mellor-Yamada Type II Model (see Appendix A) embodied in the Thermal Ocean Prediction System (TOPS, see Clancy and Pollak, 1983), the current Fleet Numerical Oceanography Center (FLENUMOCEANCEN) northern hemisphere ocean forecast model.

We begin our work by investigating the ability of linear statistical predictions, a technique intermediate in its data requirements to persistence and thermo-dynamic models. We attempt to produce current temperature profiles at an ocean station using information about current surface conditions and recent profiles at the same station. Profiles are for depths of 2.5 to 62.5 meters and are predicted using past profiles 1 to 7 days old. We search for that surface information which enable us to predict profiles below the surface with less error than persistence. The potential of statistical predictions are determined by our ability to collect this surface information on a routine basis and by the range of depths in which the predictions improve on persistence.

Several authors report success with statistical techniques, and some are applying regression techniques to ocean-atmosphere systems (Davis, 1976 and 1978; Barnett, 1984; Barnett and Hasselmann, 1979; Hasselmann and Barnett, 1981). In all of this work both the predicted variables and the predictands are averages over large regions and times of one to several months. Forecast lags are taken from one month to one year.

In Section II on Statistical Predictions of Temperatures in the Upper Ocean, we focus our attention on predictions on much smaller scales. Our prediction is for profiles at

a single location with forecast lags of days rather than months. Mesoscale and smaller events become a more important part of the variability in the temperatures. In these scales, persistence becomes the method against which all others must be judged.

Of course it is also important to compare the predictions of a forecast model with actual observations whenever possible in order to provide validation of the model and help determine its limitations. A number of investigations show the ability of Ekman-type models to predict the response of the surface wind-driven current to local wind forcing (Pollard and Millard, 1970; Kundu, 1976; Daddio et.al., 1978; Warn-Varnas et.al., 1981; Martin, 1982). However, there are relatively few comparisons of model-predicted upper-ocean current shear with observations. This is partly due to the lack of data available, a result of the difficulty involved in measuring current profiles near the surface region of the ocean. It is also partly due to the lack of attention received in simulating or forecasting shear in the ocean.

Several mixed-layer experiments have been conducted in recent years for which surface forcing and subsurface measurements of temperature and velocity are available. These include the Joint Air-Sea Interaction Experiment (JASIN), the Mixed Layer Experiment (MILE) and the Storm Transfer and Response Experiment (STREX). In Section III on Simulations of Different Environments, we describe a comparison of model-predicted currents and shears with those obtained during MILE.

Finally, in Section IV on Real-Time Shear Predictions, we present part of a larger effort to evaluate the capability of TOPS to predict some of the environmental parameters known to : (1) affect Ekman, inertial and geostrophic shear, (2) affect the propagation of internal waves and (3) have a strong correlation with the level of internal wave activity. Interest in the prediction of these parameters has increased with the recent growth in research on the generation and propagation of internal waves in the upper ocean.

The specific purposes of the current study are twofold: (1) to illustrate the real-time behavior of the upper ocean at eight oceanic stations (four in the Pacific, four in the Atlantic, Figure 31) over an annual period, and (2) to study the statistical properties of

seven chosen environmental parameters in order to provide probability distribution curves for the occurrence of given magnitude ranges of the different parameters. We summarize the results of the analysis for a 90-day period of the TOPS 24-hourly output for the period of February 1 - May 1, 1985.

II. STATISTICAL PREDICTIONS OF TEMPERATURES IN THE UPPER OCEAN ON SYNOPTIC TIME SCALES

A. Data

Ocean Weather Ship Romeo ($47^{\circ}N$, $17^{\circ}W$) provided information from nightly (22 GMT) XBT casts. The data set contained observations from May 4, 1983 to August 1, 1984. The temperature profiles were interpolated to the nine depths of Fleet Numerical Oceanography Center's TOPS grid (2.5, 7.5, 12.5, 17.5, 25.0, 32.5, 40.0, 50.0 and 62.5 meters). Approximately 65 % of the nights had casts recorded.

Observations at each station were assigned to a "spring" (warming) or "summer" (warm) season. Spring was defined as beginning 4 weeks prior to the appearance of the seasonal thermocline and ending 4 weeks after that appearance. Summer was defined as beginning with the appearance of the seasonal thermocline and ending with the onset of the fall cooling (or the end of the data in 1984). Two summers and springs were observed, allowing us to design a forecast using a season of one year and test it in that season of the other year.

Parsimonious representations of the deviations from climatology were obtained by fitting empirical orthogonal functions (EOF's) to the spring and summer deviations from climatology. Three EOF's were chosen to represent the deviations for Springs, and three were chosen for Summers. The three Spring EOF's can be used to represent 95 % of the variability about 0 in the deviations from climatology, while the three Summer EOF's can represent 90 %. Figure 21 shows the time series for the coefficients of the EOF's during Spring of 1983, which is typical of the four seasonal series. Clearly, coefficients nearby in time are highly correlated, so highly that persistence is a likely means of forecasting on time scales at least up to a week.

Table 1 displays the root mean square error as a function of depth in climatology and one-day-old persistence for the two spring seasons. Surprisingly, the precision in persistence does not increase greatly with depth. The same is true in summer months, as can also

be seen in Table 1. Day-to-day variations are the same or smaller at the very top as at the very bottom, though 62.5 meters is below the seasonal thermocline during most of the summer season. There are much larger variations in the summers in the 30 to 50 meter range at about the depth of the seasonal thermocline. In this region, large differences can occur due to small changes in the shape of the thermocline, leading to large variability.

We seek surface information which will help us predict the errors in persistence. Reports on surface forcing, including sea surface temperature (SST) from bucket readings, wind stress (WS), solar radiation and latent and sensible flux were made eight times each day, though many of these reports are missing. This data was condensed by averaging reports nearby in time as summarized in Table 2. Table 3 gives the correlations observed by season between the daily changes in temperature at four depths and the changes observed in the surface variables. Only changes in SST and WS show large correlations with changes in temperatures, and those correlations are limited to the region very near the surface which is almost always in the mixed layer.

In Appendix B, we model the multivariate series of the EOF coefficients (which represent deviations from climatology) together with series of surface data as a simple multivariate time series. We hope to use this model to incorporate surface information, producing forecasts superior to those of persistence.

B. Results

From the correlations in Table 3, it is apparent that SST and WS have the best chance of yielding good statistical forecasts. Therefore autoregressive models were fit as described in Section A for three choices of surface information ($O_2(t)$). These models will be indicated by

Stat (SS):	$O_2(t)$ is the average sea surface temperature on day t as described in Table 2.
Stat (WS):	$O_2(t)$ is average wind stress.
Stat (NC):	$O_2(t)$ is not used. No surface information is included.

Once the model is fit, forecasts can be computed given any combination of past profiles and past or current surface information. For illustration, we suppose that the forecaster has a pair of XBT profiles at times $t - 1$ and t , and surface information at times t and $t + k$. The goal is to project the profile below the surface at time $t + k$, that is, to forecast $O_1(t+k) - O_1(t)$ given $Z_1(t) = O_1(t) - O_1(t-1)$ and $O_2(t+k) - O_2(t)$. This will be referred to as a "forecast" at lag k , though it uses information on surface conditions at time $t + k$. The methods used when past surface information is used (a true forecast) are identical. While the information in the extra XBT at time $t - 1$ is not necessary, it is potentially useful if the model fitted indicates correlations across several days in the changes in EOF coefficients.

Table 4 shows the RMSE of prediction during the Spring Seasons. For the statistical forecasts, the errors are the cross validation errors. That is, forecasts were made in Spring 1984 using the forecast designed in Spring 1983 and vice versa. Thus, the errors approximate the skill of the forecasts, or their ability in data other than that on which the method was designed. For a given lag, all forecasts including climatology and persistence are computed for the same set of days $t + k$ where $Z_1(t)$ was available and $O_2(t + k)$ and $O_2(t)$ were available for O_2 both WS and SST. RMSE in climatology fluctuates slightly due to sampling error. For simplification, RMSE is reported as the SQRT(average squared error) in three depth groups: S (shallow) 2.5 to 17.5 m, M (mid) 25.0 to 40.0 m and D (deep) 50.0 to 62.5 m.

Comparing the errors in the statistical forecasts to those of persistence, we see that Stat(SS) successfully improves on persistence in the shallow depths, particularly at lags greater than 1. Below the shallow layers, no improvement is discernable. Despite the correlation of WS with changes in temperature near the surface, Stat(WS) shows no more skill than persistence or Stat(NC).

Table 5 repeats the analysis of Table 4 for the Summer forecasts. Summer errors in persistence are much larger than those for Spring, as can easily be seen in Table 2. Stat(SS) shows some slight improvement over persistence in the shallow layers, especially at longer lags. However, forecasts in the mid and deep range are worse than persistence,

indicating that the correlations observed in one summer between SST and mid to deep temperatures may be inapplicable in another summer. Neither Stat(WS) nor Stat(NC) improve on persistence.

The large errors in climatology and persistence observed in the summers are partially due to a cold core eddy moving under the station June 23, 1984 to July 27, 1984. This event greatly increased the variability of daily changes in temperatures. Table 6 gives the RMSE of predictions recalculated omitting the eddy period, since the correlation structure of temperature changes is different from that of non-eddy periods. While RMSE decreases compared to Table 5, the relationship of errors from persistence and errors from Stat(SS) are nearly the same.

The action of the statistical forecasts can be better understood by examining the actual prediction for a day. Figure 22 shows the actual profile for day 171 of the study (June 20, 1983). Four day old persistence, in the form of the profile from day 167, is also shown. Between 167 and 171 there was an increase of 1.1°C in the mixed layer temperature, while the temperatures below the thermocline remained relatively unchanged. Incorporating knowledge of the change in SST in the statistical forecast yields a prediction which closely follows the true profile in the mixed layer, the true profile in the seasonal thermocline and persistence below the thermocline. Typically, the statistical forecasts work best in this kind of situation, namely one with a large change in mixed layer temperature and relatively small change below the seasonal thermocline.

Table 7 displays the MFPE for the three models in each season. An investigator working with a single season (as in Spring 1983) would consider the trio of numbers for that season in deciding the relative value of different surface information. In every case, the investigator would correctly decide that including SST in the models would yield the best forecasts in an independent data set. However, in three of four seasons he would also decide that including WS would give better skill than using no surface information. In cross-validation, we see that the improvement due to using WS is small or non-existent. This result is due to large differences in the correlations of changes in WS to changes in temperature in different years. Changes in SST, on the other hand, maintain about the

same correlation with changes below the surface.

C. Overview

The focus of this effort was to fit a statistical model of the daily changes in temperature deviations from climatology so that forecasts could be computed of thermal profiles up to seven days in advance. The original intention was to model the process of changes in deviations without surface information, namely to fit Stat(NC). Cross validation errors showed this model to be no better than persistence, however. The major reason seems to be that the record of recent thermal profiles does not contain information which could help one predict the occasional large change in the temperatures. Since these events are so much larger in magnitude than most of the daily changes, these rather rare occurrences will contribute most to the correlations fitted in any one season. Since these large changes could either be positive or negative, the sign of the observed correlations may easily be positive in one season and negative in another. As an illustration, in Summer 1983 the sample correlation was negative between changes in the first EOF coefficient from day $t-1$ to t and day t to $t+1$. Hence a forecast was built in which large positive changes in the coefficient from day $t-1$ to t were compensated for by a predicted negative change from day t to $t+1$. The sample correlation in 1984 was positive and yielded forecasts that a large positive change from $t-1$ to t would be followed by another smaller positive change. These types of inconsistencies were present in both Springs and Summers even when the eddy period was removed from Summer 1984.

The inclusion of surface information should provide additional data with which to predict the daily temperature changes. However, the correlations actually observed between variables such as SST, WS and changes were surprisingly small. Partly, this must be due to noise in the measurement of the surface data. For instance, reported SST is actually the average of two bucket readings made one and four hours before the XBT reading. Therefore, they would normally differ from the XBT's SST by as much as $\pm 0.4^{\circ}\text{C}$.

More difficult to model are the effects of mixed layer depth on correlation. When 25 m lies within the mixed layer, we should expect changes in SST or WS to correlate well

with changes in temperature at that depth and design forecasts accordingly. Similarly, when the mixed layer depth is very shallow, forecasts should not use surface information in the forecast below the thermocline. When data from more years becomes available, it could be possible to fit more complex models which explicitly control for the depth of the mixed layer.

This work indicates that there is not enough information in the recent past of the profiles alone to build predictions which improve on persistence. However, regression methods can blend partial information on changes at the surface with information from recent profiles. This gives greatly improved prediction in the occasional (but important) case of large sudden changes in the profile.

III. COMPARISON OF MODEL-PREDICTED SHEAR WITH OBSERVATIONS DURING MILE

A. Model Description

The model used here is a one-dimensional, differential (primitive equation) mixed-layer model which employs conservation equations for temperature, salinity and the two horizontal components of momentum. As a one-dimensional model, variability is provided for in time and in the vertical, but the horizontal derivatives are assumed to be small and are neglected. Vertical mixing is parameterized by using the Mellor-Yamada Level 2 turbulence closure scheme to calculate vertical eddy coefficients. The model is driven by surface fluxes of momentum, heat and moisture. This model is used in TOPS, and a description is available in a number of references (Mellor and Durbin, 1975; Clancy and Martin, 1981; Clancy and Pollack, 1983). The model used here is as described in these references except that the turbulence length is scaled by the factor 0.2 rather than 0.1 (Equation 11, Clancy and Pollack, 1983). This change has been found to give a slight improvement in the agreement with a number of observation sets, and it will be incorporated into TOPS in the next update of that model.

B. MILE Data

MILE was conducted near Ocean Station PAPA in August and September, 1977, specifically to study the mixed layer and provide data against which models could be tested. Station PAPA is located at $50^{\circ}N$, $145^{\circ}W$ in the eastern North Pacific. Data taken during MILE included 3-hourly meteorological observations which could be used to calculate surface forcing for an ocean model and subsurface observations of temperature and current velocity every 112.5 s. The subsurface temperature and current were measured at depths from 5 to 50 m at 3 m intervals (except for 17 m) and at 70, 92, 125 and 175 m. The depths of these measurements provide sufficient resolution in the upper 50 m to allow the calculation of vertical temperature gradients and shear. Data from MILE have been analyzed by a number of investigators including Davis et al. (1981a,b), Warn-Varnas et al. (1982), Levine et al. (1983) and Rubenstein and Newman (1983).

C. MILE Simulation

The mixed-layer model was initialized from the observed temperature for August 19, the beginning of the MILE study (Figure 23). The temperature profile for this time of year was notable for the strong seasonal thermocline that existed at depths between 30 and 50 m. Most of the thermal stratification occurred at this relatively shallow depth. Velocity was initialized to zero.

Salinity variability was neglected in this study. During the summer in this region, the stratification of the upper ocean was dominated by temperature. The model salinity was initialized to a constant 33 parts per thousand and the surface moisture fluxes were set to zero.

The model was forced by surface wind stresses and heat fluxes calculated from the meteorological data. Penetration of solar radiation was described using an extinction profile for seawater Optical Type II (Jerlov, 1976). Figure 24 shows the surface wind stress and heat flux and a comparison of the observed and model-predicted sea-surface temperature (SST) and mixed-layer depth (MLD). Figure 25 shows the east and north components of the horizontal velocity at a depth of 8 m, which is generally within the mixed layer.

The SST (actually the 5 m temperature, since this is the depth of the shallowest measurements) shows the steady warming of the ocean that occurs late in the summer. On days when the winds are light, the steady warming is modulated by a diurnal fluctuation of about 0.2 C which is caused by daytime solar heating and nighttime cooling. Two storms occurred during MILE. The first on August 22-23, caused a deepening of the mixed layer to about 30 m and a drop in SST of 1.2 C. The second on Aug 31 - September 1, which was slightly weaker, caused mixing to about 26 m and a SST drop of 0.4 C.

The model reproduced the variability of the mixed-layer temperature and depth fairly well. The major discrepancy was that the model underestimated the amount of cooling that occurred during the August 22-23 storm. Analysis of the oceanic heat budget indicated that some of the discrepancy was due to advective cooling, which was not included in the

model simulation. As a result of underpredicting the cooling on August 22-23, the SST predicted by the model remained biased by about 0.4 C for the rest of the experiment. For a simulation initialized on August 25, after the storm, the model tracked the observed SST very well (Figure 26).

Inertial motions dominated the variability of both the observed and predicted surface current during MILE (Figure 25). These circular motions, which were an effect of the earth's rotation, were generated by changes in the magnitude and direction of the wind. Wind changes that were in phase with the inertial motions in the mixed layer tended to build them up, and changes that were out of phase caused damping. Horizontal gradients in the inertial motions due to the ocean density structure and the variability in the forcing caused them to disperse both horizontally and vertically. Since the one-dimensional model used here assumed horizontal uniformity, these processes were not included. The dissipation of inertial motions in the mixed layer by these processes was parameterized by damping the inertial motions numerically (using an implicit treatment of the Coriolis term) over about a 10-day timescale. The inertial motions observed during MILE had a typical amplitude of 20-30 cm/s and a period, which depended primarily on the latitude, of about 15.6 hrs. Both the amplitude and phase of the predicted inertial motions in the mixed layer agreed fairly well with the observations.

D. Comparison of Observed and Predicted Shear

Figure 27 shows observed and predicted shear profiles at specific times, and Figure 28 shows time series of shear between depths that correspond to the locations of the current meter observations. The shear between 11 and 20 m is shown because the current record at 14 m is very short (less than 4 days). Estimates of the uppermost reliable frequency response of the current meters are 2 to 8 cph (Halpern et al., 1981). In order to eliminate the considerable high frequency variability and to facilitate comparison with the model predicted shear, the time series are filtered to remove fluctuations with period less than 30 min. The high frequency variability is due to noise, such as mooring motions and measurement errors, and to surface and internal waves. Figure 29 shows a sample

comparison of filtered and unfiltered time series of shear between 26 and 29 m.

Values of shear observed in the upper ocean during MILE range from 0.0 to 0.10 $1/s$, with average magnitudes between 0.01 and 0.04 $1/s$ (based on a current-meter spacing of 3 m). The shear between 5 and 11 m (Figure 28a,b) was in or near the base of the mixed layer during most of the experiment. The magnitude of the observed and predicted shear at these depths and between 11 and 11 and 20 m (which were generally across the base of the mixed layer as shown in Figure 28c) agreed fairly well. Some agreement could be seen in the variability on synoptic and shorter timescales. Since the shear in and at the base of the mixed layer was due largely to directly wind-driven Ekman and inertial currents, the shear in this region tended to be correlated with the surface forcing.

Below 20 m the observed and predicted shear showed increasingly less agreement. Between 20 and 30 m the predicted shear (Figure 28d-g) showed two periods with strong peaks coincident with the two storms that occurred during MILE which deepened the mixed layer to these depths. Following their initial excitation, the predicted currents dissipated with an e-folding timescale of about 10 days which was imposed by the model. The observed shear between 20 and 30 m showed much more variability than the predicted shear on short (less than 24 hr) timescales. This variability did not generally appear to be well-correlated with the surface forcing, although the August 31 - September 1 storm showed up strongly in the observed shear.

Below 30 m the model showed very little shear since the mixed layer did not deepen below 30 m and the model had no means to transfer momentum to these depths other than by vertical mixing. However, the observed shear profiles (Figure 27) showed large peaks in the seasonal thermocline between 30 and 50 m depth. The time series of shear (Figures 28h-l) showed the average magnitude of the shear in the seasonal thermocline to be comparable to or larger than that in the mixed layer. The magnitude of the shear at these depths was relatively steady on a timescale of several days, but showed considerable variability on inertial and sub-inertial timescales.

The discrepancy between the predicted and observed shear in the upper 30 m was

due to a number of factors including errors in modelling, errors in the forcing and neglect of components of the current such as the geostrophic (pressure-driven) flow and tidal motions. In addition, it was speculated that some of the discrepancy between the observed and predicted shear in the upper 30 m, and most of the error below 30 m, was due to inertial wave dispersion and internal waves.

E. Inertial Wave Dispersion

Rubenstein and Newman (1982) investigated the shear in the seasonal thermocline during MILE and found the largest component to be due to inertial motions. Since these motions were below the mixed-layer, they were not driven directly by the local wind. It was likely that the inertial energy in this region was due to the dispersion of inertial motions from the surface layer.

The dispersion of inertial motions was caused by temporal and spacial variation of the surface forcing and by horizontal variation in the ocean thermal structure. As a result of the horizontal pressure gradients, there was a horizontal divergence of the surface currents and an excitation of inertial motions below the mixed layer. Such coupled inertial-gravity wave motions are referred to as inertial-gravity waves. These waves propagated inertial energy both horizontally and vertically.

During MILE, the shear throughout the water column was probably affected by the dispersion of inertial energy to some degree. In the upper 15-20 m the inertial currents were primarily driven by the local winds and so were reproduced fairly well by the model, although some discrepancies were apparent. Between 20 and 30 m the inertial motions were likely due to a mixture of both direct local wind-driving and dispersion, with dispersive effects helping to maintain shear after the mixed-layer had shallowed. Below 30 m it was speculated that the inertial motions were caused primarily by dispersion since vertical mixing did not extend to these depths.

F. Internal Waves

There was significant variability at frequencies higher than the local inertial frequency (15.6 hrs) in the shear time series between 30 and 50 m depth in the seasonal thermocline (Figures 28 and 30). Such variability also occurred at shallower depths but with reduced amplitude. Most of this variability was likely due to internal waves and may have been caused either directly by the propagation of internal waves or indirectly by interaction of the internal waves with the inertial currents.

The most prominent internal waves observed during MILE were those of semi-diurnal tidal period (12.4 hrs). Internal waves with this period were common in the ocean, and they were referred to as semi-diurnal internal tides. It was speculated that they were generated by the interaction of the barotropic tide with topographic features such as seamounts and shelf slopes. During MILE, the semi-diurnal internal tide had a typical amplitude (vertical isotherm displacement) of 10 to 15 m. This amplitude maximum occurred at the depth where the stratification was strongest, in the middle of the seasonal thermocline, which was the location of the node of the lowest order internal mode. Spectra of shear in the seasonal thermocline during MILE exhibited a significant amount of variability at the frequency of the internal tide and its first harmonic (Figure 30).

G. Forecasting Shear Below the Mixed Layer

The comparison between the observed and predicted shear showed that there was a significant amount of shear, especially below the mixed layer, that could not be accounted for with a one-dimensional mixed-layer model. This raised the question of how this shear could be predicted.

Inertial motions made up the largest component of the shear observed below the mixed layer during MILE. However, explicit forecasting of inertial shear caused by dispersion of inertial motions was difficult for several reasons. The speed at which inertial energy propagated downward from the surface depended on small scale (less than 100 km) horizontal variability of the surface forcing and ocean thermal structure which was usually not well known. Furthermore, because the vertical propagation speed was slow (typical values were estimated to be less than a few meters per day), inertial motions may have been affected by

advection, mixing and dissipation to an unknown degree. And since inertial-gravity waves propagated horizontally as well as vertically, deep inertial motions at a given location were due in part to non-local effects. Observations have been shown that the horizontal coherence and the coherence between surface and deep inertial motions in the open ocean could fall off rapidly with depth (Pollard, 1980). Only when the horizontal scales governing the generation and dispersion of inertial waves were very well known (eg. for a storm with well-established structure such as a front or hurricane – Geisler, 1970; Price 1981, 1983) was there some possibility of predicting the dispersion of inertial motions explicitly.

Explicit forecasting of high frequency internal waves will likely be beyond the limits of possibility for the foreseeable future. Forecasting low frequency internal waves such as the semi-diurnal internal seems within the range of possibility but faces problems similar to forecasting the dispersion of inertial motions. The motions are not generated in a sufficiently direct manner to be easily predicted.

With significant practical problems surrounding the explicit forecasting of shear below the mixed layer, the high correlation between the magnitude of deep shear and density stratification suggested the use of statistical methods to forecast the shear in the region. Rubenstein and Newman (1982) showed some success in predicting 15-min average values of shear during MILE using a statistical model based on density stratification and vertical spacing. Other parameters could be investigated for use in a general statistical model such as the recent history of local winds, horizontal variability of density and forcing or climatology of shear in the region.

IV. REAL-TIME SHEAR PREDICTIONS

A. Comments

Two general comments must precede our discussion of the results. First, the FLENUMOCEANCEN output was available only at 00:00Z Greenwich time, so that the Atlantic stations always fell into the local nighttime (with a time spread from 0 to 2 a.m.) and the Pacific stations always fell into the local daytime (with the time spread from 11 a.m. to 2 p.m. local time). This made the comparison of the Atlantic stations with the Pacific stations somewhat more difficult in that the diurnal effects needed to be taken into account.

The second comment concerns the vertical resolution of the TOPS grid. Several authors have shown both in the published and unpublished technical literature that the computation of BV frequency (N), shear (S) and $Ri = N/S^2$ is strongly dependent on the vertical interval over which the temperature and velocity gradients are evaluated. Rubinstein (1984) shows that a significant correlation exists between N^2 and S^2 . This correlation improves with increasing δz , partly resulting from the relative importance of noise decreasing with increasing δz . Considering the fall-off of both temperature and shear spectra with increasing wave-number, we effectively filter out components with wave-number greater than $k = 2\pi/\delta z$ from our distribution function analysis.

B. Mean Temperature Profile with Depth

Figures 31-33 display the monthly-average temperature profiles at the four North Pacific stations for the months of February, March and April, respectively. Figures 34-36 display the corresponding results for the four North Atlantic stations. Throughout the 90-day period, only two stations show the existence of a strong seasonal thermocline: stations November ($30^\circ N$, $140^\circ W$) and Victor ($34^\circ N$, $164^\circ E$), both in the North Pacific. Weak seasonal thermoclines are observed at stations Papa ($50^\circ N$, $145^\circ W$) in the Pacific and Mike ($66^\circ N$, $2^\circ E$) in the Atlantic. The others all show a more or less homogeneous layer down to the model depth of 500 m.

Only at Station B southwest of the Bering Sea ($50^{\circ}N$, $165^{\circ}W$) does a negative temperature gradient occur, and it is accompanied by a negative halocline which maintains stability. It is confined to an ~ 50 m thick layer below the mixed layer in February but then widens to ~ 75 m and 100 m in March and April, respectively. Below that lies an almost homogeneous region throughout the 90-day period.

Seasonal changes that affect the whole profiles down to 500 m occur only at the Atlantic stations Charlie ($53^{\circ}N$, $36^{\circ}W$) and Mike, with about an $\sim .75^{\circ}C$ warming at Charlie and an $\sim .75^{\circ}C$ cooling at Mike, respectively.

Stations November and Papa display an $\sim 1^{\circ}C$ cooling from February to March and no change from March until April. Station B shows an $\sim .75^{\circ}C$ cooling from February to March and an $\sim .5^{\circ}C$ warming from March to April.

C. Mean Temperature Variance Profiles

Figures 37-39 display the monthly-averaged vertical profiles of the temperature variance in the four North Pacific stations for the months of February, March and April, respectively. Figures 40-42 display the corresponding results for the four North Atlantic stations.

The profiles for February can be roughly divided into four groups: (a) the variance is dominated by a large peak at the bottom of the mixed layer (station November) or at some depth below the mixed layer (station Mike); (b) the variance profile follows the mean temperature profile, being constant in the mixed layer and continuously dropping off below it (stations Papa, Victor and Bering Sea in the Pacific, and station Romeo in the Atlantic); and (c) the profiles are composed of slowly increasing or decreasing segments (stations Charlie and Lima in the Atlantic).

The situation is notably different in March. The dominant profile is now one where modest peaks near the bottom of the mixed layer are superimposed upon otherwise constant profiles. Stations Papa and November in the Pacific still resemble class (b) of the February profiles, and station Lima has an almost constant profile.

In April, the situation again changes somewhat. Now station Victor exchanges shape with Papa and November in the Pacific, and the peak near the bottom of the mixed layer increases considerably in the Bering Sea. In the Atlantic, station Romeo goes back to a class (a) and station Charlie to a class (b) profile shape. At Lima the variance becomes totally constant with depth, and at Mike it increases toward the surface.

D. Mixed Layer Depth Variability

We must first digress here on a definition of mixed layer depth. In the past, definitions have been based either on some characteristic of the profile for temperature, density, sound speed or Richardson number. The most common criterion adopted in the numerous mixed layer simulation studies is the depth at which the temperature falls by a given value δT below its surface value. The usual value of δT employed by NORDA and Navy Postgraduate School (NPGS), who have performed the most seasonal simulations in the past, is $\delta T = .2^\circ C$ (Garwood and Adamec, 1982; Martin, 1984). Occasionally, values of $\delta T = .1^\circ C$ are used, and lately FLENUMOCEANCEN has adopted the value $\delta T = .5^\circ C$ in their evaluation of TOPS products in order to accommodate certain weaknesses in their operational acoustic models. Other criteria have utilized the depth at which the BV frequency reaches a certain value, or the density or sound velocity falls by a prescribed value below its respective surface value (Molinelli et.al., 1981). And finally, the depth at which the Richardson number Ri exceeds .23 can also be taken as the MLD, since at this depth little shear exists to produce turbulent mixing. In this paper we have adopted the $\delta T = .2^\circ C$ criteria.

Figures 43 and 44 illustrate the time evolution of the MLD at the four Pacific and the four Atlantic sites, respectively, according to the $\delta T = .2^\circ C$ criterion. Figures 45 and 46 present the corresponding results according to the Ri -number criterion. According to the temperature criterion, there is a marked "spring transition" at almost all of the Pacific stations where the MLD suddenly shallows from a winter to a summer thickness within the interval of a few days (Garwood and Adamec, 1982; Martin, 1984). The transition appears to be more pronounced (i.e. to take place over a shorter period of time) at the two stations that lie on the 50° latitude circle. However, in the Atlantic this shallowing takes

place over a much longer period. At stations Charlie and Romeo, with latitudes $50 \pm 3^\circ N$, respectively, this period is of the order of a month, from about March 15 to about April 15; at station Lima ($57^\circ N$) it is about two months, from about March 15 to May 15; and at station Mike ($66^\circ N$) it is an almost continuous process from about March 15 to June 1.

A closer examination of the time evolution of the MLD, as defined by both criteria, reveals that, in fact, there are several transitions. These transitions may signify separate events or stages of the same event separated by various time intervals. A close parallel examination of the forcing functions is needed to make some conclusions as to the exact causes and nature of these transitions.

Concentrating on the events that result in sudden shallowing trends of the MLD that endure for weeks, we have constructed four tables giving the times of these marked layer depth transitions and the mean layer depth between transitions. These tables have so far been derived from visual, semi-quantitative observation and as such have been influenced by subjective judgments. Hopefully, such procedures can be automated with objective criteria in the future.

Tables 8 and 9 present results for the $\delta T = .2^\circ C$ criterion and Tables 10 and 11 for the Ri-number criterion. We have grouped the transition periods, t_i , to fall within two-week periods (i.e. $t_i \pm 7$ days). Many of the groups have a much smaller spread about the mean. Up to seven such periods have been detected in the Atlantic and six in the Pacific (according to the Ri criterion).

Examining the results in Table 12 (with the δT criterion) for the Pacific, we note immediately that the March transition, so dominant in the Atlantic is absent, and only one station (Victor) shows a transition in April. The May transition is the dominant one and occurs at all four sites, with $t_4 = \text{May } 16.5 (\pm 6 \text{ days})$. There are two June transitions, with June 4 (± 3 days) occurring at three stations and June 18 occurring only at November. It is interesting to note that the two station pairs located on $50^\circ N$ and $32^\circ N (\pm 2)$ have their transition periods each 5 days apart, respectively. These stations constitute the vertices of a spherical rectangle since the latitudes also form pairs as $164.5^\circ W (\pm .5)$ and

142.5°W (± 2.5), respectively. On the perimeter of this rectangle, the spring transition moves around in a counterclockwise fashion with respective arrival times of 5, 3 and 5 days after leaving Victor. The stations are too far apart to ascribe the effect to synoptic weather causes, but dynamic ocean effects in the form of wave propagation may possibly be included. Most likely, this phenomena is only accidental and the transition times are determined by the local evolution of the atmospheric heat fluxes.

E. Frequency Distribution of Various Parameters

Statistical frequency distributions of mixed layer depth are shown in Figures 18-21 for the months of February through April. Two different kinds of mixed layer depths are shown. One is the temperature difference criteria of definition. This definition reflects the mixing signature on the temperature profile. The other definition, the critical Richardson number, reflects the existing depths of turbulence penetration which in turn reflects storm intensity and convective cooling. Figure 47 shows a mixed layer distribution of around 100 meters in the Pacific with the exception of station Victor which shows a distribution of around 150 meters. The difference at station Victor can be attributed to its close proximity to the Kuroshio where passing eddies tend to homogenize the temperature structure.

Figure 48 shows the analogous situation in the Atlantic. The mixed layer depths are a much deeper 150 to 400 meters, reflecting the weaker stratification that exists in the Atlantic. Figure 49 shows a turbulence penetration of 100 to 150 meters in the Pacific which agrees with the maximum mixing signature of the temperature profiles in Figure 47. Figure 50 shows the analogous situation in the Atlantic. The gaps in the critical Richardson mixed layer depth histograms reflect the absence of model grid points. The grid is stretched and varies in resolution from a few meters to a hundred meters in deeper regions. The maximum penetration of turbulence agrees with the maximum mixing depth signature on the temperature profiles (taking into account this coarse grid resolution at depth).

Figures 51-56 show profiles of the Brunt-Väisälä frequency versus depth. As expected the Brunt-Väisälä frequency peaks in the thermocline region where the sharpest tempera-

ture gradients exist. First, consider the Pacific stations for the time sequence of February, March and April. As evident from Figure 43, at the Bering Sea and Victor stations, the spring transition begins in April. This shows up at station Victor in Figures 51-53 as an eroding of a deep mixed layer and thermocline structure with the Brunt-Väisälä frequency showing a peak at what used to be the mixed layer region. At the Bering Sea station there is a less pronounced change in the mixed layer region. At stations Papa and November there is no noticeable change since the spring transition occurs in May, as shown in Figure 43. The Atlantic Ocean analogue is depicted in Figures 54-56. The peaks of the Brunt-Väisälä frequency are not as sharp in the thermocline because the stratification is weaker. Figure 44 suggests that we should see the effects of a spring transition at three of the stations. We find this to be the case.

Figures 57-64 show shear histograms (frequency distributions) at various depths and integrated configurations over depth. The Pacific histograms show higher values of shear than the Atlantic histograms. The histograms also show that higher values of shear tend to occur near the surface.

Figures 65-70 show histograms of the Richardson number distributions for the Pacific and Atlantic oceans. In the Pacific we note a more symmetric distribution than in the Atlantic, reflecting the weaker stratification of the Atlantic.

Figures 71-74 show histograms of eddy coefficients. We observe that the coefficients are larger in the Atlantic than in the Pacific. This is because the weaker stratification of the Atlantic enables a larger turbulent intensity to build up, which in turn is reflected in a larger eddy coefficient.

V. CONCLUSIONS

The focus of our study in Section II was to fit a statistical model of the daily changes in temperature deviations from climatology such that forecasts could be computed of thermal profiles up to seven days in advance. Although our original intent was to model only the process of changes in deviations, ignoring surface information, we found that cross validation errors proved this model to be no better than persistence. The major reason for this appeared to be that the record of recent thermal profiles did not contain sufficient information to predict the occasional large change in temperatures. The inclusion of surface information should provide additional data with which to predict the daily temperature changes, yet as of now there appears not to be enough information in the recent past of the profiles alone to build predictions which improve on persistence.

In Section III, a one-dimensional mixed-layer model, which employed the Mellor-Yamada Level 2 turbulence close scheme, was used to simulate the upper ocean during MILE. The model was initialized from the observed temperature and forced using surface wind stresses and heat fluxes calculated from local meteorological observations. The variability of the mixed-layer temperature and depth were predicted fairly well, the major discrepancy being an under-prediction of the cooling during the first storm in which advection appeared to play a role. The amplitude and phase of the surface wind-driven current also was in good agreement with the observations.

A comparison of observed and predicted shear showed that in the upper 20 m (which contained the mixed layer during most of the experiment) the magnitudes agreed well. Between 20 and 30 m, the predicted shear increased only during the strong wind events which deepened the mixed layer to those depths, whereas the observed shear had a more constant average magnitude and much more variability on inertial and shorter timescales. Below the deepest penetration of the mixed layer (about 30 m) the model predicted very little shear. The observations, however, showed considerable shear between 30 and 50 m, the location of the seasonal thermocline and region of strong thermal stratification. The upper 20 m, or so were reproduced fairly well due to the inertial currents being driven

mainly by local winds. The discrepancy between the observed and predicted shear below 20 m was probably due primarily to the horizontal and vertical dispersion of inertial energy and to internal waves. Between 20 and 30 m the inertial motions were likely generated by a mixture of direct local wind-driving and dispersion with dispersive effects helping to maintain shear when the mixed layer was shallow. Below 30 m the inertial motions were probably caused by dispersion since vertical mixing would not extend to those depths.

Finally, in Section IV, a data report on real-time shear prediction was presented. The oceanic forecast model, TOPS, generated its own Ekman and inertial velocity and received as input a geostrophic velocity from climatology or analysis. We forecasted the mean and variance distribution of temperature, mixed layer depth, Brunt-Väisälä frequency, scalar shear, Richardson number and eddy diffusion coefficients for the period of February 1 to May 1, 1985. The forecast was performed at four locations in the North Atlantic and four in the North Pacific. The forecasted mean and variance distribution could be used to describe the shear, acoustic, internal wave and fine-structure oceanic environment.

HIBLER ICE MODEL

I. INTRODUCTION

A hydrodynamic/thermodynamic sea ice model is presently being used at the Fleet Numerical Oceanography Center (FNOC) to predict sea ice concentration, thickness and drift. The operational model, the Polar Ice Prediction System (PIPS), is driven by atmospheric forcing from the Navy Operational Global Atmospheric Prediction System (NOGAPS) model, as well as monthly mean climatological ocean currents and oceanic heat fluxes.

Prior to the development of the PIPS model, operational Arctic sea ice prediction at FNOC consisted of empirical models that made use of the interaction between ocean currents, sea ice and winds. The first operational model, that of Skiles (1968), related ice drift to geostrophic wind and mean upper ocean currents. This model was replaced by the Thorndike and Colony (1982) model, a linear free drift model that used an updated representation of ice drift based on numerous observations of drift, geostrophic winds and mean ocean currents. Both of these models predicted only ice drift; no information on ice thickness or concentration could be obtained from them. The PIPS model, however, couples the ice movement and growth to thickness and concentration. As a result, the PIPS model is able to predict the characteristics of the ice thickness and concentration as well as temporal changes in these fields.

II. FORCASTING ICE THICKNESS AND CONCENTRATION IN THE ARCTIC

A. Model Description

The PIPS model is based on the Hibler (1979) model with the addition of thermodynamics similar to that used by Semtner (1976). Five main components are used to define the sea ice model: the momentum balance, ice rheology, ice thickness distribution, ice strength and an atmosphere-ice-ocean heat budget. The momentum balance used to describe ice drift is

$$m \frac{D\mathbf{u}}{Dt} = m f \mathbf{k} \times \mathbf{u} + \tau_a + \tau_w - mg \nabla H + \mathbf{F}, \quad (25)$$

where m is the ice mass per unit area, \mathbf{u} is the ice velocity, f is the Coriolis parameter, τ_a and τ_w are air and water stresses, g is the acceleration of gravity, H is the sea surface dynamic height and \mathbf{F} is the force due to variation of the internal ice stress. Ice is considered to move in a two dimensional field with forcing applied through simple planetary boundary layers.

The air and water stresses are defined as

$$\tau_a = \rho_a C_a |\mathbf{U}_g| \mathbf{U}_g \quad (26)$$

$$\tau_w = \rho_w C_w |\mathbf{U}_w - \mathbf{u}| [(\mathbf{U}_w - \mathbf{u}) \cos \theta + k(\mathbf{U}_w - \mathbf{u}) \sin \theta] \quad (27)$$

where \mathbf{u} is the ice drift velocity, \mathbf{U}_g is the surface wind from the NOGAPS model, \mathbf{U}_w is the geostrophic ocean current, C_a and C_w are the air and water drag coefficients, ρ_a and ρ_w are the water densities and θ is the turning angle for the water (McPhee, 1975).

The ice rheology, a viscous-plastic constitutive law, relates the ice stress to ice deformation and strength via the following equation:

$$\sigma_{ij} = 2\eta(\epsilon_{ij}, P)\epsilon_{ij} + [\zeta(\epsilon_{ij}, P) - \eta(\epsilon_{ij}, P)]\epsilon_{kk}\delta_{ij} - P\delta_{ij}/2 \quad (28)$$

In Eq. (28), σ_{ij} is the two dimensional stress tensor, ϵ_{ij} is the strain tensor, $P/2$ is a pressure or strength term, ζ and η are nonlinear bulk and shear viscosities and δ_{ij} is a delta function. Ice flows plastically for normal strain rates and deforms in a linear viscous manner for small strain rates.

Ice thickness evolves as a result of both dynamic and thermodynamic effects. The PIPS model uses a two level ice thickness approach. Ice is either thick or thin with the division between the two being 0.5 m. The compactness, A , is the area within a grid cell covered by thick ice while $(1 - A)$ is the area covered by thin ice. Thickness and compaction are defined by

$$\frac{\partial h}{\partial t} = -\frac{\partial(uh)}{\partial x} - \frac{\partial(vh)}{\partial y} + S_h + \text{diffusion} \quad (29)$$

and

$$\frac{\partial A}{\partial t} = -\frac{\partial(uA)}{\partial x} - \frac{\partial(vA)}{\partial y} + S_A + \text{diffusion} \quad (30)$$

where S_h and S_A are thermodynamic terms defined by

$$S_h = f\left(\frac{h}{A}\right)A + (1 - A)f(0) \quad (31)$$

and

$$S_A = \begin{cases} \frac{f(0)}{h_o}(1 - A) + \beta, & \text{if } f(0) > 0; \\ \beta, & \text{if } f(0) < 0. \end{cases} \quad (32)$$

In Eq. (32), β is defined as

$$\beta = \begin{cases} 0, & \text{if } S_h > 0; \\ \left(\frac{A}{2h}\right)S_h, & \text{if } S_h < 0. \end{cases} \quad (33)$$

with $f(h)$ the growth rate of ice thickness h and h_o the 0.5 m demarcation between thick and thin ice.

Ice strength, a function of the ice thickness distribution, is given by

$$P = P^* \exp[-C(1 - A)], \quad (34)$$

where P^* and C are fixed empirical constants.

The PIPS model also has the ability to determine the growth and decay rates of ice thickness. The vertical growth rates of both thick and thin ice are determined by calculating a heat budget at the top and bottom surfaces of the ice and by adding the heat absorbed by leads via lateral melting. Similar to the formulation of Semtner (1976), heat is transferred through the ice by assuming a linear temperature profile along with a constant ice conductivity. When open water absorbs heat, the heat mixes underneath the floes to decrease the vertical growth rate. Any remaining heat either causes lateral melting or raises the temperature of the fixed depth (30 m) ocean mixed layer. In the presence of an ice cover, the mixed layer temperature is always set equal to freezing. Thus, the excess heat absorbed by the leads is used for lateral melting until the ice disappears. Also, during growth conditions, ice is not allowed to form until the mixed layer reaches the freezing temperature of sea water. For a detailed description of the thermodynamic portion of the model see Hibler (1980) and Preller (1985).

B. Model Design

The operational sea ice model is defined on a subsection of the FNOC 63×63 Northern Hemisphere polar stereographic grid. The model domain includes the central Arctic, the Barents Sea and the Greenland and Norwegian Seas bounded at a line extending from Greenland through Iceland to the United Kingdom (Figure 76). These model boundaries are limited by the available oceanic forcing (see Hibler and Bryan, 1984). The model dimensions are 47×25 with 127 km grid resolution. All boundaries of the model are solid walls except for the southern boundary through the Greenland and Norwegian Seas. Outflow grid cells have been designated at this boundary. All ice which advects into these cells flows out of the basin.

The forcing for the model may be divided into two parts: atmospheric and oceanic. Atmospheric forcing from the NOGAPS model consists of surface winds, surface air tem-

perature, surface pressure, surface vapor pressure, incoming solar radiation, surface sensible heat flux and net surface heat flux. The last three fields are used to determine long wave radiation. All of the NOGAPS forcing fields are stereographic grid to the PIPS grid. The oceanic forcing is derived from the Hibler/Bryan ice ocean model (1984). These fields are interpolated from the Hibler/Bryan model grid to the PIPS grid.

C. Model Results

The model and the forcing fields were tested via a number of equilibrium "spin up" runs. In all of these tests the model was forced with the 1983 NOGAPS fields, cyclically, for a three to five year "spin up" period. The model was initialized by setting the ice drift equal to zero, defining the thickness field to be 3.3 m everywhere and defining the compactness to be 1.0 at all grid points. Table 12 presents the parameters used in all of the test cases as well as in the final version of the PIPS model.

These initial tests of the model show that the resultant thickness and concentration fields contain the observed seasonal characteristics of ice concentration and thickness. In particular, the ice thickness fields show the thickest ice, approximately 6 - 7 m (LeSchack, 1980), building up along the Canadian Archipelago and north Greenland coast. Ice thickness decreases to the north, away from the Canadian Archipelago towards the North Pole, and continues to decrease from the pole towards the Soviet coast. These patterns exist during all seasons with the average ice thickness being smaller in the summer and fall than in the winter and spring (Figure 77). Mean annual model derived ice thicknesses (Figure 78) were compared, by regions, to ice thickness derived from submarine data (Garrett, 1985). Results show good agreement between model ice thickness and data. Although the model ice thickness appears biased thin, the mean difference, 0.6 m is within the error of the Garrett data. Some difference may also be due to the fact that we are comparing 1983 model ice thicknesses to three different years of submarine data. It should also be noted that the model thickness gives a good representation of the relative variation in observed ice thickness for the given regions. The ice drift velocities are highly correlated to the 1983 NOGAPS winds and also agree well with observation. Another important

factor determined by these tests is the strong effect of oceanic heat flux, particularly in the Marginal Ice Zone. Tests which compared the results using a constant heat flux of 2 watts per square meter, a valid estimate for the central Arctic, to the results using the Hibler/Bryan monthly mean values showed a much improved ice edge in the second case. Oceanic heating appears to be a very important factor for melting ice in the Barents Sea and the Greenland Sea.

The model predicts large seasonal variability in the marginal ice zone. A typical winter thickness field shows the southern half of the Barents Sea to be basically ice free with a maximum of approximately 2.5 - 3.0 m of ice piling up against Spitzbergen. Model results also show the Barents Sea to be almost totally ice free in the summer. Along the Greenland coast, the ice extends south to cover the northern coast of Iceland in the winter but retreats dramatically in the summer.

D. Operational Model

The PIPS model is presently undergoing its OPTEST (validation by the users of the product). This OPTEST consists of two phases. In Phase I, the model is initialized by its own 24 hour forecast from the previous day. If the 24 hour forecast is not available, the model is initialized from climatology. This climatology is a model derived climatology calculated using the 1983 NOGAPS atmospheric forcing and the Hibler/Bryan oceanic forcing.

The first half of the OPTEST showed good agreement between the predicted ice drift and observation (Tucker and Hibler, 1986). The model ice thickness and concentration showed good agreement with the observed trends of ice growth and retreat. However, the model, when strickly forced by the NOGAPS forcing and the Hibler/Bryan ocean forcing, predicts too much ice in the Barents Sea and the Greenland Sea in the winter. We feel that these problems will be alleviated in the coming year when we include the temporal variability of the oceanic forcing by including a more sophisticated ocean model under the ice.

The ice edge problem is presently being addressed in the second phase of the OPTTEST. In Phase II, the PIPS model is updated (initialized) with data. The data used for updating are ice concentration values derived from the Naval Polar Oceanography Center's (NPOC) weekly analysis of ice concentration. NPOC creates a subjective hand analysis of ice concentration for both the eastern and western Arctic. The analysis is derived from various sources of remotely sensed data (infrared and passive microwave) as well as any available ship and aircraft observations. The data is digitized, sent to FNOC and then interpolated to the ice model grid. Once per week, the model concentration field is entirely replaced by the NPOC concentration field with the necessary adjustments being made to the thickness fields and heat absorption in the mixed layer. Initial PIPS model results which have been updated from the NPOC analysis show substantial improvement in the model's ability to predict ice edge location.

The PIPS model produces a 144 hour forecast (determined by the present NOGAPS forecast capability) on a daily basis. On days when the model is not being updated from the NPOC analysis, it is initialized by the previous day's 24 hour forecast. The operational model outputs the following 11 fields daily:

1. Ice thickness; Tau 0, Tau 144
2. Ice concentration; Tau 0, Tau 144
3. Divergence/convergence; Tau 48, Tau 96, Tau 144
4. Ice displacement (drift); Tau 24, Tau 144
5. Six day change in ice thickness
6. Six day change in ice concentration

where "Tau" indicates the forecast time in hours. These fields will be used by the Naval Polar Oceanography Center as guidance in the generation of a variety of products.

III. CONCLUSIONS

The Polar Ice Prediction System (PIPS), based on the Hibler (1979) ice model, has the capability of predicting fields of ice concentration, thickness and drift. It has been shown that these three model derived fields show good agreement with observations. As an operational forecast tool, the PIPS model will predict these fields out to 144 hours. Updating with data, in the form of digitized fields of ice concentration from the NPOC hand analysis, results in a marked improvement in the model's ability to predict ice edge location.

BIBLIOGRAPHY

NPE Section

Boris, J. P. and D. L. Book, "Flux-Corrected Transport i:SHASTA - A Fluid Transport Algorithm that Works", *J. Comp. Phys.* **11**, 38 (1973).

Cole, Robert H. "Underwater Explosions", Princeton University Press, Princeton, New Jersey (1948).

Ingenito, F., R. H. Ferris, W. A. Kuperman and S. N. Wolf, "Shallow Water Acoustics, Summary Report (First Phase)", *NRL Report 8179*, Naval Research Laboratory, Washington, DC (1978).

Jensen, F. B. and M. C. Ferla, "SNAP: the SACLANTCEN normal-mode acoustic propagation model", *SACLANTCEN Report SM-121*, SACLANT ASW Research Center, La Spezia, Italy (1979).

Jensen, F. B. and W. A. Kuperman, "Consistency Tests of Acoustic Propagation Models", *SACLANTCEN Memorandum SM-157*, SACLANT ASW Research Centre, La Spezia, Italy (1982).

McDonald, B. E. and J. Ambrosiano, "High Order Upwind Flux Methods for Scalar Hyperbolic Conservation Laws", *J. Comp. Phys.* **56**, 448 (1984).

McDonald, B. E., J. Ambrosiano and S. Zalesak, "The Pseudospectral Flux Correction (PSF) Method for Scalar Hyperbolic Problems", *Proceedings of the Eleventh IMACS Association for Mathematics and Computers in Simulation*, World Congress, University of Oslo, Norway (1985).

McDonald, B. E. and W. A. Kuperman, "Time Domain Formulation for Pulse Propagation Including Nonlinear Behavior at a Caustic", *J. Acoust. Soc. Am.* **81**, 1406 (1987).

McDonald, B. E. and W. A. Kuperman, "Time - Domain Solution of the Parabolic Equation Including Nonlinearity", *Comp. & Maths. w. Appls.* **11**, 843 (1985).

Plante, Daniel R., John J. Ambrosiano and B. Edward McDonald, "Compressional Waves at Fluid-Fluid Interface: Transition to Total Internal Reflection", *Advances in Computer Methods for Partial Differential Equations - VI*, (R. Vichnevetsky and R. S. Stepleman, eds.), IMACS, Rutgers University (1987).

Tappert, F. D., "The Parabolic Approximation Method", in *Wave Propagation and Underwater Acoustics*, ed. J.B. Deller and J.S. Papadakis, *Lecture Notes in Physics* **70**, (Springer - Verlag, New York, 1977).

Zalesak, S. T., "Fully Multidimensional Flux-Corrected Transport Algorithms for Fluids", *J. Comp. Phys.* **31**, 335 (1979).

TOPS Section

Akaike, H., "Autoregressive Model Fitting for Control", *Ann. Inst. Math. Stat.* **116**, 163-180 (1971).

Barnett, T. T., "Prediction of the El Nino of 1982-1983", *Mon. W. Rev.* **112**, 1403-1407 (1984).

Barnett, T. T. and K. Hasselmann, "Techniques of Linear Prediction with Application to Oceanic and Atmospheric Fields in the Tropical Pacific", *Rev. Geoph. Sp. Phys.* **17**, 949-968 (1979).

Bretherton, F. P., R. E. Davis and C. D. Fandry, "A Technique for Objective Analysis and Design of Oceanographic Experiments Applied to MODE-73", *Deep-Sea Res.* **23**, 559-582 (1976).

Clancy, R. M. and P. J. Martin, "Synoptic Forecasting of the Oceanic Mixed Layer using the Navy's Operational Environmental Data Base: Present Capabilities and Future Applications", *Bull. Am. Meteorol. Soc.* **62**, 770-784 (1981).

Clancy, R. M. and K. D. Pollak, "A Real Time Ocean Thermal Forecast System", *Prog. Oceano.* **12**, 383-424 (1983).

Daddio, E., W. J. Wiseman, Jr. and S. P. Murray, "Inertial Currents over the Inner Shelf near 30N", *J. Phys. Oc.* **8**, 728-733 (1978).

Davis, R. E., "Predictability of Sea Surface Temperature and Sea Level Anomalies over the North Pacific", *J. Phys. Oc.* **6**, 249-266 (1976).

Davis, R. E., "Predictability of Sea Level Pressure Anomalies of the North Pacific Ocean", *J. Phys. Oc.* **8**, 233-246 (1978).

Davis, R. E., R. DeSzoek and P. P. Niiler, "Variability in the Upper Ocean during MILE. Part I: The Heat and Momentum Balances", *Deep-Sea Res.* **28**, 1427-1451 (1981a).

Davis, R. E., R. DeSzoek and P. P. Niiler, "Variability in the Upper Ocean during MILE. Part II: Modeling the Mixed-Layer Response", *Deep-Sea Res.* **28**, 1453-1475 (1981b).

Garwood, R. W. and D. A. Adamec, "Model Simulations of Seventeen Years of Mixed Layer Evolution at Ocean Station Papa", *NPGS Tech. Rep. NPS68-82-006* (1982).

Geisler, J. E., "Linear Theory of the Response of a Two Layer Ocean to a Moving Hurricane", *Geophys. Fluid Dyn* **1**, 249-272 (1970).

Halpern, D., R. A. Weller, M. G. Briscoe, R. E. Davis and J. E. McCullough, "Intercomparison Tests of Moored Current Measurements in the Upper Ocean", *J. Phys. Oc.* **86**, 419-428 (1981).

Harding, J. M., R. H. Preller and S. A. Piacsek, "Statistics of Vertical Shear from a Hemispheric Model", *NORDA Tech. Note 206* (1983).

Hasselmann, K. and T. P. Barnett, "Techniques of Linear Prediction for Systems with Periodic Statistics", *J. Atmos. Sci.* **38**, 2275-2283 (1981).

- Jerlov, N. G., *Marine Optics*, New York: Elsevier (1976).
- Kundu, P. K., "An Analysis of Inertial Oscillations Observed near Oregon Coast", *J. Phys. Oc.* **6**, 879-893 (1976).
- Levine, M. D., R. A. DeSzoek and P. P. Niiler, "Internal Waves in the Upper Ocean during MILE", *J. Phys. Oc.* **13**, 240-257 (1983).
- Martin, P. J., "Mixed-Layer Simulation of Buoy Observations taken during Hurricane Eloise", *J. Geophys. Res.* **87**, 409-427 (1982).
- Martin, P. J., "Simulation of Mixed Layer at OWS November and Papa with Several Models", *J. Geophys. Res.* **90**, 903 (1984).
- Martin, P. J., S. A. Piacsek, J. French and A. Warn-Varnas, "Comparison of Model-Predicted Shear with Observations During MILE", *NORDA Tech. Note 328* (1986).
- Mellor, G. L. and P. A. Durbin, "The Structure and Dynamics of the Ocean Surface Mixed Layer", *J. Phys. Oc.* **5**, 718-728 (1975).
- Mellor, G. L. and T. Yamada, "A Hierarchy of Turbulence Closure Models for Planetary Boundary Layers", *J. Atmos. Sci.* **31**, 1791-1806 (1974).
- Molinelli, E., J. Donelson and L. Lilly, "Mixed Layer Depth Distributions from SVSTD Data", *NAVOCEANO Tech. Rep. TR 271* (1981).
- Niiler, P. P. and S. A. Piacsek, "The Prospectus for Forecasting Internal Wave Statistics", *NORDA Tech. Note, in preparation* (1984).
- Piacsek, S. A. and G. M. Dawson, *in preparation* (1985).
- Pollard, R. T., "Properties of Near-Surface Inertial Oscillations", *J. Phys. Oc.* **10**, 385-398 (1980).

Pollard, R. T. and R. C. Millard, Jr., "Comparison Between Observed and Simulated Wind-Generated Inertial Oscillations", *Deep-Sea Res.* **17**, 813-821 (1970).

Preller, R. H. and S. A. Piacsek, "Vertical Shear from TOPS", *NORDA Tech. Note 300* (1985).

Price, J. P., "Internal Wave Wake of a Moving Storm. Part 1: Scales, Energy Budget, and Observations", *J. Phys. Oc.* **13**, 949-965 (1983).

Priestley, M. B., *Spectral Analysis and Time Series, Vol. II*, London: Academic Press (1981).

Rubinstein, D. M., "Upper Ocean Shear During Jasin: A Deterministic and Statistical Analysis", *Tech. Rep. SAI-84/1027*, Science Applications, Inc. (1984).

Rubinstein, D. M., "Vertical Dispersion of Inertial Waves in the Upper Ocean", *J. Geophys. Res.* **88**, 4368-4380 (1983).

Rubinstein, D. M. and F. C. Newman, "Statistical Analysis of Upper Ocean Time Series of Vertical Shear", *SAI-83-751-WA*, Science Applications, Inc. (1982).

Warn-Varnas, A. C. and G. M. Dawson, "An Analysis of Modeled Shear Distribution during MILE", *NORDA Tech. Note 84* (1981).

Warn-Varnas, A. C., G. M. Dawson and P. J. Martin, "Forecast and Studies of the Oceanic Mixed Layer during the MILE Experiment", *Geophys. Astrophys. Fluid Dyn.* **17**, 63-85 (1981).

Warn-Varnas, A., J. French, S. Piacsek, P. Martin and J. Harding, "Real-Time Shear Predictions", *NORDA Tech. Note 307* (1986).

Hibler Ice Model Section

- Garrett, R. P., "Temporal and Spatial Distributions of Arctic Sea Ice Thickness and Pressure Ridge Statistics", *NPS Report 68-85-009*, Naval Postgraduate School, Monterey, CA (1985).
- Hibler, W. D., "A Dynamic Thermodynamic Sea Ice Model", *J. Phys. Oc.* **9**, 815-846 (1979).
- Hibler, W. D., "Modeling a Variable Thickness Sea Ice Cover", *Monthly Weather Review* **108**, 1944-1973 (1980).
- Hibler, W. D. and K. Bryan, "Ocean Circulation: Its Effects on Seasonal Sea-Ice Simulations", *Science* **224**, 489-491 (1984).
- LeSchack, L. A., *Arctic Ocean Sea Ice Statistics Derived from the Upward-Looking Sonar Data Recorded during Five Nuclear Submarine Cruises*, LeSchack Associates Ltd., Silver Spring, MD (1980).
- McPhee, M., "Ice-Ocean Momentum Transfer for the AIDJEX Ice Model", *AIDJEX Bulletin* **29**, 93-111 (1975).
- Preller, R. H., "The NORDA/FNOC Polar Ice Prediction System (PIPS)-Arctic: A Technical Description", *NORDA Report 108*, Naval Ocean Research and Development Activity (1985).
- Semtner, A. J., Jr., "A Model for the Thermodynamic Growth of Sea Ice in Numerical Investigations of Climate", *J. Phys. Oc.* **6**, 379-389 (1976).
- Skiles, F. L., "Empirical Wind Drift of Sea Ice", Arctic Drifting Stations, the Arctic Institute of North America (1968).
- Thorndike, A. S. and R. Colony, "Sea Ice Motion in Response to Geostrophic Winds", *J. Geophys. Res.* **87**, 5845-5892 (1982).
- Tucker, W. B., III and W. D. Hibler III, "An Evaluation of the Polar Ice Prediction System - Phase I", *CRREL Report* (1986).

Appendix A

An Experiment in Data Assimilation

Using the Kalman Filter

Section 1. Introduction

This is an outline of an experiment currently underway studying the use of the Kalman Filter for assimilating data into a one dimensional model of the mixed layer. We will use the non-advective Mellor-Yamada Level 2 model (MYL2) initialized from an XBT profile at OWS Romeo to make 3 and 5 day forecasts. Approximate sea surface temperatures from bucket thermometers will be assimilated into the model forecasts as they become available. The resulting statistical-dynamical forecasts will be compared to observed XBT profiles, and the RMSE errors compared to those of persistence and of the model without data assimilation.

There are two purposes. First, we will study the ability of approximate surface temperature information to keep a model forecast "on track" at a variety of depths in the mixed layer and in the seasonal thermocline. Second, we will illustrate the many problems involved in an application of the Kalman Filter to a useful physical model, and document the ways those problems are approached in this experiment. This should provide a set of experience for future applications.

I begin by outlining the mechanics of the Kalman Filter, and enumerating some of the technical problems in its use. In Section 3, I define the Filter for this application. In Section 4, I discuss proposed solutions to the technical problems.

Section II. The Kalman Filter

We begin by assuming the dynamic model can be written as a linear system.

$$w_{k+1} = \Upsilon_{k+1} w_k + F_{k+1} u_{k+1} + \epsilon_{k+1} \quad (2.1)$$

where w_k is an $nx1$ vector denoting the true state of the system at time k . Υ_{k+1} is an nxn transition matrix expressing the dynamics of the system, whose elements are independent of the state vector w_k . u_{k+1} is an $mx1$ vector of forcing conditions, and F_{k+1} an nxm matrix expressing their effect on the new state vector. We make the simplifying assumption that F and u are known exactly.

We assume that ϵ_{k+1} is an $nx1$ random vector with $\mathcal{E}(\epsilon_{k+1}) = 0$, $\text{var}(\epsilon_{k+1}) = Q_{k+1}$, and $\text{cov}(\epsilon_k, \epsilon_{k+j}) = 0$ if $j \neq 0$. Q_{k+1} is the error covariance matrix expressing the mean square error in the model when initialized from perfect data and forecast forward a single time step.

Beginning with an initial estimate of the state of the system w_0^a and an error covariance matrix for this estimate, P_0^a , we proceed as follows. At each time step:

$$w_{k+1}^f = \Upsilon_{k+1} w_k^a + F_{k+1} u_{k+1} \quad (2.2)$$

w_{k+1}^f ($nx1$) is the dynamic forecast for time $k+1$. It is made by projecting forward the analysis w_k^a for time k . The expected squared error for the forecast is described by the error covariance matrix P_k^f

$$P_{k+1}^f = \mathcal{E} \left((w_{k+1}^f - w_{k+1}) (w_{k+1}^f - w_{k+1})^T \right) = \Upsilon_{k+1} P_k^a \Upsilon_{k+1}^T + Q_{k+1} \quad (2.3)$$

Here P_k^a is the error covariance matrix for the analysis w_k^a .

$$P_k^a = E \{ (w_k^a - w_k)(w_k^a - w_k)^T \} \quad (2.4)$$

Let x_{k+1} be a $p \times 1$ vector of observations obtained since time k . We assume that these observations are related to the true state vector, and the relationship is expressed by:

$$x_{k+1} = H_{k+1} w_{k+1} + \eta_{k+1} \quad (2.5)$$

where H_{k+1} is a known $p \times n$ matrix, and η_{k+1} a $p \times 1$ random vector with mean 0 and covariance matrix R_{k+1} . We define an innovations vector:

$$z_{k+1} = x_{k+1} - H_{k+1} w_{k+1}^f \quad (2.6)$$

z_{k+1} expresses the apparent discrepancy between the model forecast, w_{k+1}^f and the observations. When z_{k+1} is 0, no discrepancy was observed. The Kalman Filter blends the innovations with the forecast using the Kalman Gain Matrix

$$K_{k+1} = P_{k+1}^f H_{k+1}^T (H_{k+1} P_{k+1}^f H_{k+1}^T + R_{k+1})^{-1} \quad (2.7)$$

The analysis, which is a blend of model forecast and data is

$$w_{k+1}^a = w_{k+1}^f + K_{k+1} z_k = w_{k+1}^f + K_{k+1} (x_{k+1} - H_{k+1} w_k^f) \quad (2.8)$$

The error covariance matrix for the analysis is computed as

$$P_{k+1}^a = (I - K_{k+1} H_{k+1}) P_{k+1}^f \quad (2.9)$$

At the end of this iteration, a new forecast is begun for the next time step using w_{k+1}^a and P_{k+1}^a which, together, describe the filter state at any

one time.

Any application of the Kalman Filter first requires that several numerical issues be settled, and various covariances used by the Filter be estimated. Here we list these items where the reader can observe their part in Equations 2.1-2.9. In Section 4, we discuss the approach used in this work for each item.

1. Actual dynamic models are rarely linear. The transition matrix \mathbf{T}_k often contains components which are functions of the state variables.

2. The bulk of the computational load is in the update of the forecast covariance matrix (Eqn 2.3). Each multiplication of \mathbf{T} by a column of \mathbf{P} is computationally equivalent to an iteration of the forecast. Since $2n$ of these multiplications are performed in each time step, it is easily seen that this work must be made as efficient as possible for the computation to be feasible.

3. To begin the iteration, we require an initial estimate of the state vector, \mathbf{w}_0^a , and an estimate of its error covariance matrix \mathbf{P}_0^a .

4. To compute the new error covariance matrix for the forecast, \mathbf{P}_k^f , we need the error covariance matrix \mathbf{Q}_k . This matrix describes the error properties of the model, initialized from perfectly correct data, for a single time step. While the entries in this matrix are usually small, they have an important cumulative effect on the Filter. It is easily seen that if $\mathbf{P}_0^a=0$ and $\mathbf{Q}_k=0$, then $\mathbf{P}_k^f=0$. The filter will assume the model is perfect, and discard the information in the observations \mathbf{x}_k when computing the analysis. As \mathbf{Q}_k increases, the model is assumed decreasingly accurate, and more weight will be placed on \mathbf{x}_k in the analysis.

5. The accuracy of the observations \mathbf{x}_k , as expressed in \mathbf{R}_k must be estimated. The relative size of \mathbf{R}_k and entries in \mathbf{P}_k control the weight

given the observations x_k relative to the model forecast w_k^f in computing the analysis w_k^a .

Section III. Experimental Design, An Overview

The non-advective form of the MYL2 model forecasts values of temperature (T) and the Ekman velocities (U and V) at selected depths on a numerical grid. On a grid with $N+1$ points, the state vector has dimension $3N \times 1$

$$w_k = \begin{pmatrix} T_k(1) \\ \vdots \\ T_k(N) \\ U_k(1) \\ \vdots \\ V_k(N) \end{pmatrix} \quad (3.1)$$

The values at the $N+1^{\text{st}}$ depth are held constant throughout the forecast period, so are not included in the state vector.

Suppose an approximate sea surface temperature is available at time $k+1$.

$$\begin{aligned} x_{k+1} &= \text{SST at time } k+1 = (1 \ 0 \ 0 \ \dots \ 0) \begin{pmatrix} T_{k+1}(1) \\ \vdots \\ \vdots \end{pmatrix} + \eta_{k+1} \\ &= H_{k+1} w_{k+1} + \eta_{k+1} \end{aligned} \quad (3.2)$$

H_{k+1} is the $1 \times 3N$ row vector with a 1 in the first place and zeroes thereafter. η_{k+1} is a scalar which represents the difference in the bucket temperature and the true temperature.

At OWS Romeo (47°N , 17°W) XBT temperature profiles are available every 12 hours. Surface observations including sea surface temperature from

buckets and heat fluxes are available every three hours. (Some of this data is missing.) We initialize the model with an XBT temperature profile on the interval from 0 to 200 meters. A typical short term forecast uses time steps of 600 seconds and a grid spacing of 5 meters. N is 40, and the state vector has dimension $n \times 1 = 120 \times 1$. Every 3 hours, or 18 time steps, an approximate SST will be blended with the forecast using the Kalman Filter as described in Section 2. The RMSE of the three and five day forecast errors for temperature will be compared to those of persistence, and to those of the model forecast without using the assimilation of the SST.

This scheme is summarized in Figure **79**.

Section IV. Specifying the Filter

In this Section, I discuss the ways Issues 1-5, listed at the end of Section 2, have been or will be decided.

1. Non-linearity in the model

The MYL2 model is non-linear in that the transition matrix Υ_{k+1} uses entries which depend on eddy coefficients, which in turn depend on the temperatures and velocities. For example, the updating procedure for T is defined by

$$L_{k+1}T_{k+1} = T_k + B_{k+1} \quad (4.1)$$

B_{k+1} is an $n \times 1$ vector expressing surface forcing and the extinction of solar radiation. L is a tridiagonal matrix whose coefficients are functions of the Richardson number computed using T_k^a , U_k^a and V_k^a .

The usual approach for nonlinear models is the Extended Kalman Filter. In this method, the entries in L (or Υ) are simply computed as estimated from the current analysis of the state, and the resulting errors in the computation of the error covariance matrix are ignored. This is the method adopted here.

We will ignore errors in the components of L , essentially treating them as if they were known perfectly. This necessarily introduces some sub-optimal performance into the filter, and some underestimation of the true variance of the forecast error. The effect of this and other filter design imperfections will be seen when we compare the size of actual errors in the statistical dynamical forecasts with the computed expected error covariances.

2. Computation of P_k^f explicitly or implicitly.

As written in Eqn 2.1, the Kalman Filter requires an explicit representation using a transition matrix Υ_{k+1} . In fact, the numerical code used at NORDA (written by P. Martin) uses an implicit scheme as written in Eqn 4.1. There are two choices for procedure.

- a. An explicit representation can be achieved from (4.1) by inverting the tridiagonal matrix L_{k+1} . This produces

$$T_{k+1} = L_{k+1}^{-1} T_k + L_{k+1}^{-1} B_{k+1} = \Upsilon_{k+1} T_k + \Upsilon_{k+1} B_{k+1} \quad (4.2)$$

The error covariance P_{k+1}^f , produced as in Eqn 2.3 requires two multiplications of $n \times n$ matrices to produce $\Upsilon_{k+1} P_k^{aT} \Upsilon_{k+1}$. This time consuming process is best avoided.

- b. The new covariance matrix P_{k+1}^f can be produced using the implicit representation with L_{k+1} . If $P_{(i)}$ is the i^{th} column of P_k^a , then a multiplication $P_{(i)}^* = \Upsilon_{k+1} P_{(i)}$ is equivalent to solving $L_{k+1} P_{(i)}^* = P_{(i)}$. Hence, the product $\Upsilon_{k+1} P_k^{aT} \Upsilon_{k+1}$ may be produced by first applying the implicit algorithm n times to columns of P to produce $\Upsilon_{k+1} P_k^a$. A transpose produces $P_k^{aT} \Upsilon_{k+1}$, and another n applications of the implicit procedure produces $\Upsilon_{k+1} P_k^{aT} \Upsilon_{k+1}$.

The implicit procedure described in b is considerably faster than the explicit multiplication. However, the explicit procedure need not be fully carried out at each time step. Instead, the cumulative transition matrix $A = \Upsilon_{k+1} \Upsilon_k \Upsilon_{k-1} \dots$ need only be updated at each step, and the matrix P_{k+1}^f be produced only when observations are to be blended.

Both an implicit and explicit scheme have been coded and checked at the University of North Florida by D. Mohr. This code will be shipped to J. French at NORDA by Oct. 5, 1986. After it is installed and rechecked at NORDA, benchmark timing tests will be run to compare the speed of each

algorithm.

3. Initialization of w_0^a and P_0^a .

The forecasts are initialized by setting the temperatures equal to those of an interpolated XBT profile and the velocities equal to 0. We will assume there is no error in the temperature initialization.

The error symmetric covariance matrices P can be better understood by looking at the following decomposition:

$$P_0^a = \begin{bmatrix} P^{TT} & P^{TU} & P^{TV} \\ P^{UT} & P^{UU} & P^{UV} \\ P^{VT} & P^{VU} & P^{VV} \end{bmatrix}$$

Here P^{TT} is the covariance matrix for the errors in temperature, P^{TU} is the cross covariance matrix for the errors in temperature with those in velocity, etc. The assumption that there is no error in the initialization for temperature implies $P^{TT}=P^{TU}=P^{TV}=P^{UT}=P^{VT}=0$.

To estimate reasonable values for the error variance in the velocities, we turn to the MILE Data. This data set contains temperatures and velocities for a series of observations at a station PAPA in the North Pacific. While this Station is very different from OWS ROMEO, its data can be used to at least estimate the magnitude and shape of covariance functions.

The entries in P^{UU} , for example, are $\mathcal{E}(U(i)U(j))$ where $U(i)$ is the actual U velocity at depth i . We turn to the sample moments observed in a subsample of 134 observations in the MILE data.

$$\overline{uv}_{ij} = \sum U(i)V(j) / 134$$

The sample moments \overline{uu}_{ii} and \overline{vv}_{ii} have maximum values of 27,000 and

19,000 cm^2/sec^2 at the surface. The moments decrease to around 10,000 and 7,000 cm^2/sec^2 by the 50m depth. As a first approximation for the entries along the diagonals of P^{UU} and P^{VV} I propose a value of 25,000 in the initial position (for depth 0m), decreasing linearly to 9,000 at the 11th position (50m) and remaining constant thereafter.

Errors at nearby depths are surely closely related. However, initially, we will take values off the diagonals in P^{UU} and P^{VV} to be zero, together with all the entries in P^{UV} and P^{VU} . By examining the cross sample moments in the MILE Data, these entries will be better estimated in the future.

4. Estimation of Q_k .

To estimate the error properties of the model, initialized from 'perfect' data, we turn to the MILE Data mentioned in Part 3 above. A subsample of the large data set was created by selecting pairs of records one hour apart in time, with the first record of each pair 7 hours apart in time. That is, records were selected at times 0, 1, 7, 8, 14, 15, ... hours. The goal of selecting pairs 7 hours apart was first to obtain observations more nearly independent than those 112.5 seconds apart as in the original data set. Second, by selecting a 7 hour stagger, our sampling interval is relatively prime to the 24 hour diurnal, 12 hour semidiurnal and 15-16 hour inertial frequencies.

For each pair, the model was initialized with the temperatures and salinities for the first record, and forecast forward for six 600-second time steps, or one hour. The resulting forecast was compared to the actual observations in the second forecast. The sample covariances for the errors have been computed by Jon French. As of 9/25/86 we have begun smoothing this rough data, to find a tractable approximate covariance function.

5. Estimation of R_k .

Since our observations consist of a single number, the sea surface temperature from bucket readings, R_k consists of simply the Mean Square difference in the bucket temperature and the temperature from an XBT near the surface, within one time step (600 seconds) of each other. From historical data at OWS Romeo, we know that a sea surface temperature from buckets, and the shallowest point on an XBT thermal profile taken an hour later, will have a Root Mean Square Difference of about $.16^{\circ}\text{C}$. This gives a maximum value of R_k of $(.16)^2$. Since the Filter will use time steps of 10 minutes, we assume an appropriate value for R_k is more like $(.05)^2$ to $(.10)^2$.

Appendix B

1. Statistical Methods

A process $Z(t)_{rx1}$ consisting of r measurements at time t is said to follow a stationary mean 0 vector autoregressive process of order 1 if

$$E(Z(t)) = \emptyset_{rx1} \quad (1)$$

$$G(k)_{rxr} = \text{cov}(Z(t+k), Z(t)) \quad \text{for all } t \quad (2)$$

$$Z(t+1) = B_{rxr} Z(t) + e(t) \quad (3)$$

The innovation process $e(t)$ is assumed to follow a multivariate normal distribution with mean \emptyset , variance matrix V_{rxr} and $\text{cov}(e(t+k), e(t)) = \emptyset$ when $k \neq 0$. Under these conditions

$$G(k) = B^k G(\emptyset) \quad k > 0 \quad (4)$$

$$G(\emptyset) = B G(\emptyset) B^t + V \quad (5)$$

Both $G(\emptyset)$ and V must be positive definite matrices, if the stationarity condition in (2) is fulfilled.

In an observed series $O(t)$ where persistence is very strong, the stationarity condition often fails. Then the observed process is usually differenced so that $Z(t) = O(t) - O(t-1)$.

Once B and $G(\emptyset)$ (or V) are estimated, linear statistical forecasting proceeds via the Gauss-Markov Theorem (see Bretherton, Fandry and Davis 1976.) Let Y be a vector to be predicted, and X a vector of predictor variables, both with mean 0. Then the unbiased minimum variance linear prediction of Y is $Y' = X' E(XX')^{-1} E(XY')$.

In our application $O'(t) = (O_1'(t) | O_2'(t))$ consists of $O_1(t)$, the vector of 3 EOF coefficients used to represent deviations from climatology at time t , and $O_2(t)$ is a vector of measurements describing surface conditions at time t . $Z(t) = O(t) - O(t-1)$ is the vector representing changes in deviations and

changes in surface conditions.

We wish to predict $Y = O_1(t+k) - O_1(t) = \sum_{i=1}^k Z_1(t+i)$ given

$$X = \begin{pmatrix} Z_1(t) \\ O_2(t+k) - O_2(t) \end{pmatrix} = \begin{pmatrix} Z_1(t) \\ \sum_{i=1}^k Z_2(t+i) \end{pmatrix}$$

The covariance matrices $E(XX')$ and $E(XY')$ can be computed from B and $G(0)$ using (4). The predicted temperature profile can be constructed from Y by

$$\text{Profile}(t+k)_{9 \times 1} = E_s O_1(t) + E_s Y + \text{climatology}(t)_{9 \times 1}$$

where E_s is the 9×3 matrix whose columns are the EOF's for appropriate seasons.

2. Estimating B , $G(0)$

First estimates of B and $G(0)$, denoted B^* and G^* are provided by the ordinary multivariate regression of the observed $Z(t)$ on $Z(t-1)$ and the lag (0) sample covariance matrix of the $Z(t)$. Two problems arise. First, because ocean data sets are incomplete, many observations will not be paired with an observation on the previous day. A method which only uses points where immediately preceding observations exist wastes valuable data. Second, the resulting B^* and G^* will not necessarily represent a stationary process, since $V^* = G^* - B^* G^* B^{*'} (applying (5))$ will not necessarily be positive definite. The fitted process will be useless for inference or simulation.

The maximum likelihood criterion will be applied to the original estimates. The negative log-likelihood of the observed $Z(t)$ at times t_2, t_2, \dots, t_n conditional on $Z(t_1)$ is approximately minimized using Marquardt-Levenberg procedures, first over choices of B , leaving G fixed at G^* , then over choices of G , and finally, over B again. By forcing the minimizing routine to compute a large value when the choice of B or G yields

non-positive definite V , the fitted process will be an acceptable one.

3. Avoiding Overfitting

The dangers of overfitting in oceanographic data have been discussed by Davis (1978), Barnett and Hasselmann (1979) and others. We shall control for overfitting by cross-validation, that is by checking the results developed using one year's season on the data from the other year's season. This method has been found superior to all others, since it allows the researcher to check for shifts in the underlying physical process which would nullify any apriori computation of skill. (See Berk, 1984.)

When separate seasons are not available for cross-validations, researchers require some calculation of skill which will guide them in the selection of informative covariates (our surface information, or $O_2(t)$.) In the autoregressive setting in which we are working, the most appropriate is the Akaike Final Prediction Error (Akaike, 1971.) Let $S(M)$ be the sample covariance matrix of the lag-one prediction errors from a model M (that is, a list of covariates $O_2(t)$ and estimates of B and $G(0)$). Akaike recommends choosing M to minimize

$$MFPE(M) = (1-(p+q)/n)^{-p} (1+(p+q)/n)^p S(M) \quad (6)$$

Here p is the dimension of the process being predicted (in our case 3) and q the number of covariates, that is the dimension of $O_2(t)$. The determinant $S(M)$ will be large when models are underfit, and will reduce as covariates are added. The first two factors will increase as q = number of covariates is increased. The minimum is achieved when goodness of fit is balanced off against the penalty for extra covariates. In practice, Akaike's method yields a few models with similar MFPE all of which should give acceptable results. We will check the results from the MFPE analysis against the results from the cross-validations. Large discrepancies in the results must mean that forecasts developed in one year are not always appropriate the next.

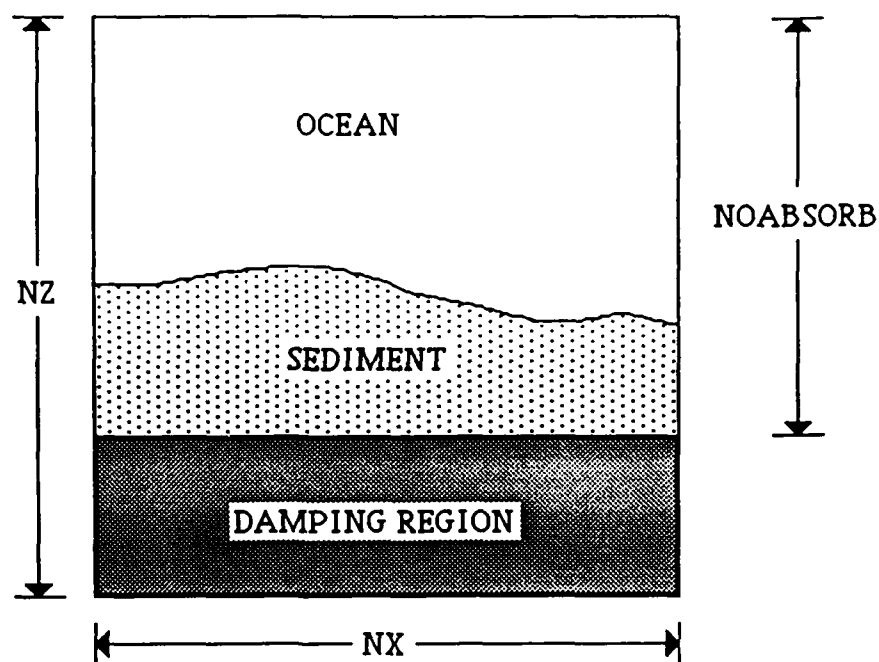


FIGURE 1: SHALLOW OCEAN GRID

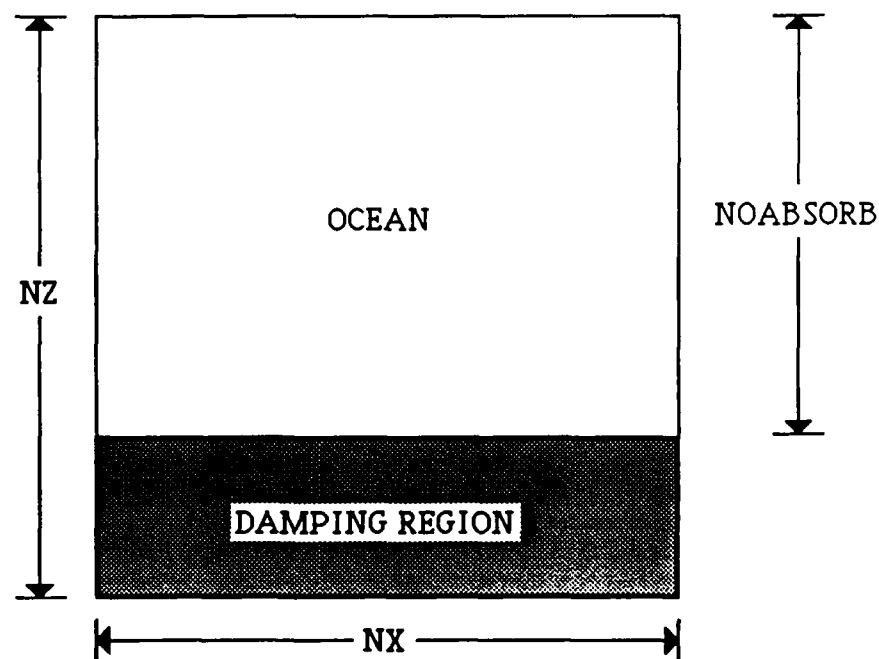


FIGURE 2: DEEP OCEAN GRID

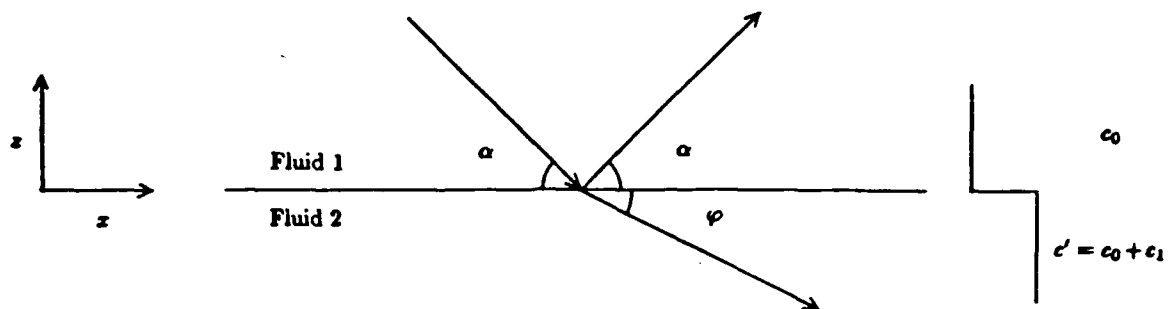


Figure 3. Plane wave incident from fluid 1 to fluid 2, with $c_0 < c'$ and $\alpha > \phi$. c_0 is sound speed in fluid 1, c' is sound speed in fluid 2, α is angle of incidence (reflection) and ϕ is angle of transmission.

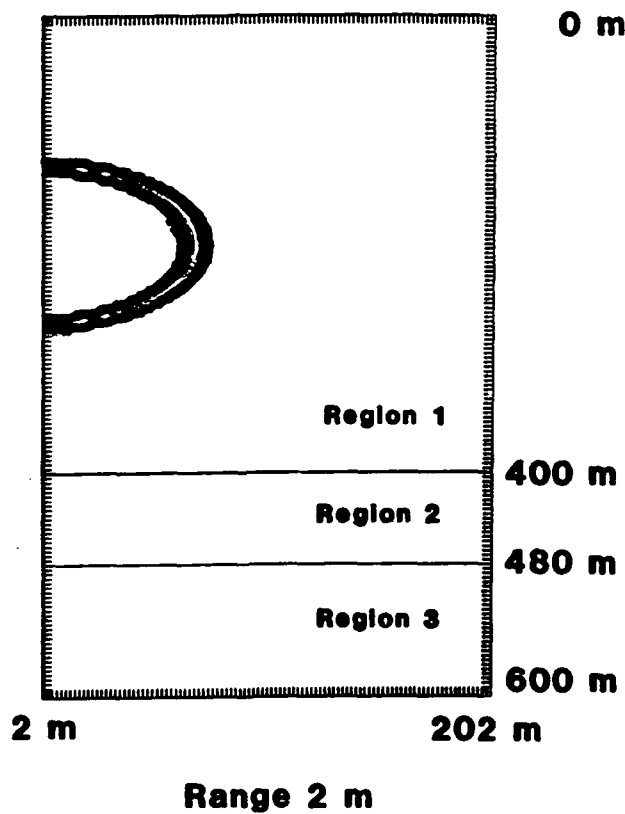
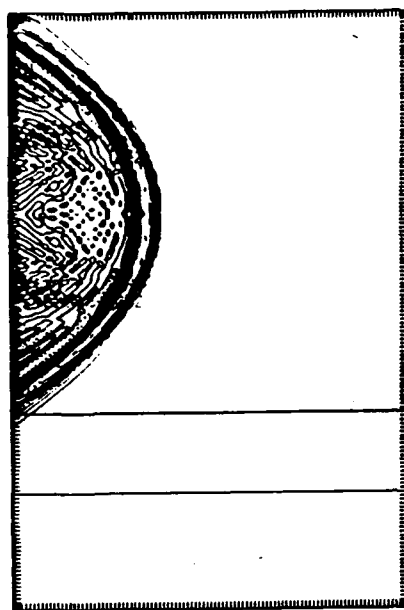
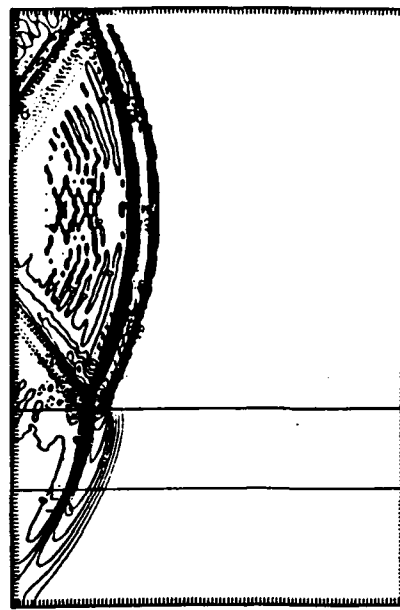


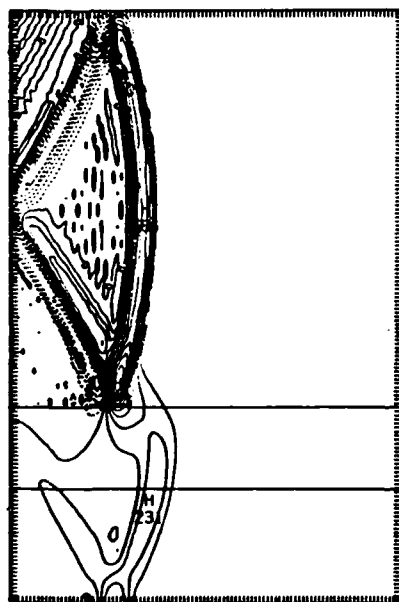
Figure 4. Simulation window with initial waveform. Regions 1 and 2 are fluids with sound speeds 1500 m/s and 1600 m/s and depths of 400 m and 80 m respectively. Region 3 is a damping region with sound speed 1600 m/s and depth of 120 m. The width is 200 m.



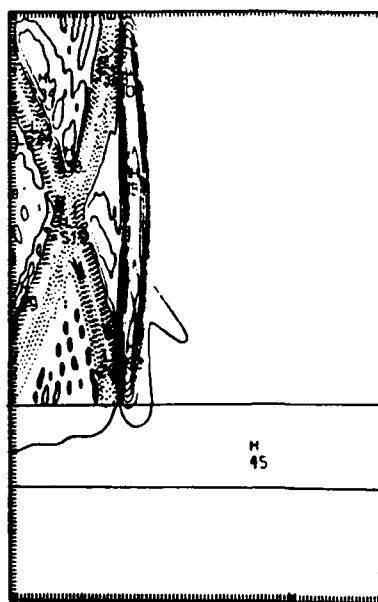
Range 225 m



Range 750 m

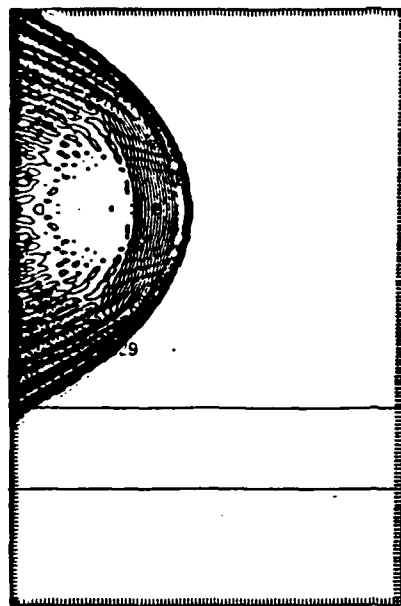


Range 1200 m

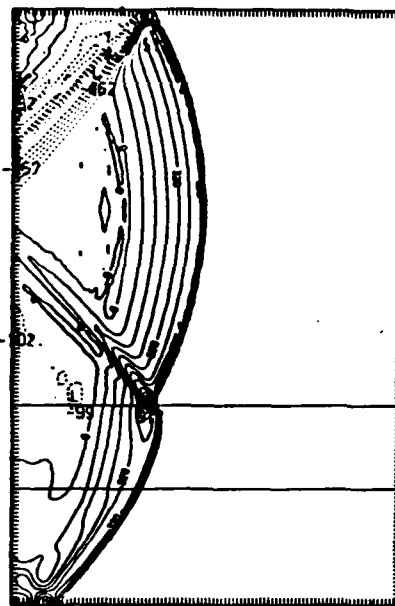


Range 2400 m

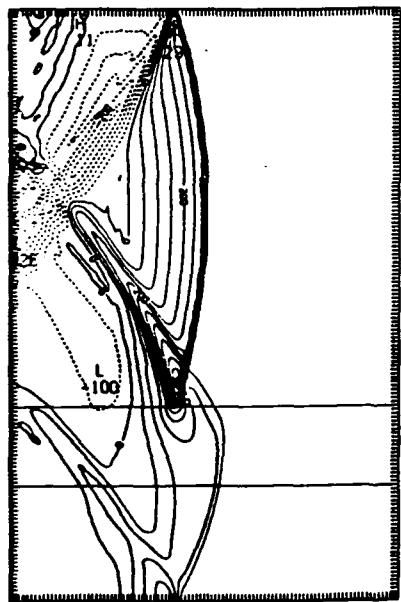
Figure 5. Linear simulation ($\beta = 0$) with initial conditions of Figure 4.



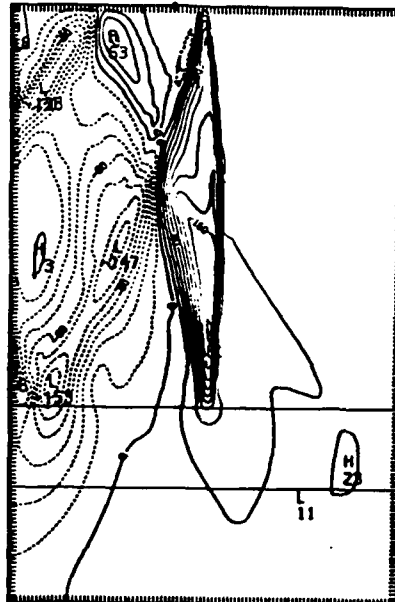
Range 205 m



Range 730 m

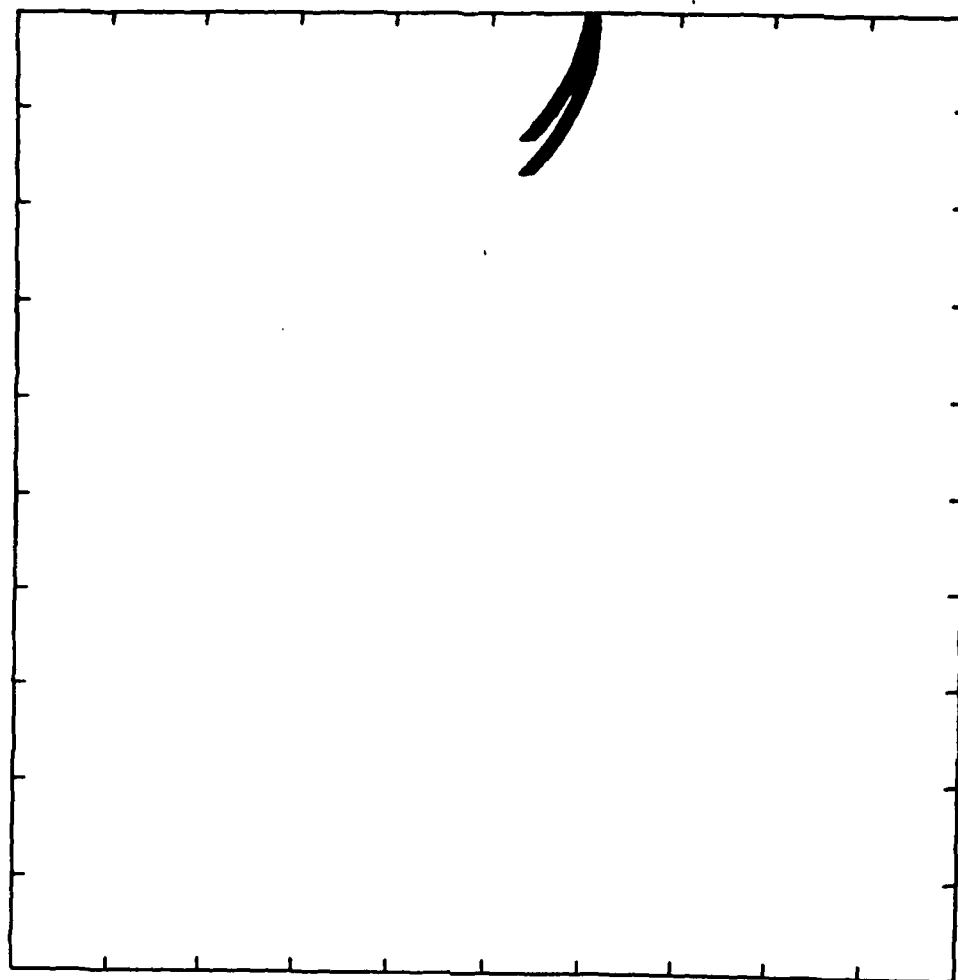


Range 1200 m



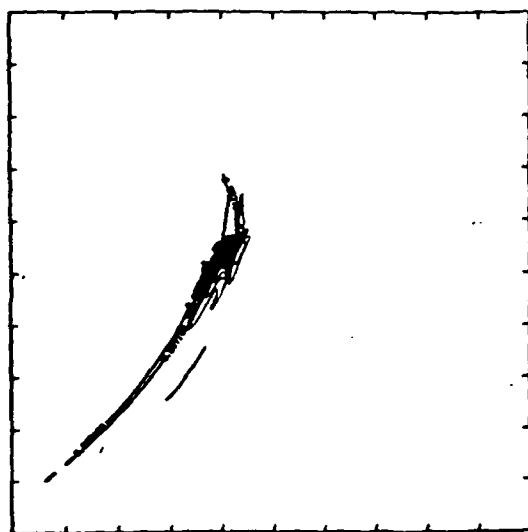
Range 2650 m

Figure 6. Nonlinear simulation ($\beta = 3.5$) with initial conditions of Figure 4.

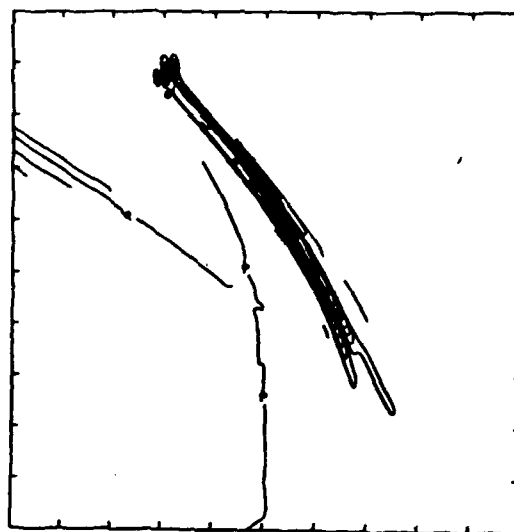


RANGE = 4194.00 M NSTEP = 0

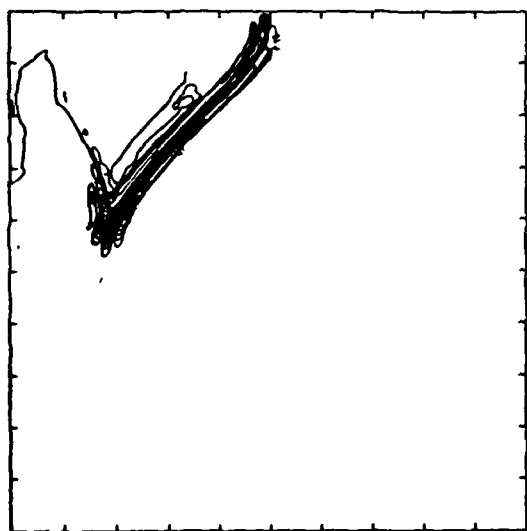
Figure 7. Simulation window with initial waveform for deep ocean. Initial range of frame is 4194 m (range of left hand side). Width of frame is 1050 m, total depth of frame is 6000 m with bottom 400 m for damping. Sound speeds in ocean are 1540 m/s at surface, 1495 m/s at depth of 1000 m and 1560 m/s at depths of 5500 m to 6000 m. Intermediate depths are linearly interpolated from these values.



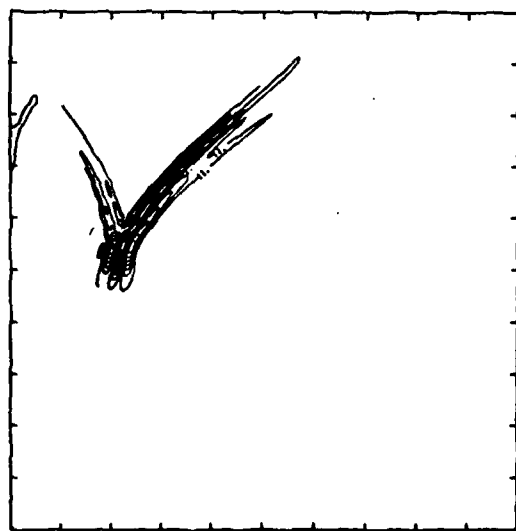
RANGE = 19294.00 M NSTEP = 2000



RANGE = 41944.00 M NSTEP = 5000



RANGE = 64594.00 M NSTEP = 8000



RANGE = 72144.00 M NSTEP = 9000

Figure 8. Linear deep ocean simulation ($\beta = 0$) with initial conditions of Figure 7.

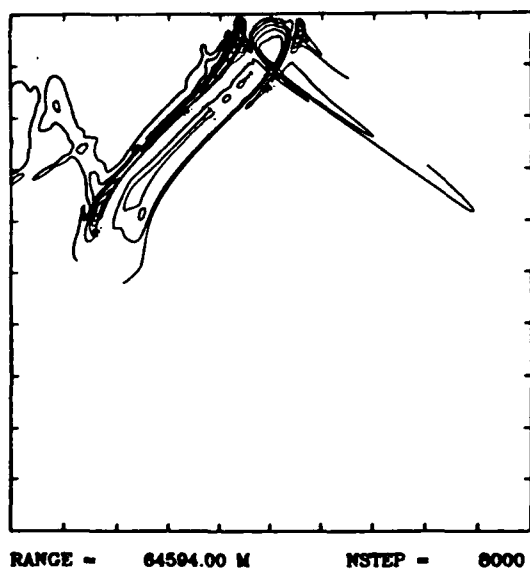
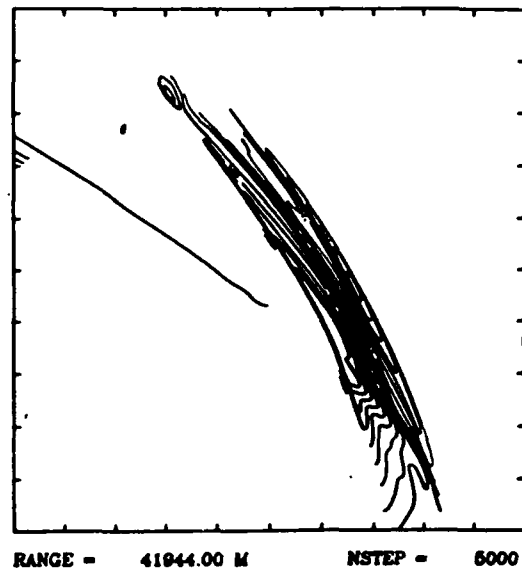
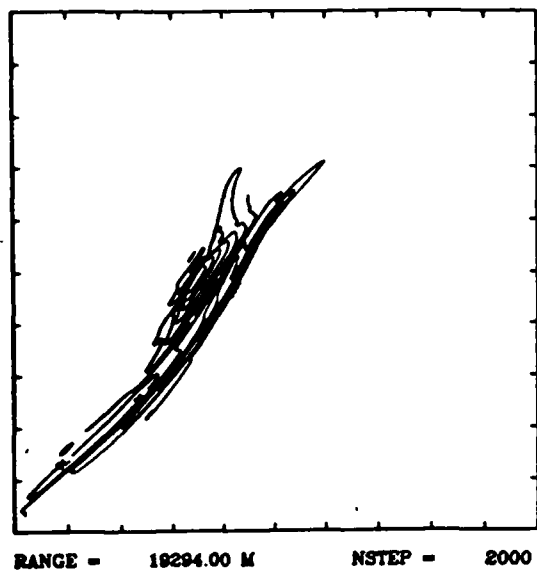
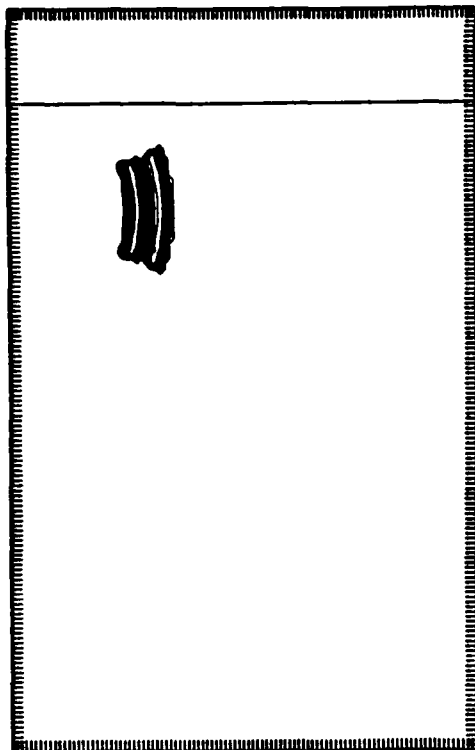
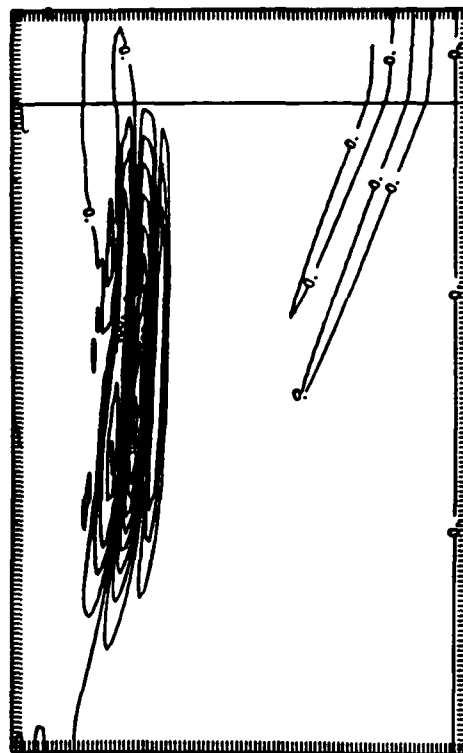


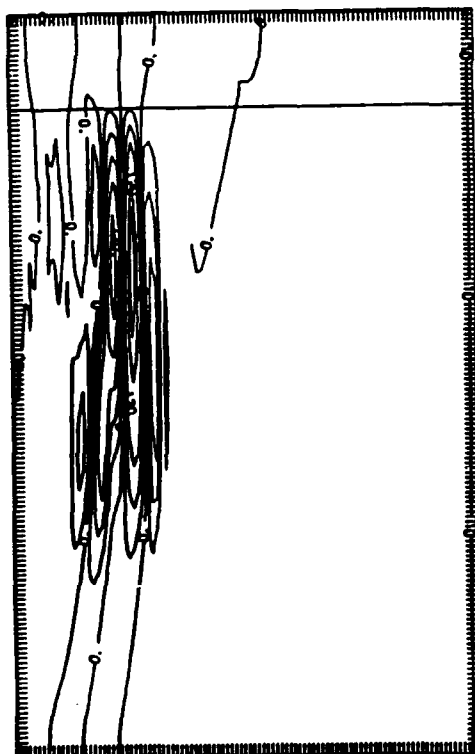
Figure 9. Nonlinear deep ocean simulation ($\beta = 3.5$) with initial conditions of Figure 7.



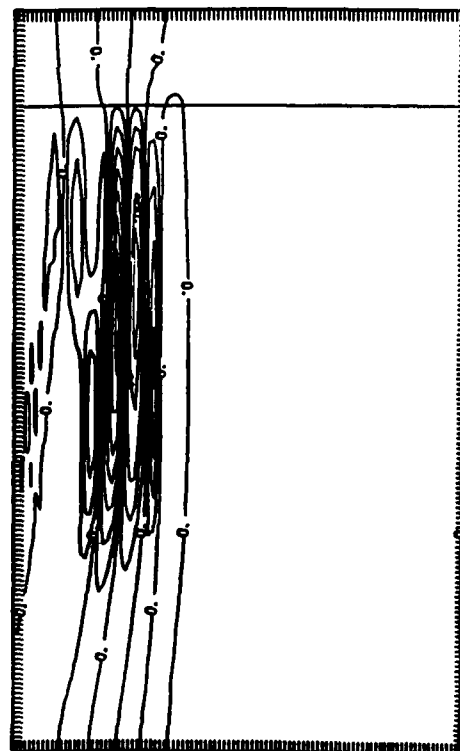
RANGE (METERS)
4.95



RANGE (METERS)
3956.95

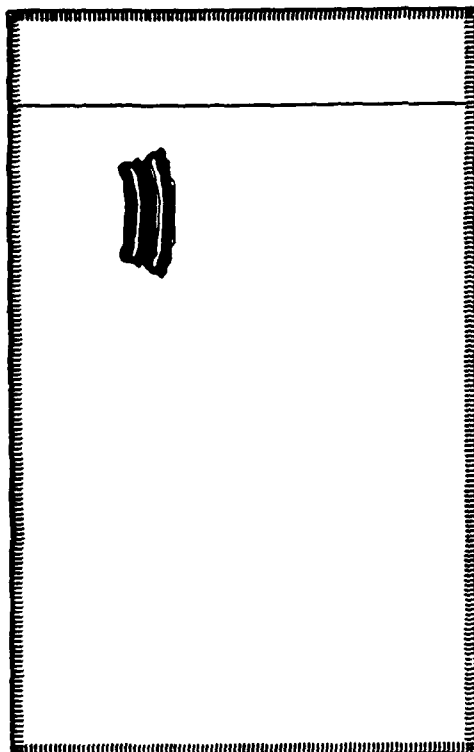


RANGE (METERS)
15812.95

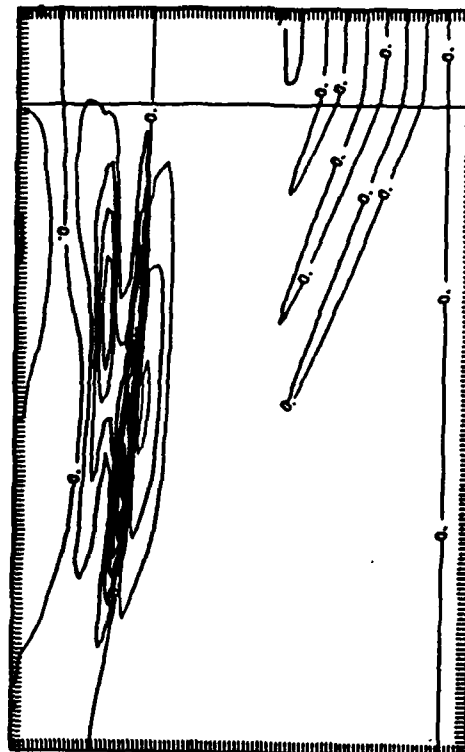


RANGE (METERS)
19764.95

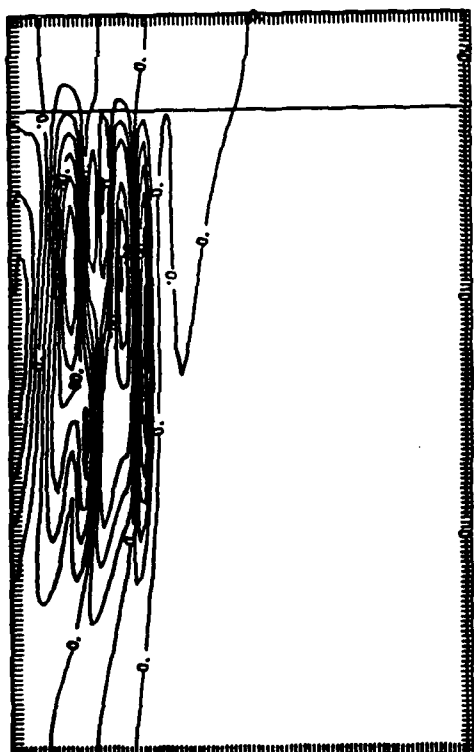
Figure 10. Linear ice simulation ($\beta = 0$).



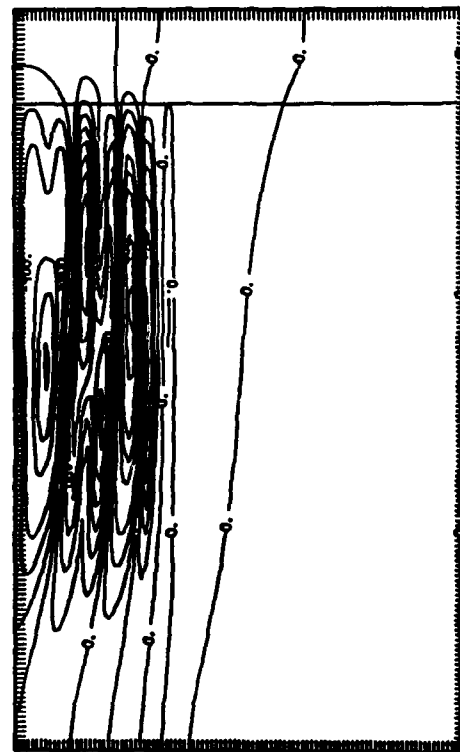
RANGE (METERS)
4.95



RANGE (METERS)
3876.03



RANGE (METERS)
15732.03



RANGE (METERS)
19684.03

Figure 11. Nonlinear ice simulation ($\beta = 3.5$).

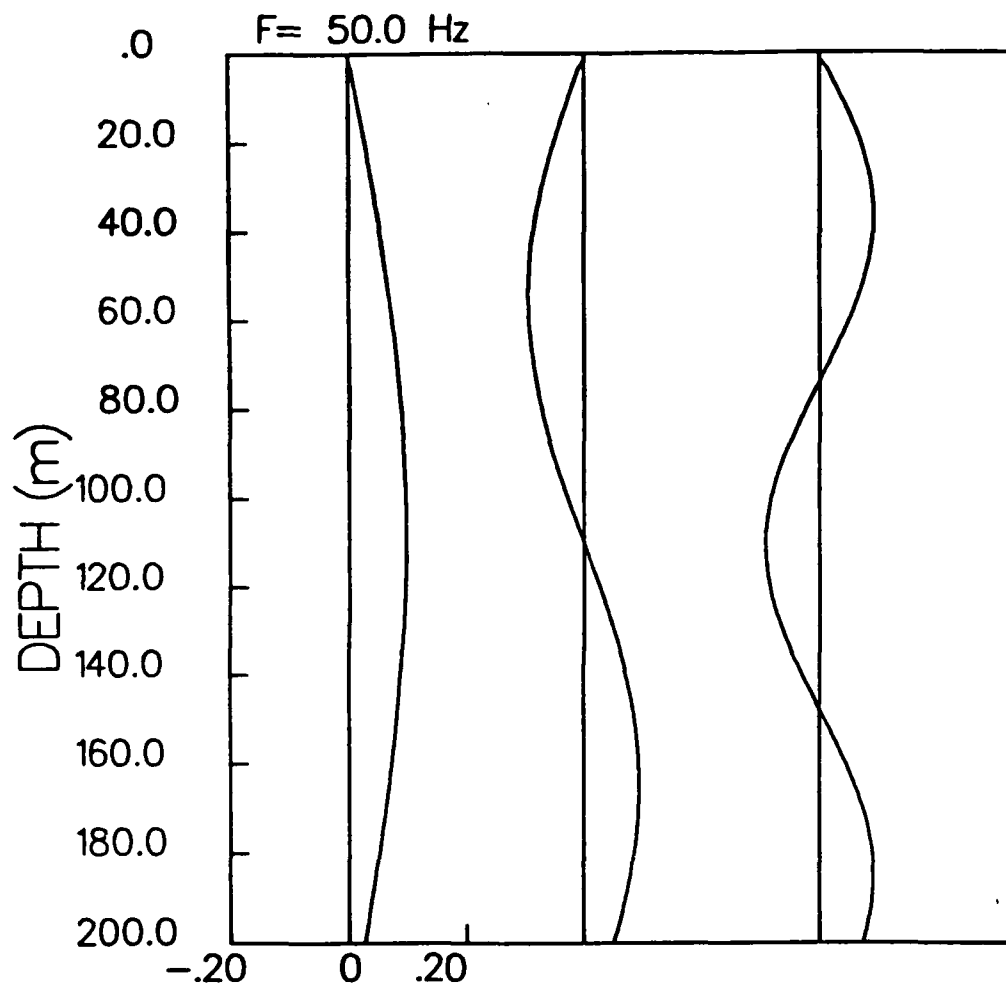
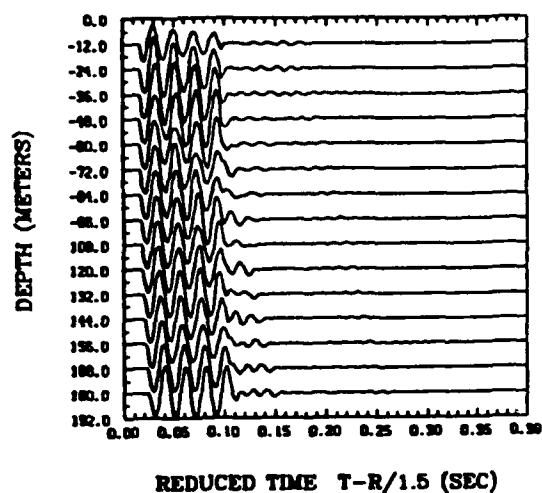


Figure 12. First, second and third modes from Normal Modes calculation.

RANGE = 600 M



RANGE = 20000 M

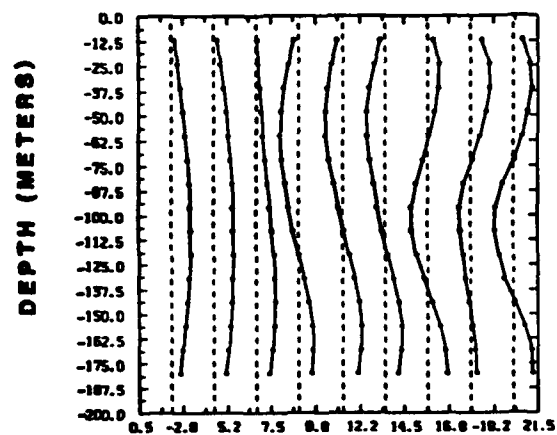
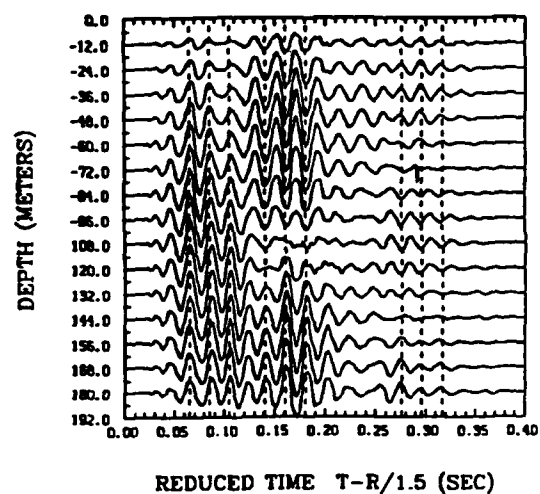
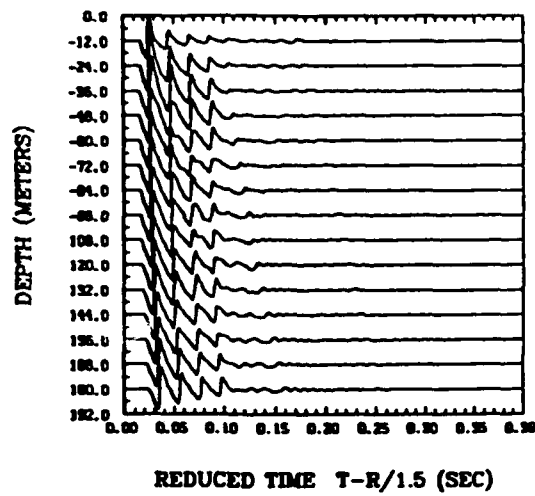


Figure 13. Linear case. Hydrophone readings at (a) 600 m and (b) 20000 m in range, and (c) mode structures found at range of 20000 m. Dashed, vertical lines in (b) mark where mode structures in were taken.

RANGE = 600 M



RANGE = 20000 M

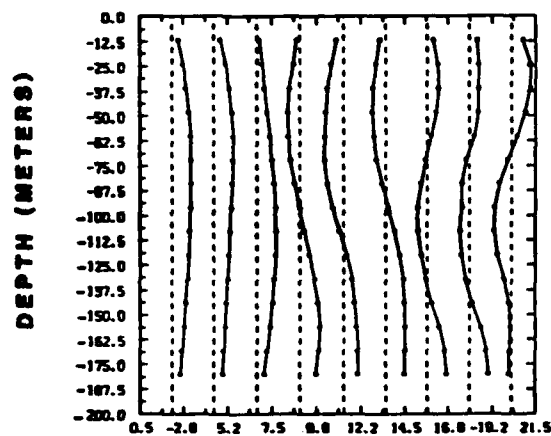
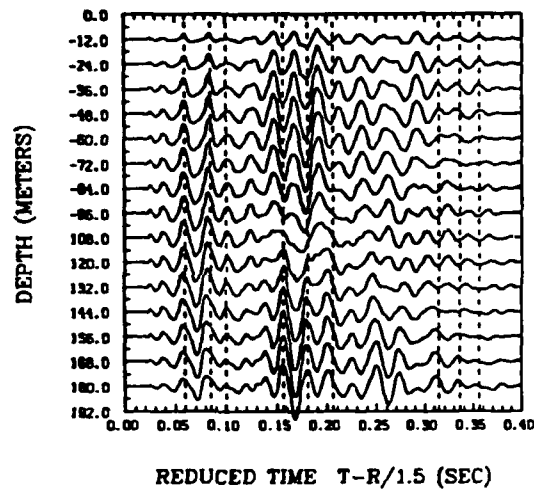


Figure 14. Nonlinear case of Figure 13.

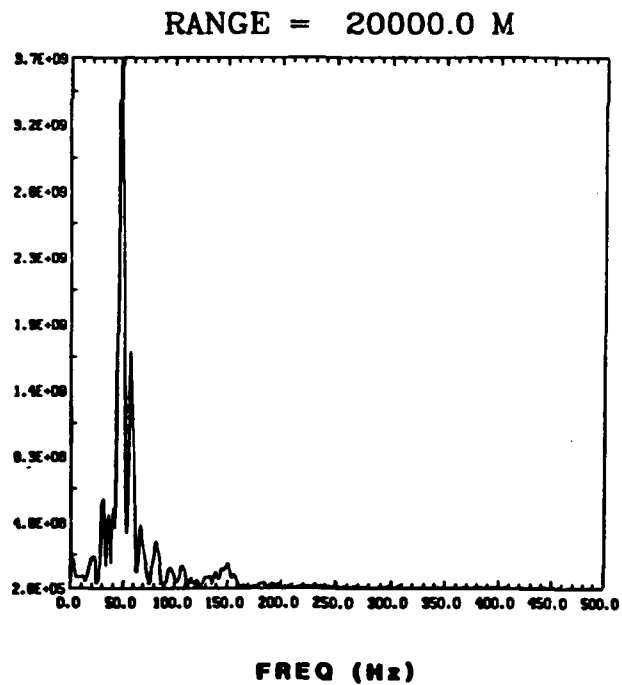
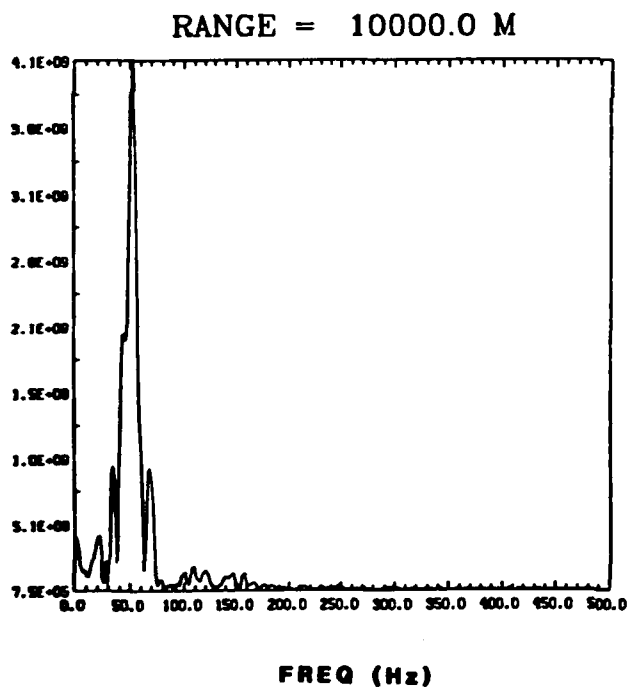
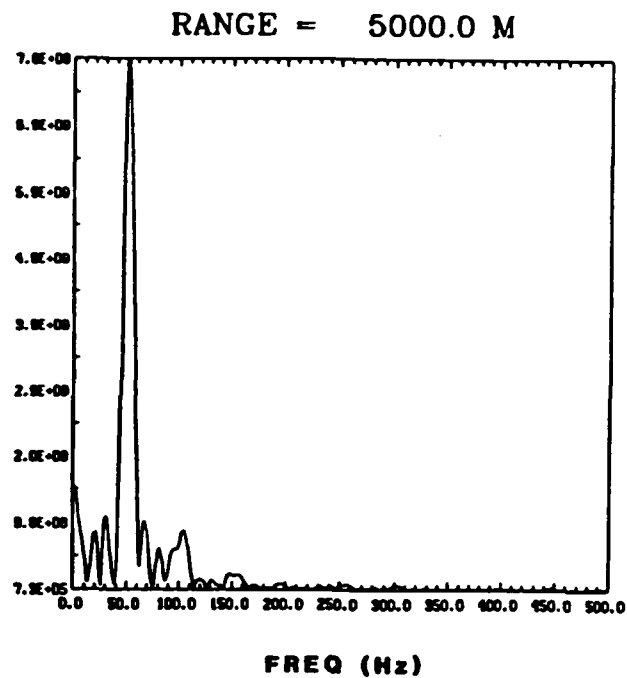
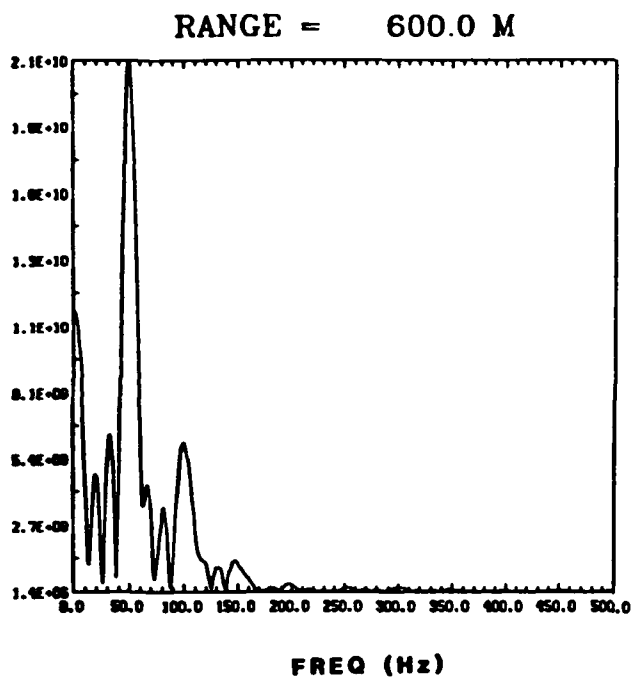


Figure 15. Linear case. Spectra at ranges of (a) 600 m, (b) 5000 m, (c) 10000 m and (d) 20000 m.

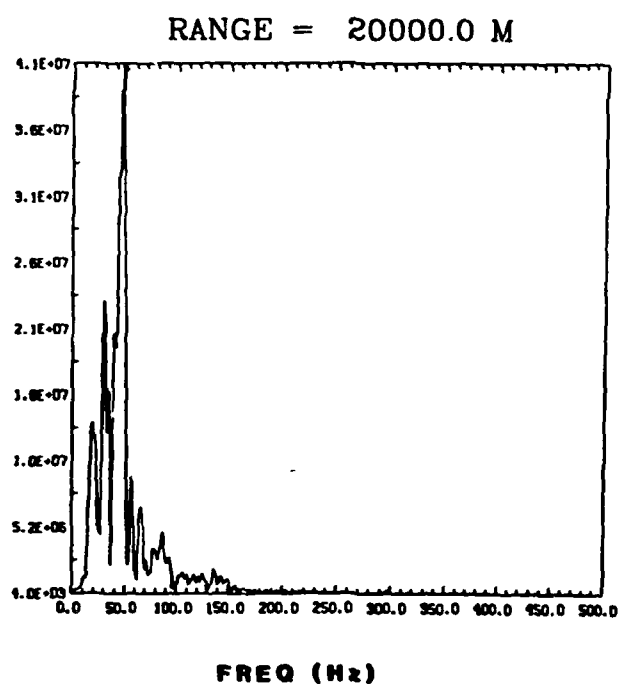
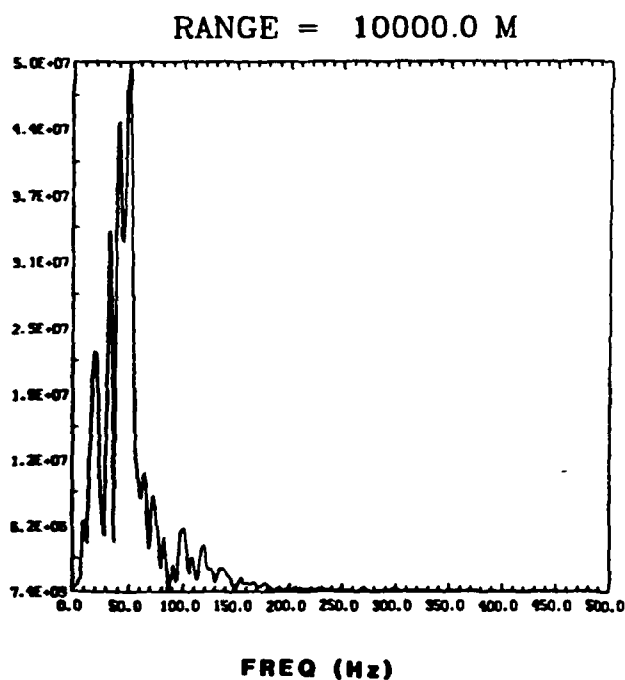
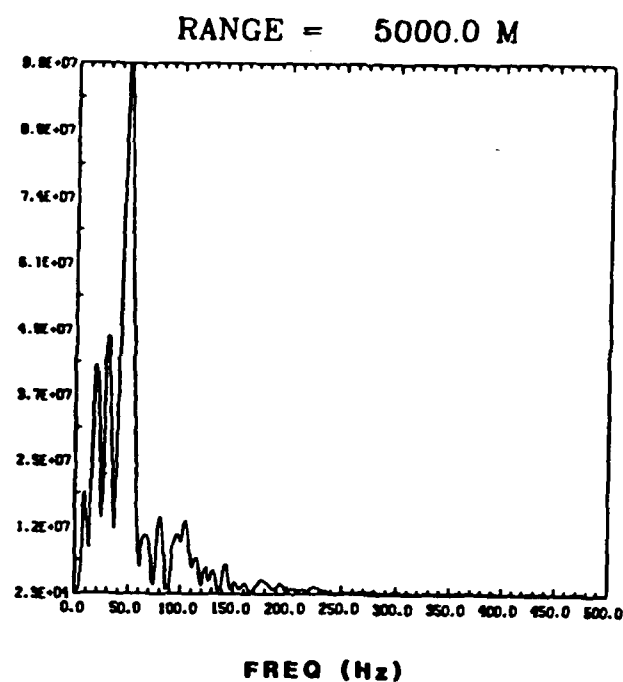
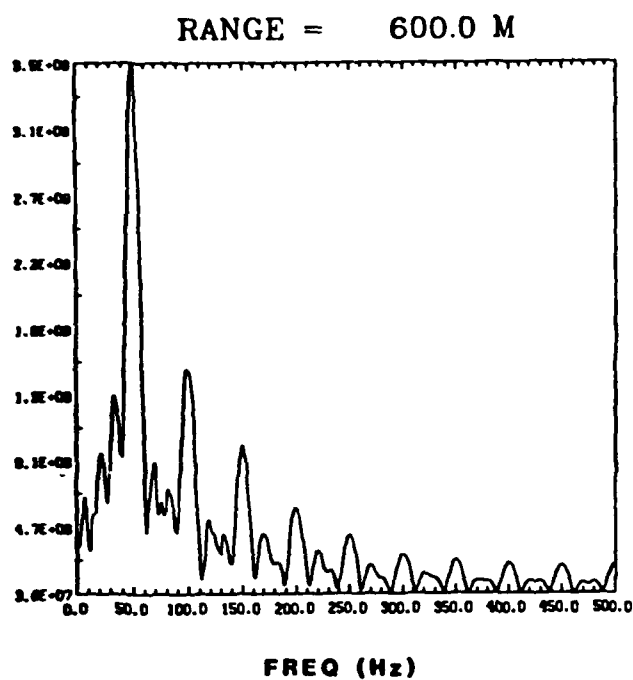
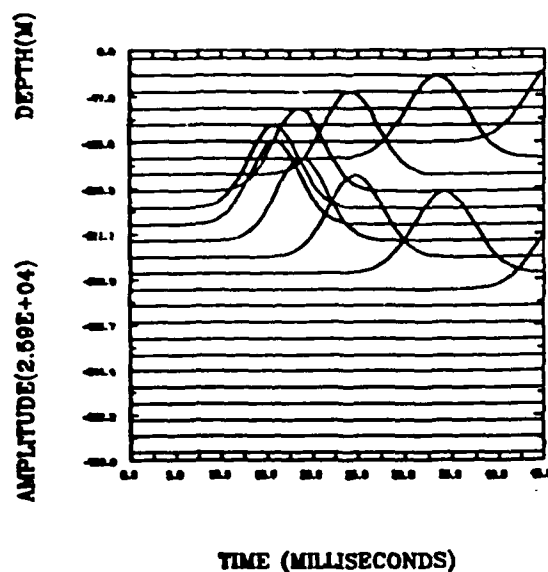
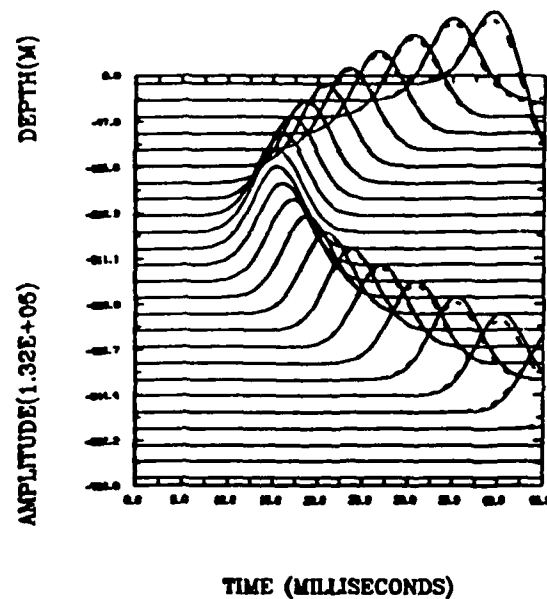


Figure 16. Nonlinear case of Figure 15.

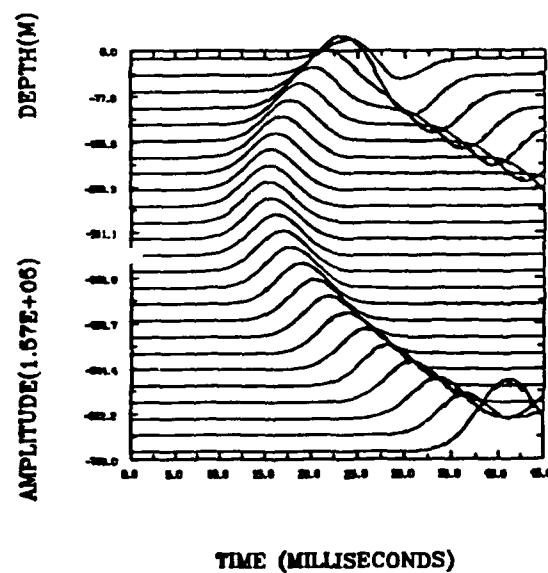
RANGE (KM) = 0.1



RANGE (KM) = 0.9



RANGE (KM) = 2.2



RANGE (KM) = 4.2

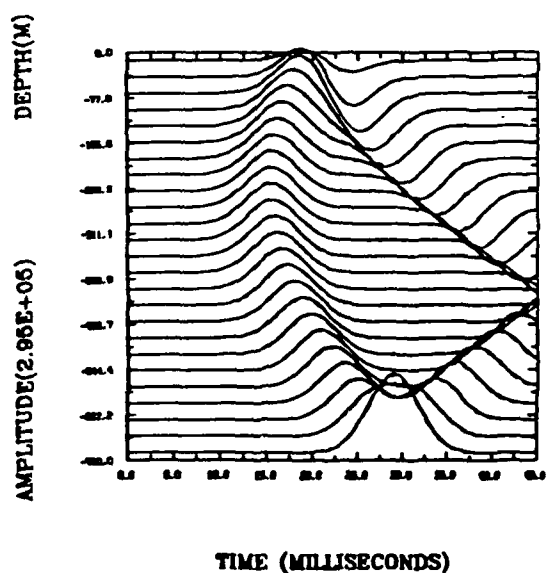


Figure 17. NPE (solid) and analytic (dashed) cross-sections of pressures on grid at ranges of (a) .1 km, (b) .9 km, (c) 2.2 km and (d) 4.2 km.

AD-A193 363

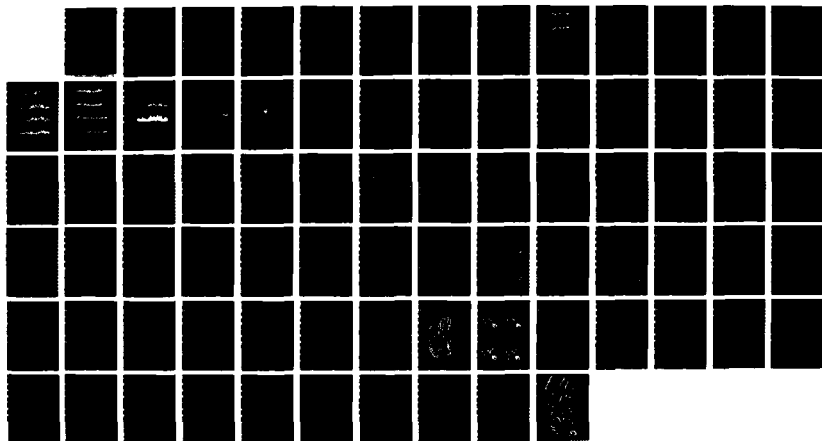
RESEARCH ON OCEAN FORECASTING AND NONLINEAR WAVE
PROPAGATION AND NUMERICAL HYDRODYNAMICS IN THE OCEAN
(U) BERKELEY RESEARCH ASSOCIATES INC CA JAN 88
BRA-88-W016R N00014-85-C-0680

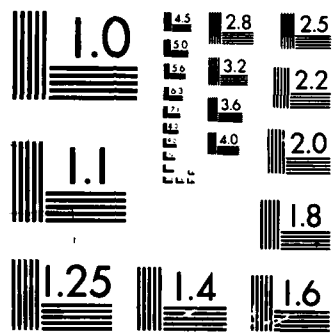
2/2

UNCLASSIFIED

F/G 8/3

NL





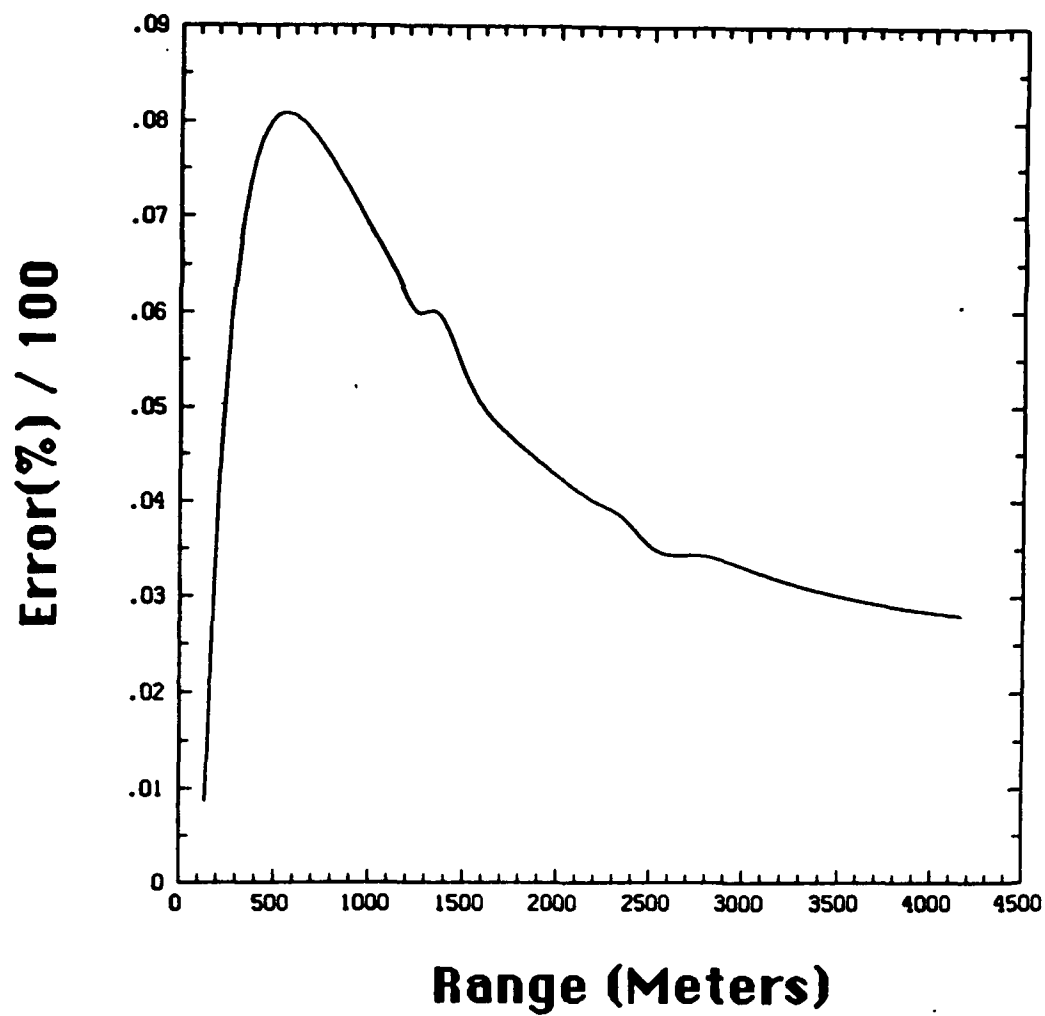


Figure 18. Error plot for case shown in Figure 17.

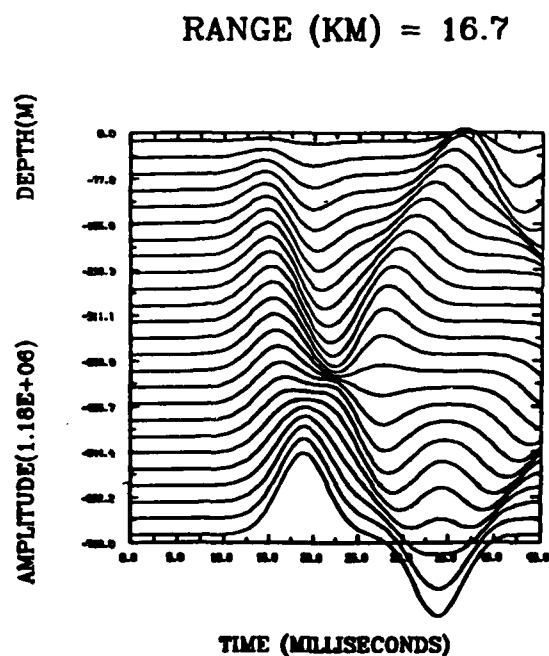
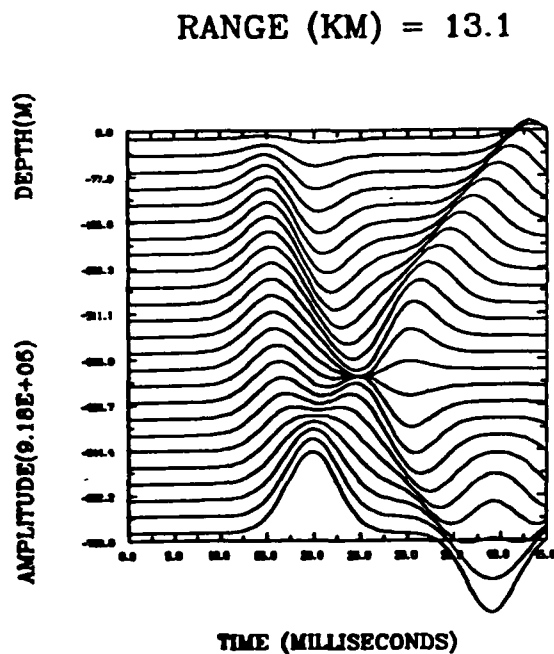
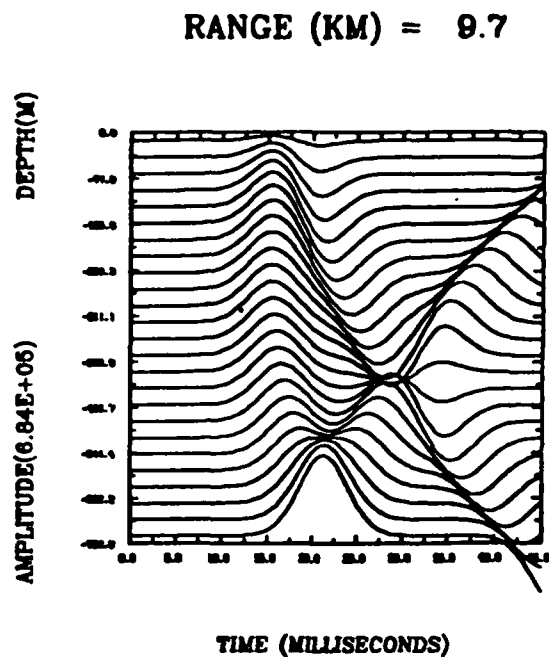
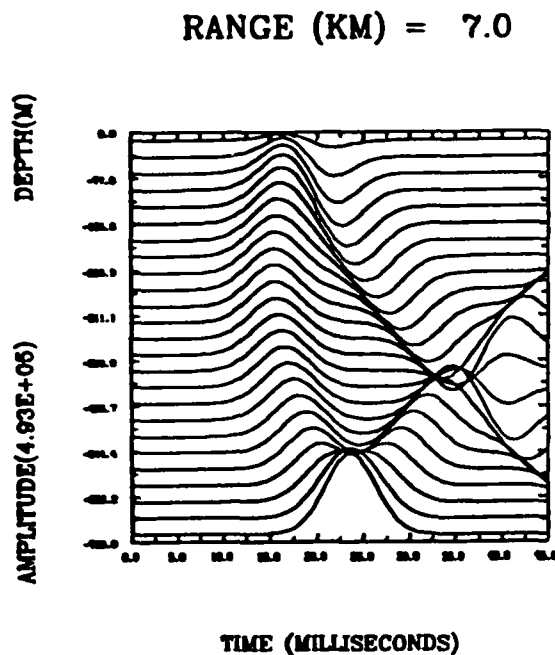


Figure 19. NPE (solid) and analytic (dashed) cross-sections of pressures on grid at ranges of (a) 7.0 km, (b) 9.7 km, (c) 13.1 km and (d) 16.7 km.

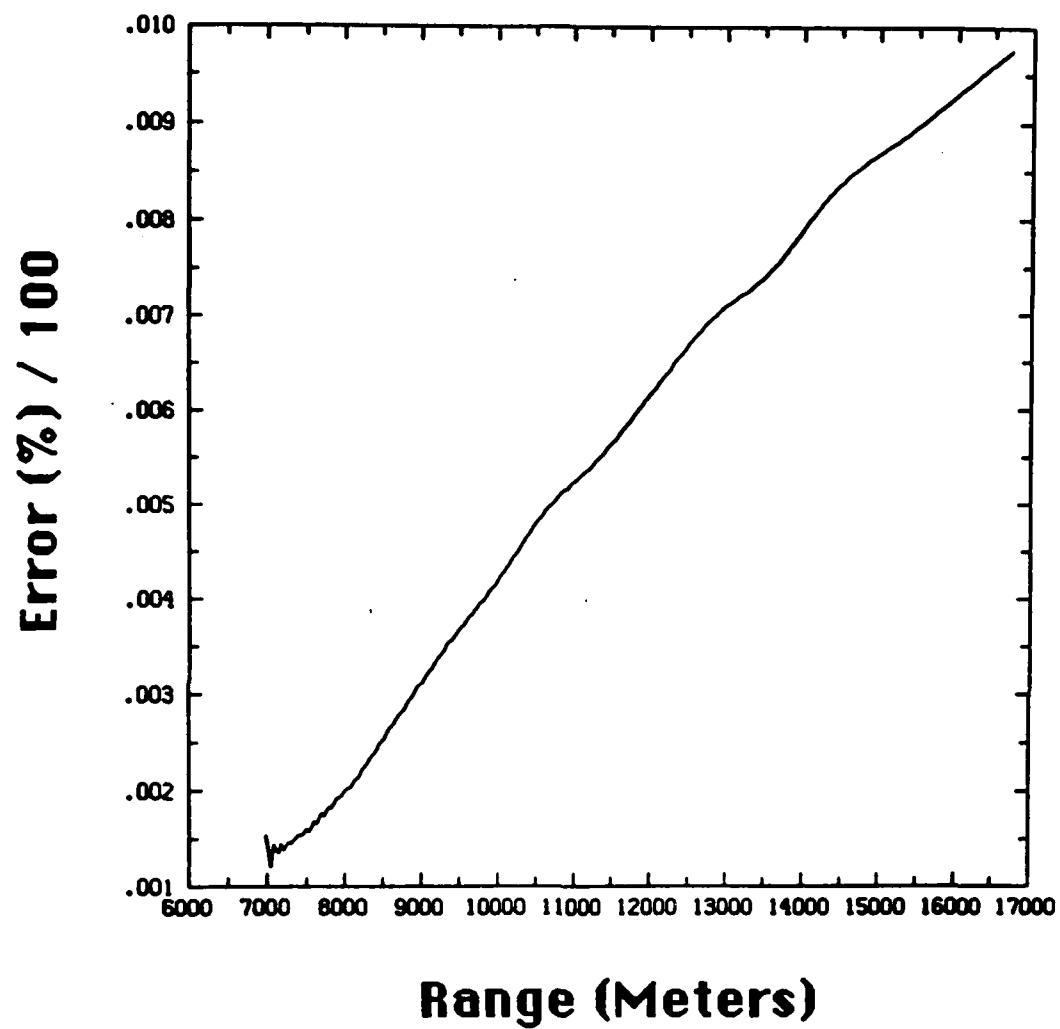


Figure 20. Error plot for case shown in Figure 19.

FIGURE 21
COEFFICIENTS OF EMPIRICAL ORTHOGONAL
FUNCTIONS AT OWS ROMEO, SPRING 1983

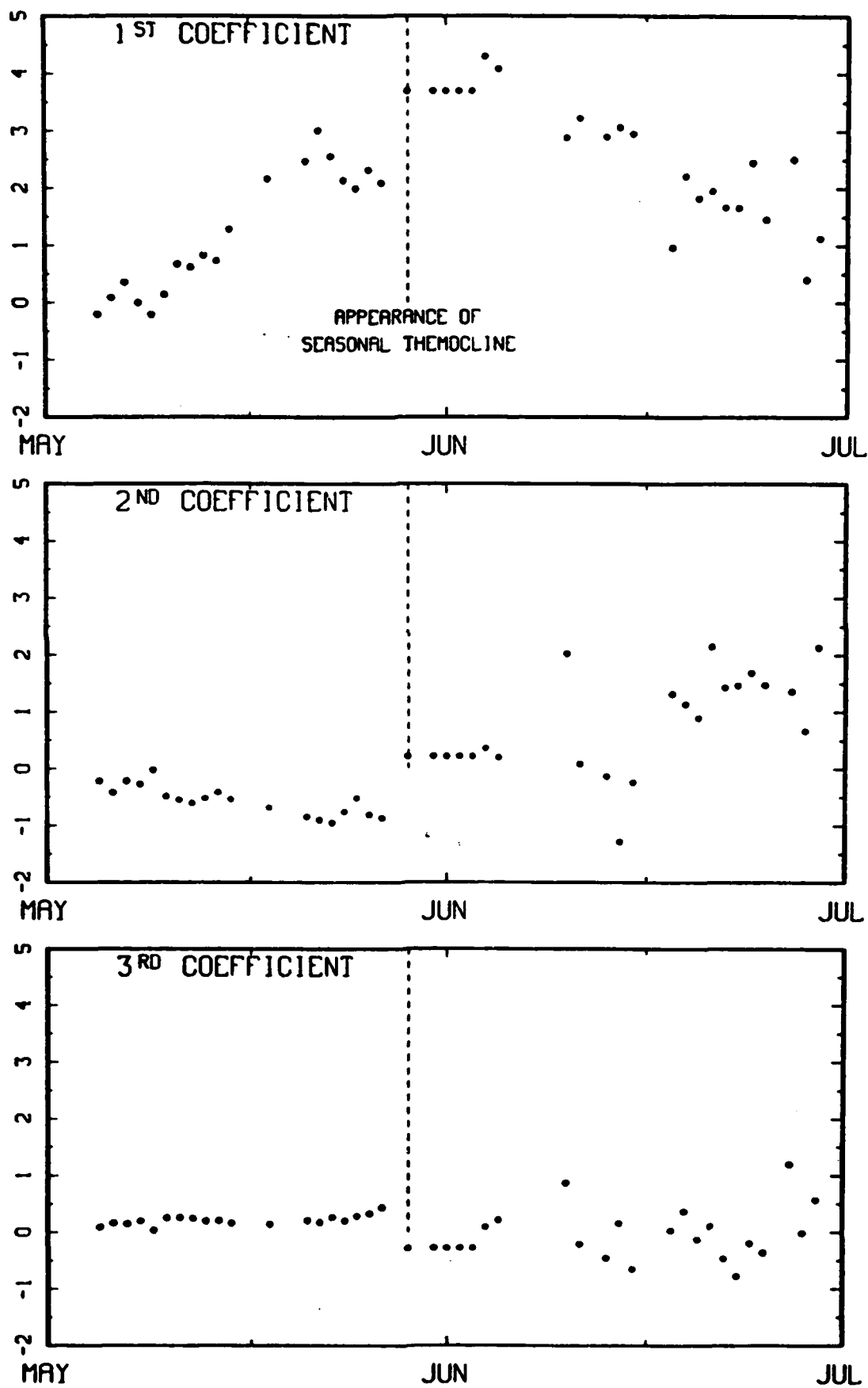
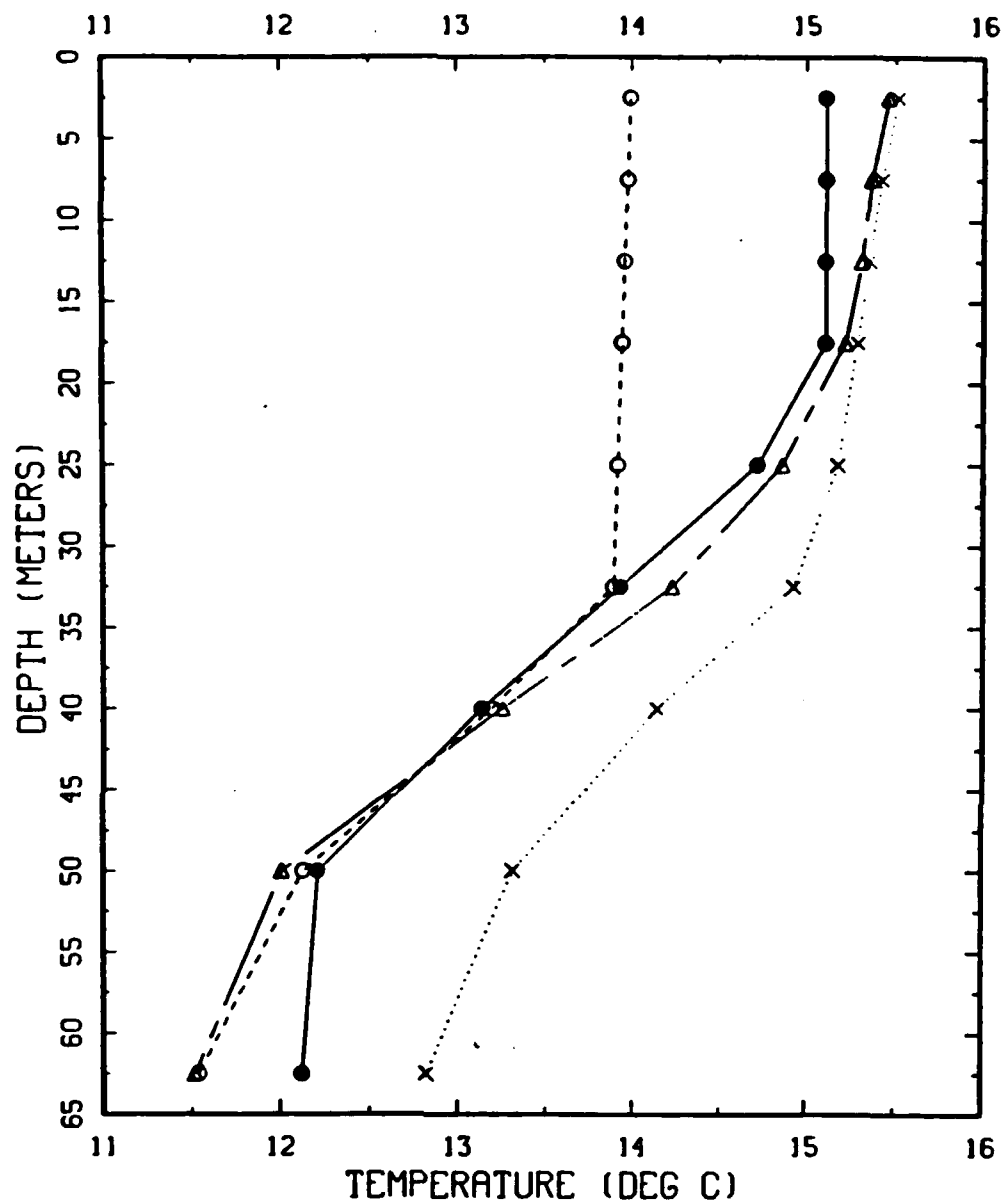


FIGURE 22
FORECASTS OF THE TEMPERATURE PROFILE
FOR DAY 171 - JUNE 20, 1983



- — ● Actual profile day 171
- x x Climatology for day 171
- - - - ○ Persistence from day 167 (log 4)
- △ — — △ Statistical forecast using SST and Z₁(167) (log 4)

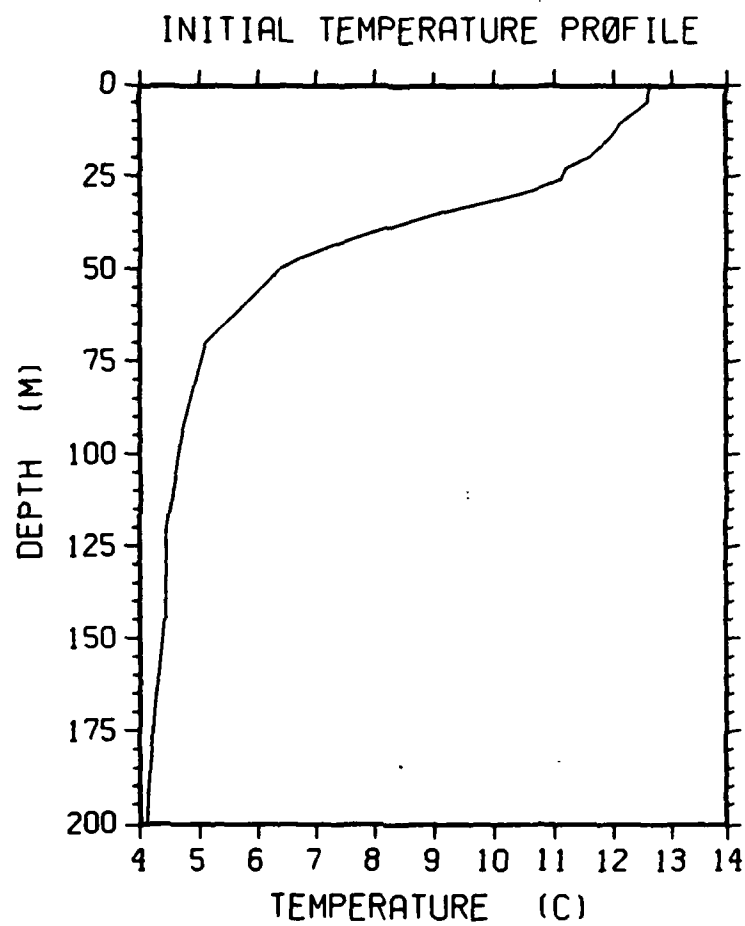


Figure 23 Initial temperature profile for the MLE simulation.

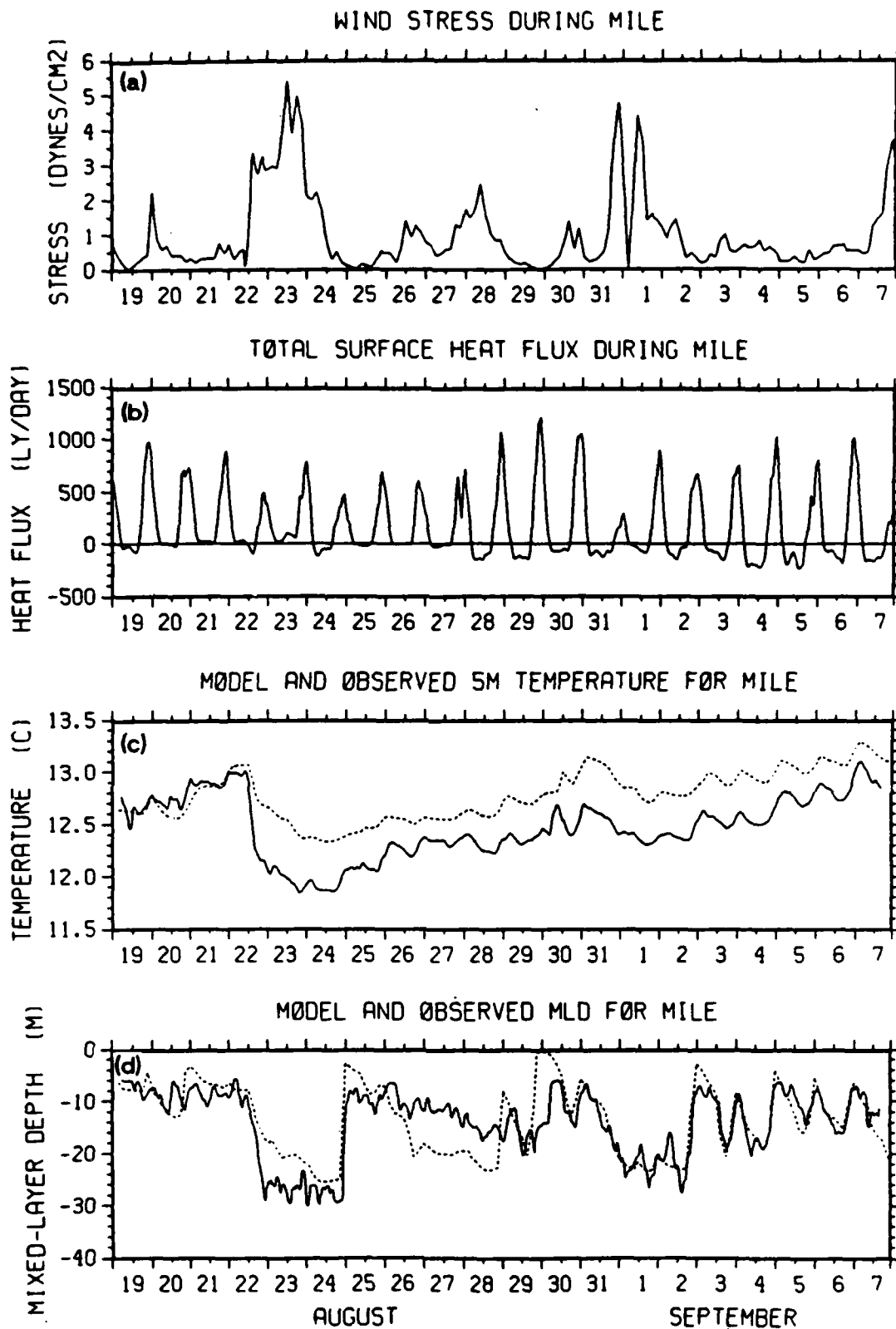


Figure 24 (a) Surface wind stress and (b) net surface heat flux during MLE, and observed (solid line) and predicted (dashed line) (c) 5-m temperature and (d) mixed-layer depth.

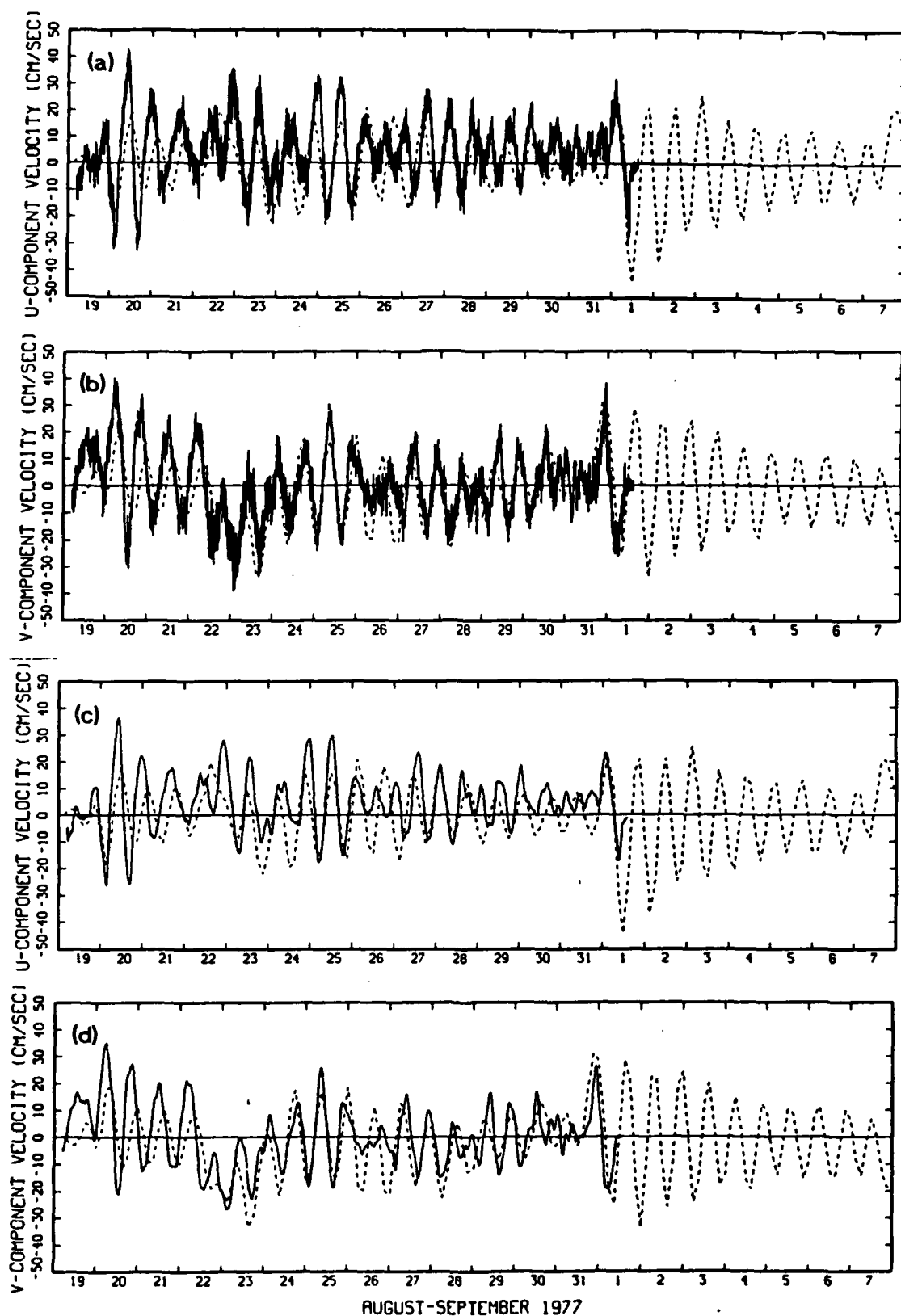


Figure 25 Observed (solid line) and predicted (dashed line) (a) east-west and (b) north-south components of the current at 8 m depth. (c) and (d) show the same comparison, but with the observed current smoothed with a 2-hour filter.

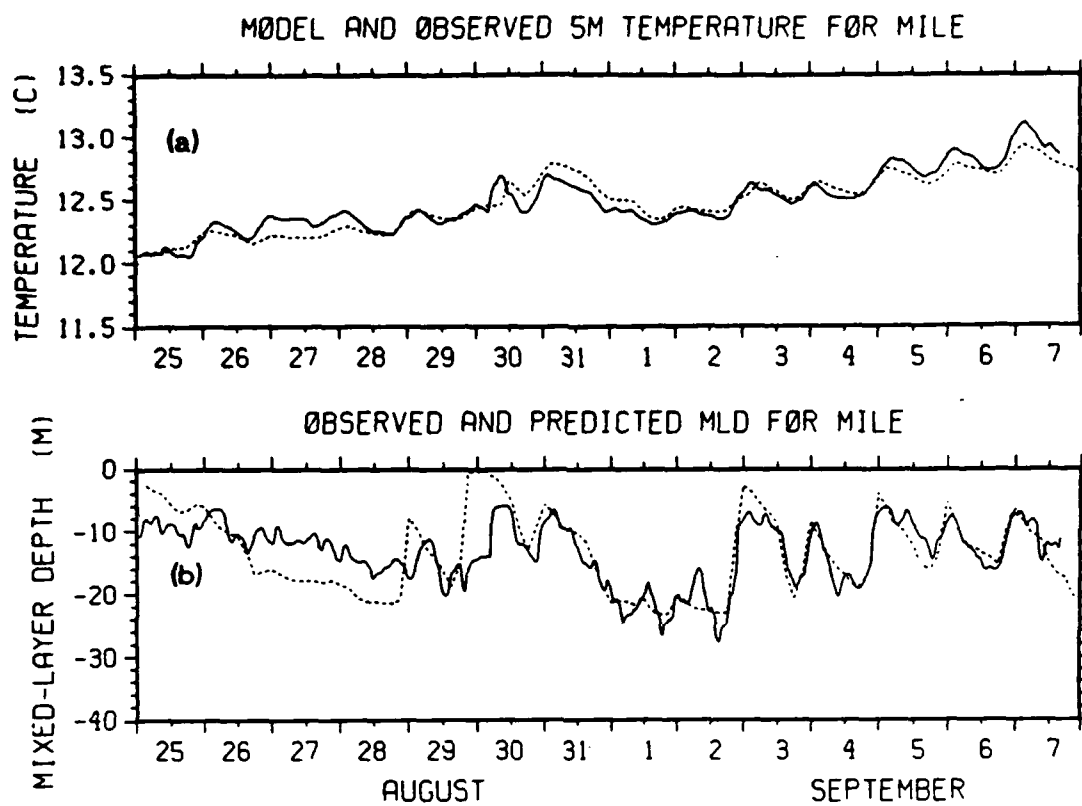


Figure 26 Observed (solid line) and predicted (dashed line) (a) 5-m temperature and (b) mixed-layer depth for a simulation started on August 25, after the August 22-23 storm.

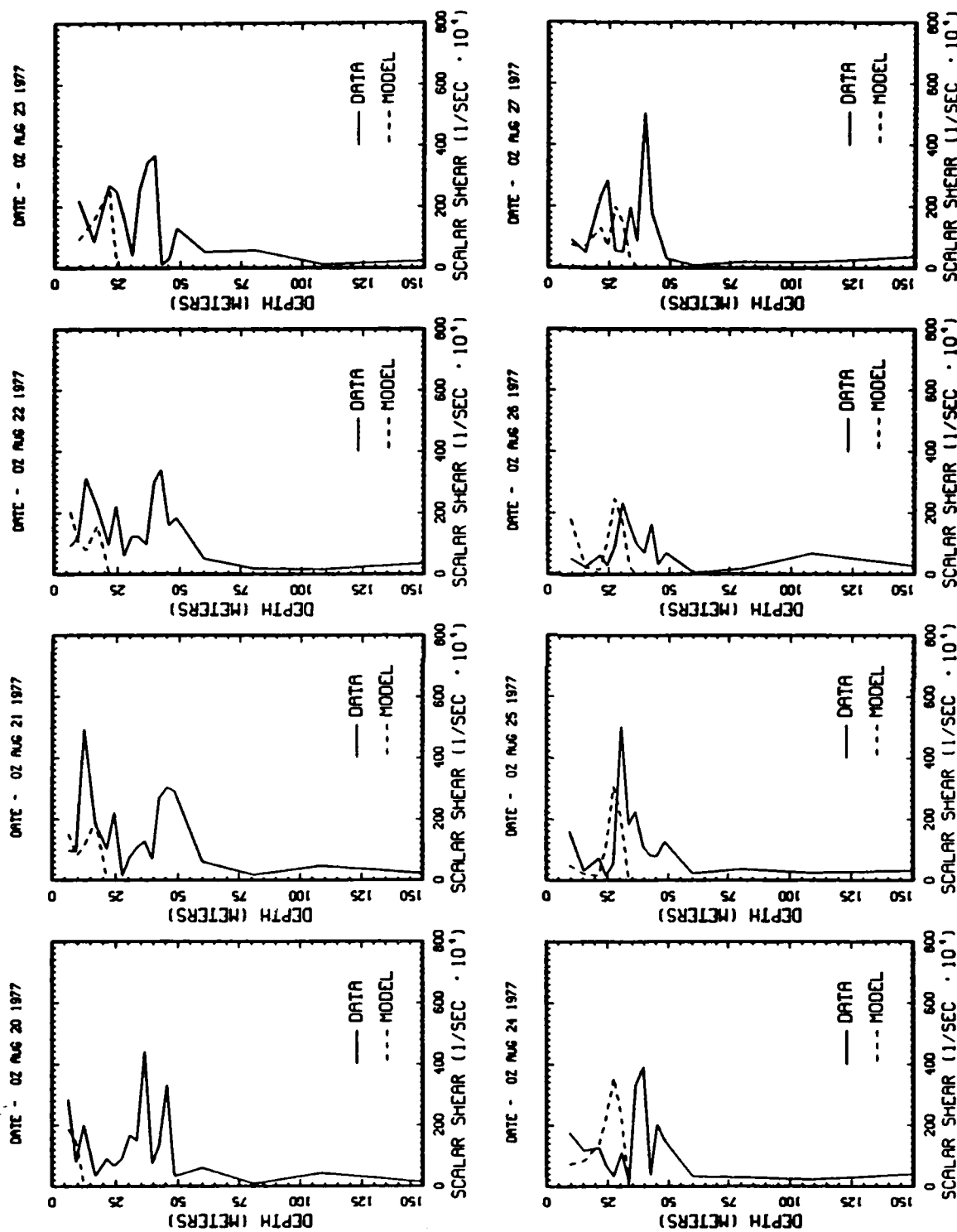


Figure 27 a Observed (solid line) and predicted (dashed line) shear profiles at 00Z from August 20 to August 27.

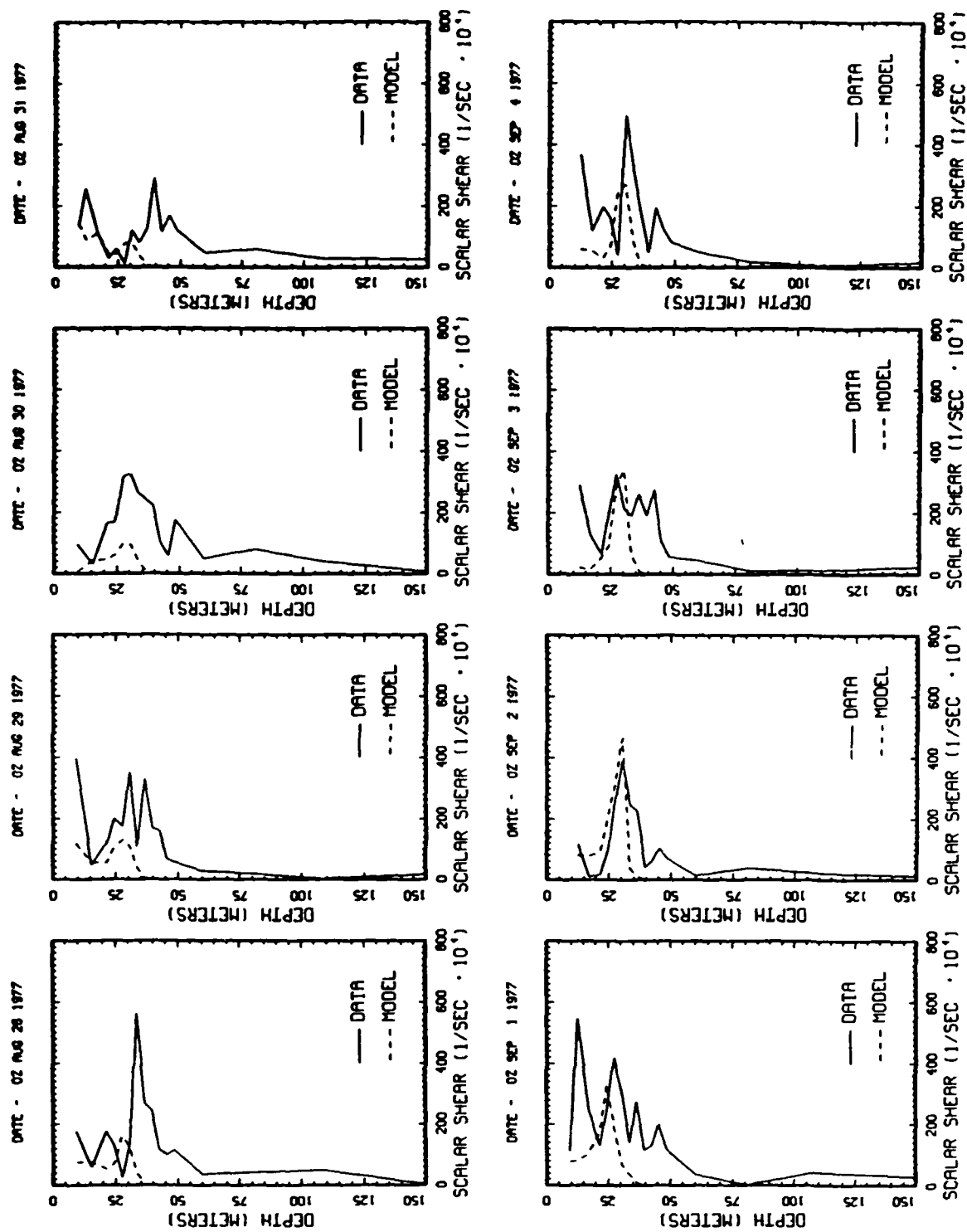
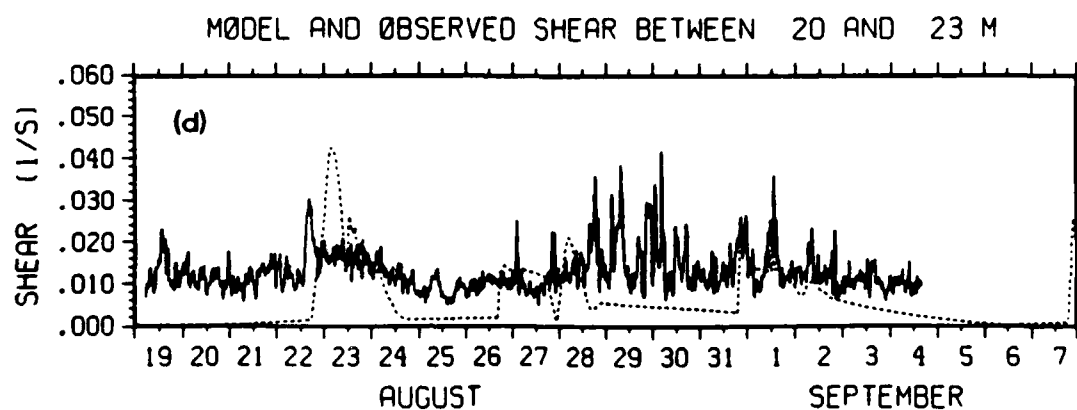
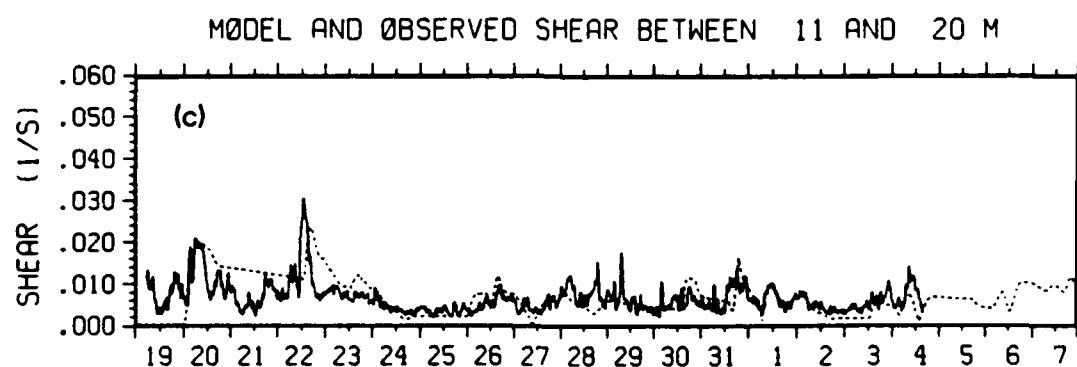
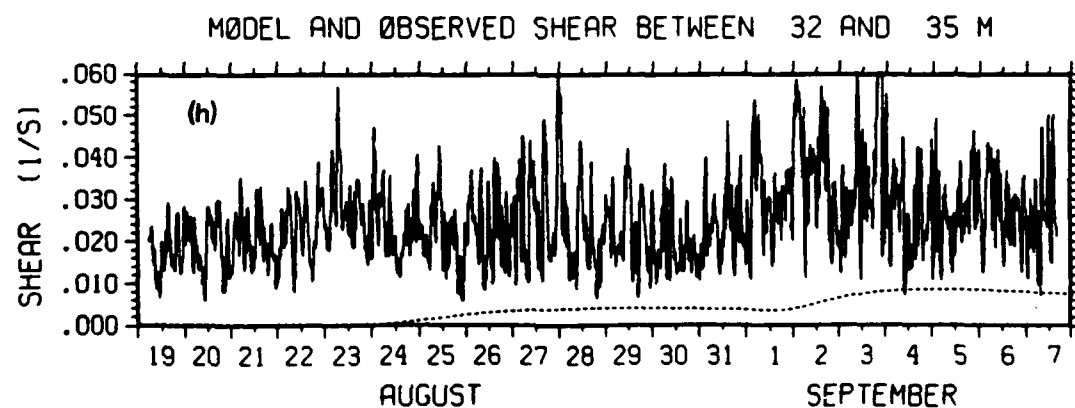
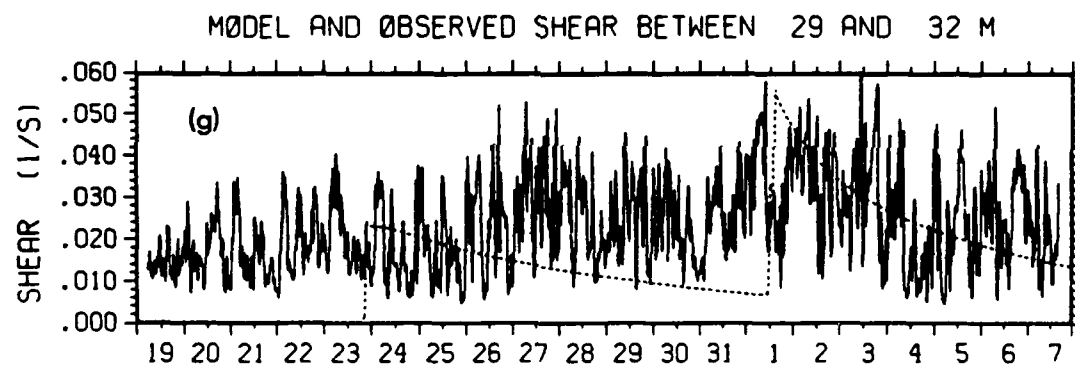
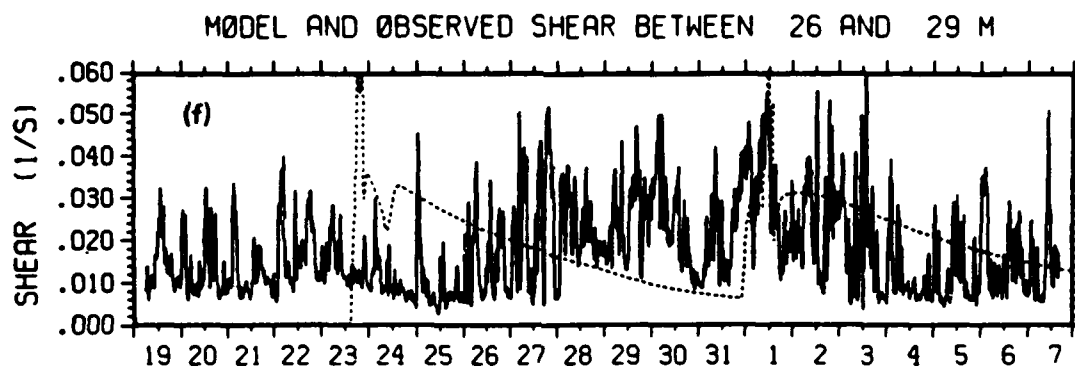


Figure 27 b Observed (solid line) and predicted (dashed line) shear profiles at 00Z from August 28 to September 4.



Observed (solid line) and predicted (dashed line) shear during MILE between (a) 5 and 8 m depth, (b) 8 and 11 m depth, (c) 11 and 20 m depth, and (d) 20 and 23 m depth. The observed time series of shear have been filtered to eliminate frequencies above 2 cph.



Observed (solid line) and predicted (dashed line) shear during MLE between (e) 23 and 26 m depth, (f) 26 and 29 m depth, (g) 29 and 32 m depth, and (h) 32 and 35 m depth.

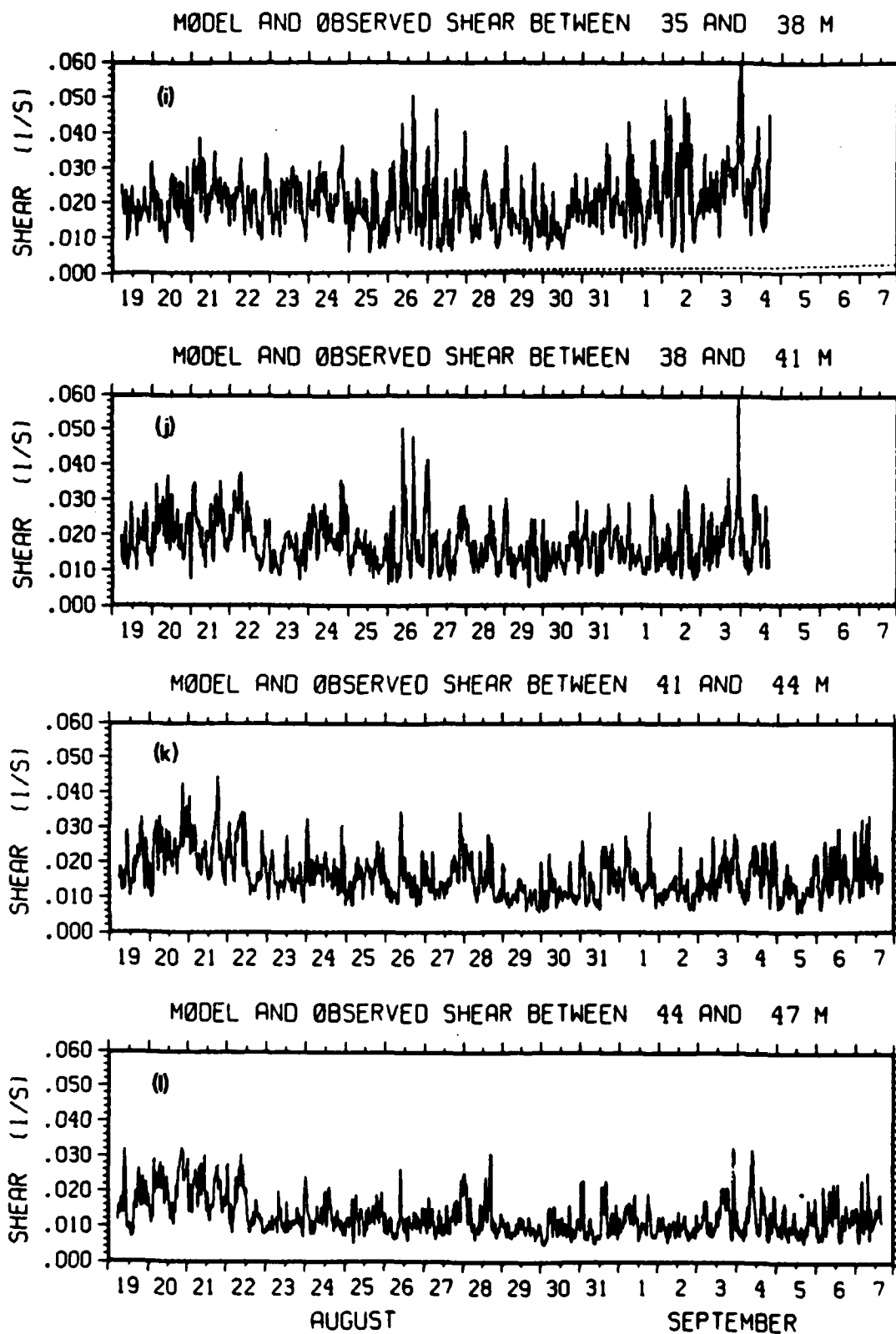


Figure
281-1

Observed (solid line) and predicted (dashed line) shear during
MLE between (i) 35 and 38 m depth, (j) 38 and 41 m depth,
(k) 41 and 44 m depth, and (l) 44 and 47 m depth.

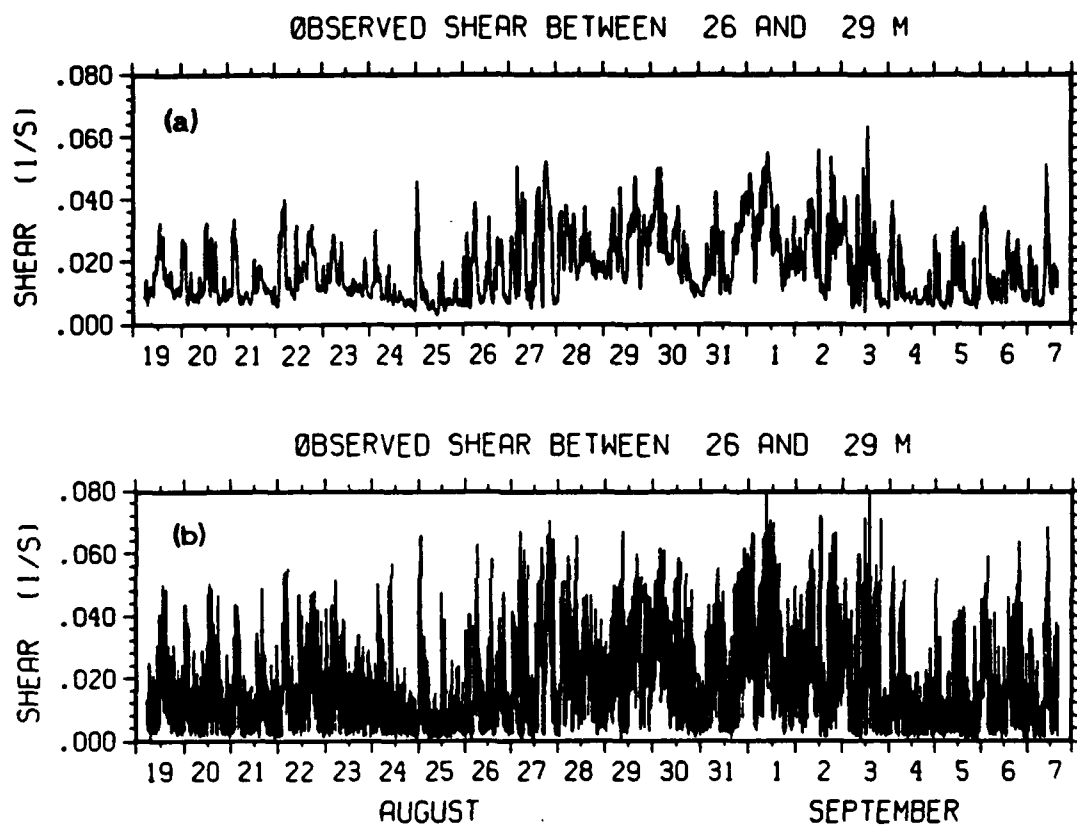


Figure 29 Comparison of (a) filtered and (b) unfiltered shear time series between 26 and 29 m depth.

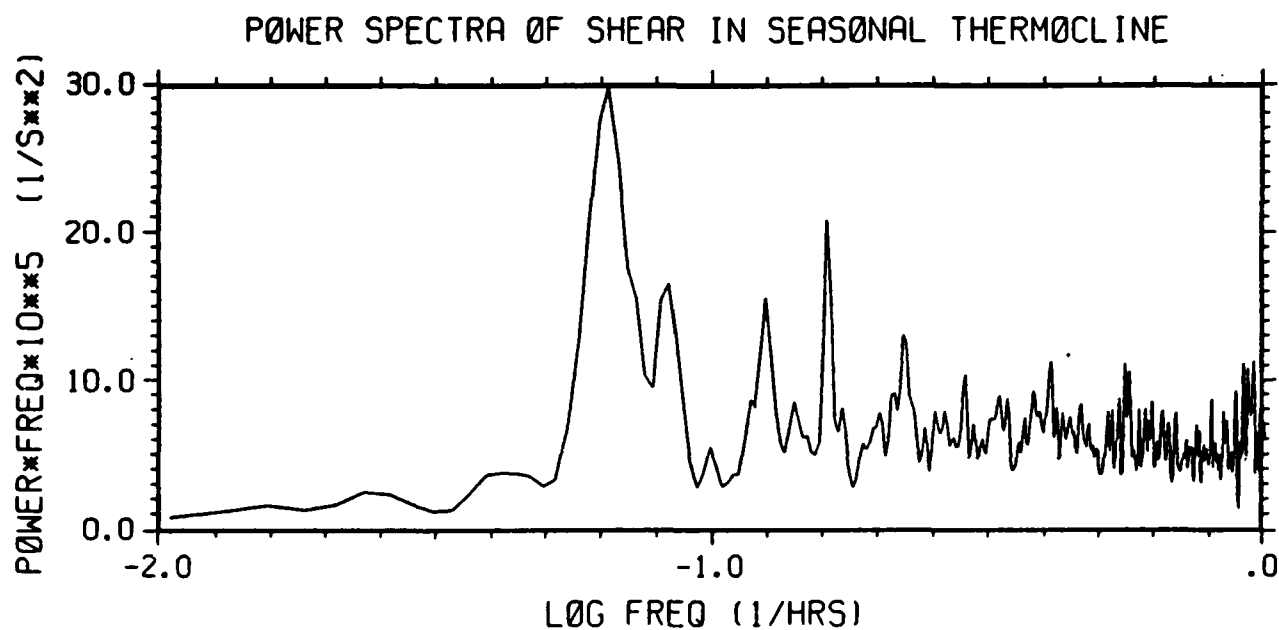


Figure 30 Variance-conserving power spectra of E-W component of shear in the seasonal thermocline. The most prominent peak corresponds to the inertial frequency (.064 cycles/hr) and the peak just to its right corresponds to the semi-diurnal internal tide (.0806 cycles/hr). The other two prominent peaks occur at the location of the first harmonics of the inertial and semi-diurnal tidal frequencies.

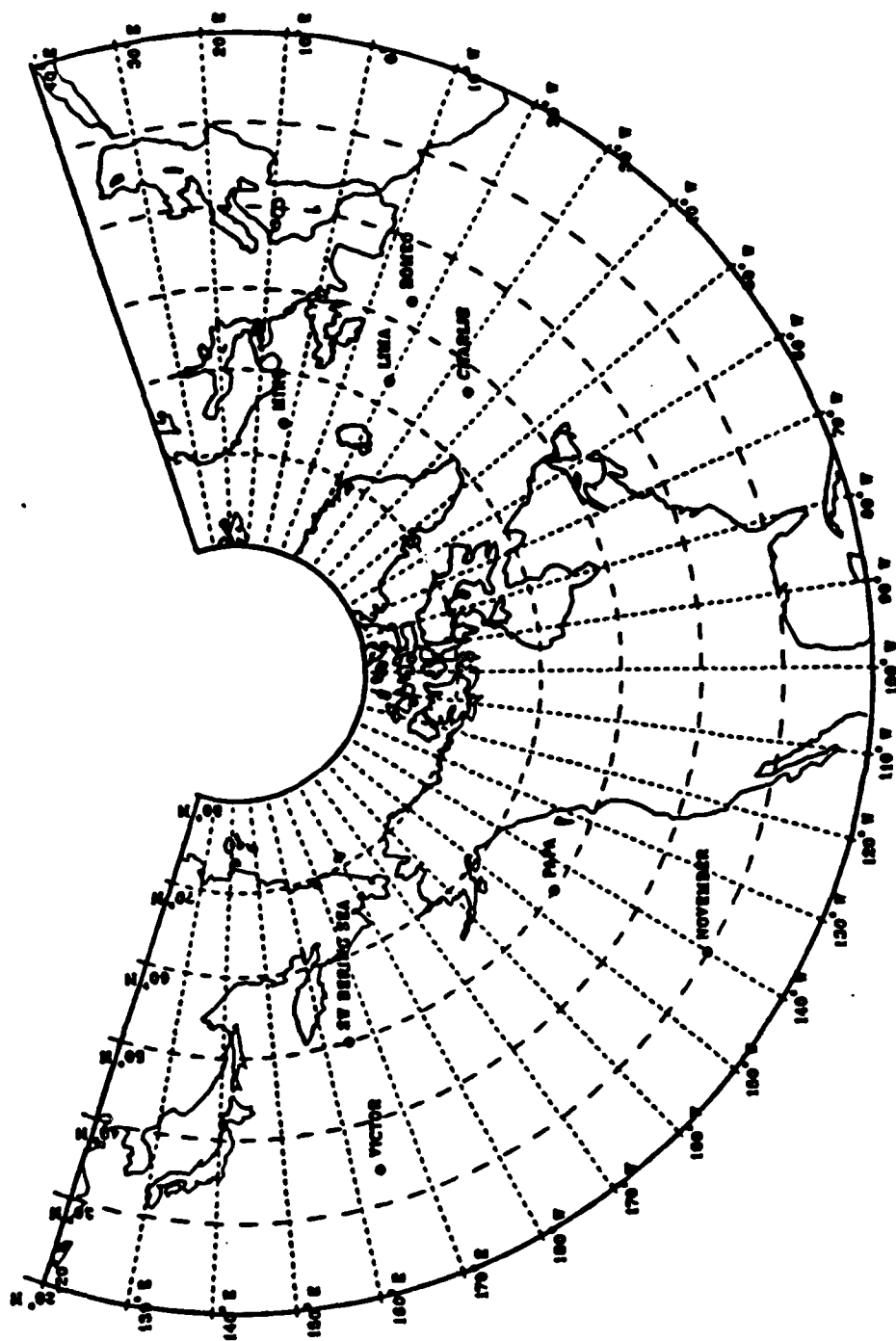


Figure 31 Map of Station Locations.

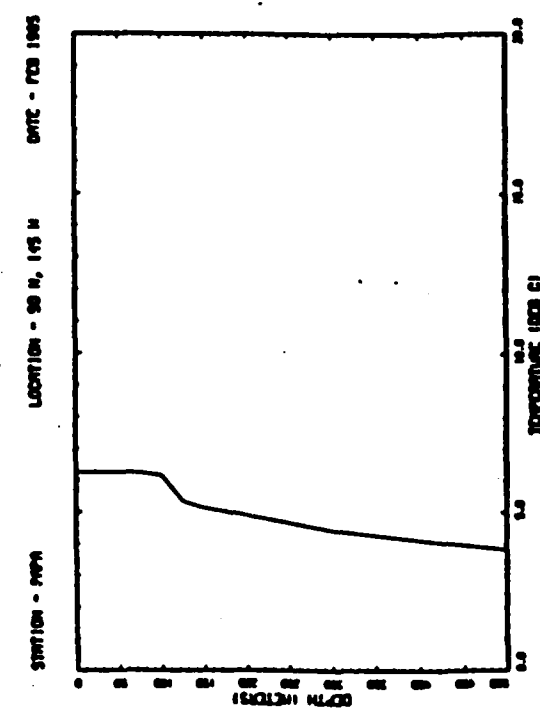
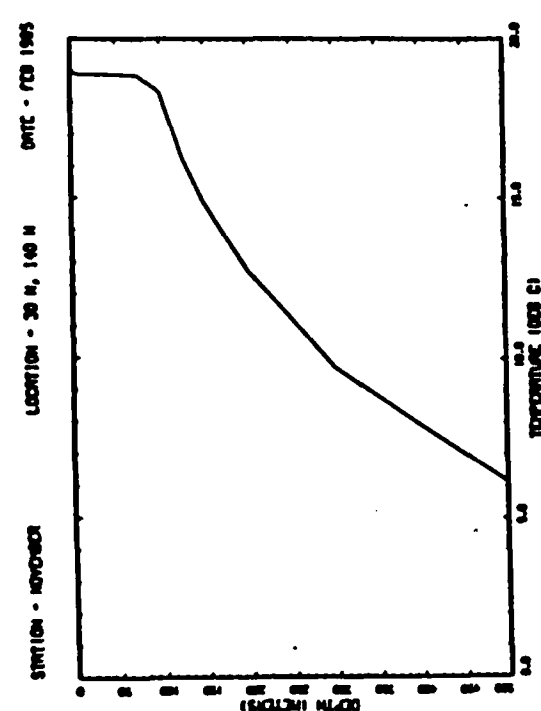
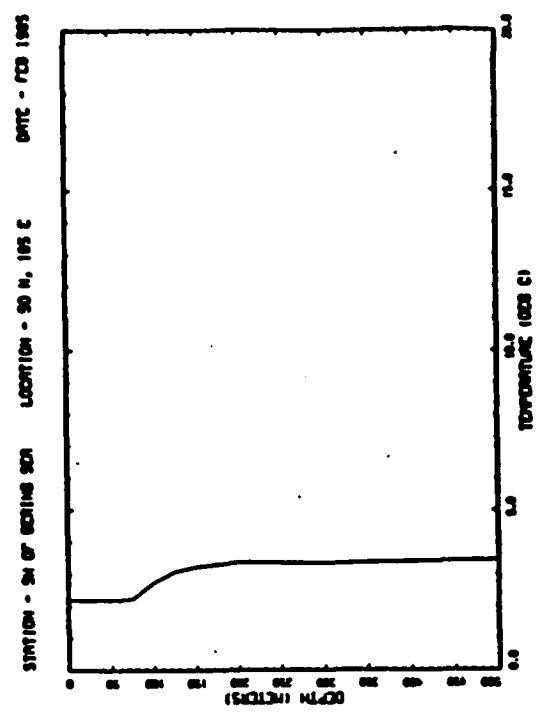
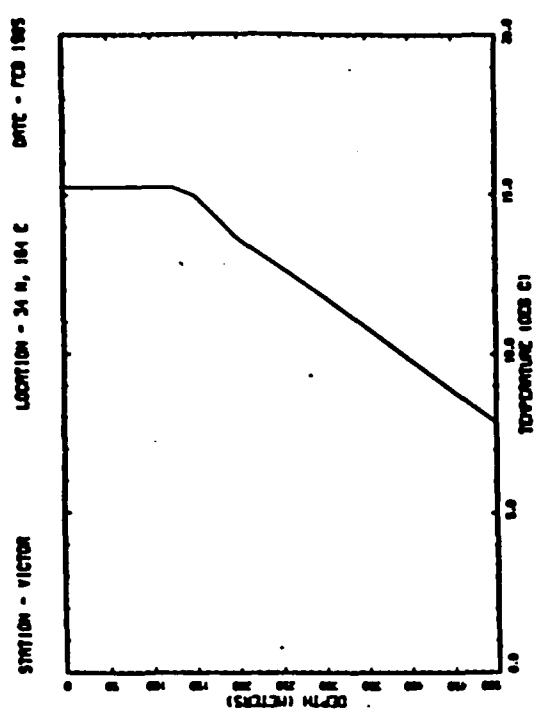


Figure 3.2 Monthly-averaged vertical temperature profiles at the 4 North Pacific stations for the month of February.

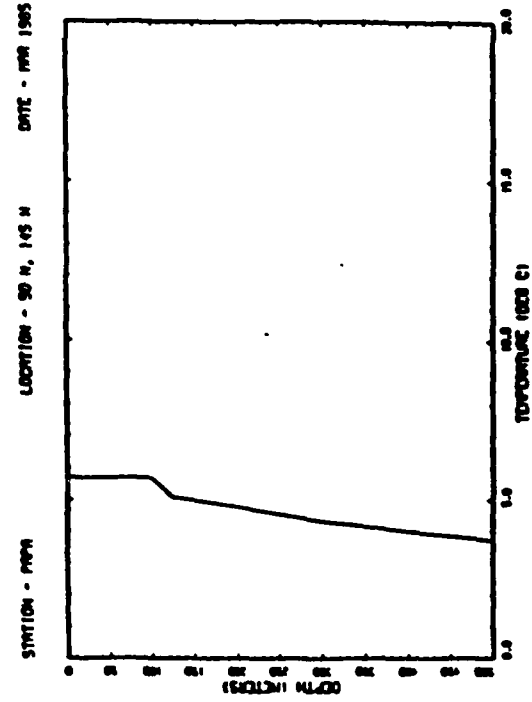
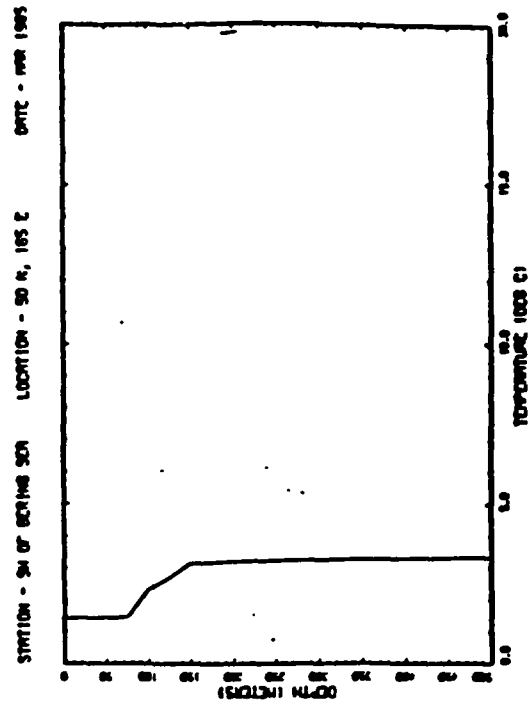
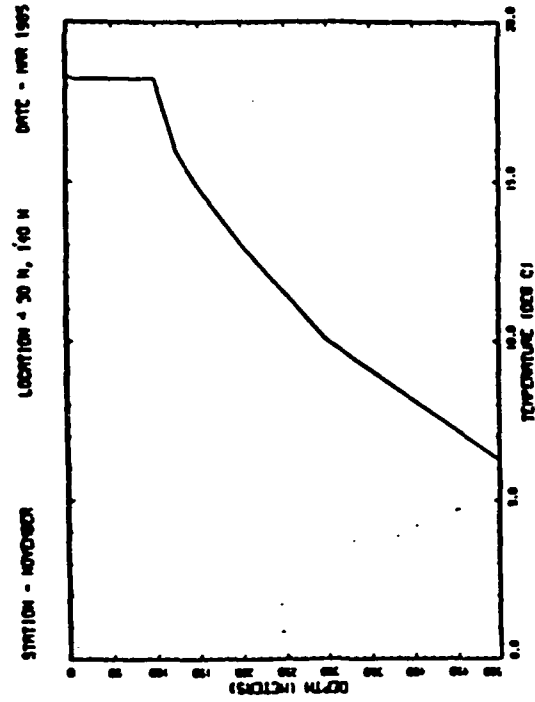
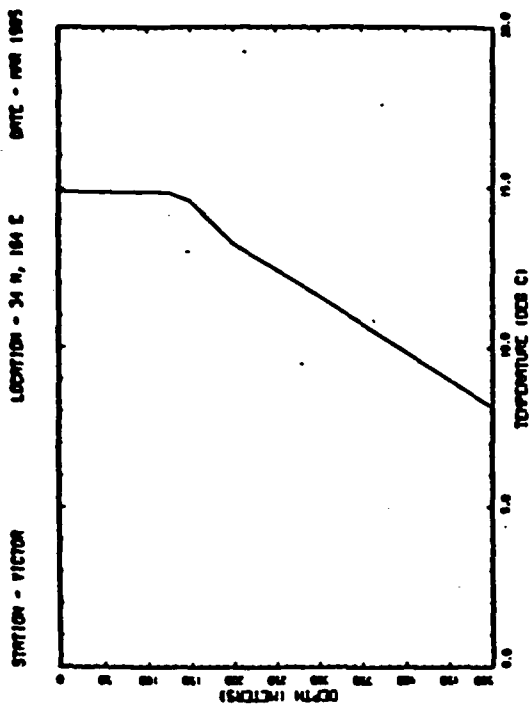


Figure 33 Monthly-averaged vertical temperature profiles at the 4 North Pacific stations for the month of March.

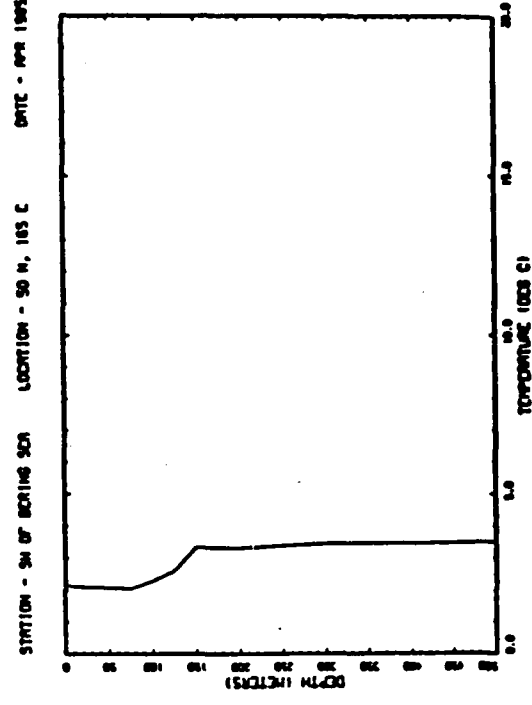
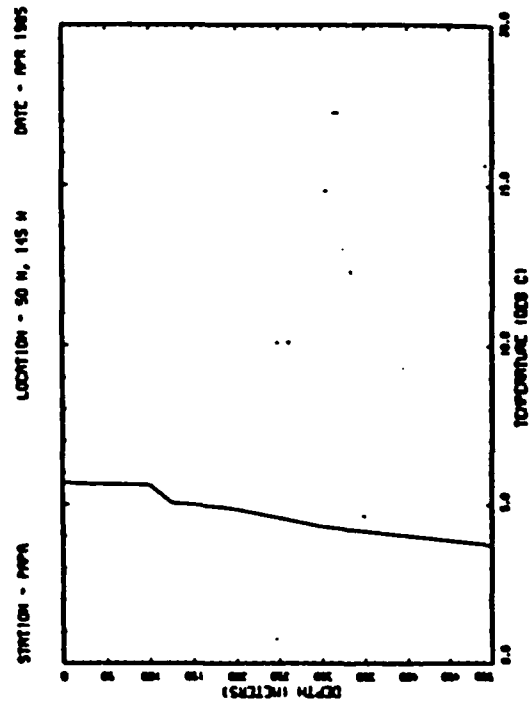
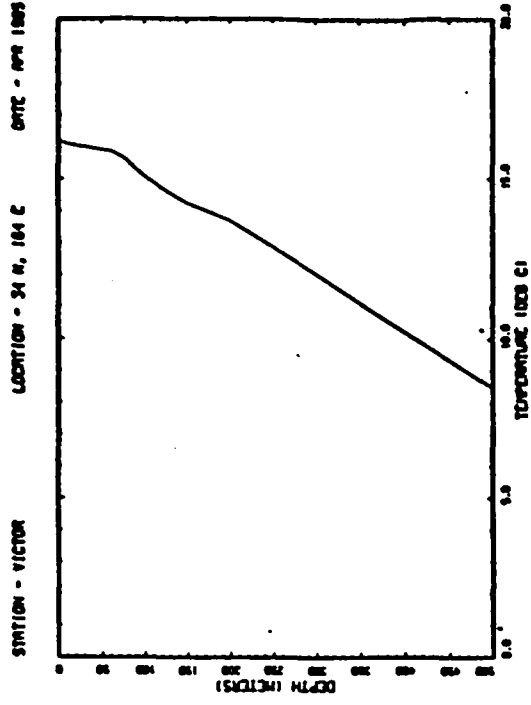
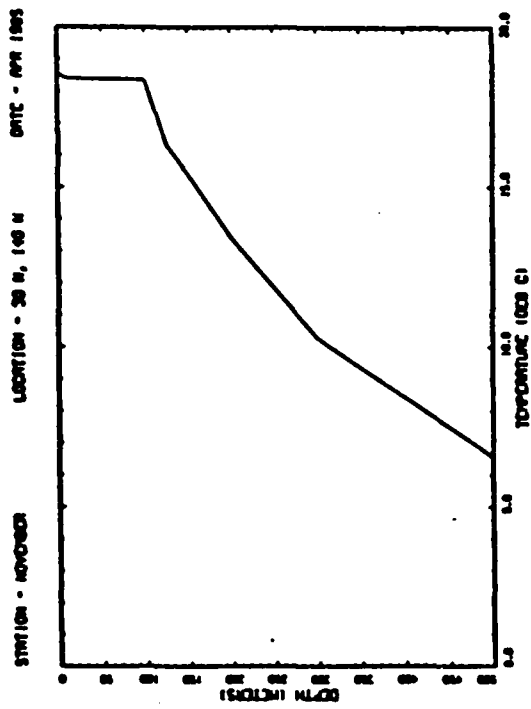


Figure 34 Monthly-averaged vertical temperature profiles at the 4 North Pacific stations for the month of April.

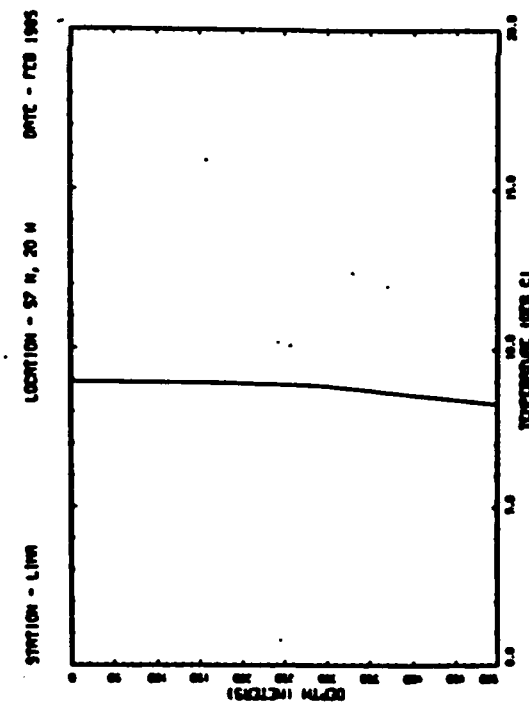
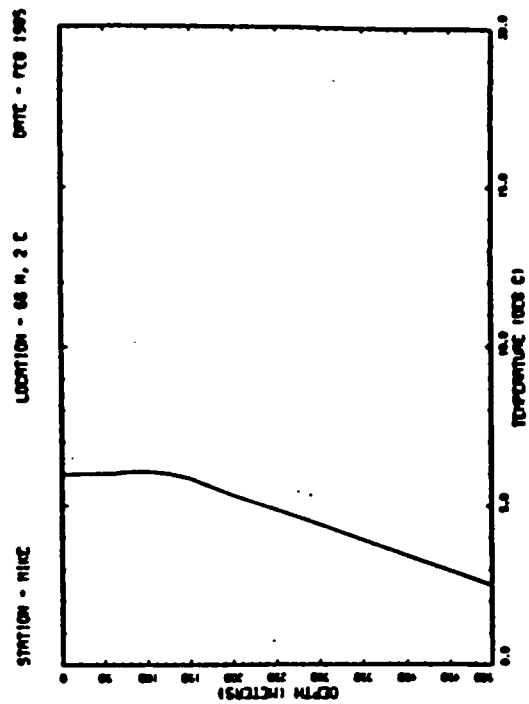
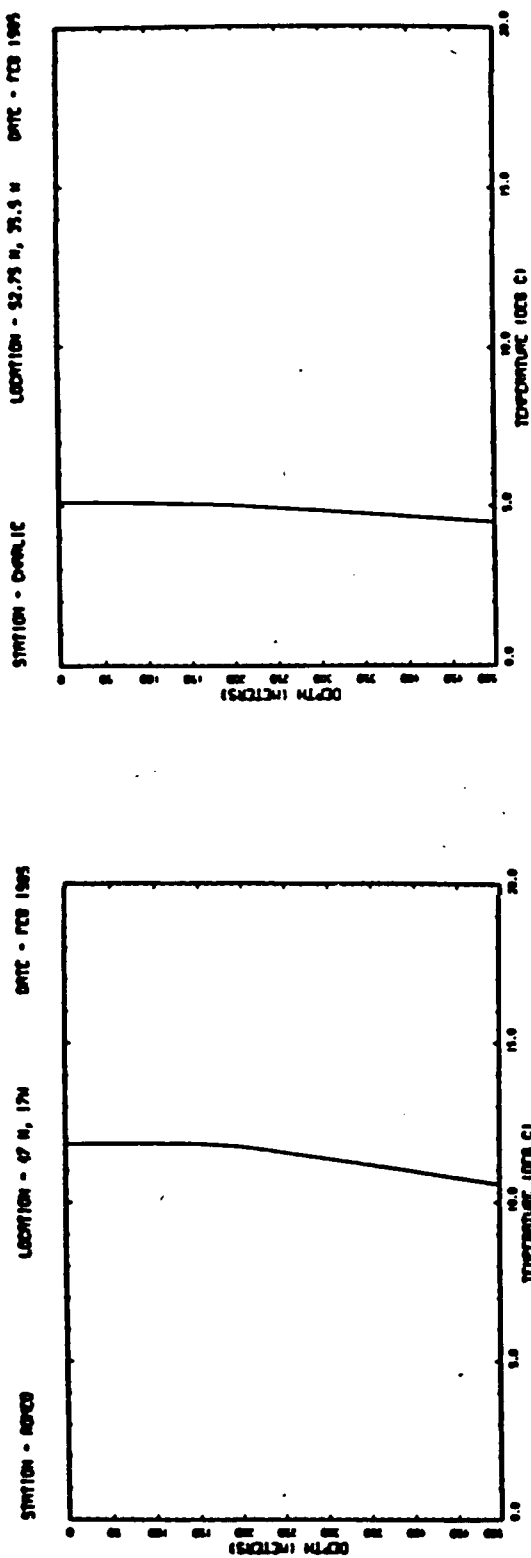


Figure 3.5 Monthly-averaged vertical temperature profiles at the 4 North Atlantic stations for the month of February.

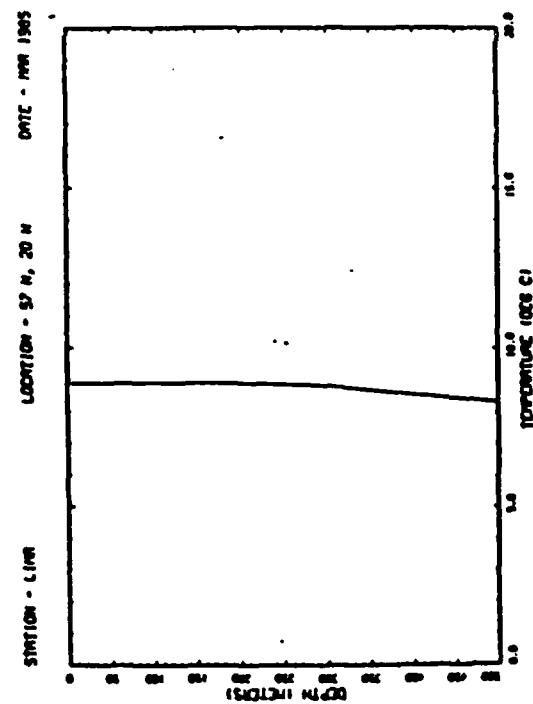
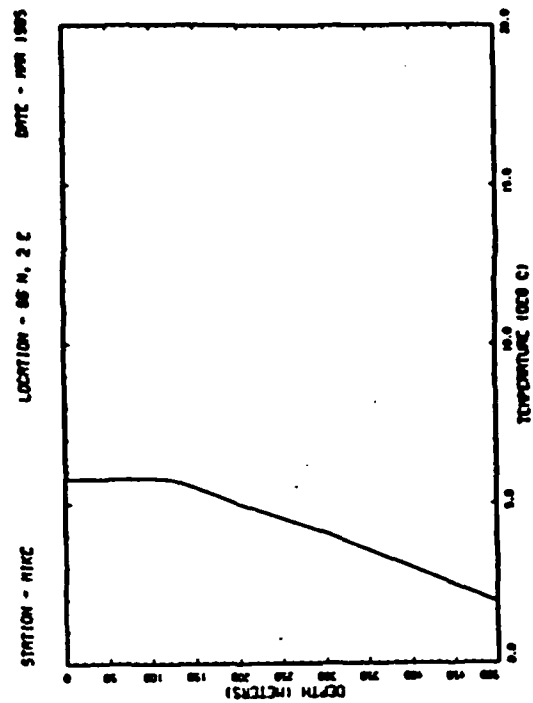
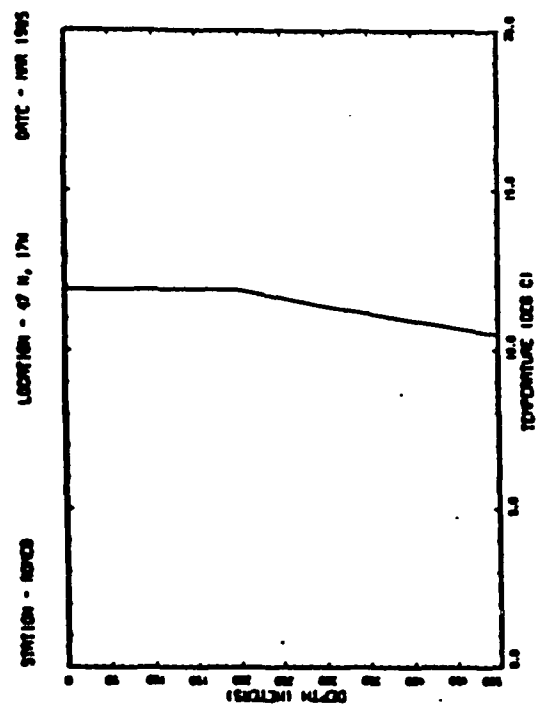
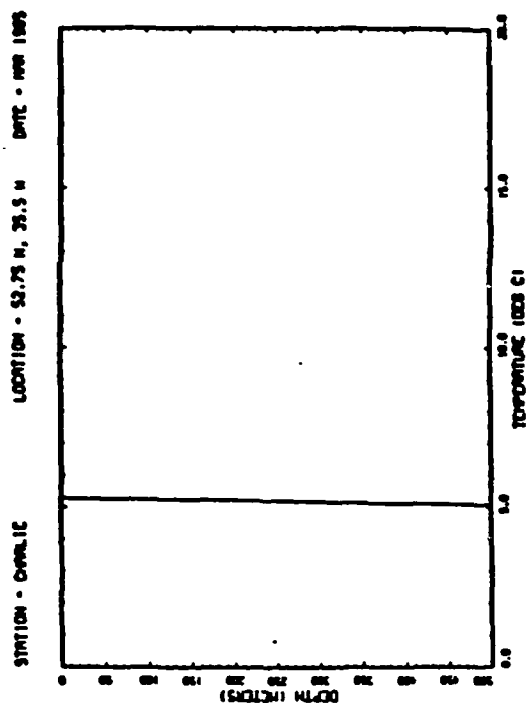


Figure 36 Monthly-averaged vertical temperature profiles at the 4 North Atlantic stations for the month of March.

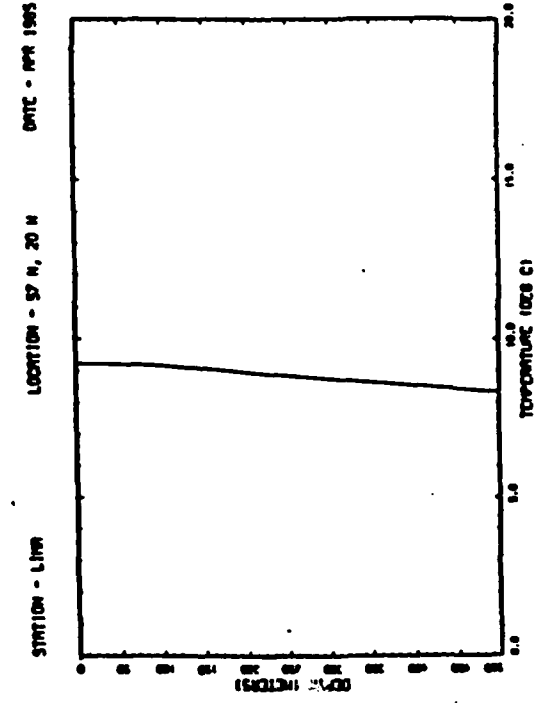
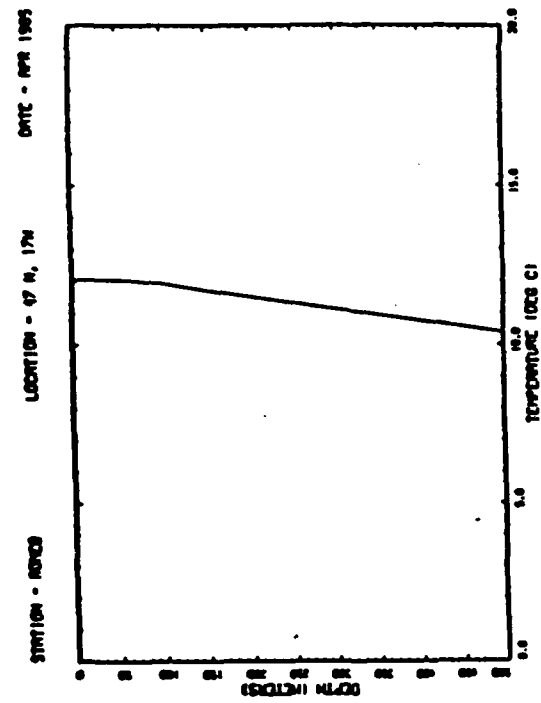
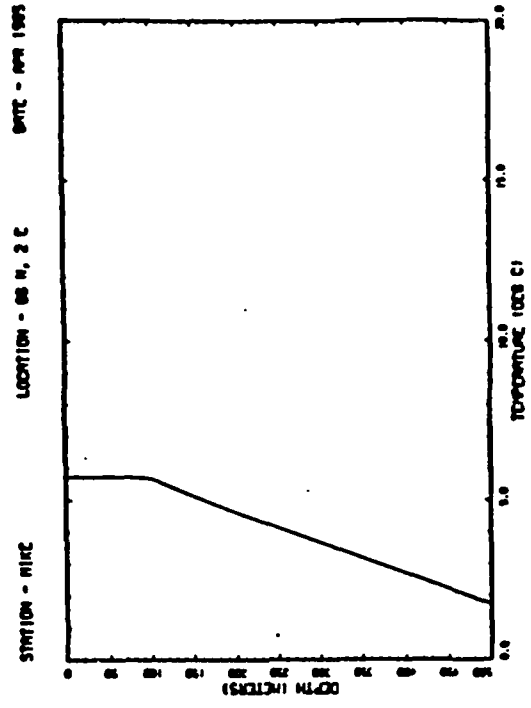
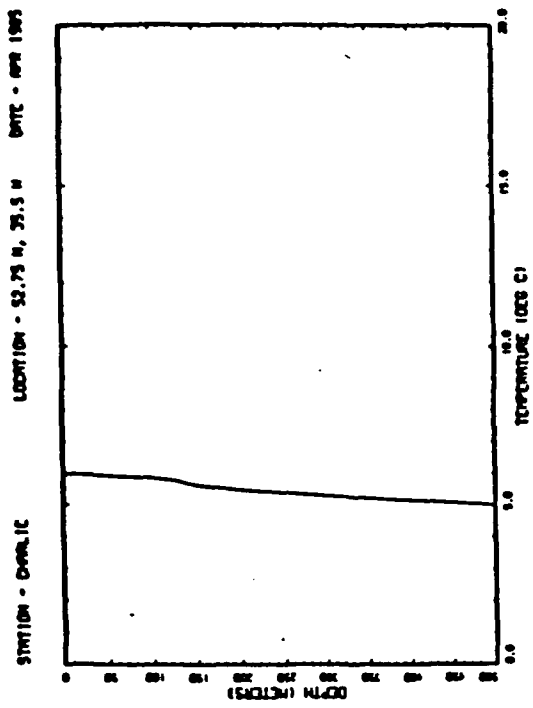


Figure 37 Monthly-averaged vertical temperature profiles at the 4 North Atlantic stations for the month of April.

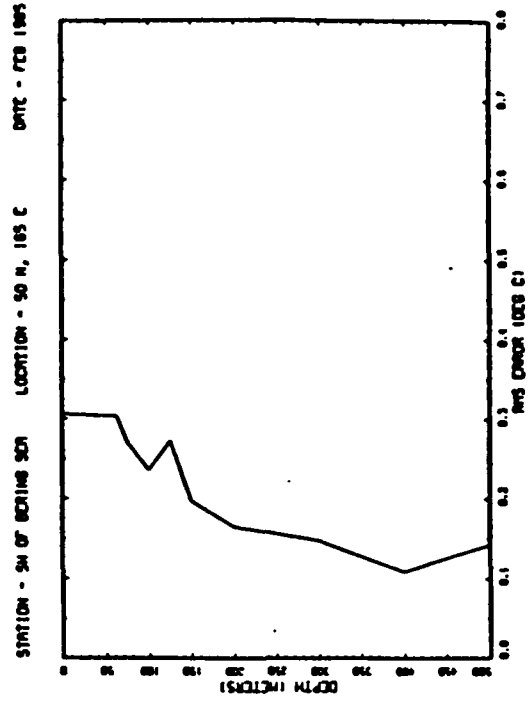
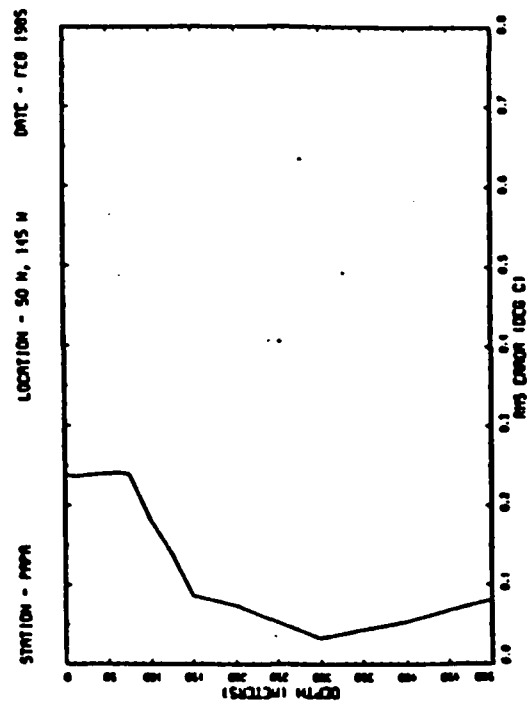
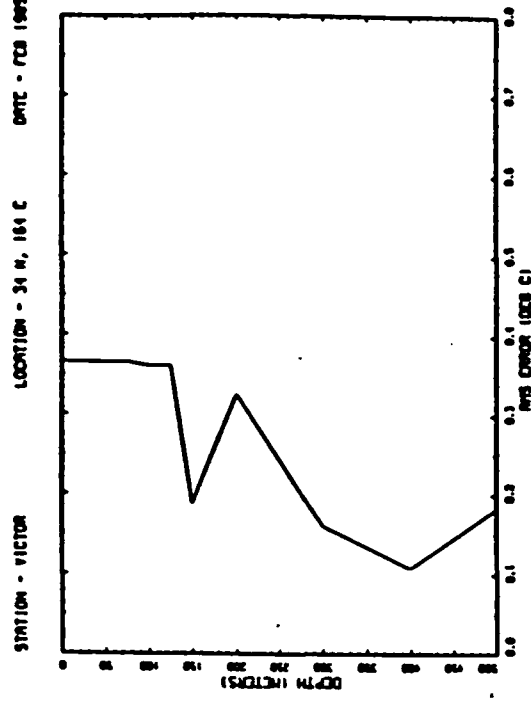
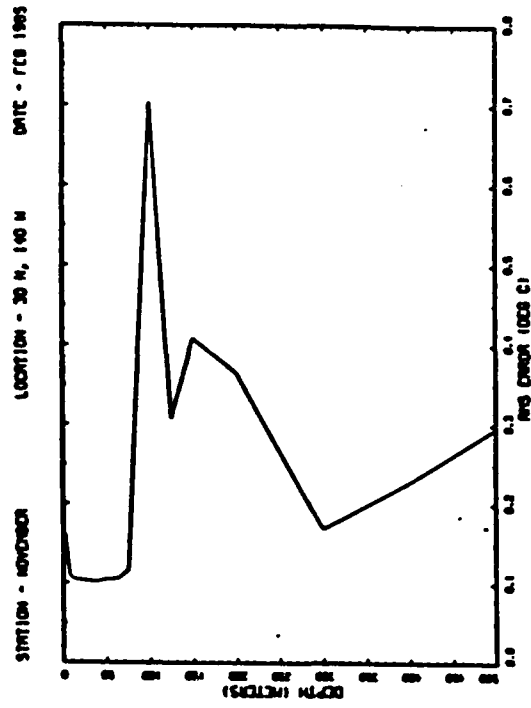


Figure 38 Monthly-averaged vertical profiles of the temperature variance at the 4 North Pacific stations for the month of February.

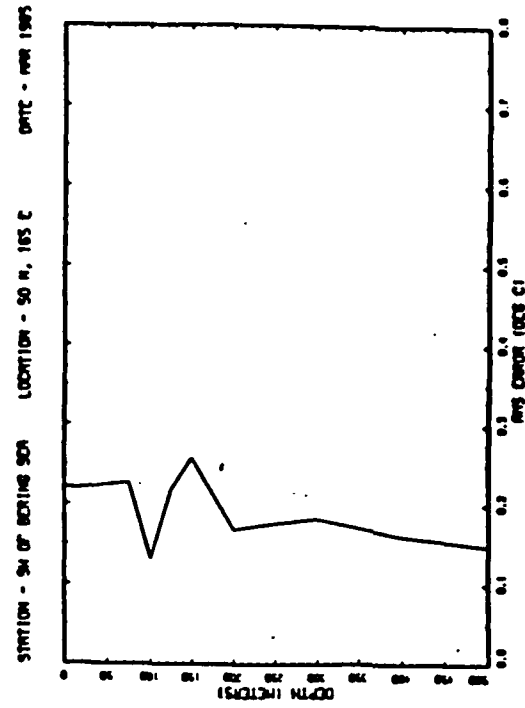
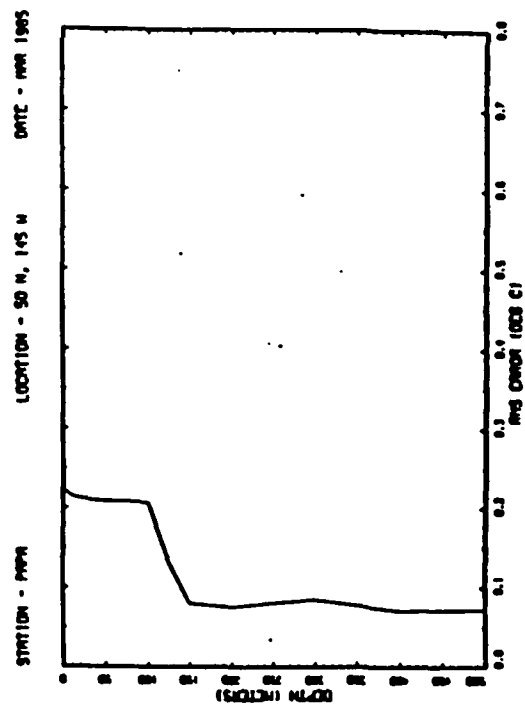
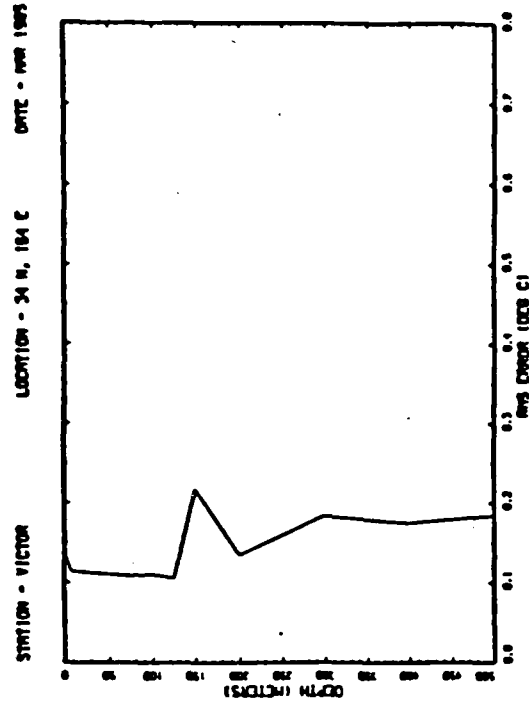
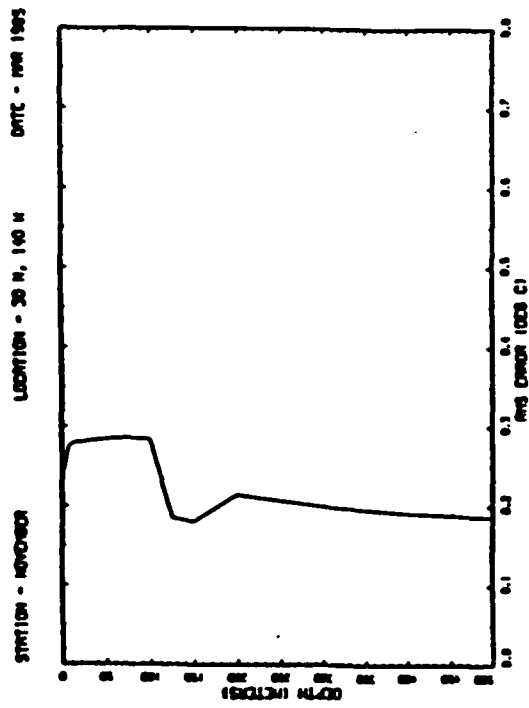


Figure 39 Monthly-averaged vertical profiles of the temperature variance at the 4 North Pacific stations for the month of March.

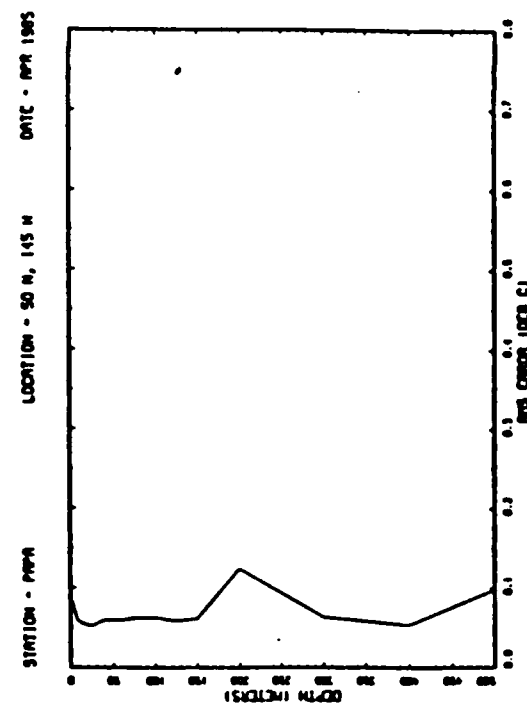
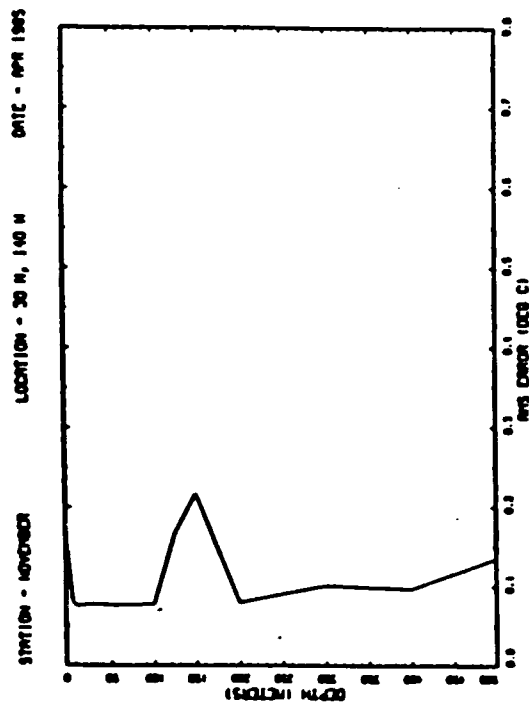
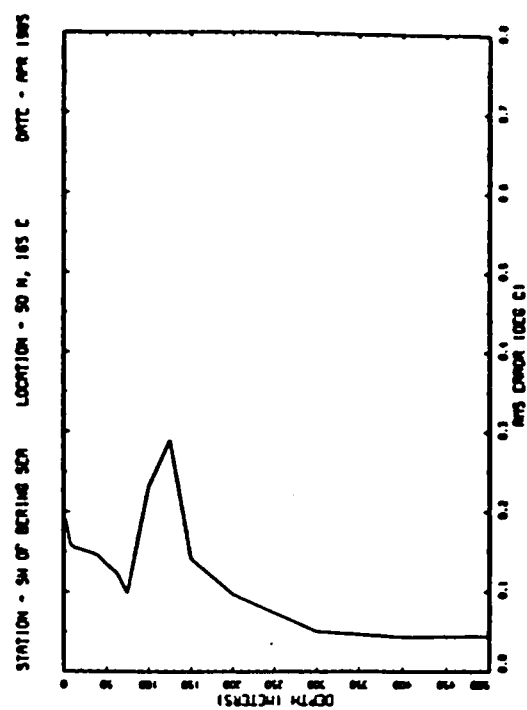
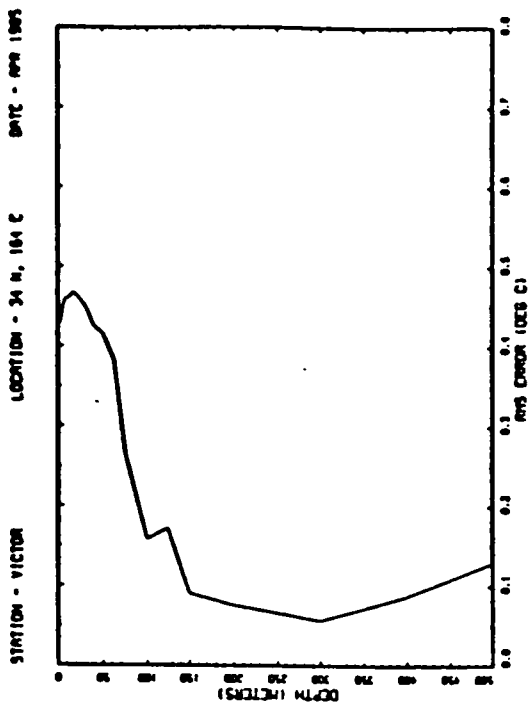


Figure 40 Monthly-averaged vertical profiles of the temperature variance at the 4 North Pacific stations for the month of April.

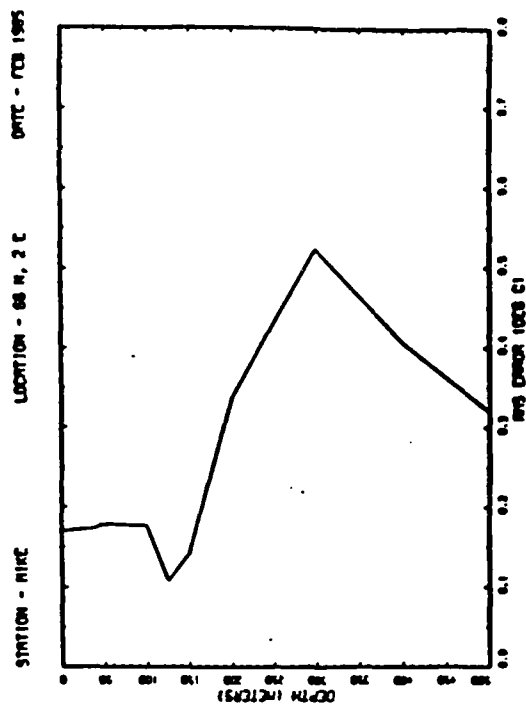
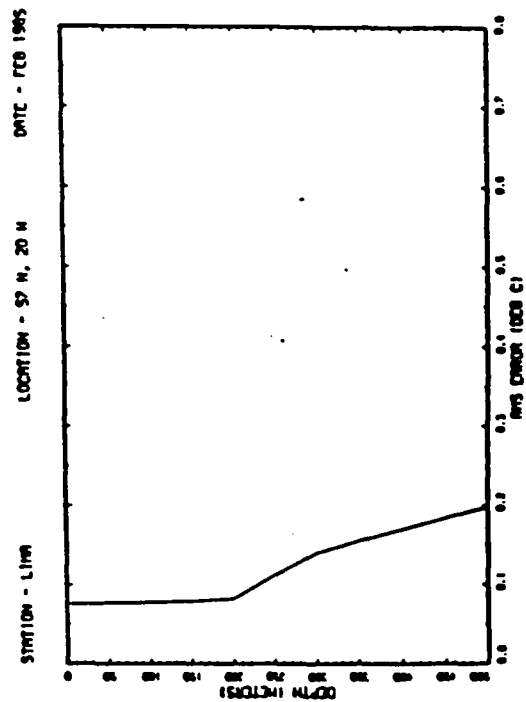
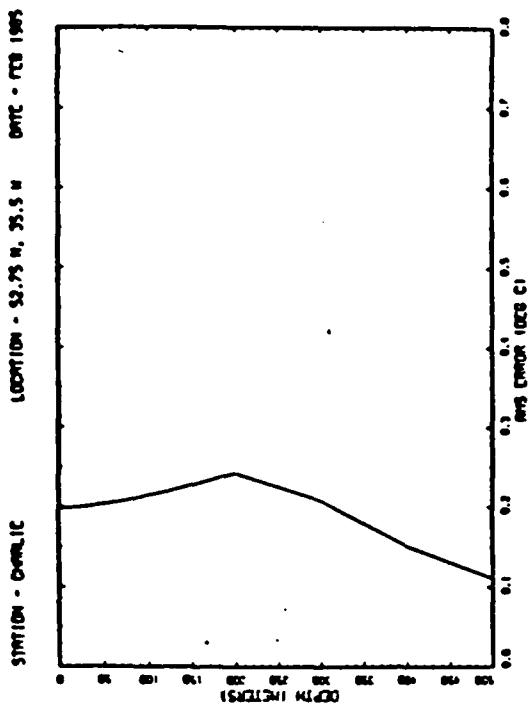
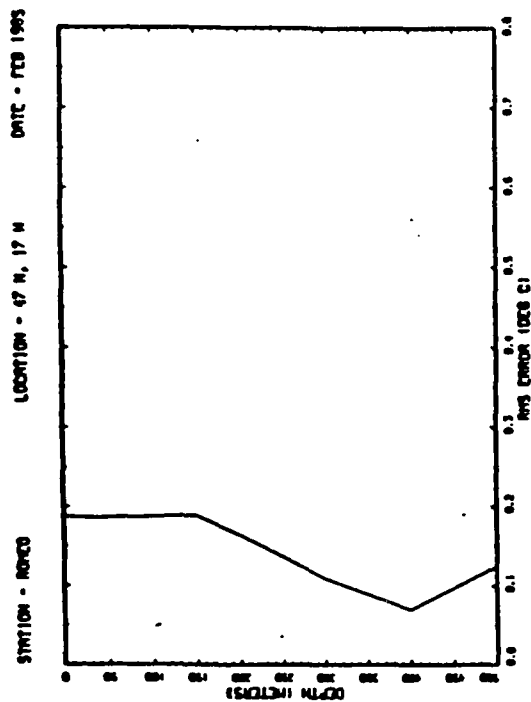


Figure 4 1 Monthly-averaged vertical profiles of the temperature variance at the 4 North Atlantic stations for the month of February.

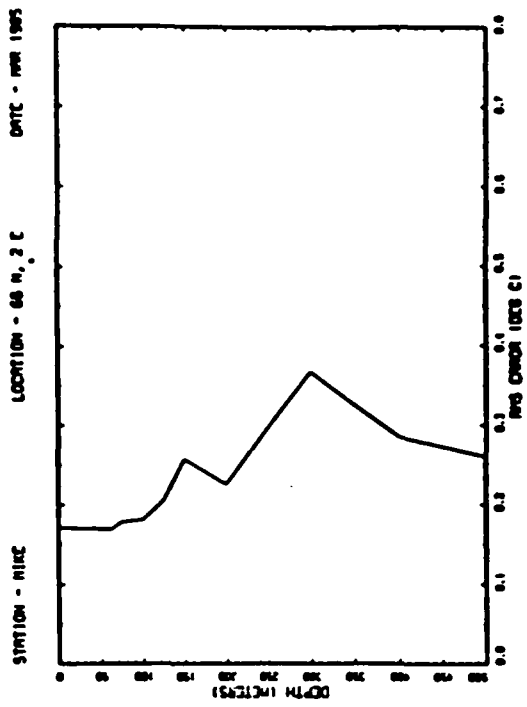
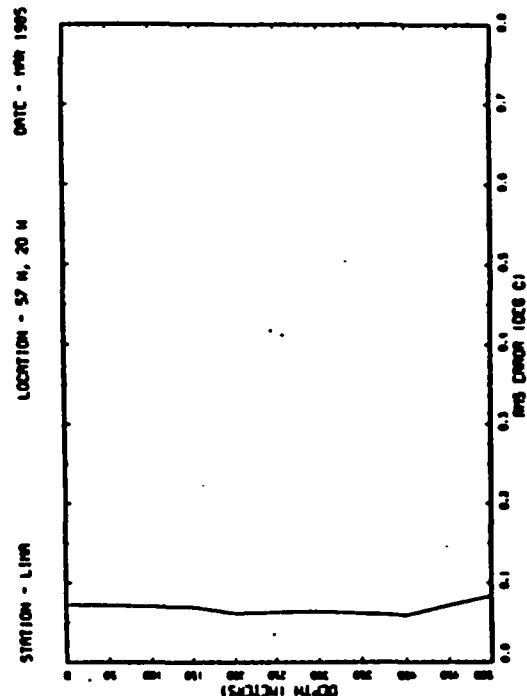
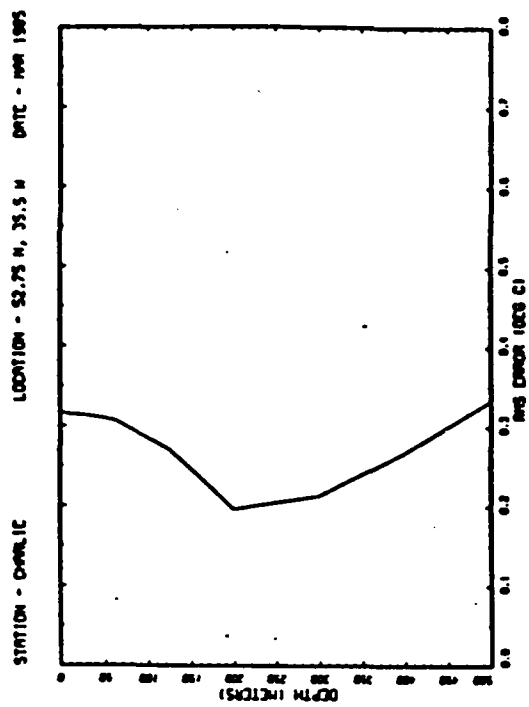
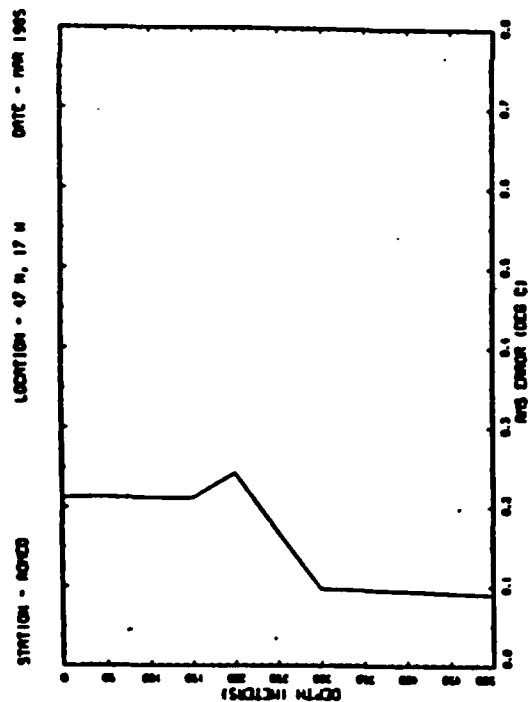


Figure 4.2 Monthly-averaged vertical profiles of the temperature variance at the 4 North Atlantic stations for the month of March.

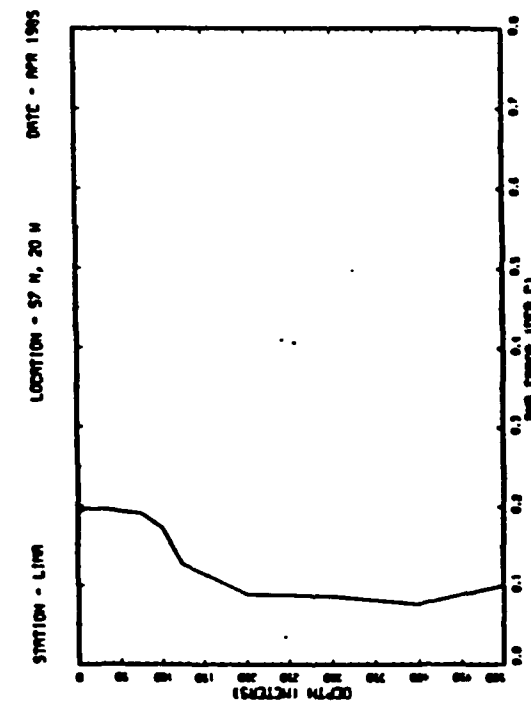
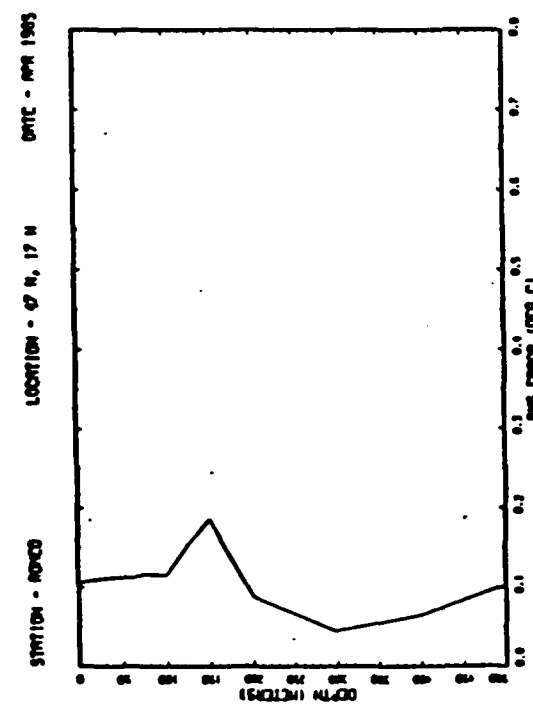
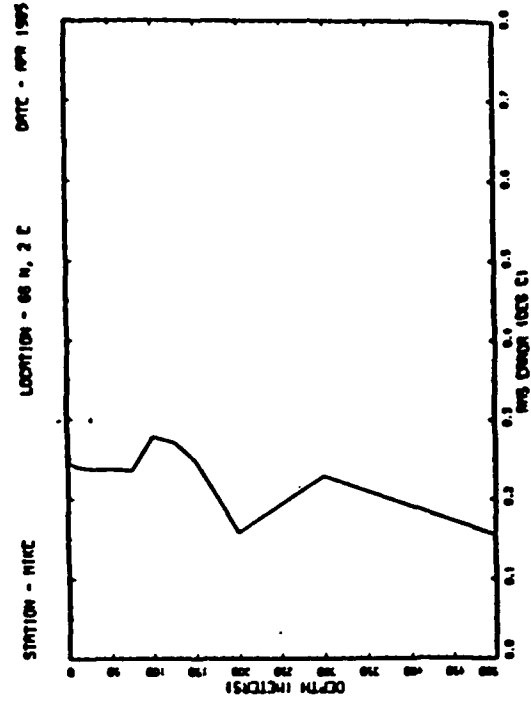
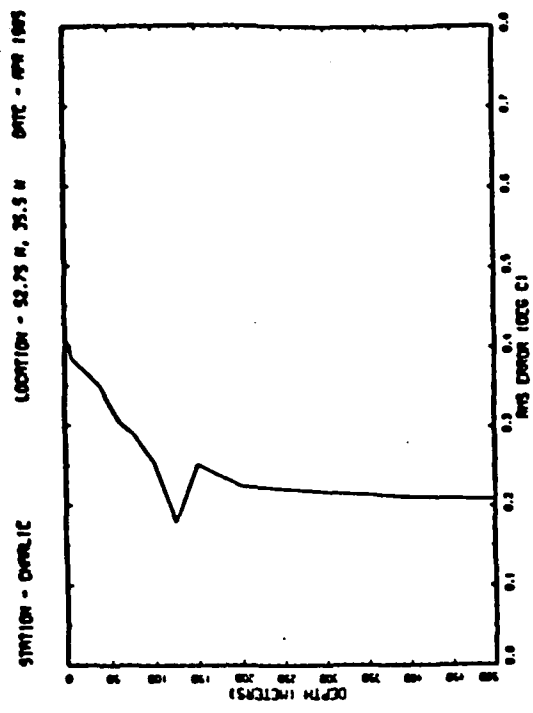


Figure 4.3 Monthly-averaged vertical profiles of the temperature variance at the 4 North Atlantic stations for the month of April.

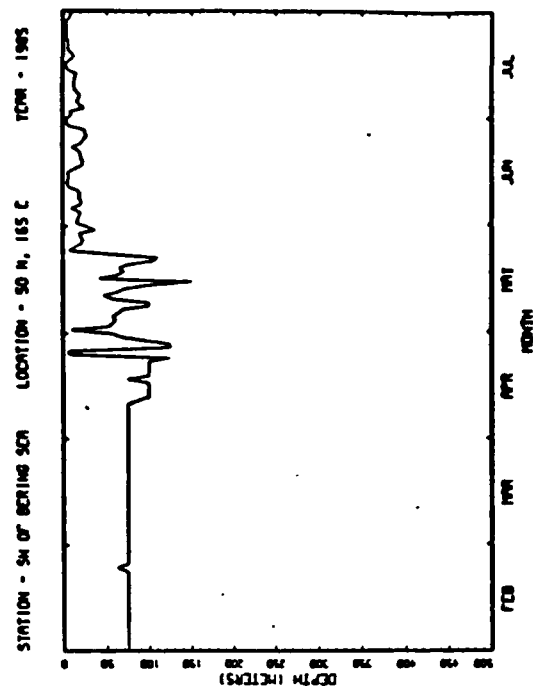
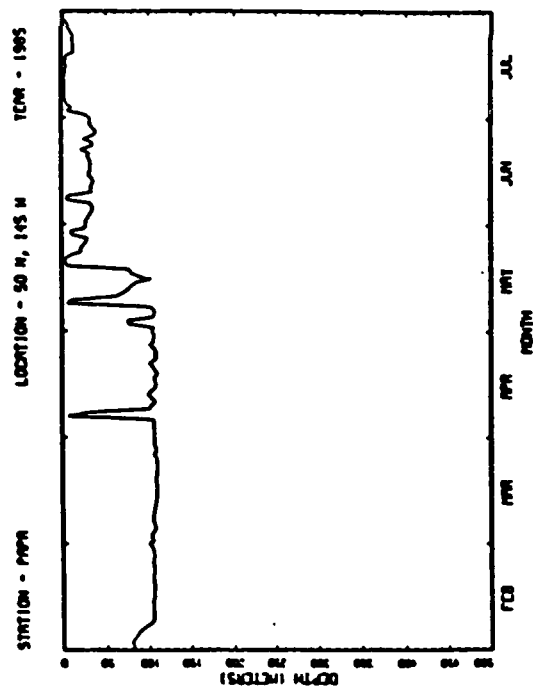
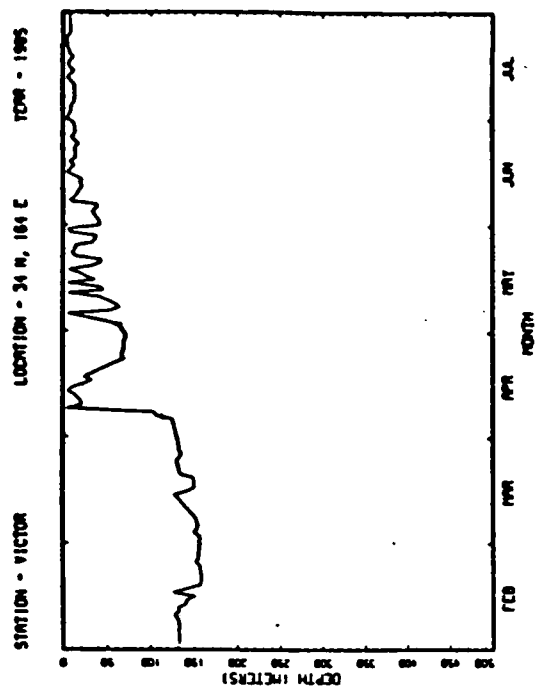
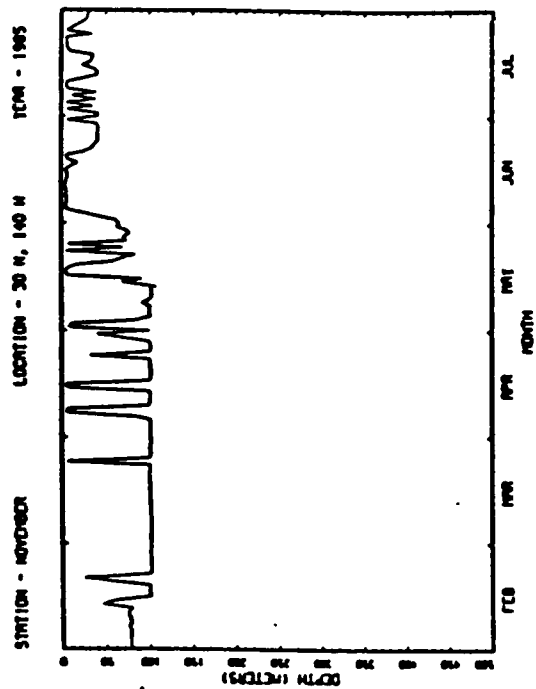


Figure 4.4 Time evolution of the mixed layer depth for the months of February through July at the 4 North Pacific stations according to a $\Delta T = .2^{\circ} \text{C}$ criterion.

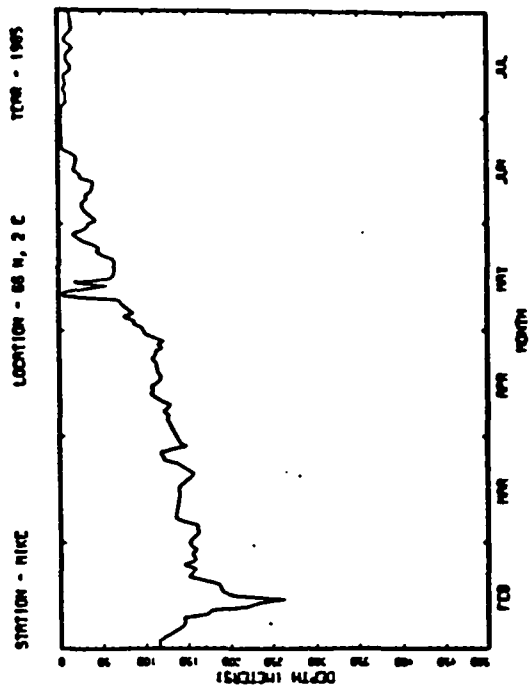
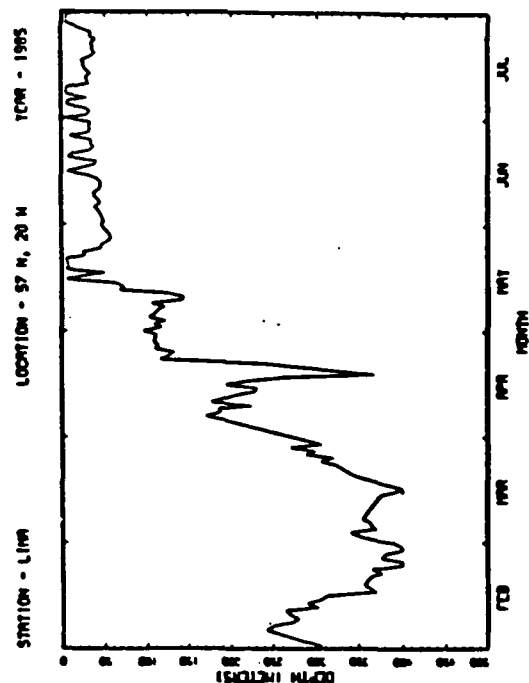
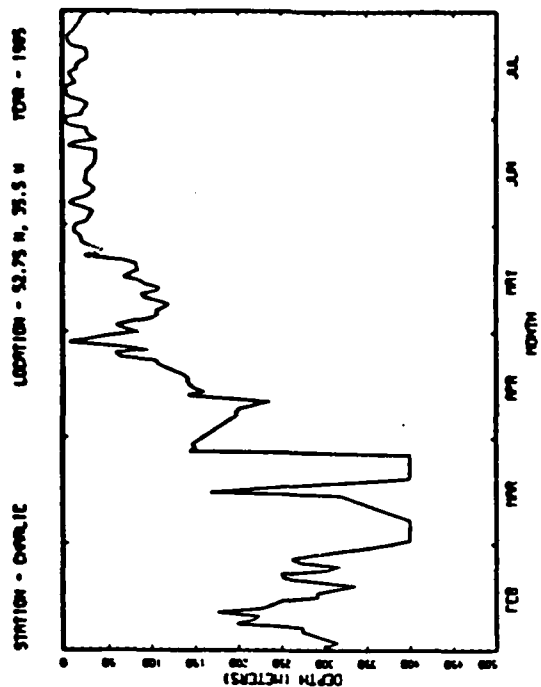
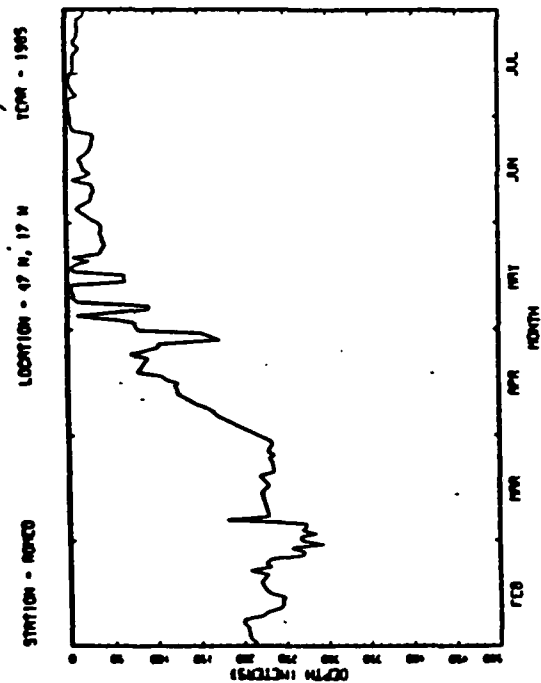


Figure 4.5 Time evolution of the mixed layer depth for the months of February through July at the 4 North Atlantic stations according to a $\Delta T = .2^{\circ} \text{C}$ criterion.

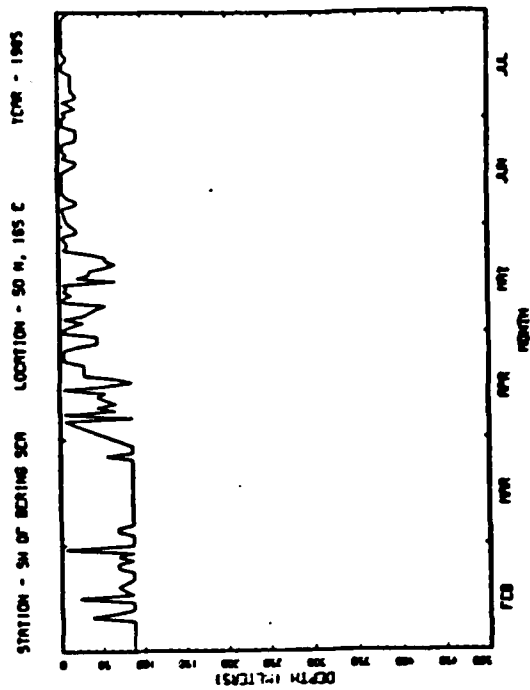
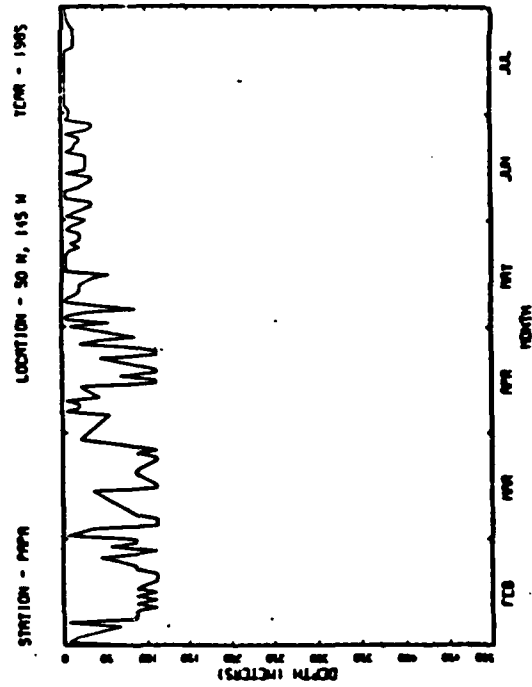
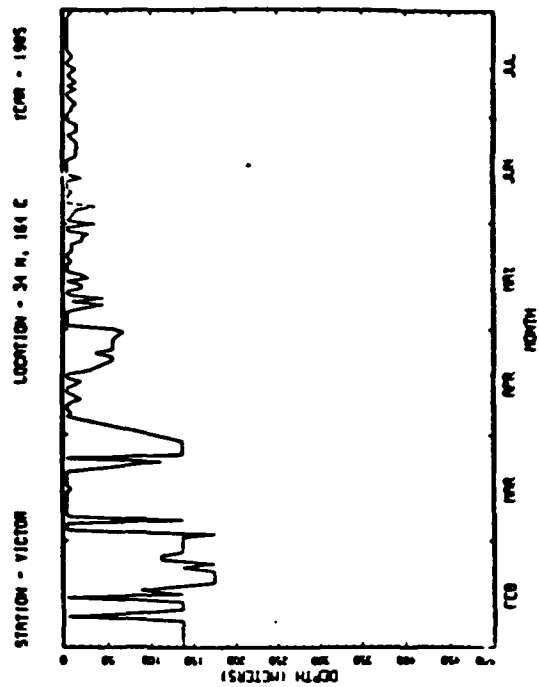
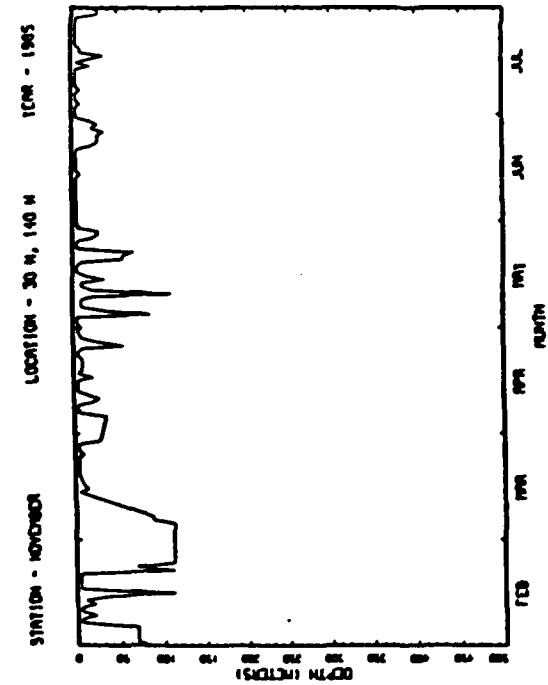


Figure 4.6 Time evolution of the mixed layer depth for the months of February through July at the 4 North Pacific stations according to a critical Richardson number $Ri = .23$ criterion.

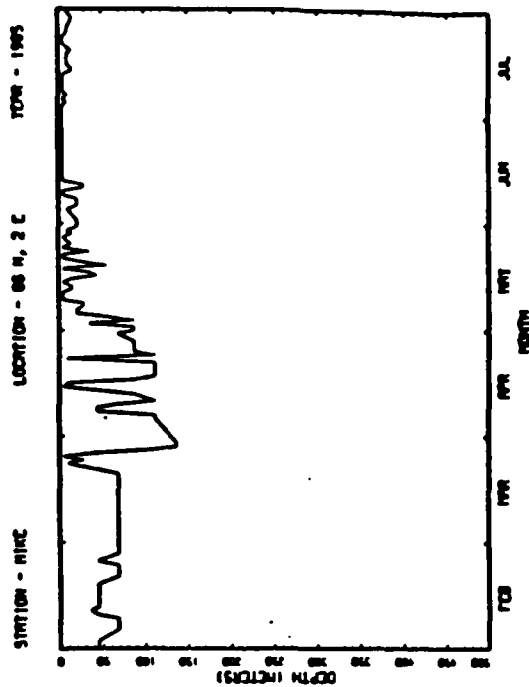
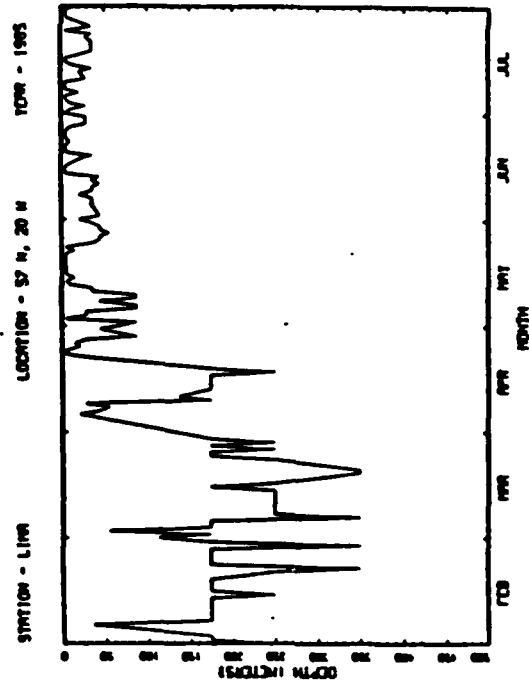
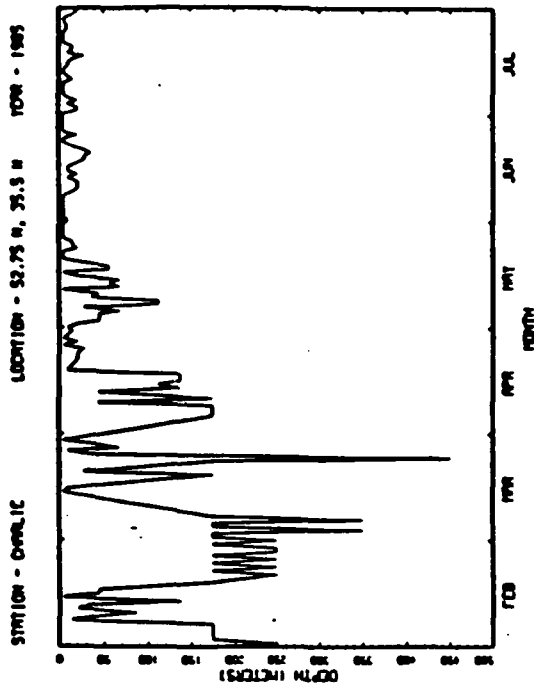
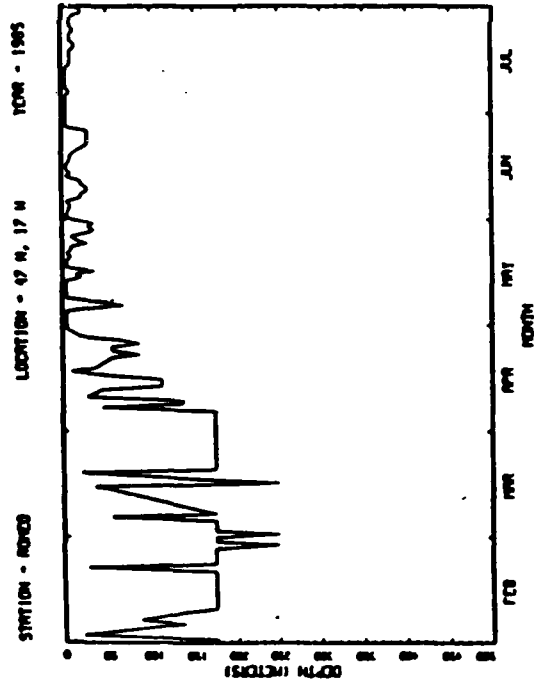


Figure 4 7 Time evolution of the mixed layer depth for the months of February through July at the 4 North Atlantic stations according to a critical Richardson number $Ri = .23$ criterion.

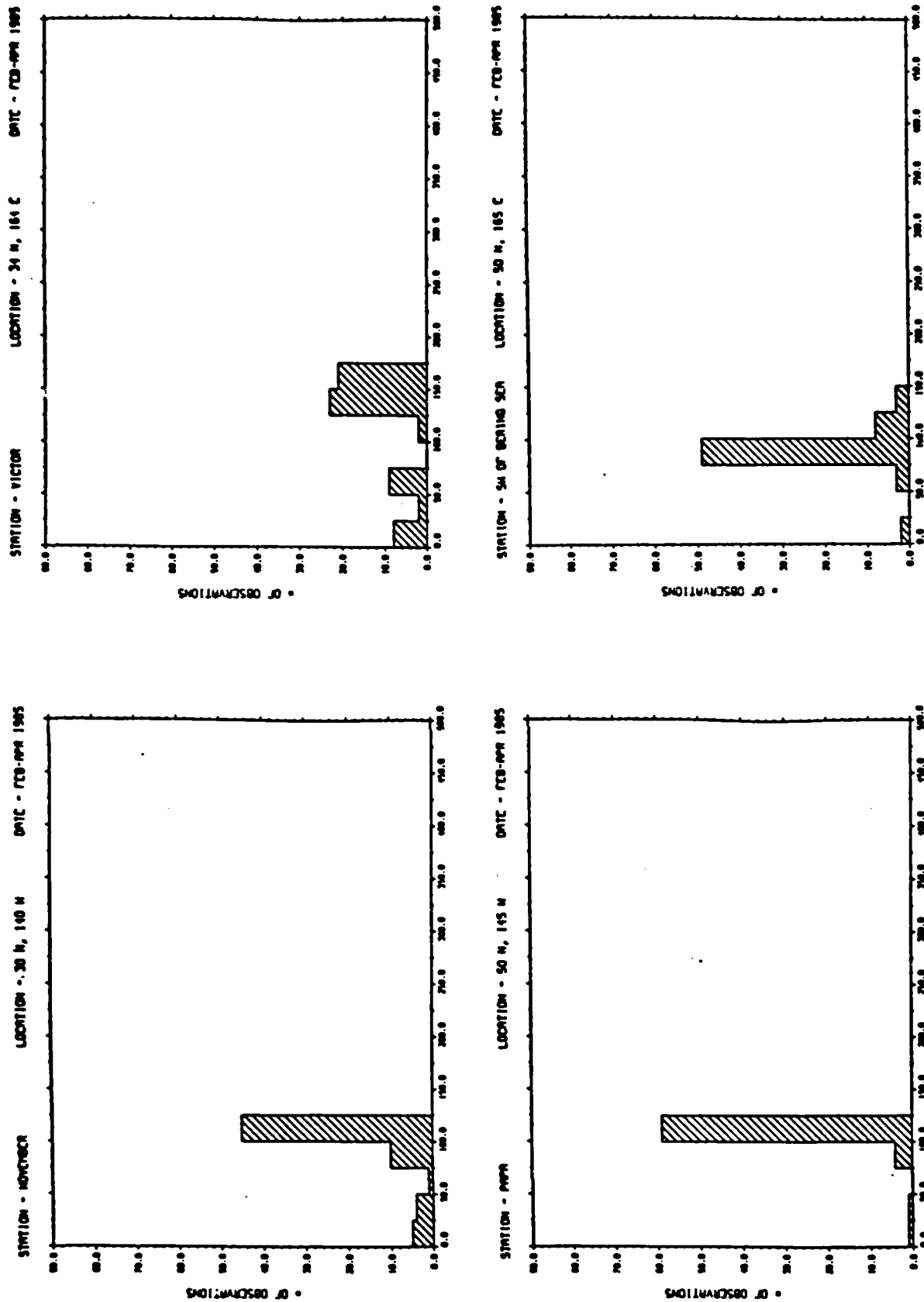


Figure 48 Distribution of the mixed layer depth for the months of February through April at the 4 North Pacific stations according to a $\Delta T = .2^{\circ} \text{C}$ criterion.

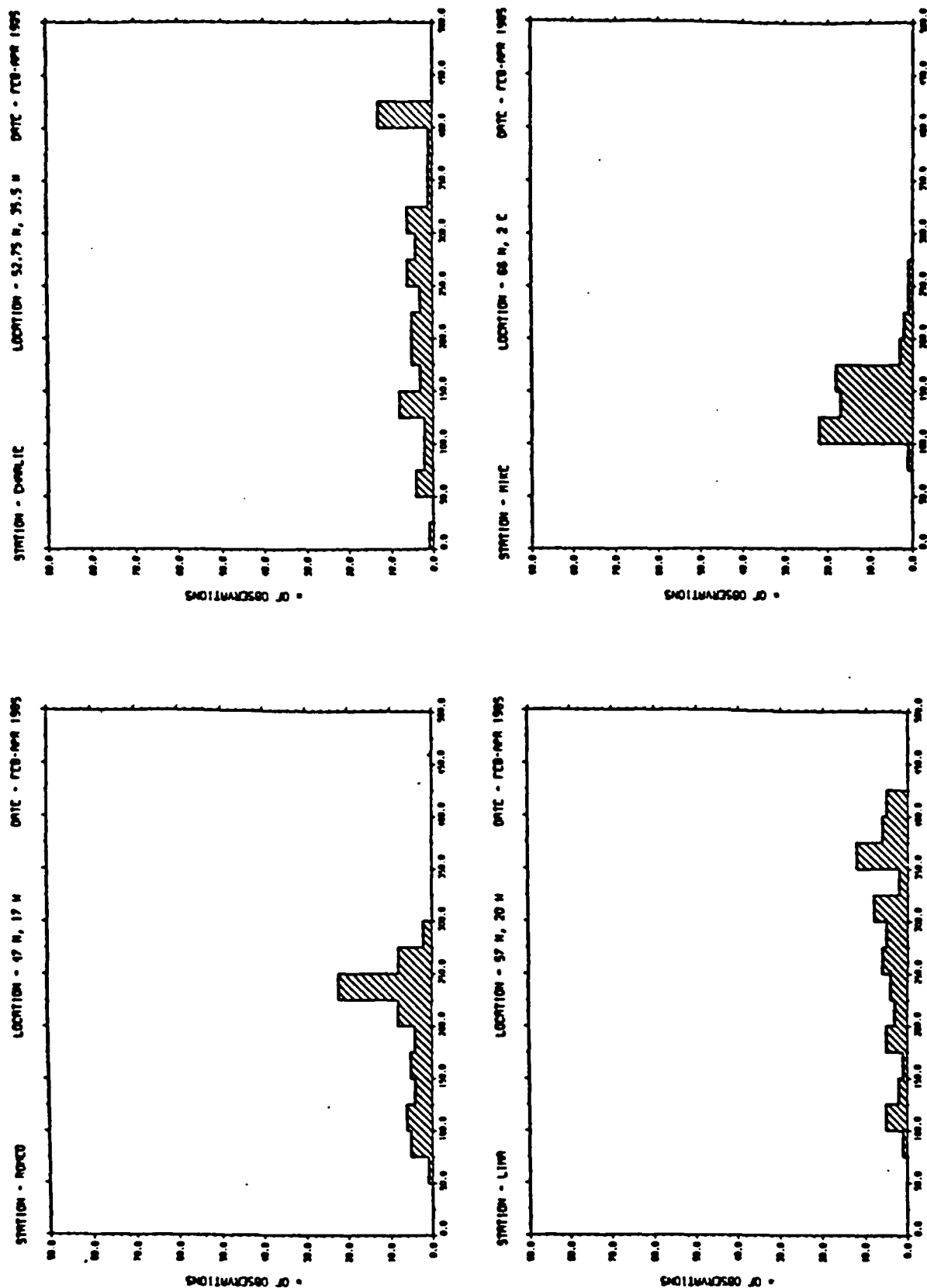


Figure 49 Distribution of the mixed layer depth for the months of February through April at the 4 North Atlantic stations according to a $\Delta T = .2^{\circ} \text{C}$ criterion.

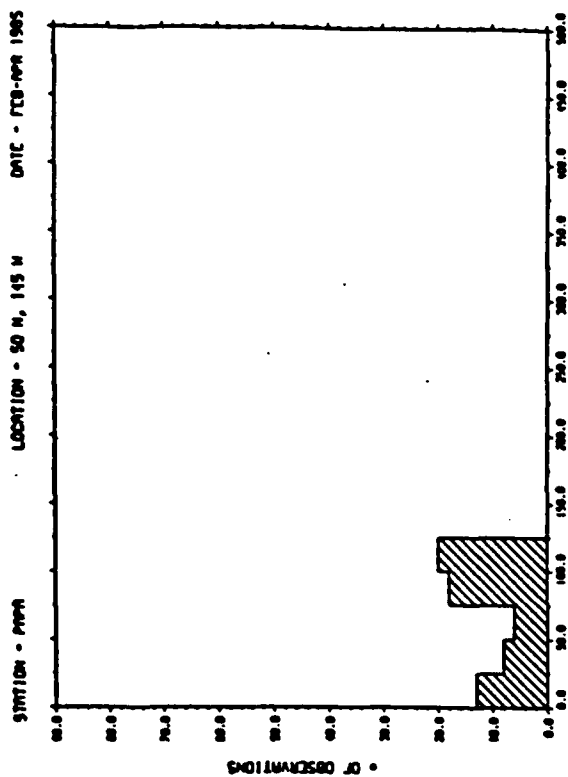
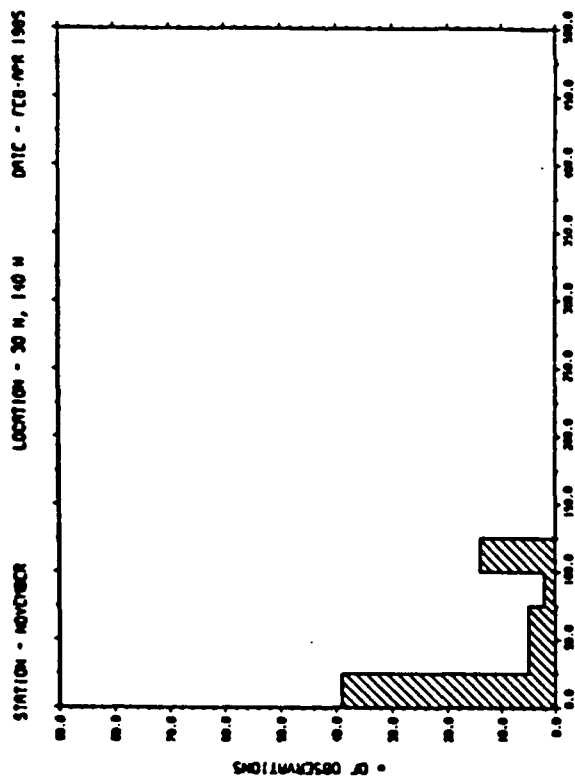
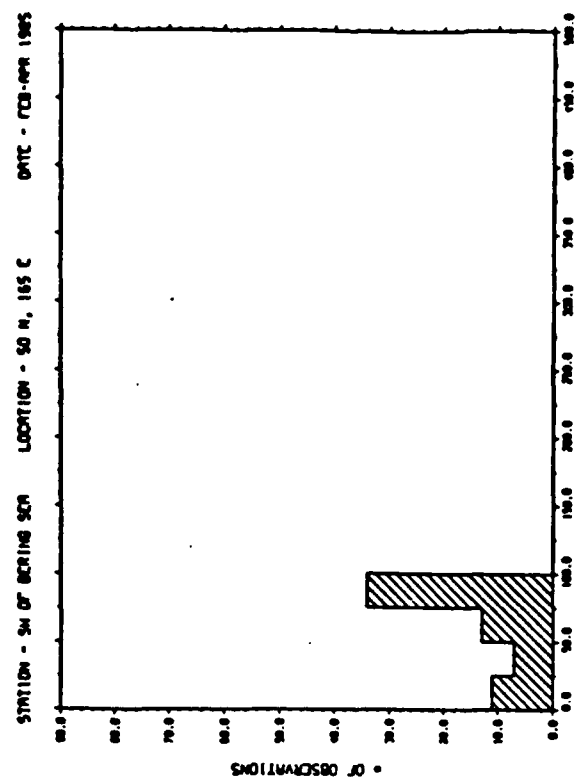
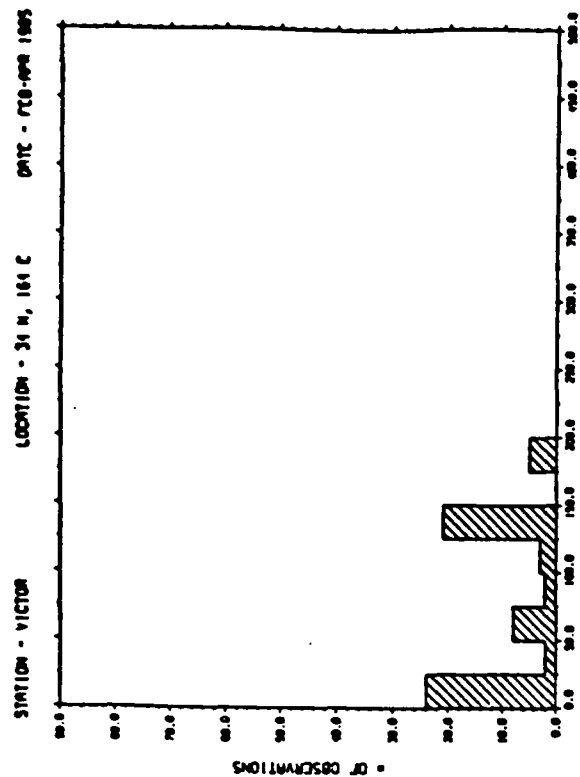


Figure 50 Distribution of the mixed layer depth for the months of February through April at the 4 North Pacific stations according to a critical Richardson number $Ri=0.23$ criterion.

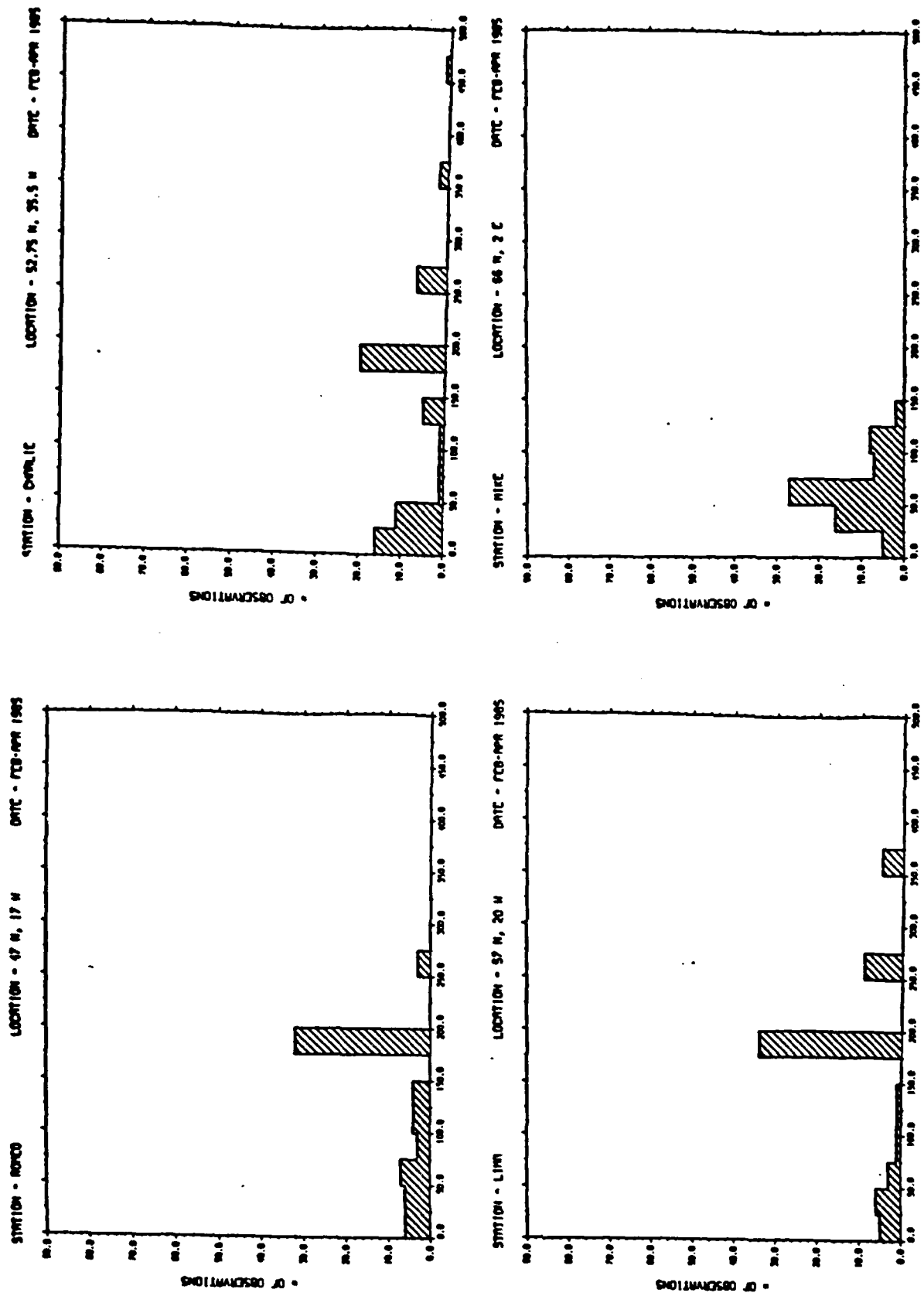


Figure 5.1 Distribution of the mixed layer depth for the months of February through April at the 4 North Atlantic stations according to a critical Richardson number $Ri = .23$ criterion.

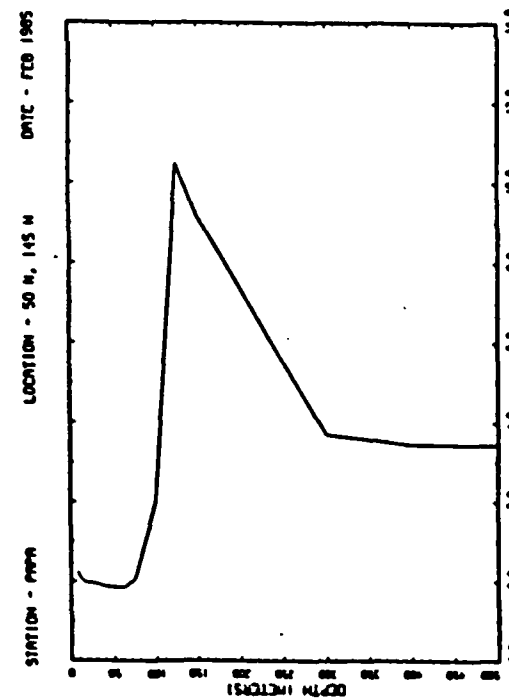
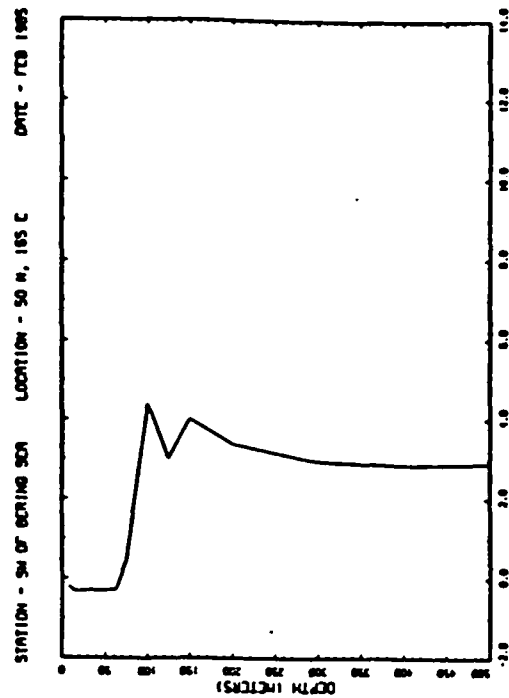
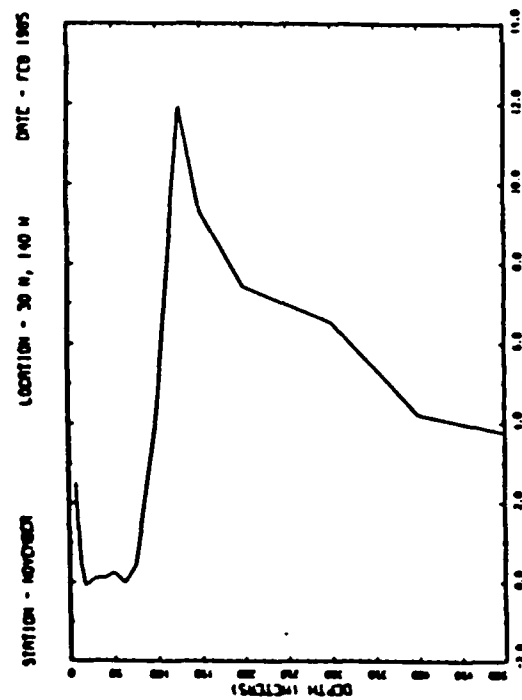
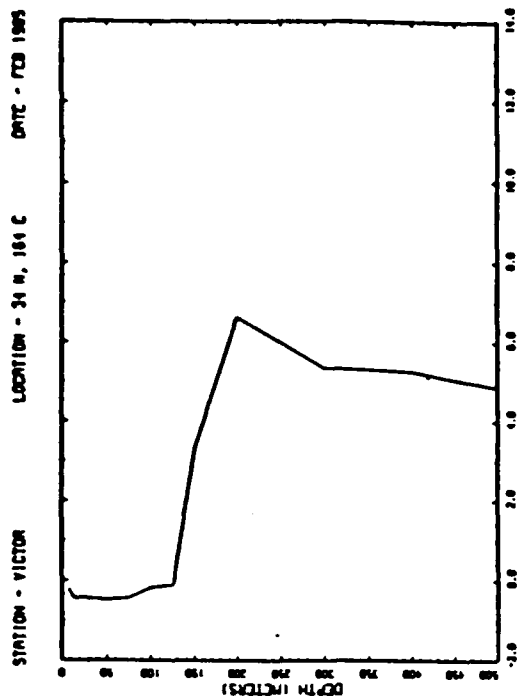


Figure 52 Monthly-averaged vertical profiles of the Brunt-Väisälä frequency ($\text{radians s}^{-1} \times 10^6$) at the 4 North Pacific stations for the month of February.

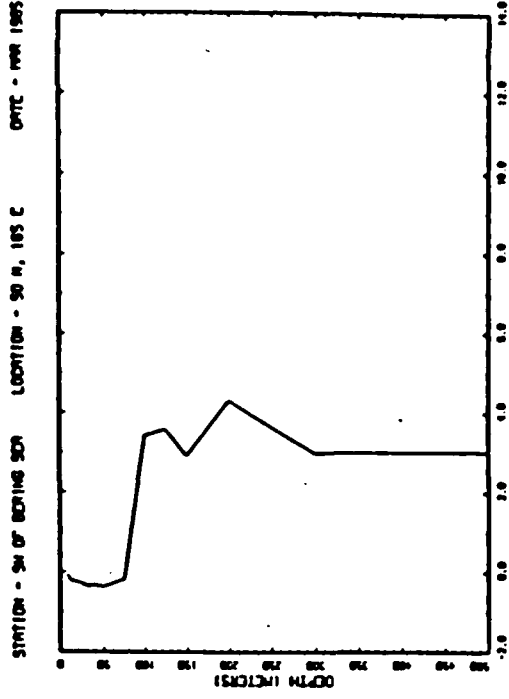
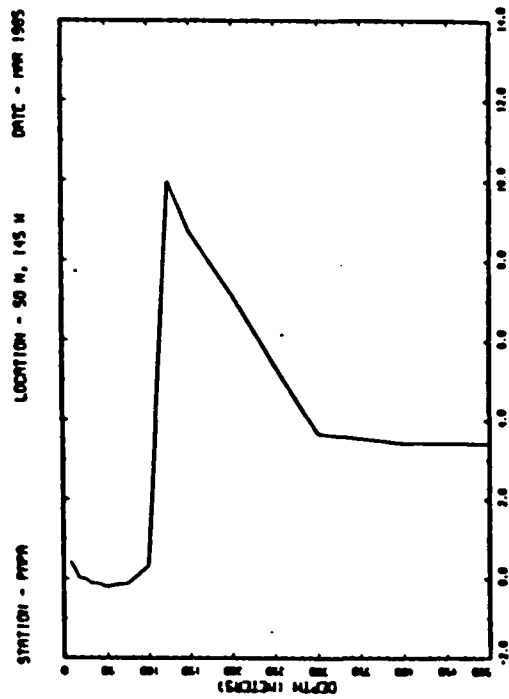
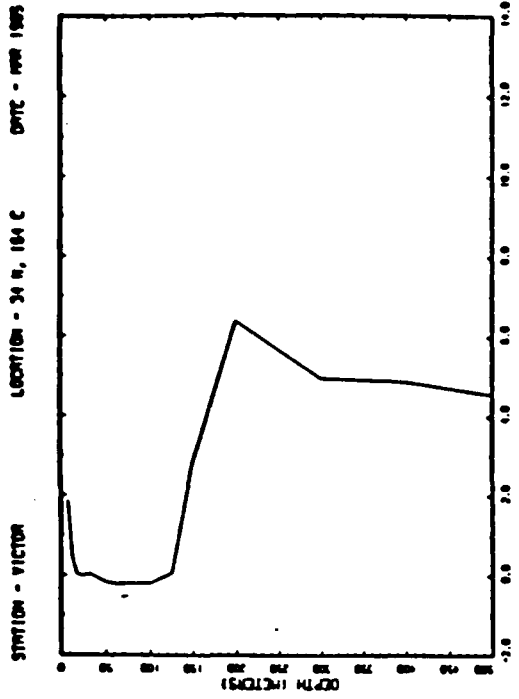
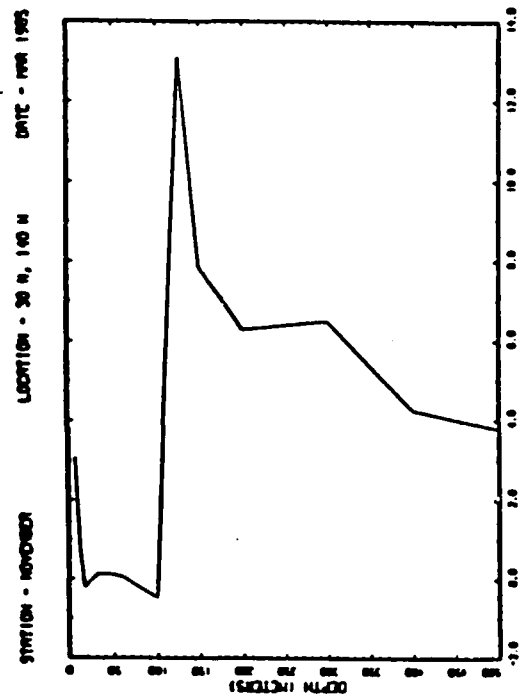


Figure 53 Monthly-averaged vertical profiles of the Brunt-Väisälä frequency (radians $s^{-1} \times 10^6$) at the 4 North Pacific stations for the month of March.

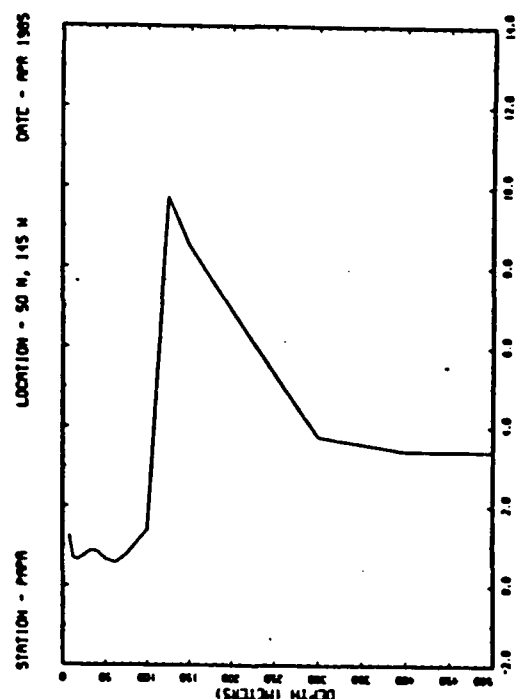
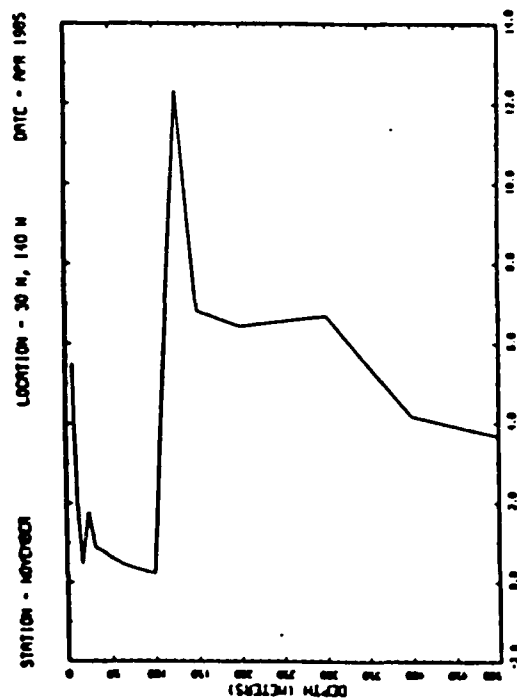
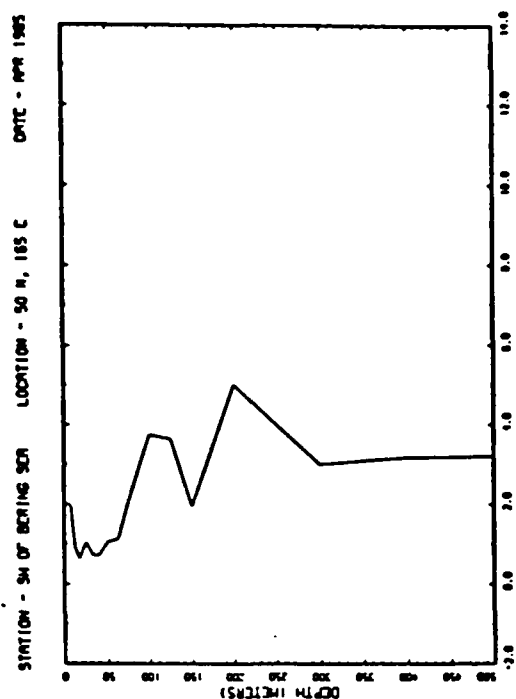
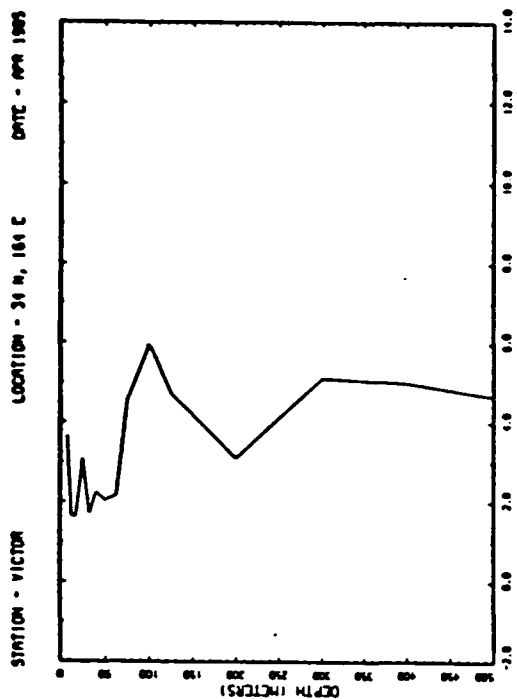


Figure 54 Monthly-averaged vertical profiles of the Brunt-Väisälä frequency ($\text{radians s}^{-1} \times 10^6$) at the 4 North Pacific stations for the month of April.

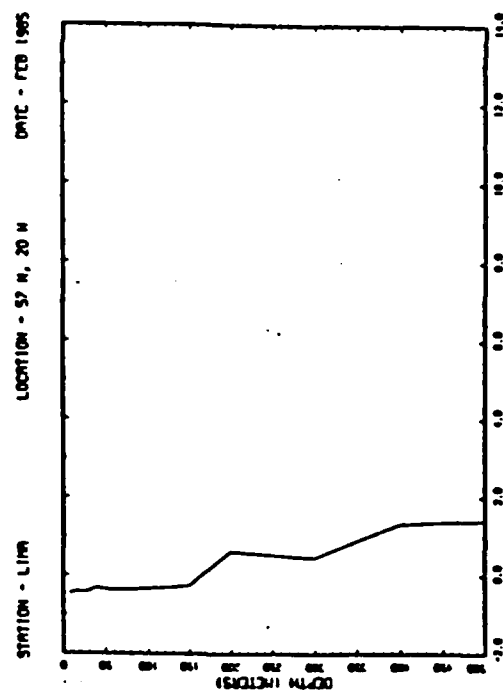
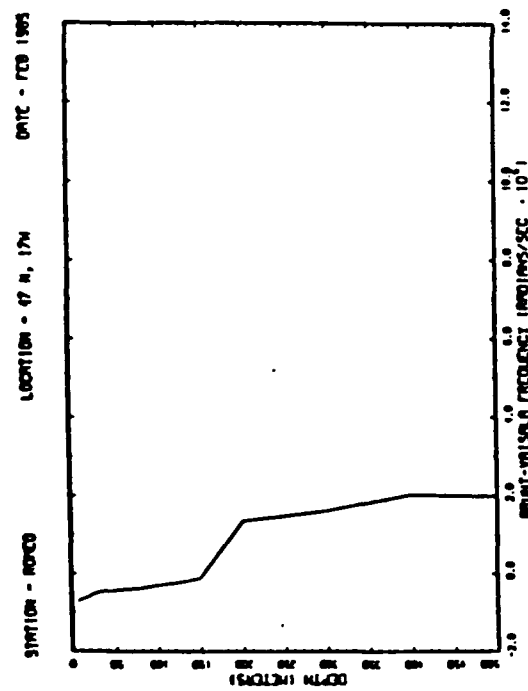
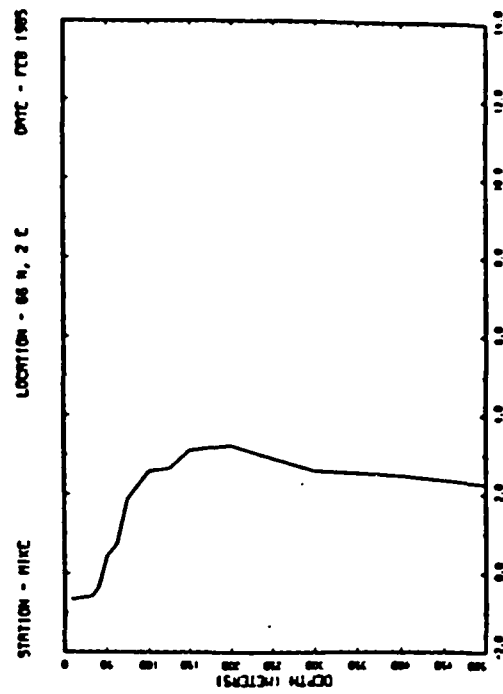
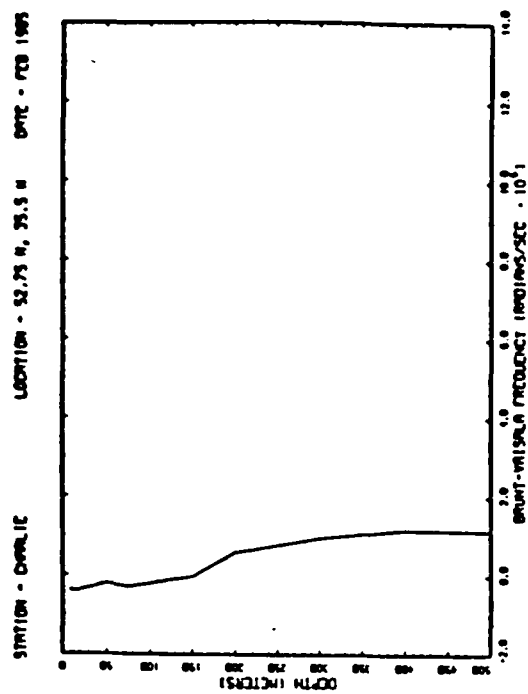
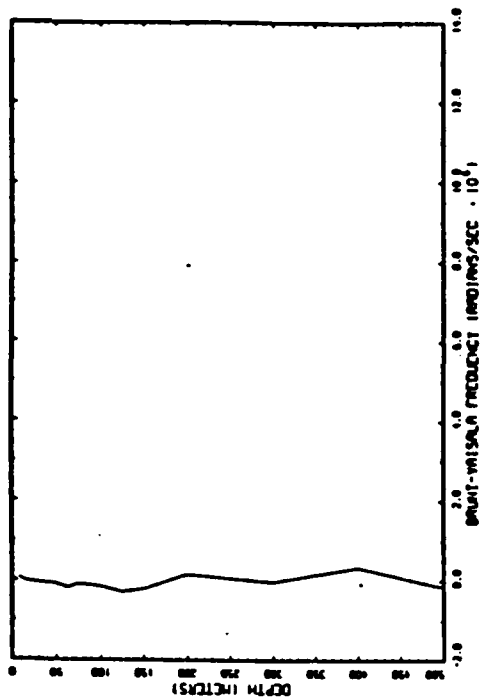
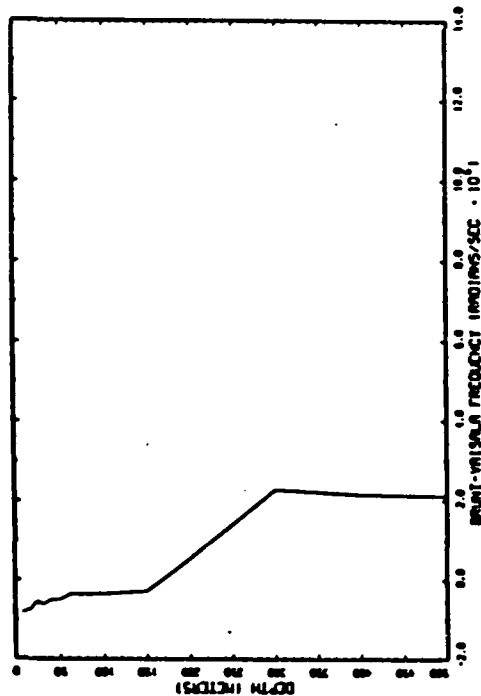


Figure 55 Monthly-averaged vertical profiles of the Brunt-Väisälä frequency ($\text{radians s}^{-1} \times 10^6$) at the 4 North Atlantic stations for the month of February.

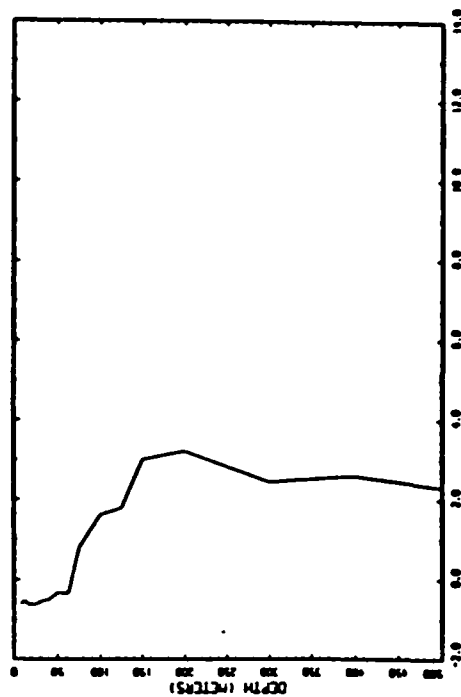
STATION - OVALLE LOCATION - 52.75 N, 25.5 W DATE - MAR 1965



STATION - ROKO LOCATION - 47 N, 17 W DATE - MAR 1965



STATION - RICE LOCATION - 66 N, 2 E DATE - MAR 1965



STATION - LINA LOCATION - 57 N, 20 W DATE - MAR 1965

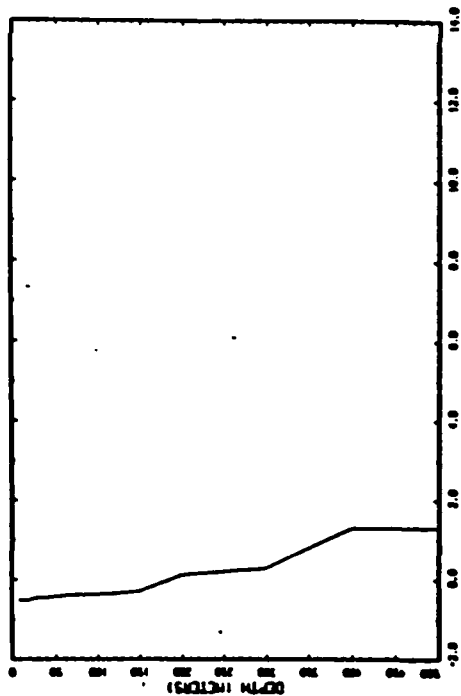


Figure 56 Monthly-averaged vertical profiles of the Brunt-Väisälä frequency (rad/s $\times 10^3$) at the 4 North Atlantic stations for the month of March.

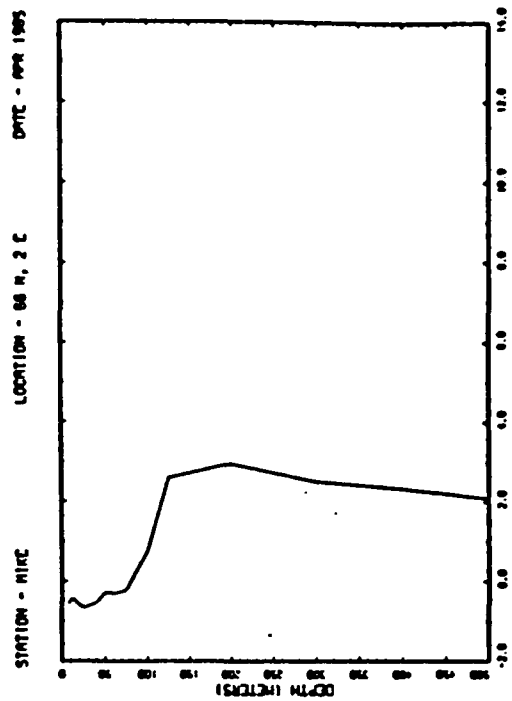
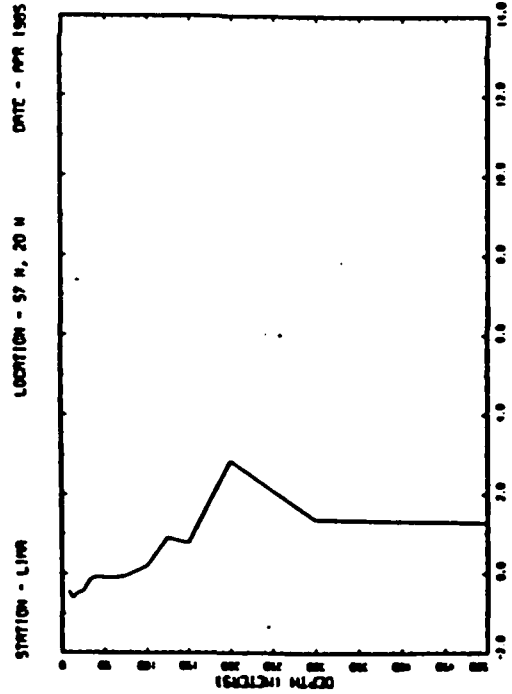
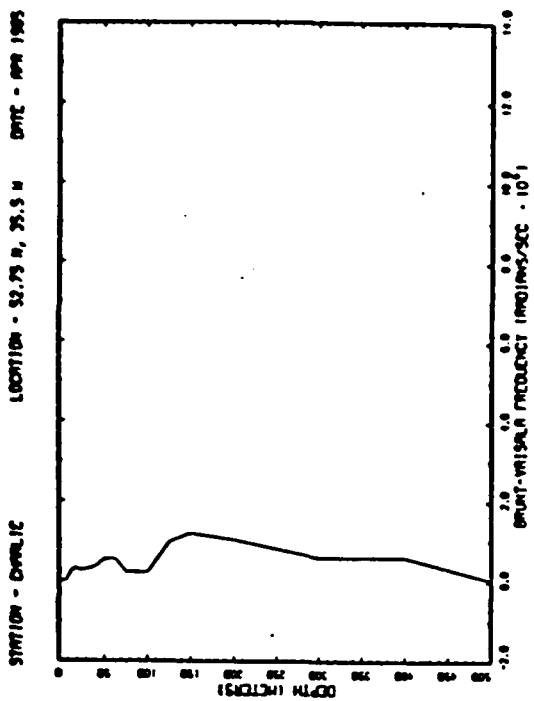
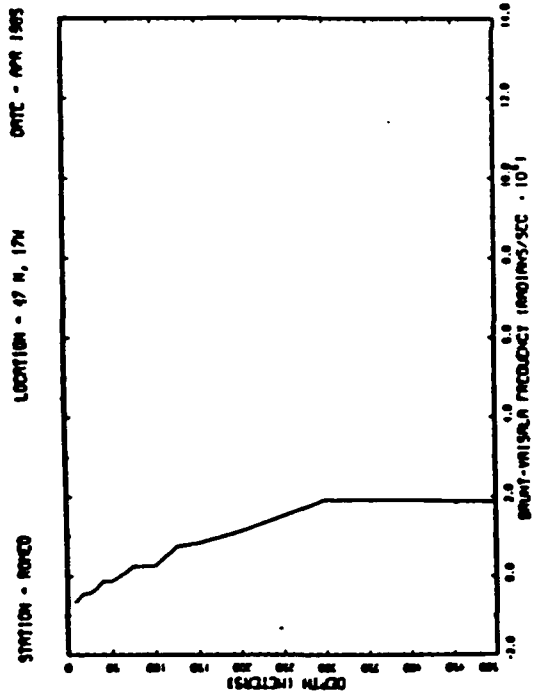


Figure 57 Monthly-averaged vertical profiles of the Brunt-Väisälä frequency (radians $s^{-1} \times 10^3$) at the 4 North Atlantic stations for the month of April.

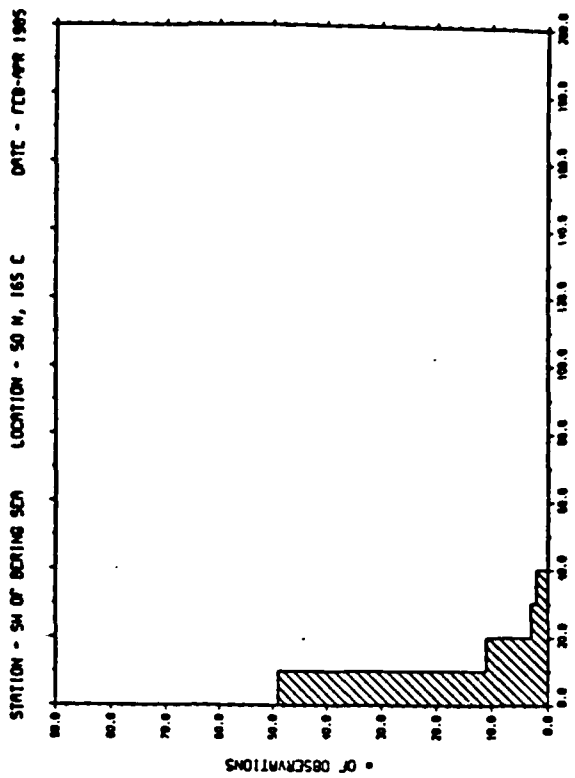
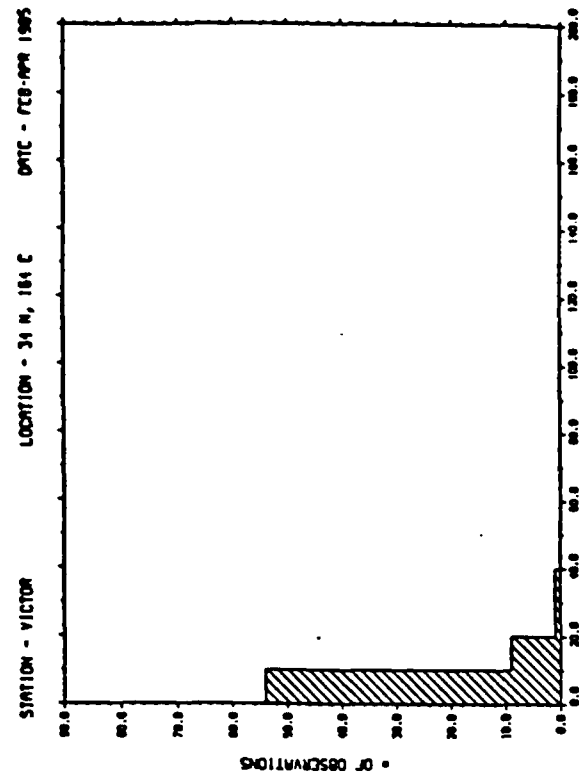
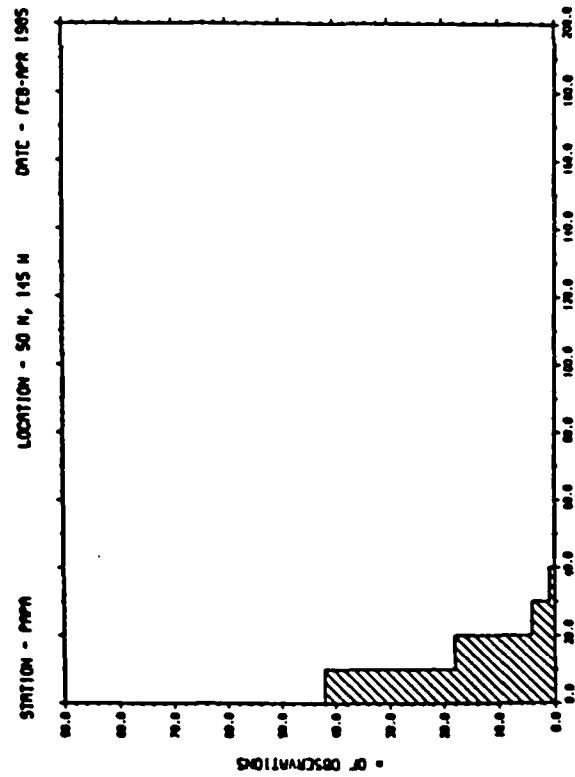
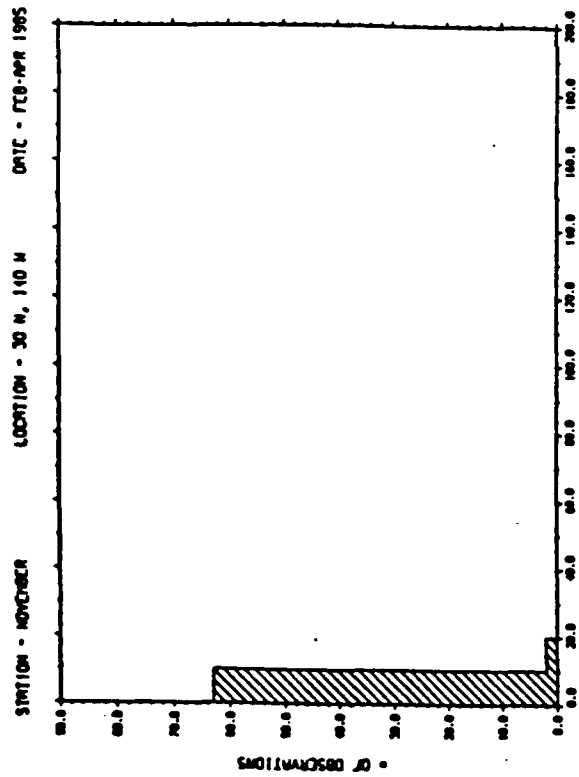


Figure 58 Distribution of the 50 m shear ($s^{-1} \times 10^4$) for the months of February through April at the 4 North Pacific stations.

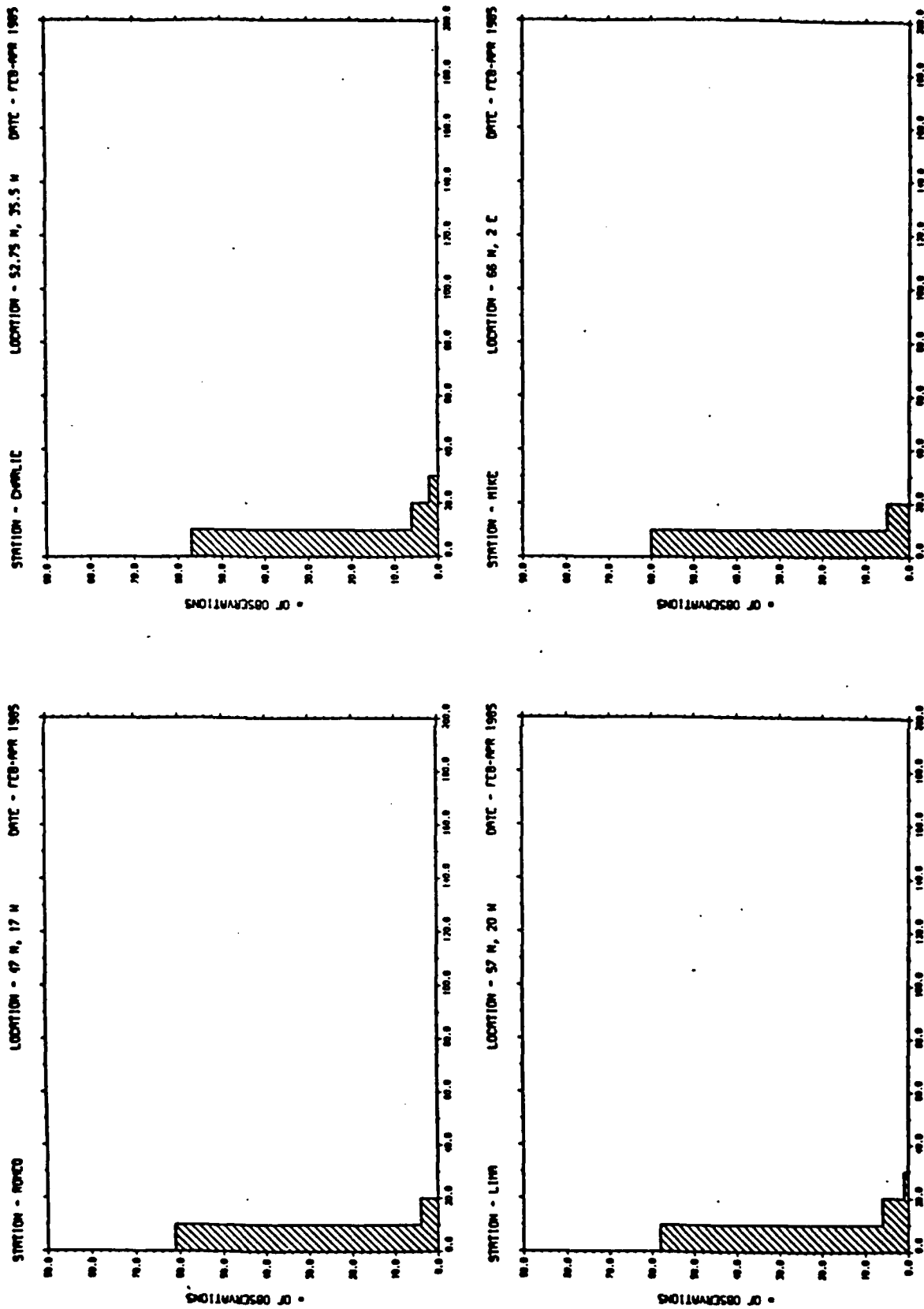


Figure 59 Distribution of the 50 m shear ($s^{-1} \times 10^4$) for the months of February through April at the 4 North Atlantic stations.

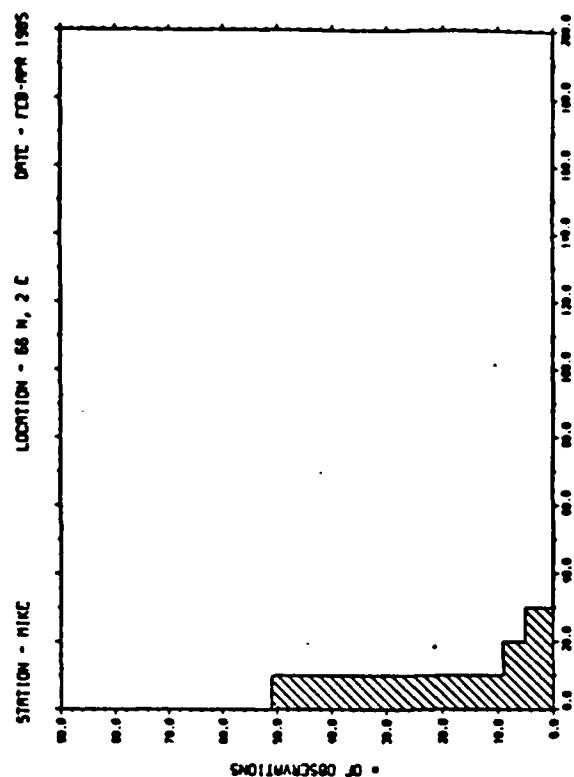
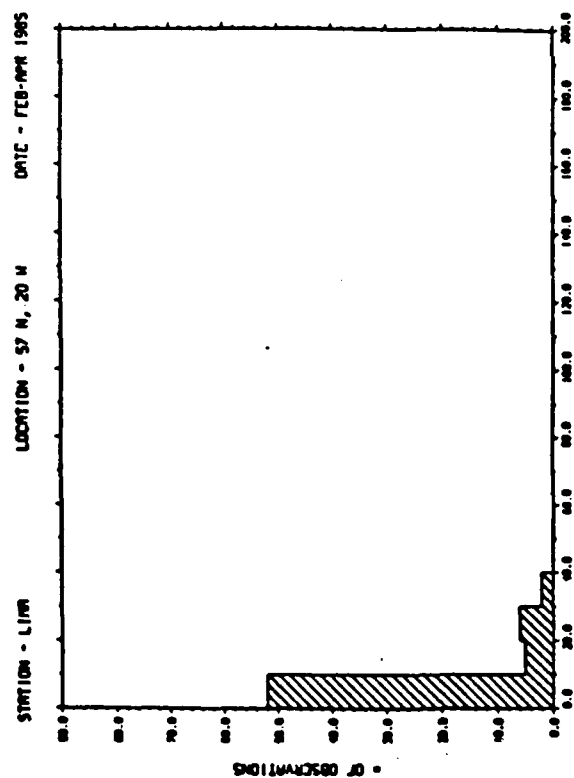
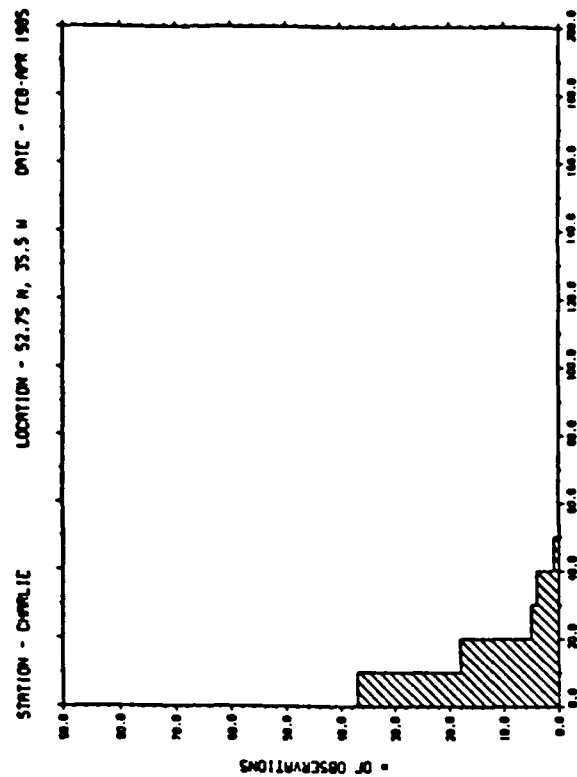
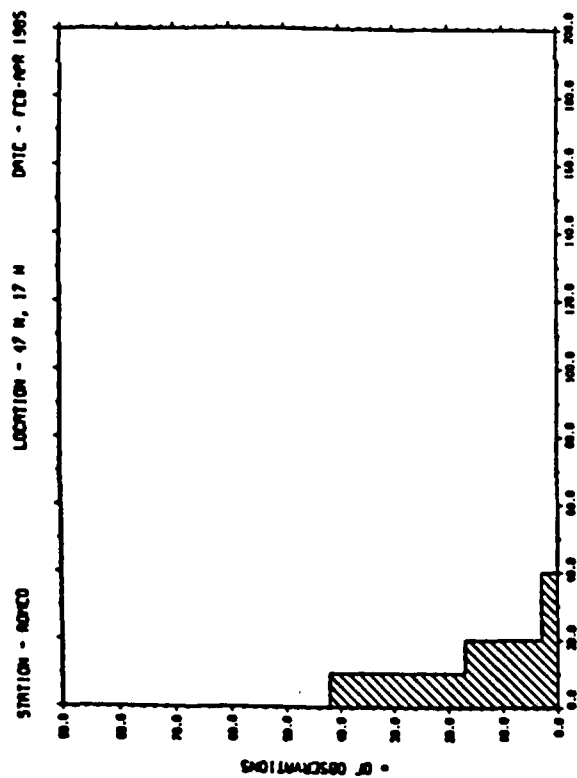


Figure 60 Distribution of the 25 m shear ($s^{-1} \times 10^4$) for the months of February through April at the 4 North Atlantic stations.

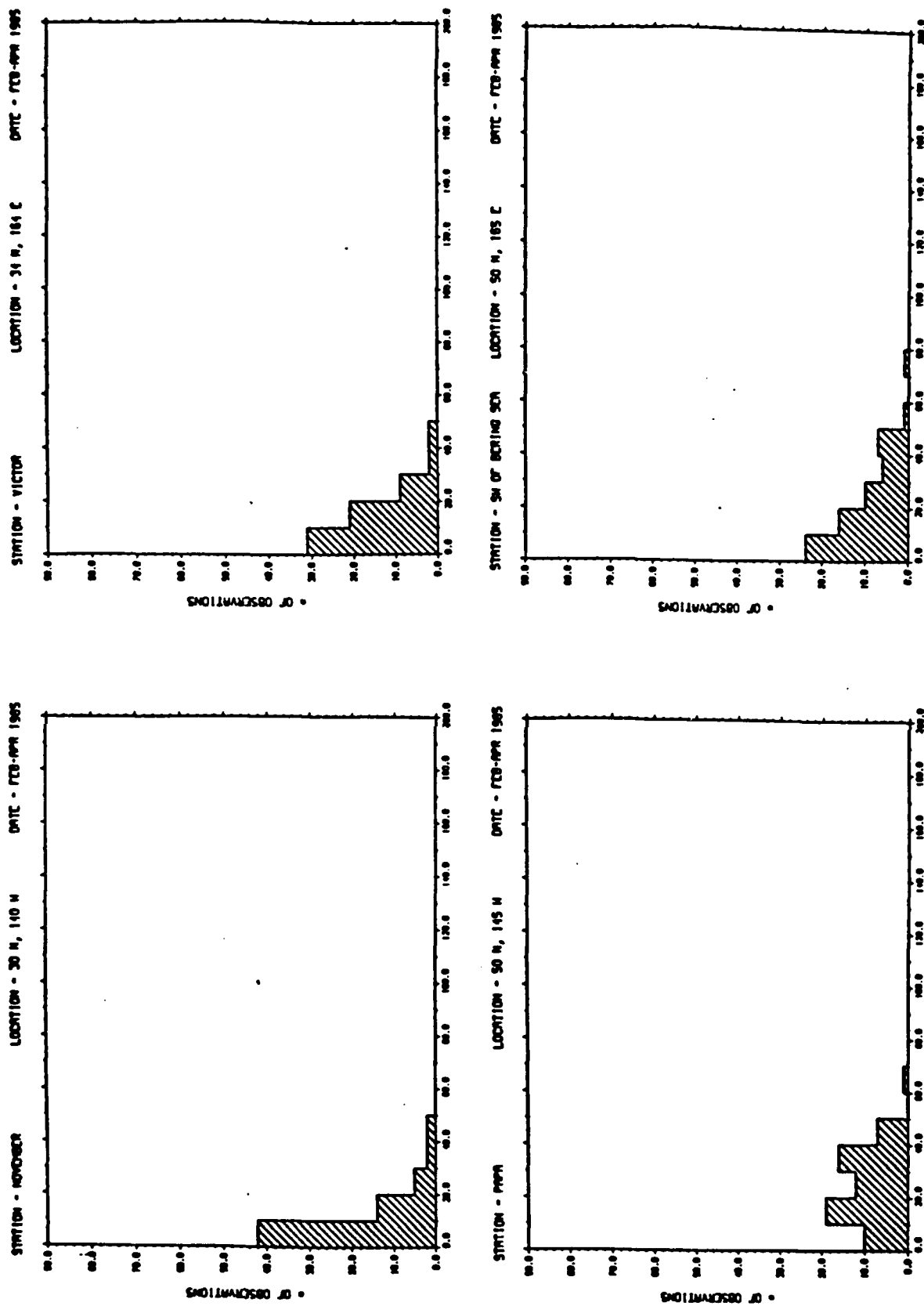


Figure 6.1 Distribution of the 25 m shear ($s-1 \times 10^4$) for the months of February through April at the 4 North Pacific stations.

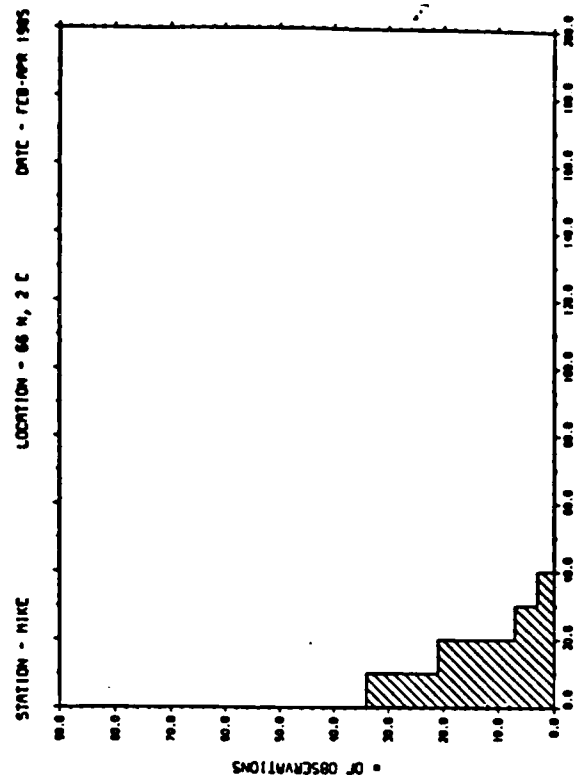
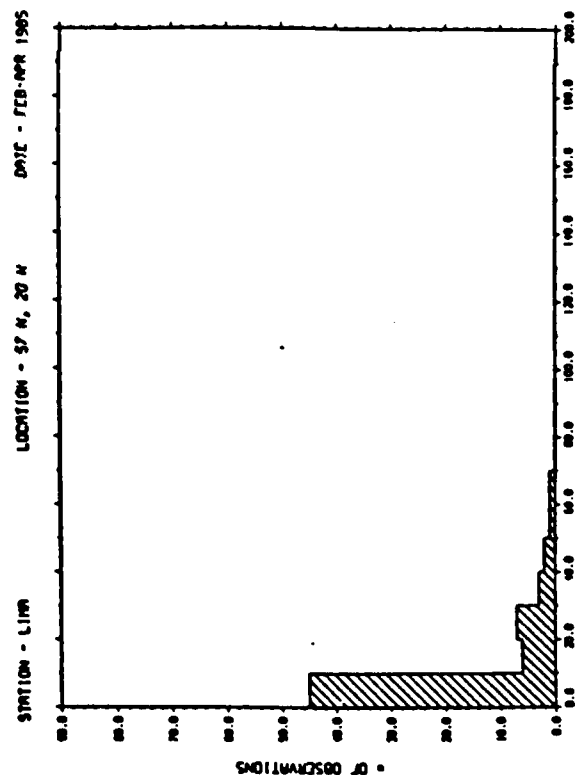
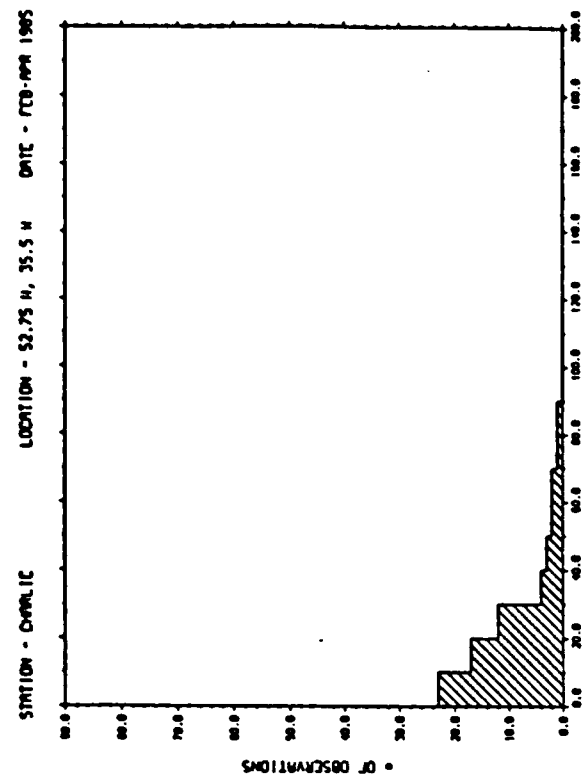
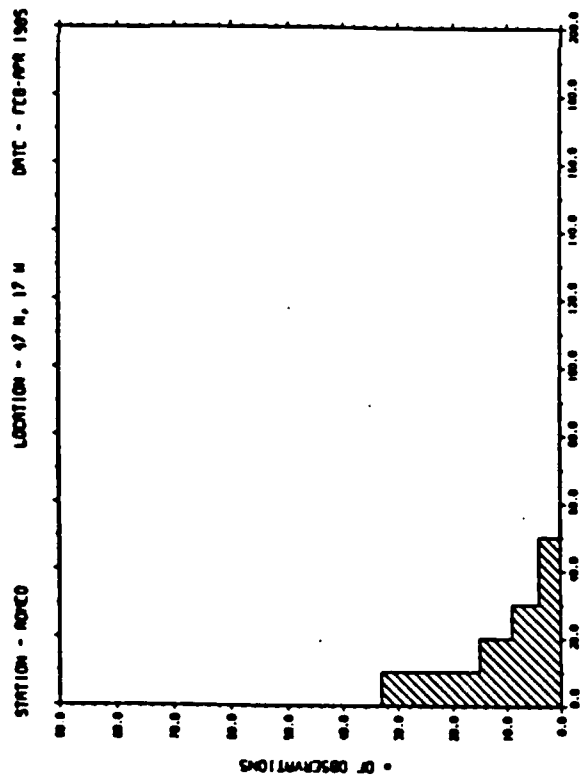


Figure 62 Distribution of the 12.5 m shear ($s-1 \times 10^4$) for the months of February through April at the 4 North Atlantic stations.

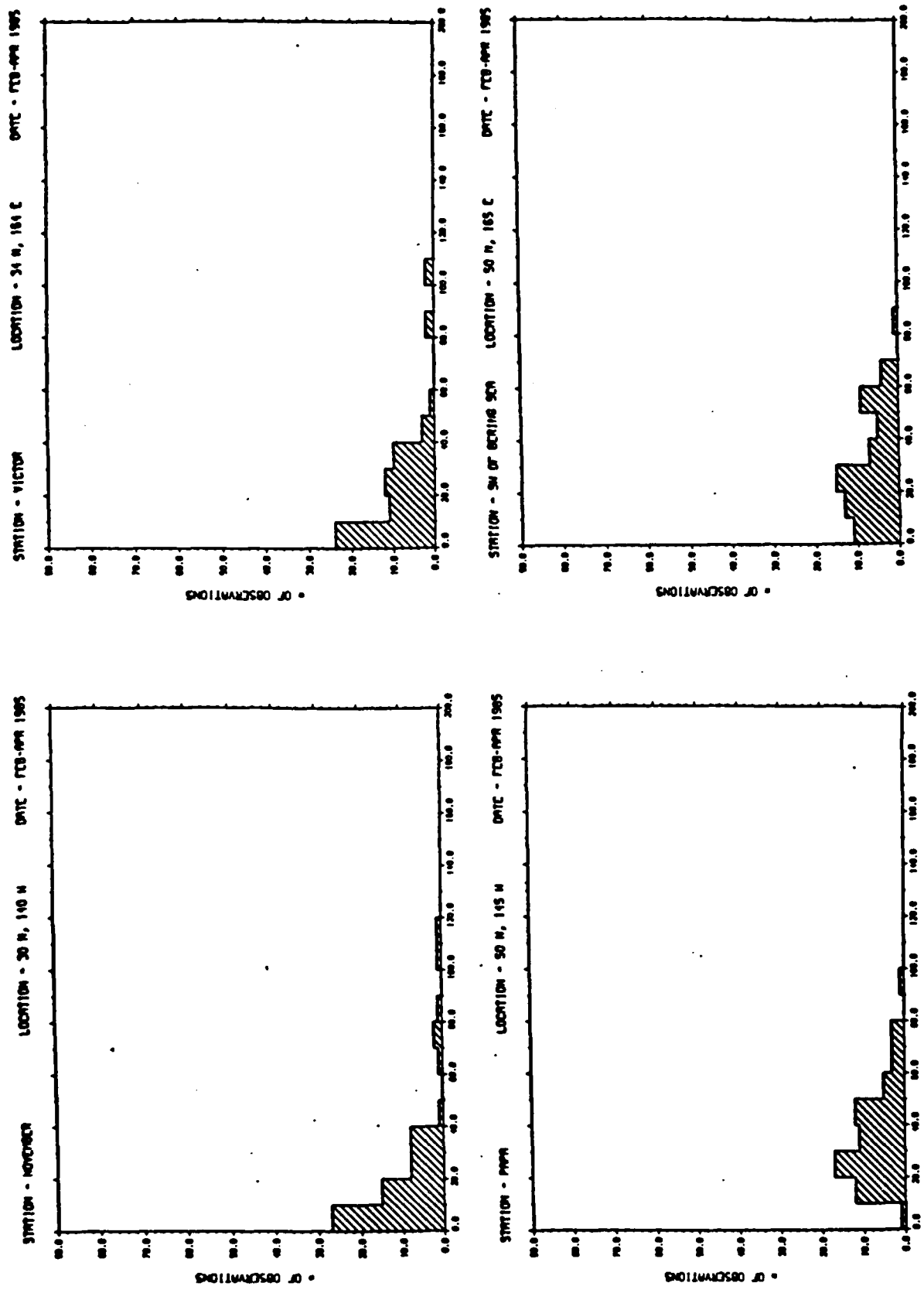


Figure 63 Distribution of the 12.5 m shear ($s^{-1} \times 10^4$) for the months of February through April at the 4 North Pacific stations.

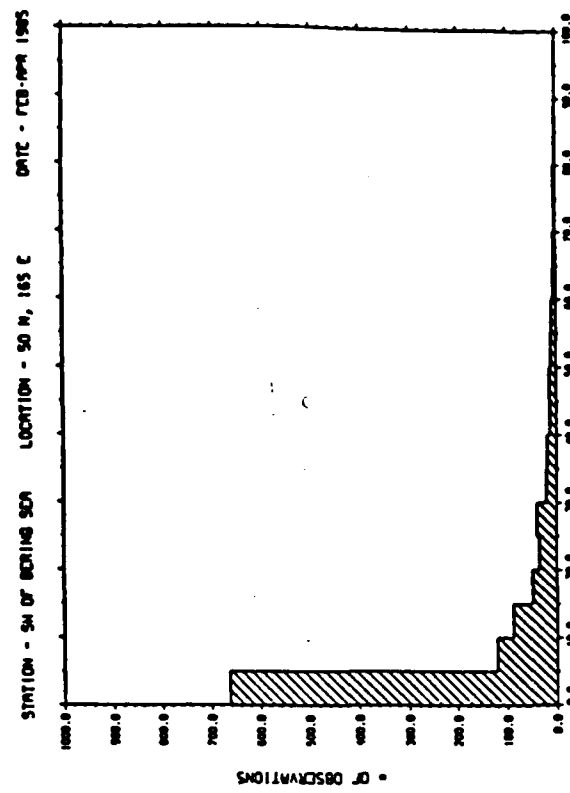
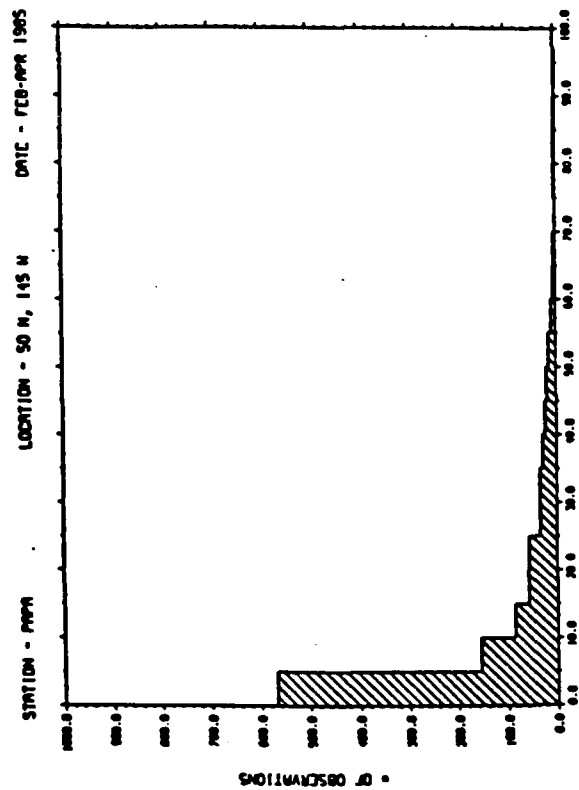
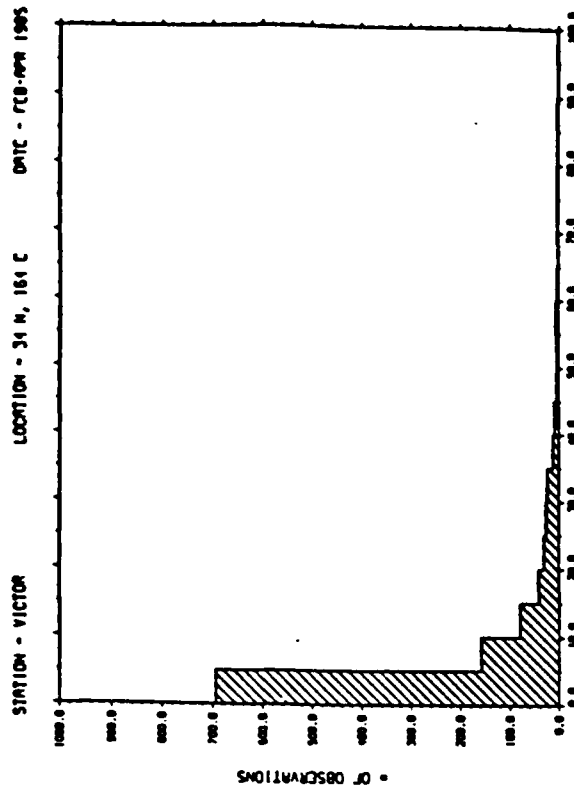
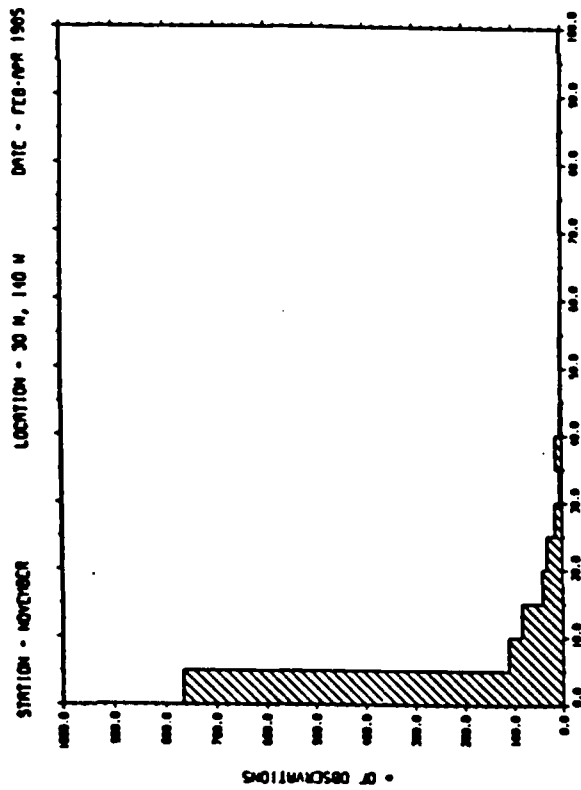


Figure 64 Distribution of the shear ($s^{-1} \times 10^4$) summed over all 17 depth levels for the months of February through April at the 4 North Pacific stations.

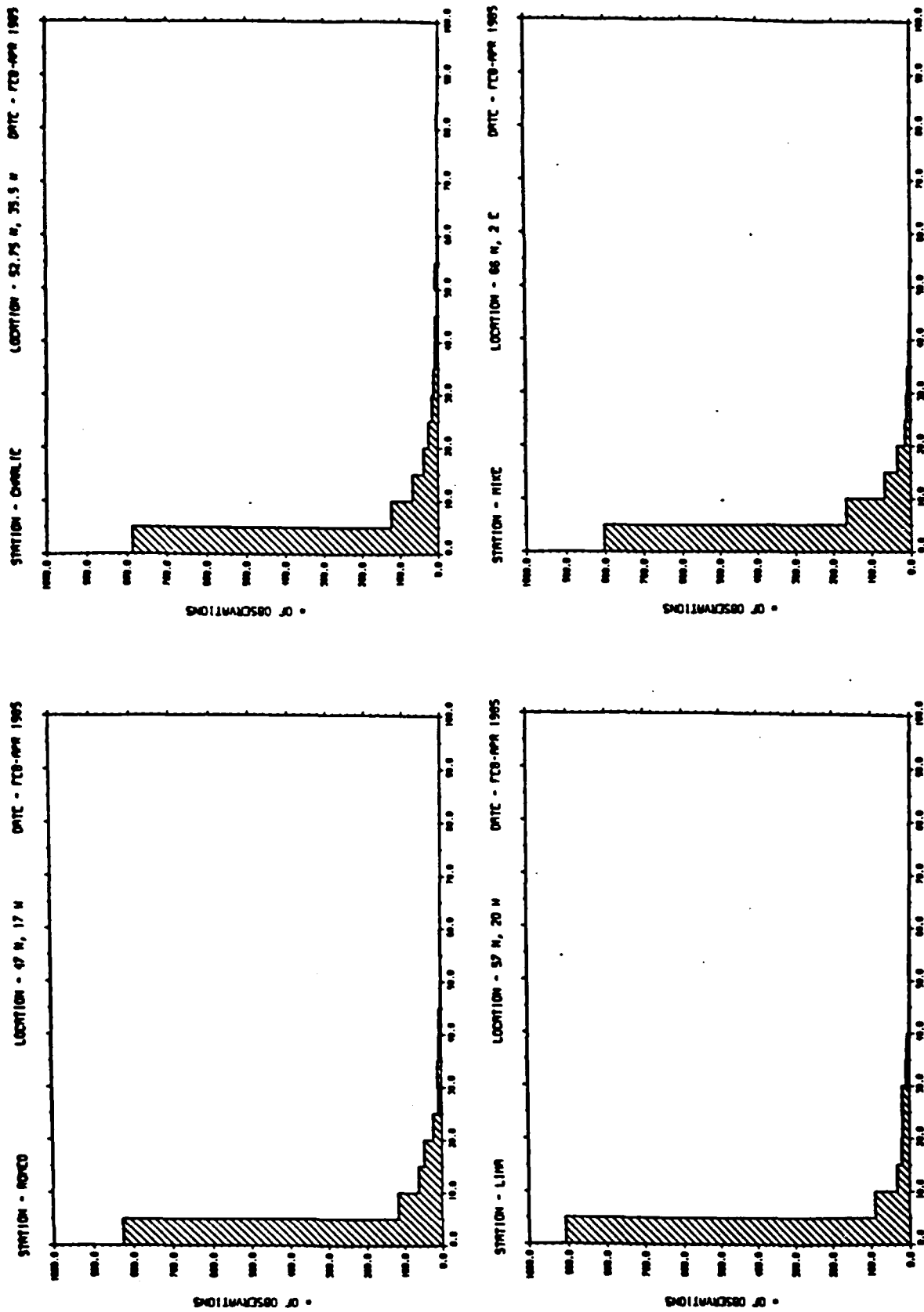


Figure 65 Distribution of the shear ($s^{-1} \times 10^4$) summed over all 17 depth levels for the months of February through April at the 4 North Atlantic stations.

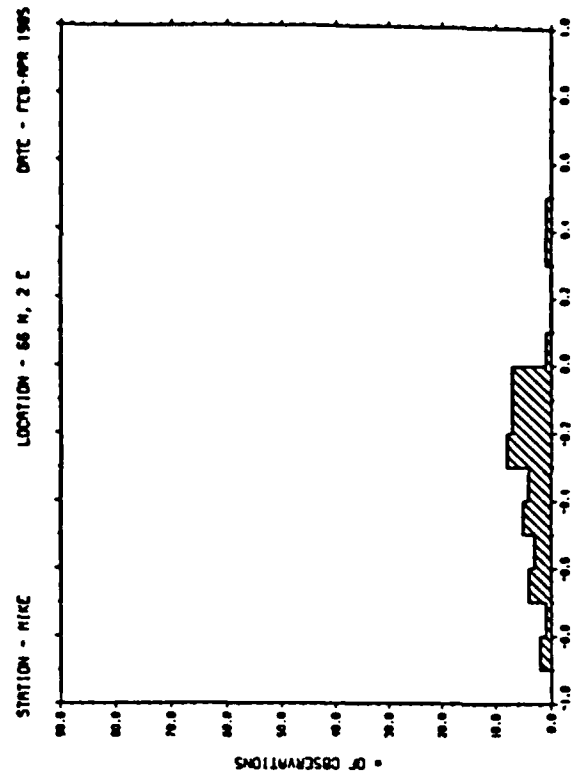
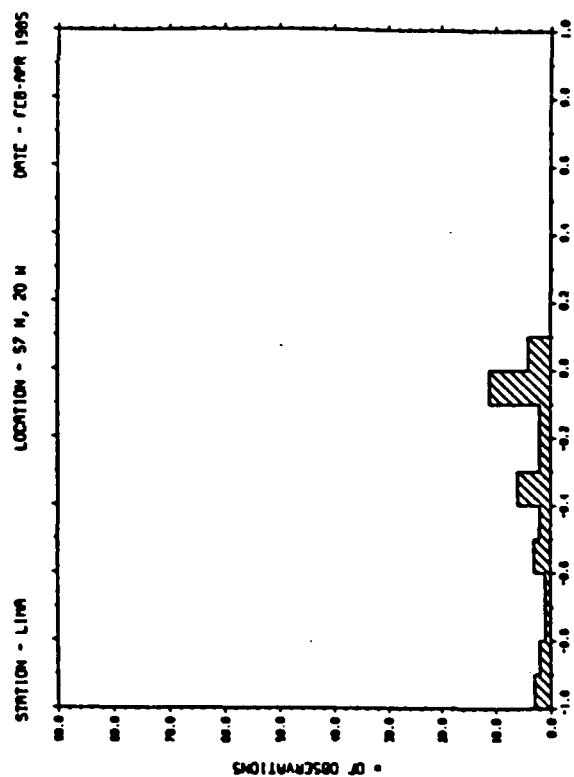
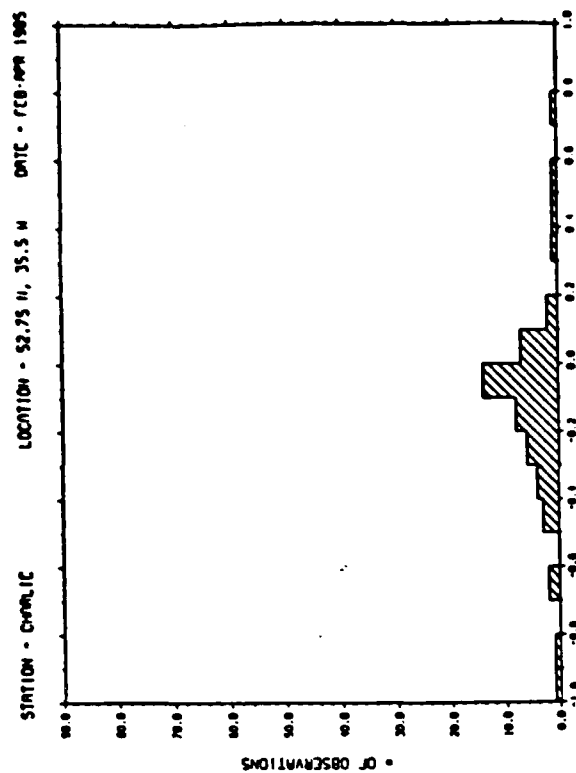
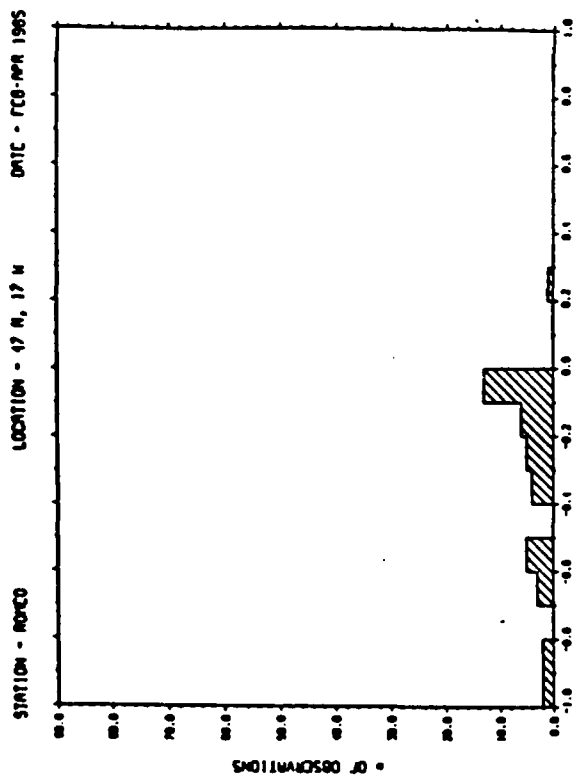


Figure 66 Distribution of the 10 m Richardson number for the months of February through April at the 4 North Atlantic stations.

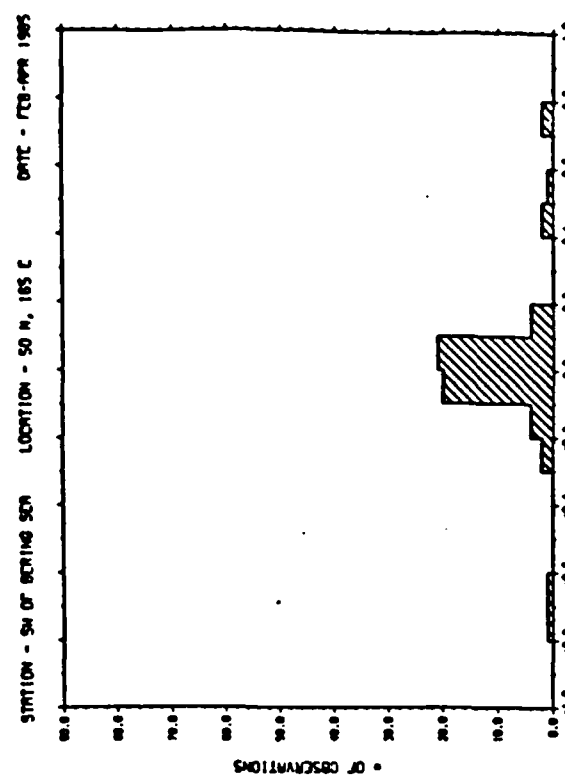
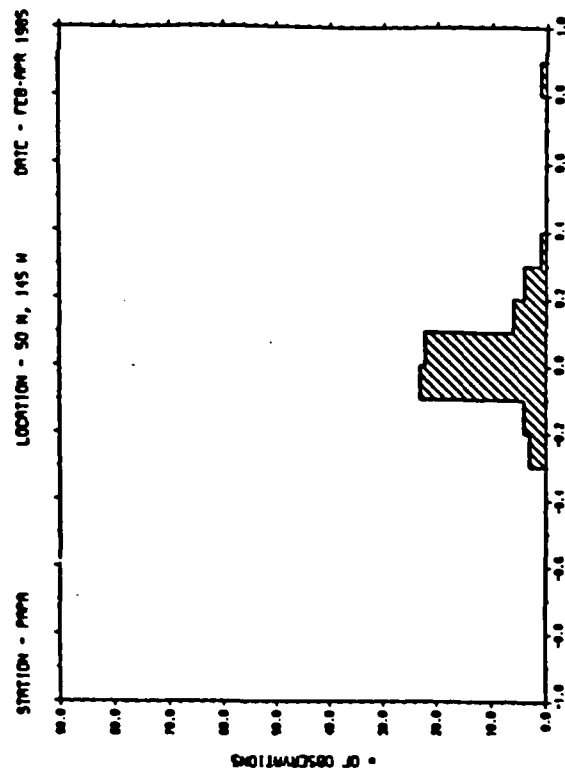
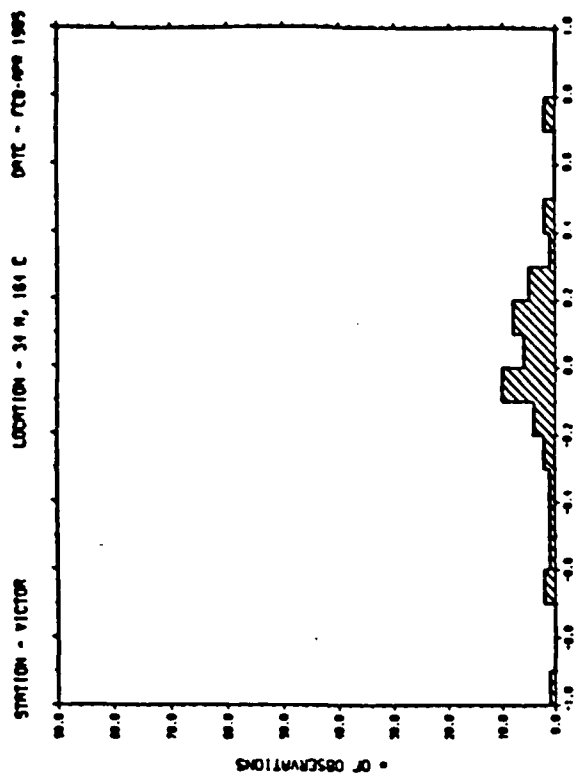
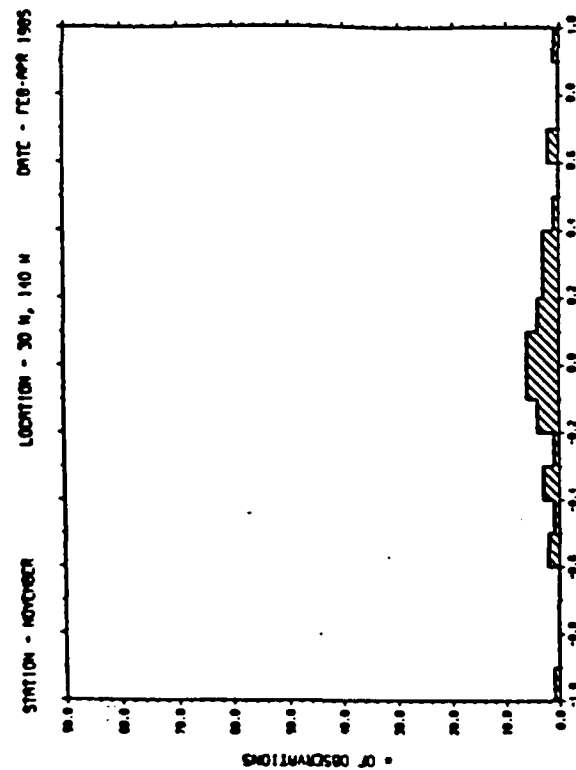


Figure 67 Distribution of the 10 m Richardson number for the months of February through April at the 4 North Pacific stations.

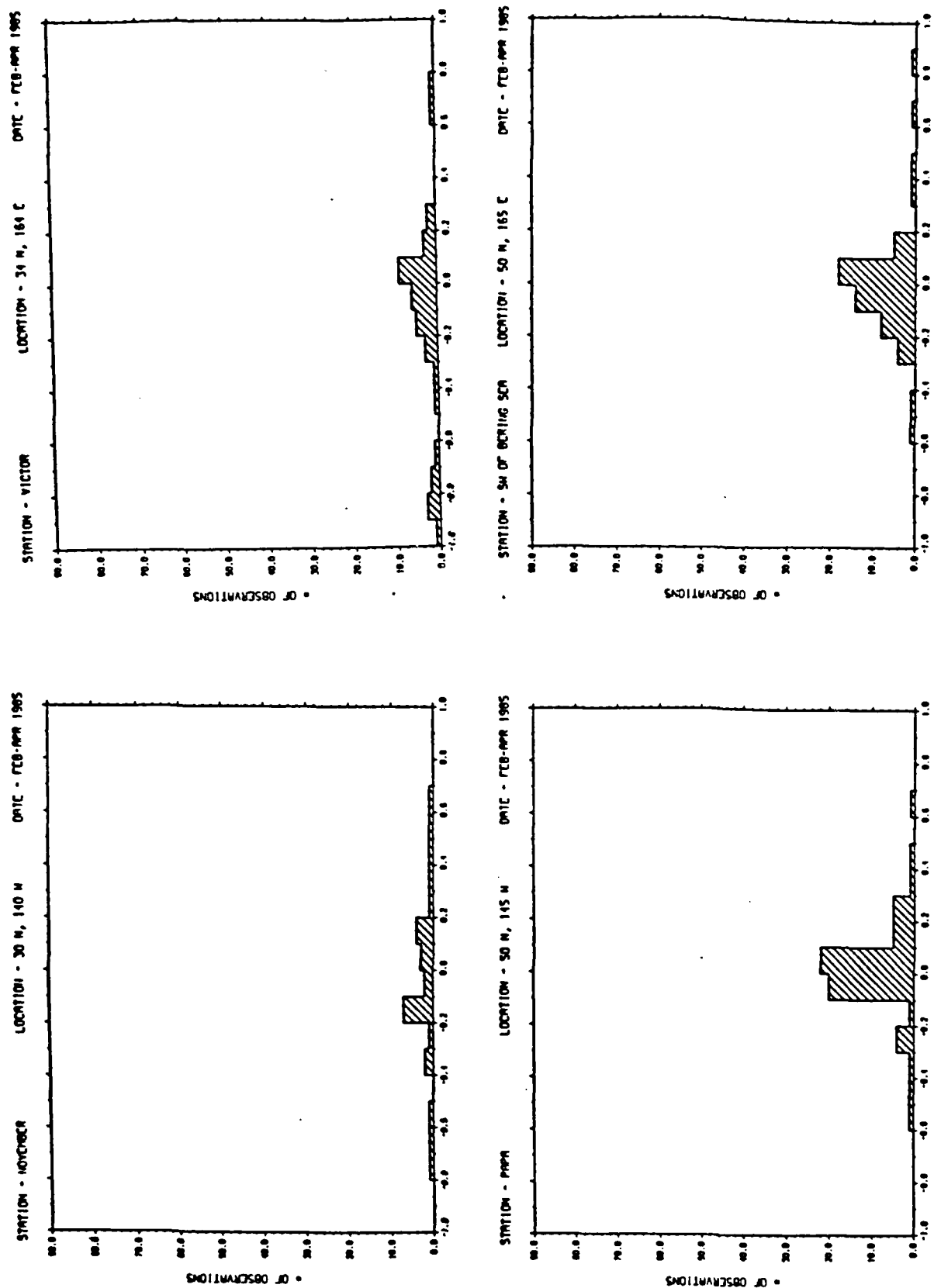


Figure 68 Distribution of the 21.3 m Richardson number for the months of February through April at the 4 North Pacific stations.

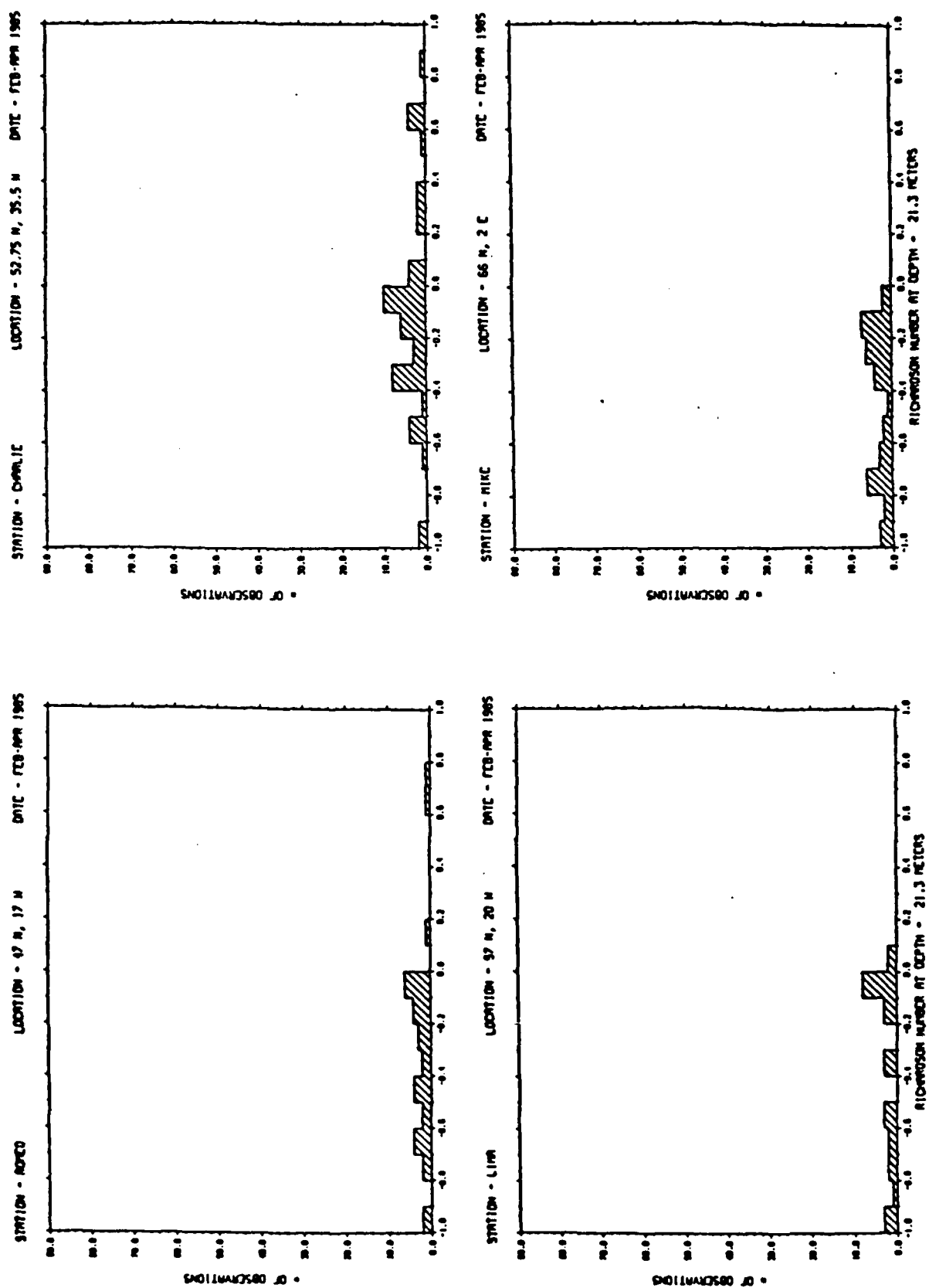


Figure 69 Distribution of the 21.3 m Richardson number for the months of February through April at the 4 North Atlantic stations.

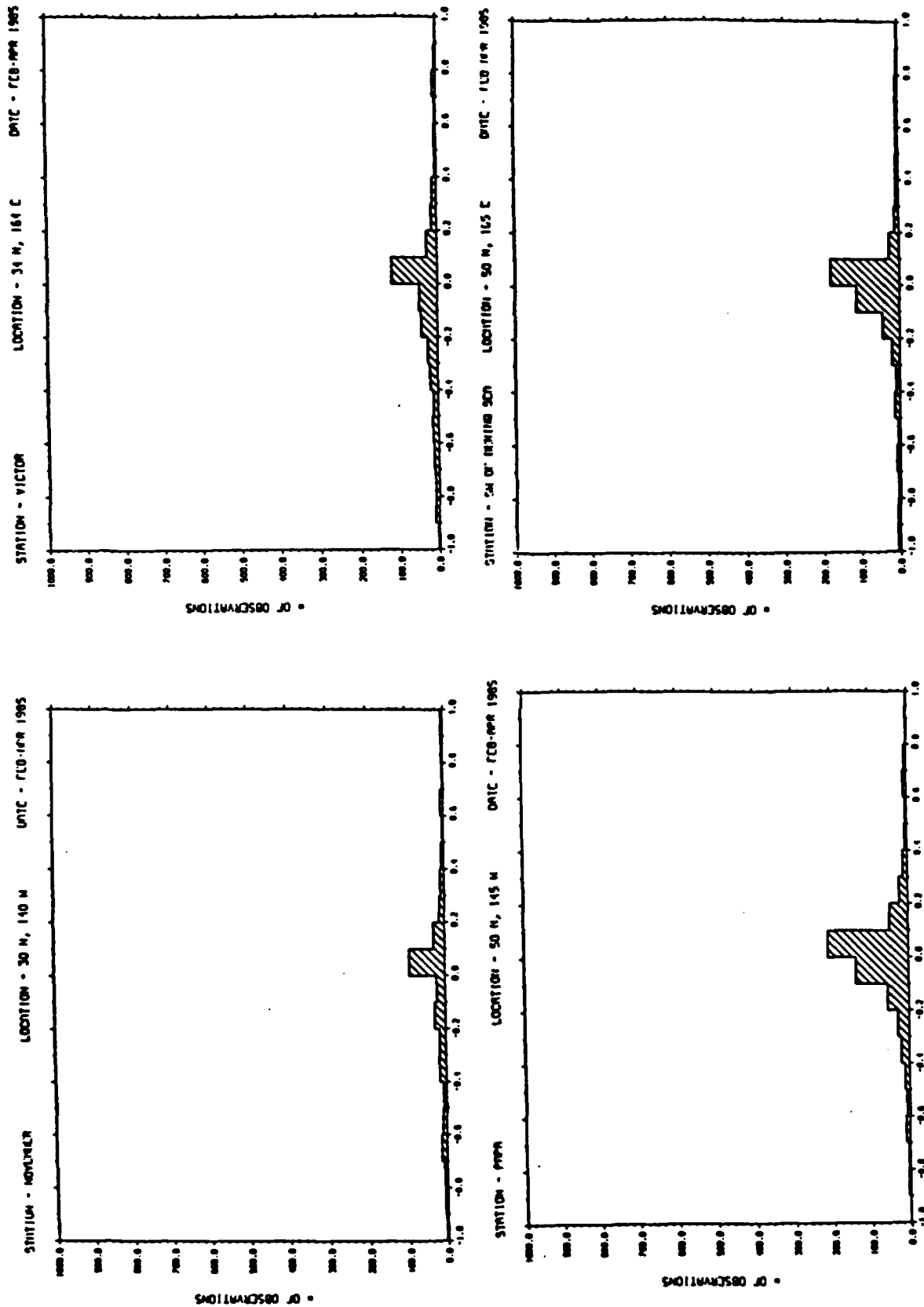


Figure 70 Distribution of the Richardson number summed over all 17 depth levels for the months of February through April at the 4 North Pacific stations.

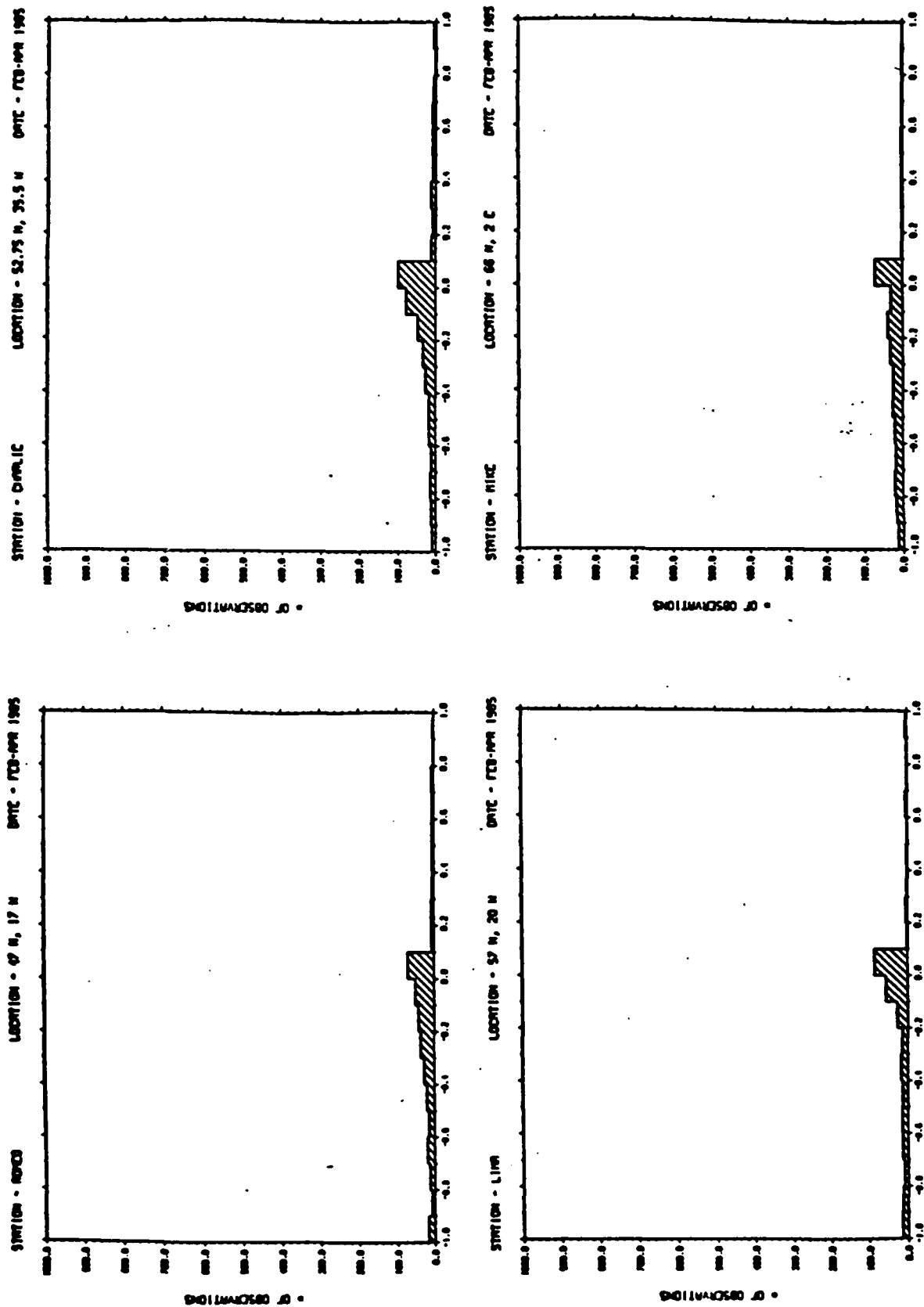


Figure 7 1 Distribution of the Richardson number summed over all 17 depth levels for the months of February through April at the 4 North Atlantic stations.

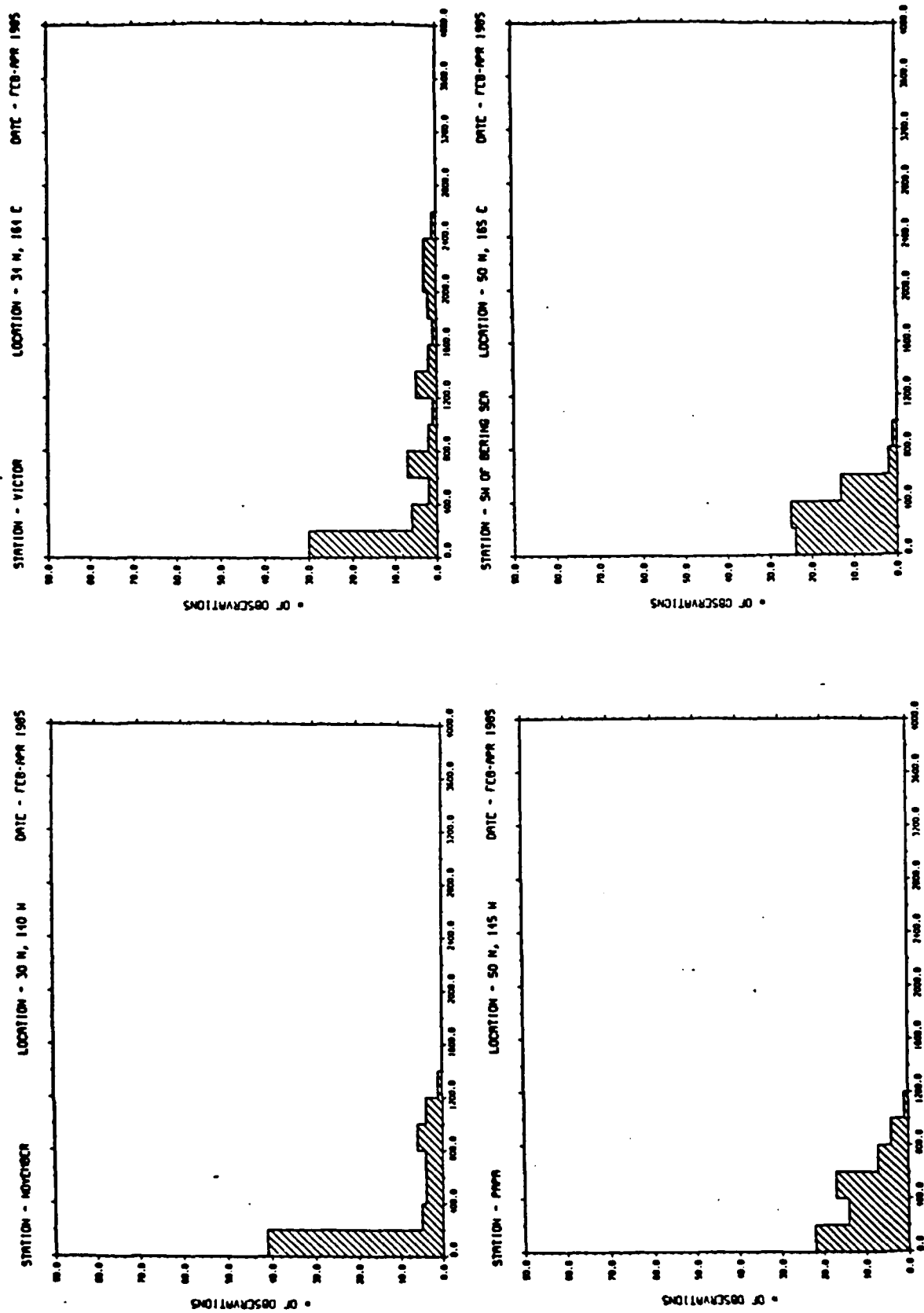


Figure 72 Distribution of the 5 m eddy coefficient of momentum for the months of February through April at the 4 North Pacific stations.

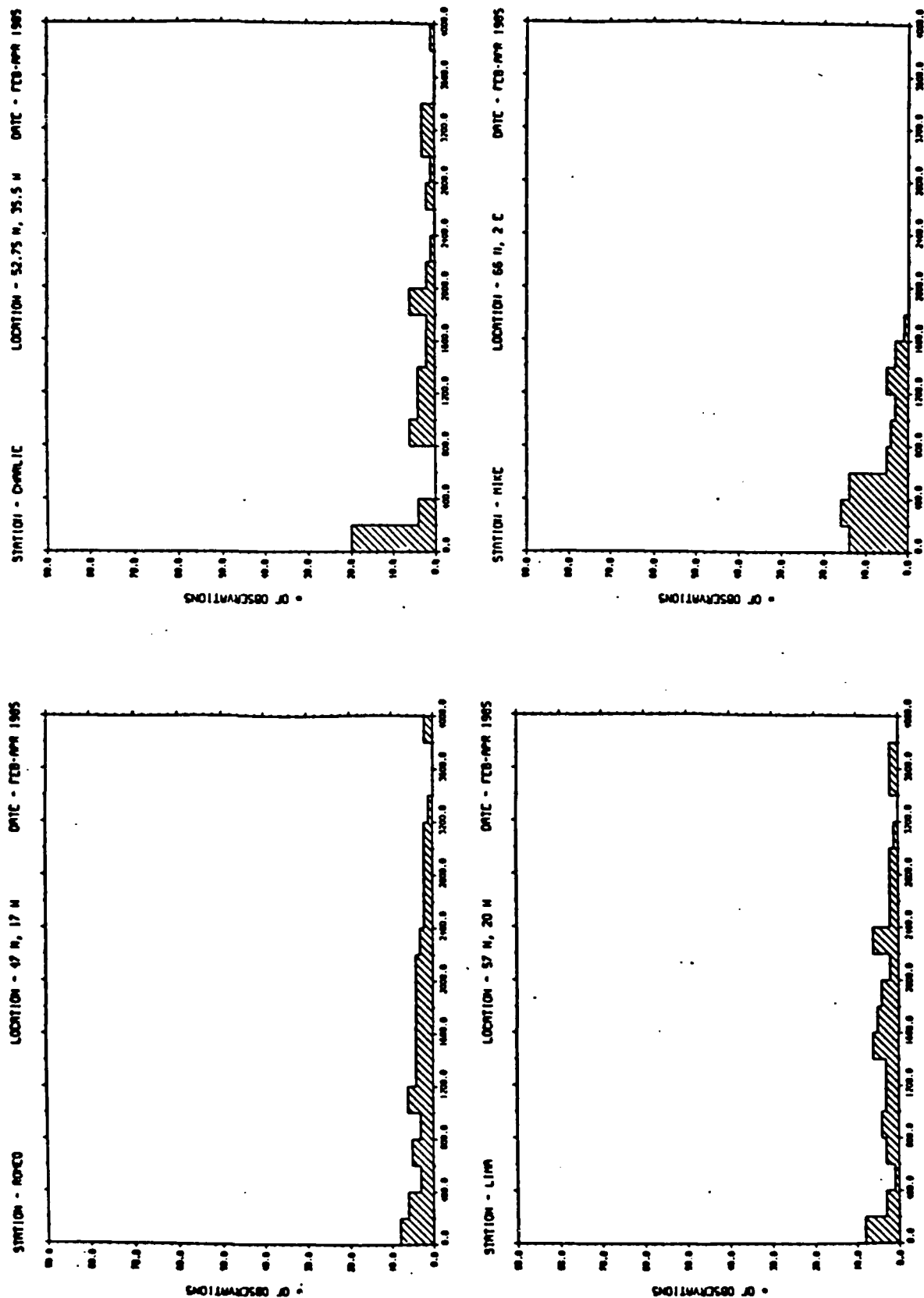


Figure 73 Distribution of the 5 m eddy coefficient of momentum for the months of February through April at the 4 North Atlantic stations.

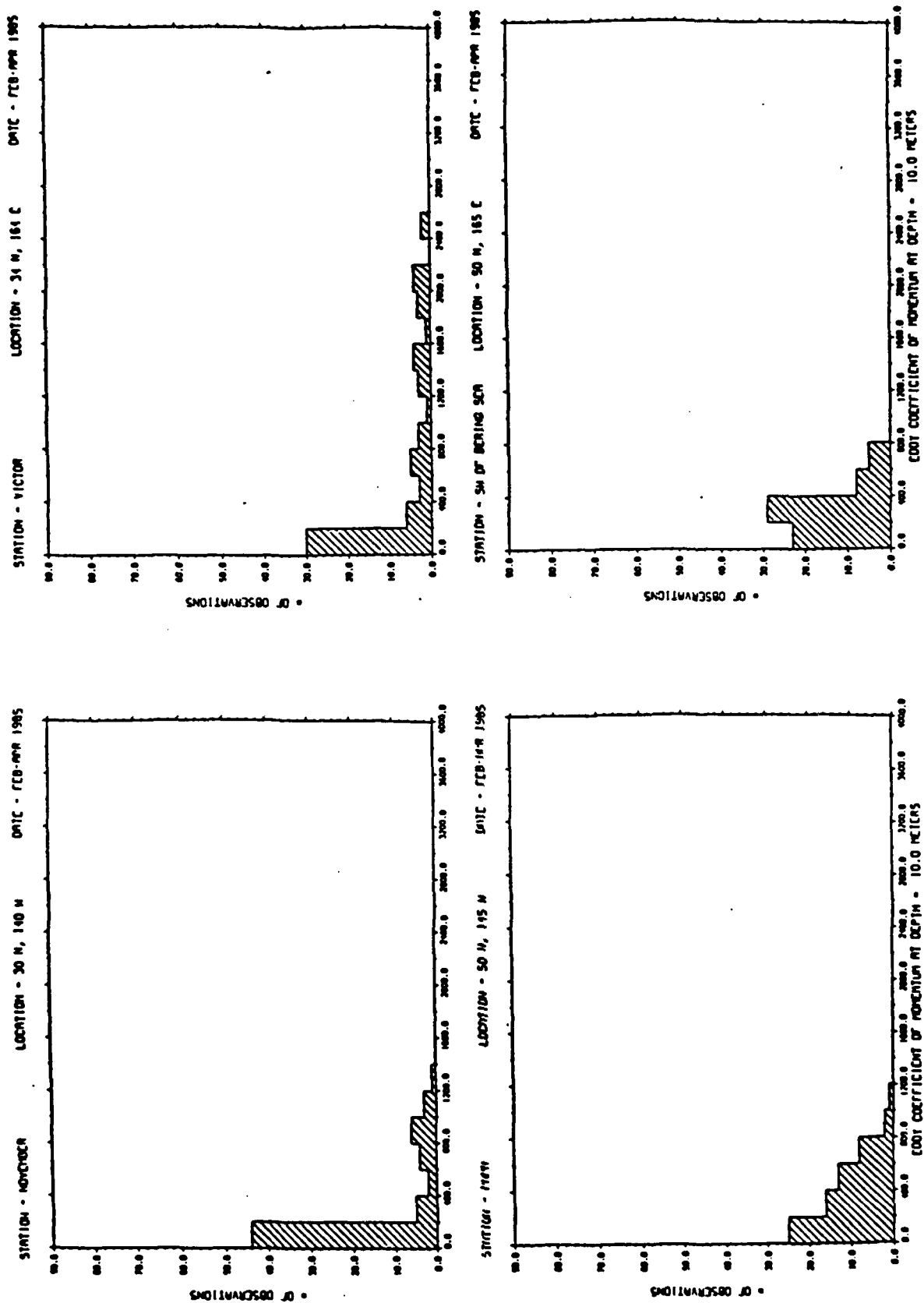


Figure 74 Distribution of the 10 m eddy coefficient of momentum for the months of February through April at the 4 North Pacific stations.

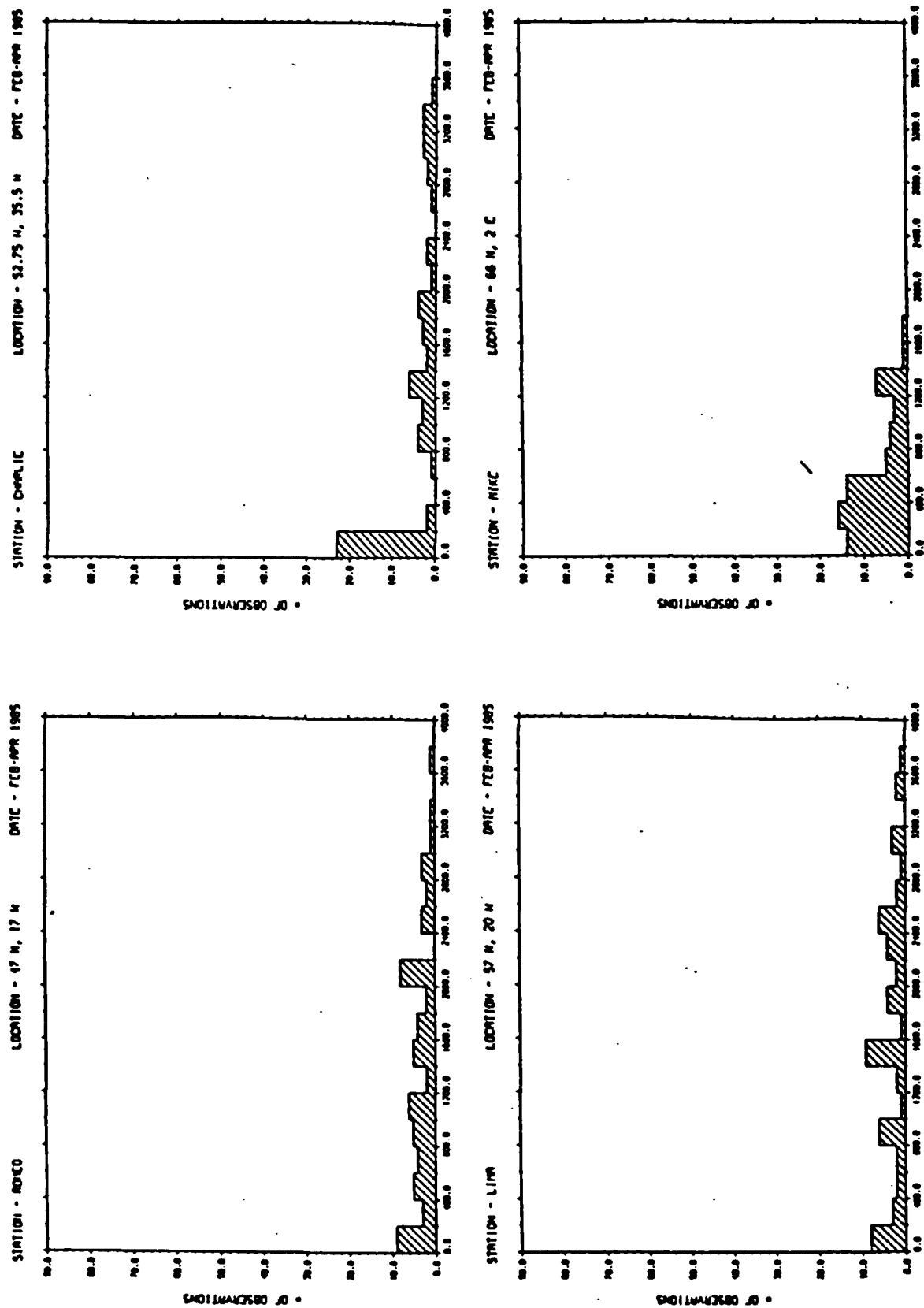


Figure 75 Distribution of the 10 m eddy coefficient of momentum for the months of February through April at the 4 North Atlantic stations.

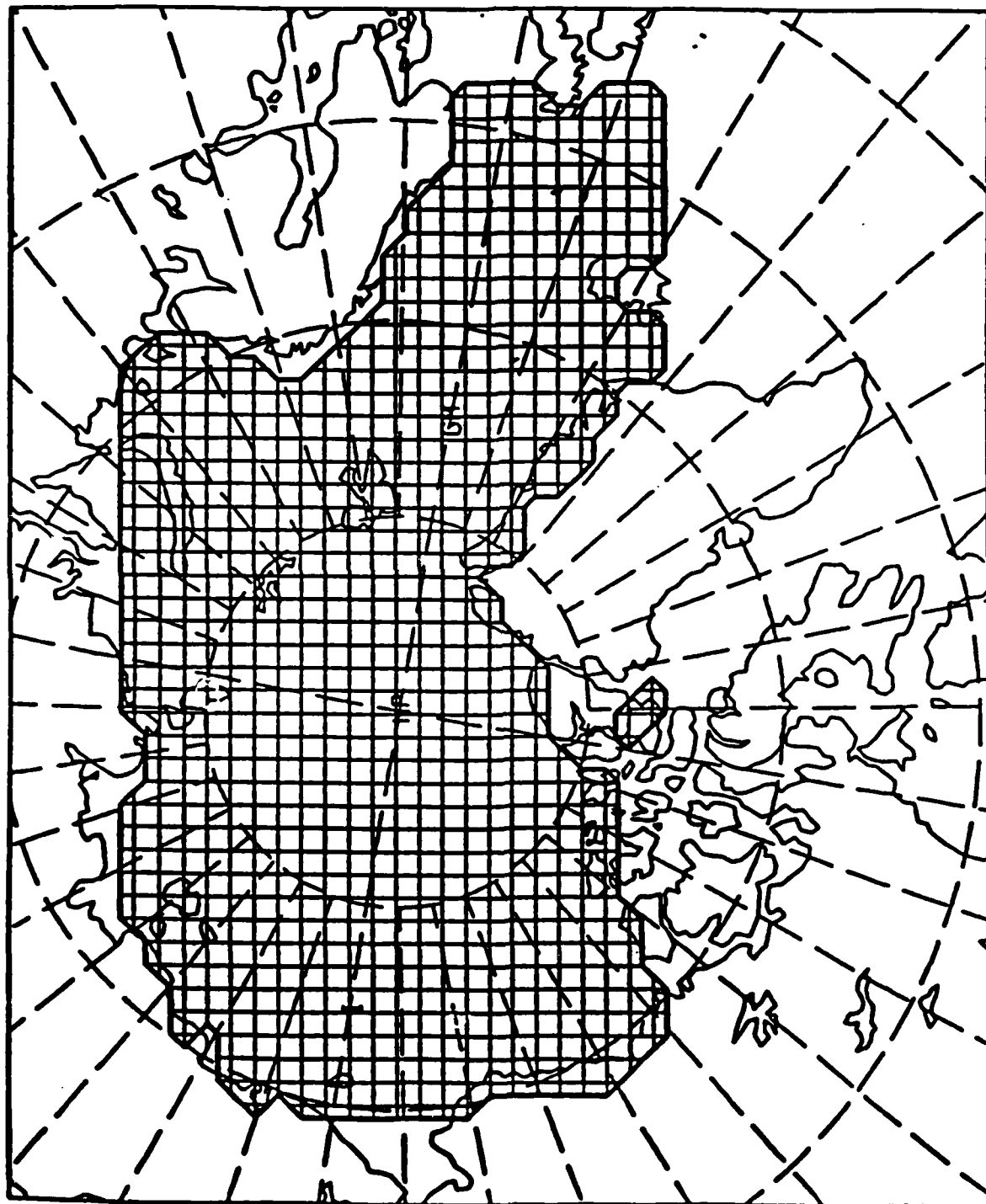


Figure 76 Polar Ice Prediction System (PIPS) grid

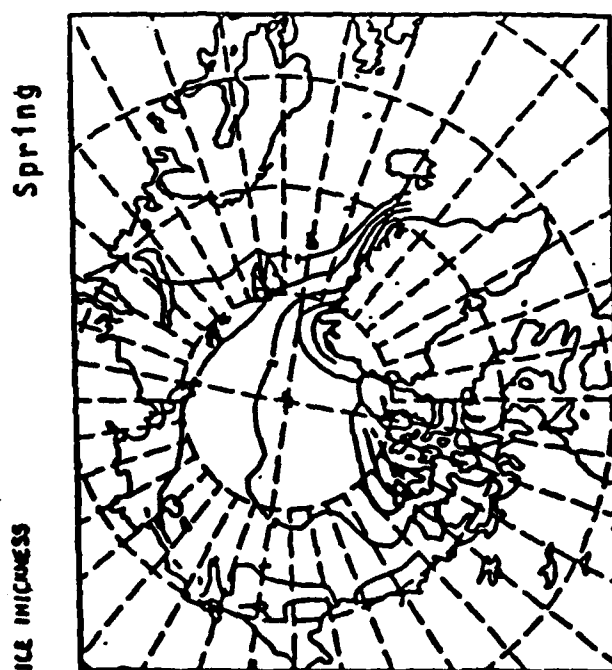
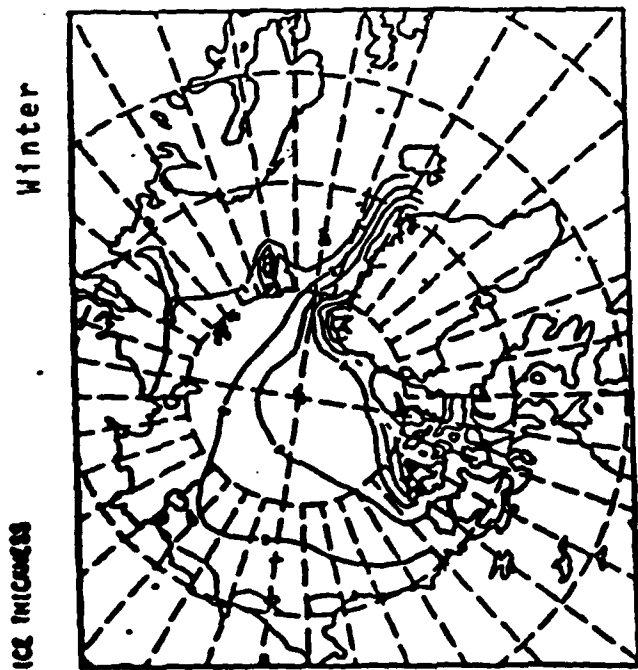
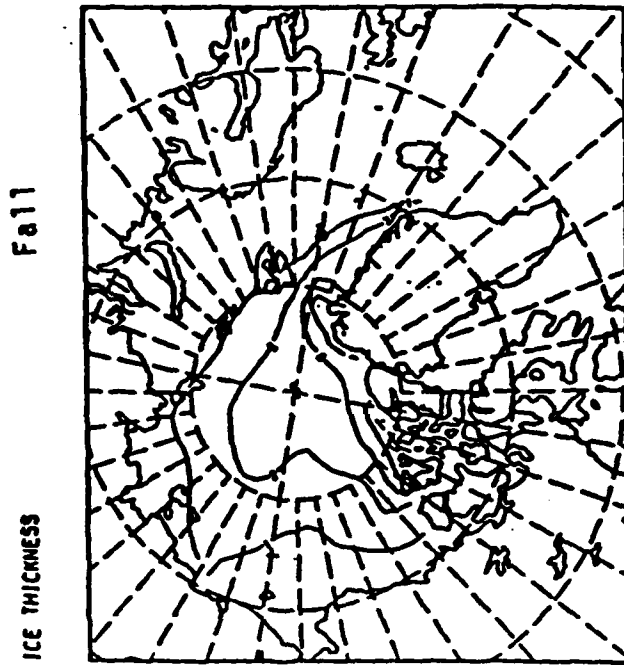
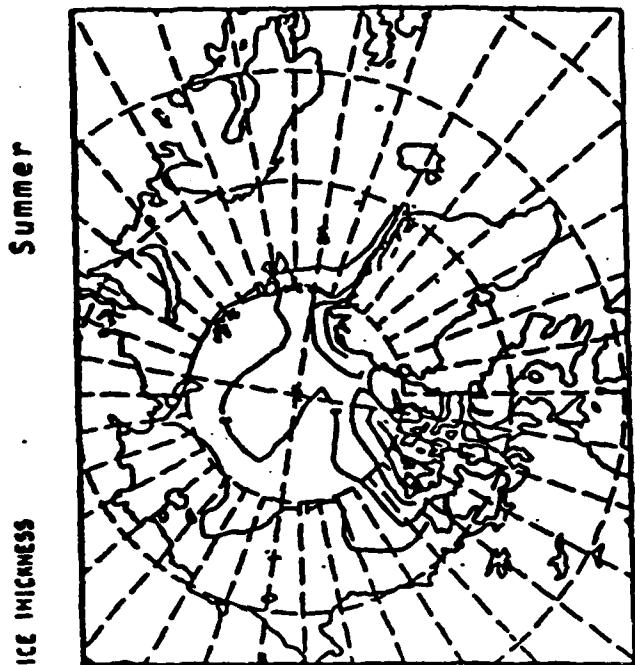


Figure 77 Seasonal contours of ice thickness from the PIPS model forced with 1983 NOGAPS Atmospheric forcing and Hibler/Bryan ocean forcing. Contours in 1 m intervals.

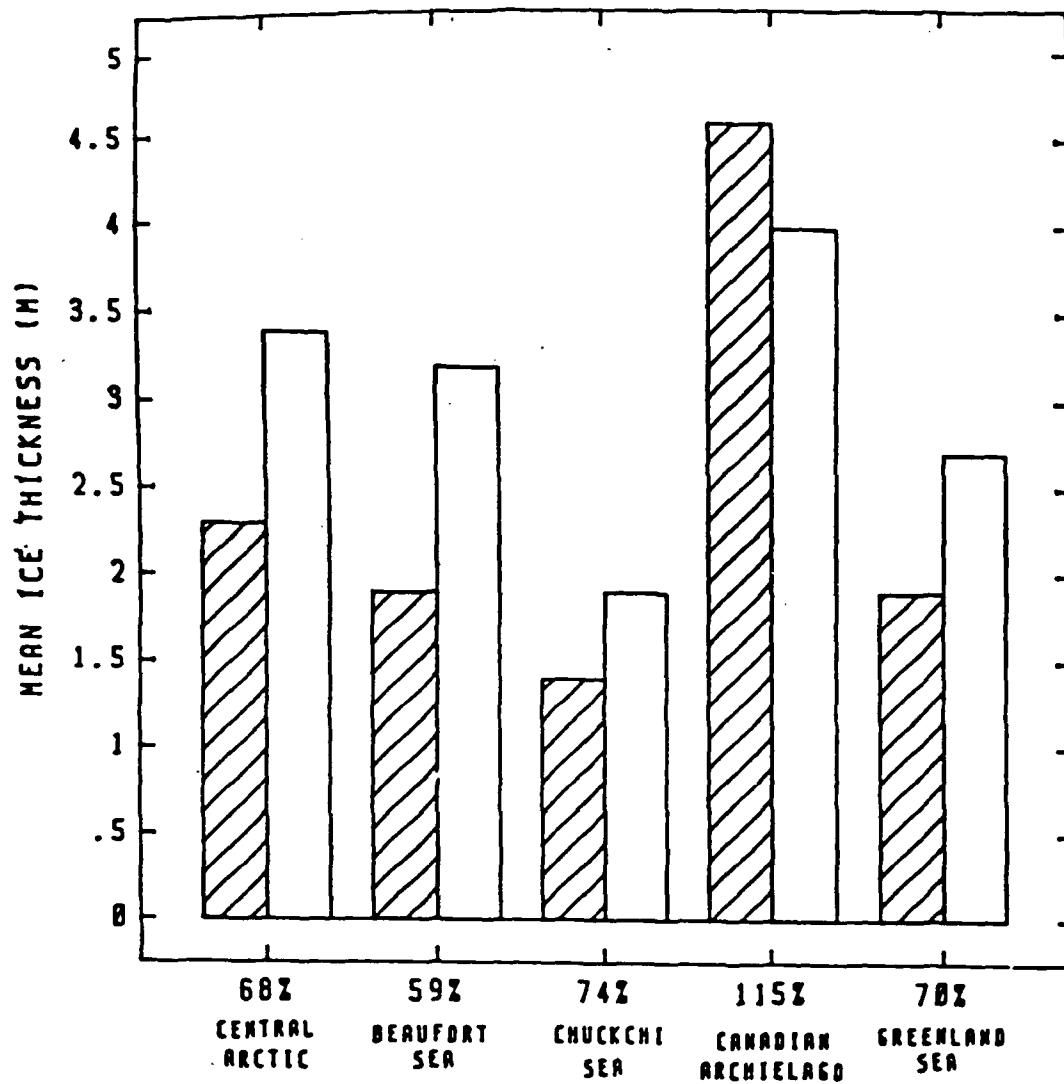
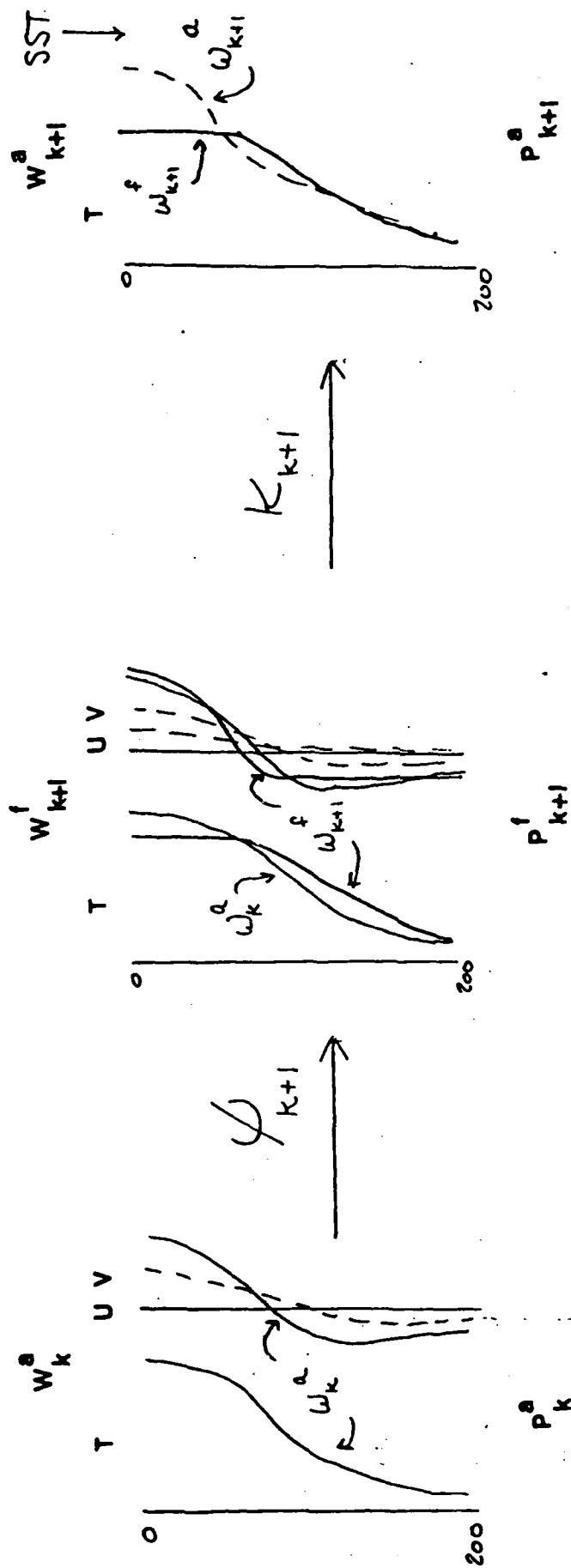


Figure 78. Mean annual ice thickness from the model (hatched bar) and observations (open bar) for different regions. Numbers below each bar indicate the ratio, expressed as percent, of modeled to observed thickness.

FIGURE 79 SUMMARY OF STEPS IN KALMAN FILTER



Step 1. Begin with an analysis and its error covariance matrix:

w_k^a and p_k^a

Step 2: Use the model, expressed by ϕ_{k+1} , to compute the forecast w_{k+1}^f and its error covariance matrix p_{k+1}^f

Step 3: If an SST available, blend it with the forecast to produce the new analysis and its error covariance matrix:

w_{k+1}^a and p_{k+1}^a

TABLE 1. ROOT MEAN SQUARE ERROR IN ONE-DAY PREDICTIONS.
All errors are computed on the same days, which had wind and
sea surface data available for the statistical forecasts.

SPRING

Depth	Climatology	Persistence	Stat(SS)	Stat(WS)	Stat(NC)
2.5	.64	.23	.20	.25	.29
7.5	.61	.21	.18	.22	.27
12.5	.60	.20	.18	.21	.25
17.5	.59	.35	.20	.23	.26
25.0	.62	.35	.34	.34	.31
32.5	.76	.33	.36	.36	.31
40.0	.77	.35	.34	.35	.30
50.0	.74	.25	.25	.25	.23
62.5	.62	.22	.27	.26	.23

SUMMER

2.5	.91	.41	.36	.43	.46
7.5	.90	.40	.35	.41	.44
12.5	.88	.44	.37	.40	.41
17.5	.94	.56	.57	.52	.52
25.0	1.06	.80	.79	.74	.77
32.5	1.31	1.08	.93	.94	1.03
40.0	1.32	.89	.83	.86	.92
50.0	1.23	.92	.84	.87	.81
62.5	1.15	.61	.72	.75	.70

RMSE in °C.

TABLE 2. SURFACE DATA AVAILABLE FOR
USE IN PREDICTIONS

SST -- Sea Surface Temperature from bucket readings
average of observations at 18 and 21GMT

WS -- Wind Stress
average of observations at 12, 15, 18 and 21GMT

SOL2 - Solar Radiation
average of observations at 12 and 15GMT

LAT2 - Latent Flux
average of observations at 12 and 15GMT

LAT3 - Latent Flux
average of observations at 18 and 21GMT

SEN2 - Sensible Flux
average of observations at 12 and 15GMT

SEN3 - Sensible Flux
average of observations at 18 and 21GMT

AIR -- Air Temperature
average of observations at 18 and 21GMT

TABLE 3. CORRELATIONS OF CHANGES IN TEMPERATURES AT VARIOUS DEPTHS WITH THE SIMULTANEOUS CHANGES IN SURFACE VARIABLES.

SPRINGS

Depth	SST	WS	SOL2	LAT2	LAT3	SEN2	SEN3	AIR
2.5	.884	-.489	.172	.164	.088	.137	.007	.231
12.5	.757	-.414	.238	.186	.079	.194	-.060	.042
25.0	-.067	-.110	.075	-.050	.018	.150	-.098	-.308
50.0	-.198	.184	-.077	.020	-.074	-.065	-.056	-.054

SUMMERS

Depth	SST	WS	SOL2	LAT2	LAT3	SEN2	SEN3	AIR
2.5	.861	-.491	.147	.231	.155	-.088	-.106	.273
12.5	.504	-.181	.122	.130	.110	.067	.009	.263
25.0	.023	-.012	-.093	.101	.118	.068	.068	.129
50.0	.017	.152	-.037	-.115	-.152	.017	.015	.118

TABLE 4. ROOT MEAN SQUARE ERRORS IN PREDICTIONS FOR SPRING PROFILES,
AT DIFFERENT FORECAST LAGS AND DEPTH GROUPS.

Lag	n	Climatology			Persistence		
		S	M	D	S	M	D
1	48	.61	.72	.68	.21	.34	.24
2	42	.60	.73	.68	.35	.37	.27
3	40	.57	.71	.62	.42	.33	.36
4	41	.53	.72	.62	.53	.47	.37
5	39	.55	.75	.63	.57	.43	.41
6	37	.54	.74	.60	.63	.49	.43
7	39	.59	.78	.65	.67	.51	.46

Lag	n	Stat (SS)			Stat (WS)			Stat (NC)		
		S	M	D	S	M	D	S	M	D
1	48	.19	.35	.26	.23	.35	.25	.27	.31	.23
2	42	.22	.34	.27	.36	.33	.27	.35	.32	.26
3	40	.25	.36	.36	.42	.36	.35	.42	.42	.42
4	41	.35	.51	.38	.56	.45	.36	.55	.44	.27
5	39	.39	.45	.39	.58	.39	.38	.58	.41	.40
6	37	.45	.49	.41	.63	.46	.40	.64	.47	.43
7	39	.57	.56	.43	.71	.49	.43	.69	.50	.45

RMSE in °C

S = SQRT (average squared error) at depths 2.5, 7.5, 12.5 and 17.5 m
M = SQRT (average squared error) at depths 25., 32.5 and 40 m
D = SQRT (average squared error) at depths 50. and 62.5 m

TABLE 5. ROOT MEAN SQUARE ERROR IN PREDICTIONS FOR SUMMER PROFILES
AT DIFFERENT FORECAST LAGS AND DEPTH GROUPS

Lag	n	Climatology			Persistence		
		S	M	D	S	M	D
1	65	.91	1.23	1.19	.46	.93	.78
2	61	.86	1.24	1.07	.50	1.07	.93
3	62	.86	1.34	1.21	.53	1.22	.89
4	66	.87	1.34	1.16	.70	1.27	.93
5	65	.94	1.14	.94	.84	.88	.91
6	63	.94	1.09	.99	.93	1.02	1.08
7	68	.90	1.27	1.13	.91	1.41	1.17

Lag	n	Stat (SS)			Stat (WS)			Stat (NC)		
		S	M	D	S	M	D	S	M	D
1	65	.42	.85	.78	.44	.85	.81	.46	.91	.76
2	61	.50	1.16	.96	.53	1.10	.91	.53	1.06	.87
3	62	.51	1.31	1.02	.59	1.20	.85	.59	1.24	.86
4	66	.67	1.42	1.18	.73	1.28	.92	.73	1.15	.91
5	65	.73	1.10	1.22	.83	.91	.90	.84	.87	.89
6	63	.78	1.26	1.40	.97	1.01	1.07	.93	.98	1.00
7	68	.80	1.62	1.56	.88	1.38	1.15	.90	1.36	1.15

RMSE in °C

S, M and D as in Table 4.

TABLE 6. ROOT MEAN SQUARE ERROR IN PREDICTIONS FOR SUMMER PROFILES, EXCLUDING EDDY IN 1984, AT DIFFERENT FORECAST LAGS AND DEPTH GROUPS.

Lag	n	Climatology			Persistence		
		S	M	D	S	M	D
1	41	1.00	1.01	.90	.41	.63	.56
2	40	.89	.99	.68	.41	.81	.65
3	40	.91	1.01	.81	.45	.87	.58
4	43	.92	1.04	.83	.71	.97	.60
5	44	1.00	1.03	.73	.88	.97	.70
6	42	1.02	.98	.68	.99	1.10	.81
7	44	.94	.93	.71	.91	1.14	.69

Lag	n	Stat (SS)			Stat (WS)			Stat (NC)		
		S	M	D	S	M	D	S	M	D
1	41	.33	.58	.63	.41	.64	.59	.42	.59	.58
2	40	.35	.73	.66	.46	.79	.69	.46	.77	.65
3	40	.40	.87	.63	.51	.87	.58	.51	.87	.54
4	43	.57	1.02	.82	.74	.96	.68	.73	.96	.64
5	44	.70	1.15	.88	.88	.98	.70	.89	.97	.66
6	42	.78	1.35	.99	.99	1.08	.81	1.00	1.07	.72
7	44	.71	1.37	.80	.88	1.19	.77	.91	1.19	.64

RMSE in °C.

S, M and D as in Table 4.

TABLE 7. AKAIKE'S MFPE FOR MODELS FIT TO INDIVIDUAL SEASONS.

	Spring 1983	Spring 1984
Stat (SS)	.0003	.000007
Stat (WS)	.0113	.000495
Stat (NC)	.0075	.000516
	Summer 1983	Summer 1984
Stat (SS)	.025966	.164246
Stat (WS)	.166347	.414407
Stat (NC)	.44303	.72612

TABLE 8A: PACIFIC STATIONS

	Lat/Lon	t2	t4	t5	t6
Bering Sea	50N/165E	-	5/23	-	-
Papa	50N/145W	-	5/18	6/6	-
November	30N/140W	-	5/15	6/1	6/18
Victor	34N/164E	4/7	5/10	6/6	-
Mean		4/7	5/16	6/4	6/18

TABLE B: ATLANTIC STATIONS

	Lat/Lon	t1	t4	t4'	t5	t6	t7
Mike	66N/2E	3/27	-	5/7	5/19	6/13	-
Lima	57N/20W	3/15	4/22	-	5/12	6/14	-
Charlie	53N/36W	3/25	4/22	-	5/20	-	-
Romeo	47N/17W	3/28	-	5/4	5/20	-	6/25
Mean		3/24	4/22	5/5	5/18	6/13	6/25

TABLE 9a: PACIFIC STATIONS

	Lat	D1	D12	D23	D34	D4
Papa	50	110	110	30	30	10
Bering Sea	50	75	75	20	20	20
November	30	100	100	70	10	40
Victor	34	140	70	40	15	15
Mean	41	106	89	40	19	21

TABLE b: ATLANTIC STATIONS

	Lat	D1	D12	D23	D34	D4
Mike	66	160	80	80	40	15
Lima	57	340	260	110	50	30
Charlie	53	310	180	90	30	30
Romeo	47	230	120	40	40	10
Mean	56	260	260	80	40	21

TABLE 10a: PACIFIC STATIONS

	t1	t2	t3	t4	t5	t6
Papa	-	-	4/22	5/12	-	6/26
Bering Sea	-	-	4/19	5/22	-	-
November	3/13	-	4/23	5/22	-	-
Victor	-	4/4	5/1	-	6/6	-
Mean	3/13	4/4	4/26	5/19	6/6	6/26

TABLE b: ATLANTIC STATIONS

	t1	t2	t3	t4	t5	t6	t7
Mike	3/22	-	-	-	5/4	6/11	-
Lima	3/26	4/9	-	4/22	5/12	6/12	-
Charlie	3/23	4/10	4/17	4/23	5/18	-	6/23
Romeo	-	4/6	4/17	4/25	-	-	6/25
Mean	3/24	4/8	4/17	4/23	5/11	6/11	6/24

TABLE 1 1a: PACIFIC STATIONS

	D1	D12	D23	D34	D45	D56	D6
Papa	110	110	110	60	30	30	5
Bering Sea	90	90	90	50	15	15	15
November	110	20	20	60	15	15	15
Victor	140	140	40	25	25	10	10
Mean	112	90	85	49	21	18	11

TABLE b: ATLANTIC STATIONS

	D1	D12	D23	D34	D45	D56	D67	D7
Mike	70	110	110	110	110	30	10	10
Lima	350	170/ 90	170	170	90	40	30	30
Charlie	250	175/ 90	150	75	50	20	15	15
Romeo	250	175/ 175	110	90	25	25	25	10
Mean	260	173/ 115	135	110	70	29	20	15

Table 12 Parameters used in the numerical simulation

Parameter	Definition	Value
C_a	Drag coefficient of air	0.0027
C_w	Drag coefficient of water	0.0055
C	Empirical constant in the strength equation	20
e	Ratio of the principal axis of the elliptic yield equation	2
f	Coriolis parameter	$1.46 \times 10^{-4} \text{ sec}^{-1}$
h_0	Thickness limit between thick and thin ice	0.5 m
ρ_i	Density of ice	$0.91 \times 10^3 \text{ kg m}^{-3}$
ρ_a	Density of air	1.3 kg m^{-3}
P^*	Pressure constant	$2.75 \times 10^4 \text{ N m}^{-2}$
$\Delta x = \Delta y$	Horizontal grid spacing	127 km
Δt	Time step	1 day
ζ_{\max}	Nonlinear bulk viscosity	$(P/4) \times 10^9 \text{ kg s}^{-1}$
η_{\max}	Nonlinear shear viscosity	ζ_{\max}/e^2
ϕ	Turning angle of air	0°
θ	Turning angle of water	25°
H_i	Initialization ice thickness	3.3 m

END

DATE

FILM

DTIC

7-85